OPTICAL FIBRE SENSING FOR PHYSICAL AND BIOCHEMICAL HEALTH MONITORING

Chenyang He, MSc

Thesis submitted to the University of Nottingham
for the degree of Doctor of Philosophy

DECEMBER 2020

Abstract

This research focuses on the development and characterization of optical fibre sensors for physical and biochemical health monitoring. This requires fabrication and evaluation of the appropriate functional sensing films. Optical fibre sensing platforms have been considered as a promising platform due to a variety of advantages such as small dimensions, the capability of working in high electromagnetic interference (EMI) environments and the potential for remote sensing. This PhD thesis aims to investigate and evaluate the possibilities to use optical fibre sensors associated with functional coatings for physical or biochemical parameter measurements. Different functional coatings are deposited onto the optical fibre as the selective material to measure distinct parameters in health monitoring that include the following physical parameters: relative humidity and temperature; biochemical parameters: an anti-cancer drug and an antibody. Sensors were fabricated, characterised and calibrated in the laboratory and practical measurements of these parameters were undertaken, i.e. humidity monitoring during exercise for example.

The humidity sensor was fabricated by coating a silica nanoparticle based hydrophilic film on the optical fibre tip through the Layer-by-Layer technique. The developed humidity sensor has a linear response to relative humidity with a sensitivity of 3.02 mV/%RH (R^2=0.96) over the range of 50 to 80 %RH. The sensor then was applied in a human body humidity dynamic monitoring during an indoor exercise volunteer study to monitor the effect of textile properties (polyester and cotton) on humidity. Considering the body motion caused bending losses, a bare optical fibre was added in the sensing system for reducing the influence from motion artifacts. The promising performance of the humidity sensor demonstrated the capability of dynamic humidity monitoring and also showed that polyester provided better moisture wicking properties than cotton [1].

In the investigation of the temperature optical fibre sensors, two types of thermochromic material, the microencapsulated reversible thermochromic leuco ink *and thermochromic liquid crystal were deployed. These were deposited onto a fibre tip for temperature measurement due its advantages of having visualized thermochromism in the appropriate temperature range and also having low cost. The thermochromic liquid crystal coated optical fibre temperature sensor demonstrated a relatively higher sensitivity to temperature (~4.5 nm/°C) with no significant hysteresis compared to the reversible thermochromic leuco ink coated temperature sensors [2].*

Moreover, an optical fibre hybrid sensor for monitoring relative humidity and temperature was developed and explored in this thesis by coating the optical fibre tip with silica nanoparticles-based film for relative humidity, and a thermochromic liquid crystal for temperature. The developed sensor has a response to relative humidity with linear sensitivity of 0.43 %/RH% (R^2 =0.973) in the range of 55% to 90% and response to temperature with a linear sensitivity of 3.97 nm/°C (R^2 =0.993) in the range of 28 – 46 °C. The sensor also shows low crosstalk between each of the sensing parameters, indicating it has the potential to be both a humidity and temperature monitor in healthcare applications.

Regarding biochemical parameters, a long period grating optical fibre sensor associated with molecular imprinting polymer for Dabrafenib, a type of anti-cancer drug, has been developed and tested. The sensor demonstrated high sensitivity in serum of 15.2 pm/(μg·mL^{-1}) (R^2=0.992) when exposed to varying concentrations of Dabrafenib in serum. The selectivity of the proposed sensor was also investigated by comparing the response to Dabrafenib and a structurally similar compound, 2-Aminoquinoline with relative lower sensitivity of 2.5 pm/(μg·mL^{-1}) (R^2=0.994) [3].

An antibody (Immunoglobulin G – called "IgG") sensor was fabricated by combining the antibody affinitive peptide with a long period grating. The IgG-binding peptide supplies a controllable binding affinity compared to antibody-antigen interaction due to the non-covalent bonds of the peptide's amino acid, which allows development of a reversible optical fibre immunosensor. The antibody binding data of the developed sensor fits the Langmuir isotherm and the sensor demonstrated high sensitivity of 6.55 nm/(ng/mm^2) with a detection limit of 16.8 pg/mm^2 for the detection of IgG antibody. This peptide coated long period grating sensor showed a *low cross-sensitivity to IgM (Immunoglobulin M) as well. In addition, a microfluidic system has been developed for standardising conditions for flow of liquid over the sensor. The partial reversibility of the sensor has been demonstrated by an overall decrease in the response with repeated exposure of the sensor to IgG. The peptide-antibody affinity can be finely tuned by modification of the sequence of peptide's amino acid. This work is delayed by the lab closures in the period of COVID-19 pandemic. Therefore, distinct peptides with different amino acid sequence will be tested outside of this thesis.*

Author's research publications

Journal papers:

1. C. He, U. H. Ledezma, P. Gurnani, T. Albelha, K. J. Thurecht, R. Correia, S. P. Morgan, P. Patel, C. Alexander and S. Korposh, "Surface polymer imprinted optical fibre sensor for dose detection of dabrafenib," *Analyst*, no. 145, pp. 4504-4511, 2020.

2. C. He, S. Korposh, F. U. Hernandez, L. Liu, R. Correia, B. R. Hayes-Gill and S. P. Morgan, "Real-Time Humidity Measurement during Sports Activity using Optical Fibre Sensing," *Sensors*, vol. 20, no. 7, pp. 1904, 2020.

3. R. Sinha, F. U. Hernandez, C. He, S. Korposh, R. Correia, A.M. Norris, C. Liu, B.R. Hayes-Gill and S.P. Morgan, "Development and validation of a novel fibre-optic respiratory rate sensor (FiRRS) integrated in oxygen delivery devices," *Journal of Physics D: Applied Physics*, https://doi.org/10.1088/1361-6463/abd061.

4. Z. Tang, D. Gomez, C. He, S. Korposh, S. P. Morgan, R. Correia, B. R. Hayes-Gill, K. Setchfield and L. Liu "A U-shape fibre-optic pH sensor based on hydrogen bonding of ethyl cellulose with a sol-gel matrix," *Journal of Lightwave Technology*, https://doi.org/10.1109/JLT.2020.3034563.

5. L. Liu, F. Grillo, F. Canfarotta, M. Whitcombe, S. P. Morgan, S. Piletsky, R. Correia, C. He, A. Norris and S. Korposh "Carboxyl-Fentanyl detection using optical fibre grating-based sensors functionalised with molecularly imprinted nanoparticles," *Biosensors and Bioelectronics*, under review.

Conference papers:

6. C. He, U. H. Ledezma, P. Gurnani, T. Albelha, S. Korposh, R. Correia, S. P. Morgan, P. Patel and C. Alexander, "Detection of Dabrafenib using Optical Fibre Long Period Grating Sensor Modified with Surface Imprinted Polymers for Dose Detection and Prevention of Cancer Resistance." *Biophotonics Congress: Clinical and Translational Biophotonics. Optical Society of America,* Washington, DC, United States, pp. TTh3B. 2, 2020.

7. C. He, S. Korposh, R. Correia, B. R. Hayes-Gill and S. P. Morgan, "Optical fibre temperature sensor based on thermochromic liquid crystal." *Seventh European Workshop on Optical Fibre Sensors*, International Society for Optics and Photonics, Vol. 11199, pp. 1119908, 2019.

8. L. Liu, C. He, S. P. Morgan, R. Correia and S. Korposh, "A fiber-optic localized surface plasmon resonance (LSPR) sensor anchored with metal organic framework (HKUST-1) film for acetone sensing." *Seventh European Workshop on Optical Fibre Sensors*, International Society for Optics and Photonics, Vol. 11199, pp. 111990Z, 2019.

Acknowledgements

Firstly, I would like to express my gratitude to my wonderful supervisors Prof. Steve Morgan, Prof. Barrie Hayes-Gill, Dr Sergiy Korposh and Dr Ricardo Correia, for guiding me to pursue a PhD degree at the University of Nottingham, for their motivation, comments and patience throughout the project. Thanks for everything I have learned in this ‘big family’.

I also would like to thank my colleagues and friends in the research group: Liangliang Liu, Chong Liu, Ulises Hernandez, David Gomez, Qimei Zhang, Hattan Ballaji, James Bradbury, Sandor Erdody, Chalani Abeywardena, Nadia Afroze and Wan Zaki Wan for their support and help.

I would like to thank to Prof. Cameron Alexander, Prof. Poulam Patel, Pratik Gurnani and Thais Albelha for the meetings we had which helped me think about the fabrication of molecular imprinting polymer in anti-cancer drug detection project. Thanks to Dr Patrick Tighe and Dr Alexander Tarr for supplying peptides in the antibody measurements.

Moreover, I would like to thank the Nanoscale and Microscale Research Centre (nmRC), University of Nottingham for providing the training and permission to access the facilities. Thanks to Mike Parsley and Peter Rigby from LCR Hallcrest Ltd for thermochromic liquid crystal supply and useful discussions.

At last I would like to express my deepest gratitude to my wife, Xiaoyun Wu. It would not be possible without your priceless love and support throughout the period of my PhD.

Table of Contents

List of Figures

List of Tables

List of acronyms

(3-Aminopropyl) triethoxysilane (APTES)

2-(N-Morpholino)ethanesulfonic acid hydrate (MES)

2,2-Dimethoxy-2-phenylacetophenone (DMPA)

2-aminoquinoline (2-AQ)

3-(Trimethoxysilyl) propyl methacrylate (TMSPMA)

Absolute humidity (AH)

Analog-to-digital converter (ADC)

Carbon nanotubes (CNT)

Charge-coupled device (CCD)

Chloroform ($CHCl_3$)

Dabrafenib molecularly imprinted polymer sensor (DAB MIP sensor)

Deionised water (DI water)

Dimethyl sulfoxide (DMSO)

Disodium hydrogen phosphate (DSP)

Electromagnetic (EM)

Electromagnetic interference (EMI)

Endotracheal tube (ETT)

Enzyme-linked immunosorbent assay (ELISA)

Ethylene glycol dimethacrylate (EGDMA)

Fabry-Perot interferometer (FPI)

Fetal bovine serum (FBS)

Fibre Bragg grating (FBG)

Fourier transform infrared spectrometry (FTIR)

Full width at half maximum (FWHM)

Health Protection Agency (HPA)

Heat and moisture exchanger (HME)

Immunoglobulin (Ig)

Immunoglobulin G (IgG)

isopropyl alcohol (IPA)

Layer-by-Layer (LbL)

Light emitting diode (LED)

Limit of detection (LoD)

Liquid-crystal display (LCD)

Long period grating (LPG)

Mach-Zehnder interferometer (MZI)

Magnetic resonance imaging (MRI)

Membrane attack complex (MAC)

Methacrylic acid (MAA)

Michelson interferometer (MI)

Mitogen-activated protein kinase (MAPK)

Molecular imprinted polymer (MIP)

Moving Average Filter (MAF)

Multi-mode fibre (MMF)

N-(3-Dimethylaminopropyl)-*N*′-ethylcarbodiimide hydrochloride (EDC)

Nephropathia epidemica (NE)

Non-imprinted LPG (NIP LPG)

Numerical aperture (NA)

Optical fibre humidity sensor (OFHS)

Optical fibre sensor (OFS)

Optical fibre temperature sensor (OFTS)

Phase matching turning point (PMTP)

Phosphate buffered saline (PBS)

Polarization maintaining fibre (PMF)

Poly(allylamine hydrochloride) (PAH)

Poly(ethylene glycol) methacrylate (PEGMA)

Polydimethylsiloxane elastomer (PDMS)

Potassium dihydrogen phosphate (KDP)

Potassium hydroxide (KOH)

Reduced graphene oxide (rGO)

Refractive index (RI)

Relative humidity (RH)

Reversible thermochromic leuco ink (RT-leuco-ink)

Scanning electron microscope (SEM)

Silica Nanoparticles (SiO_2 NPs)

Single-mode fibres (SMF)

Sodium hydroxide (NaOH)

Standard deviation (SD)

Superluminescent Diode (SLD)

Surface plasmon resonance (SPR)

Tetrakis-(4-sulfophenyl)porphine (TSPP)

Therapeutic drug monitoring (TDM)

Thermochromic (TC)

Thermochromic liquid crystal (TLC)

Transimpedance amplifier (TIA)

Tungsten disulphide (WS_2)

Ultraviolet (UV)

Volatile Organic Compound (VOC)

Chapter 1: Introduction

1.1 Aims and objectives

It is important to monitor human health whether through physical parameters or biological parameters in clinical applications. In this thesis, the main aim of this research is to investigate and evaluate the deployment of optical fibre sensors with functional coatings for both physical and biochemical parameter measurements. Different functional coatings are deposited onto an optical fibre as the selective material to measure parameters highly relevant in health monitoring that include:

Physical parameters: relative humidity and temperature;

Biochemical parameters: an anti-cancer drug and an antibody.

Different optical fibre sensing platforms including in-fibre grating and reflection based optical fibre are investigated and applied with different functional coatings for specific parameter measurement.

The following objectives have been listed to achieve the aims of this research:

- A summary of the background knowledge about the target analytes: the role and importance of humidity, temperature, anti-cancer drug and antibody in health monitoring and their conventional detection techniques. Understanding the fundamentals, types and applications of optical fibre sensing platforms, especially reflection based and long period grating.

- To develop a reflection based optical fibre sensor that can be used for relative humidity sensing in healthcare application with a detectable range up to 90%.

- To investigate a thermochromic based optical fibre temperature sensor with appropriate measuring range that satisfies the human body temperature range (28 – 37 °C).

- To investigate an optical fibre sensor that can measure the relative humidity and temperature simultaneously.

- To develop an in-fibre grating based optical fibre sensor for particular anti-cancer drug (Dabrafenib) detection in serum.

- To investigate the possibility of reversible detection of antibody using a long period grating based optical fibre sensor.

1.2 Structure of the thesis

Chapter 1: Introduction provides the aims and objectives of the research, thesis structure and the novelty statement.

Chapter 2: Background and related detection techniques for target analytes describes the target analytes in different health monitoring applications. The summary of state-of-the-art sensing techniques for the detection of Relative Humidity (RH), temperature, Dabrafenib anti-cancer drug and Immunoglobulin G (IgG) is provided and their current main limitations will be discussed. The current optical fibre sensing techniques are also given.

Chapter 3: Optical fibre sensors introduction covers the introduction of the components for assembling an optical fibre sensor. The fundamental types of optic sensor platforms and configurations are introduced. The deposition methods used in this research are introduced.

Chapter 4: Relative humidity measurement using an optical fibre sensing system reports the progress over the development and fabrication of a reflection based relative humidity sensor which coated a hydrophilic functional film on the fibre tip. This chapter provides the methodology of the film fabrication, deposition onto the surface of an optical fibre tip and characterization by scanning electron microscope (SEM). A volunteer study using this sensor for monitoring humidity from human body during the exercise is presented.

Chapter 5: Investigation of thermochromic material in optical fibre temperature sensing shows the potential of temperature measurement using thermochromic material coated optical fibre sensor. This chapter includes the principle of different types of thermochromic material and methodology of the film deposition onto an optical fibre. The sensitivity and hysteresis towards temperature is examined and presented.

Chapter 6: Tip-based hybrid optical fibre sensor for simultaneous humidity and temperature measurement presents a hybrid optical fibre sensor for monitoring humidity and temperature simultaneously. The proposed sensor is associated with two functional films described in Chapter 4 and 5. The performance including response time, sensitivity and crosstalk of the hybrid sensor coated with the functional material proposed in Chapter 4 and 5 are described.

Chapter 7: Dabrafenib detection by using a surface polymer imprinted long period grating shows the fabrication of long period grating based molecular imprinted polymer Dabrafenib (a type of anti-cancer drug) sensor. This chapter describes the methodology of the film fabrication and deposition onto a long period grating. The performance of the sensor is reported.

Chapter 8: LPG based antibody measurement with flow system presents a long period grating optical fibre sensor associated with an antibody binding peptide for detection of antibody and a micro fluidic measurement set-up. The methodology of the functional coating fabrication and deposition is described. The performance of the sensor is reported.

Chapter 9: Conclusions provides the summary of the thesis and the future work.

1.3 Novelty statement of this research

This thesis demonstrated five optical fibre sensors that are fabricated using distinct functional coatings onto the optical fibre surface for sensing individual or multiple parameters, contributing to several physical or biochemical health monitoring applications.

As presented in Chapter 4, a new approach to monitoring humidity in garments based on optical fibre sensing was demonstrated. The optical fibre relative humidity sensor was developed by coating with a hydrophilic film (SiO_2 nanoparticles) through the Layer-by-Layer technique. In addition, bending losses were considered and partially compensated by including an uncoated reference fibre which enables measurements to be made during exercise. This study also provided the promising humidity monitoring results on the human body during sporting activity (cycling in this case) through a healthy volunteer study.

The most popular optical fibre temperature sensor used in healthcare application is based on a fibre Bragg grating which shows reliable performance and a wide sensing range [4]. However, the fabrication processes of in-fibre grating based sensors are relatively expensive and the experimental set-up for grating sensors are sophisticated. In this thesis a new approach to measure temperature in range of human body based on thermochromic material with optical fibre was investigated in Chapter 5. The thermochromic liquid crystal coated optical fibre sensor presented a visible response to temperature by tracking the wavelength shift of the reflection light peak in the measured spectrum.

In Chapter 6, a novel hybrid optical fibre sensor for measuring humidity and temperature simultaneously using the functional coatings described in Chapter 4 (hydrophilic film based on SiO_2 nanoparticles) and Chapter 5 (thermochromic liquid crystal) was developed. This hybrid sensor is able to measure humidity via the intensity change from the reflection spectrum while temperature measurement is achieved via tracking the wavelength shift within the same spectrum. In addition, the proposed sensor demonstrates low crosstalk between humidity and temperature. Chapter 6 also provided a calculation of absolute humidity using the measured temperature and relative humidity. The hybrid optical fibre sensor is potentially useful in clinical applications such as monitoring the range of moisture and temperature of air delivered to laryngectomized patients.

To the best of the author’s knowledge, there are limited publications for the deployment of an optical fibre sensing platform for the measurement of anti-cancer drugs. In Chapter 7, a long period grating optical fibre sensor modified with molecular imprinting polymer for Dabrafenib, a type of anti-cancer drug, measurement was reported. Such a sensor presented sensitive Dabrafenib detection with a limit of detection (1.71 $\mu g \cdot mL^{-1}$). Moreover, this Dabrafenib sensor presented a low cross sensitivity to a structurally similar compound.

In the last part of this thesis (Chapter 8), an antibody in-fluidic sensing system based on a long period grating coated with an antibody (Immunoglobulin G) affinity peptide was reported. In order to supply a fluid measurement condition, a silicone microfluidic chamber cast by a 3D-printed mould was used for holding the LPG sensor. Such a sensor presented an encouraging result in measuring Immunoglobulin G with a detection limit of 16.8 $pg \cdot mm^{-2}$. This work was delayed due to COVID-19 related lab closures. The rest of characterisation and experiments with extra peptides will be undertaken in future – outside of this thesis.

Chapter 2: Background and related detection techniques for target analytes

2.1 Introduction

This chapter covers the background information and a literature review related to the research conducted in this thesis. Initially, a brief introduction to the target analytes in different health monitoring applications are given. The summary of state-of-the-art sensing techniques for the detection of Relative Humidity (RH), temperature, anti-cancer drug and antibody are provided and their current main limitations discussed. Sensing techniques related to optical fibre sensing are introduced in Chapter 3.

2.2 Background and related works for target analytes

2.2.1 Temperature and humidity in health monitoring

Temperature and humidity are important parameters which should be controlled and adjusted in the application of human health [5] and clinical treatment [6]. Humidity can be divided into absolute and relative humidity: absolute humidity (AH) is the mass of water vapour in the air, relative humidity (RH) is the ratio of vapour partial pressure to the saturated vapour pressure at a given temperature [7].

Tsutsumi *et al.* reported that low indoor humidity level has positive effect on human wellbeing, however, subjects reported being more tired in the case of when the humidity reaches above 70% RH [8]. In sports performance, Maughan *et al.* reported that the cycling time to exhaustion was reduced by 8.6 min, 14.5 min and 22.1 min when environment relative humidity (RH) levels were increased from 24% RH to 40%, 60% and 80% RH respectively [9]. Although human core body temperature is maintained in a comfort zone even during the work and sports activities due to the thermoregulatory system [6], the skin surface humidity has a strong influence on thermal comfort [10].

In some clinical applications such as laryngectomy surgery, the upper respiratory tract is bypassed. As a result, the micro-climatic condition, especially temperature and humidity level in the nasal cavity and pharynx is changed. This can lead to some complications such as increased sputum production and chronic pulmonary disorders, all due to long term, abnormal nasal air-conditions [11]. In another example, moisture and temperature must be strictly controlled at an appropriate level during mechanical ventilation of critically ill patients, with the risk of respiratory mucosal injury, caused by drying and cooling air [12, 13]. A study by Zuur *et al.* presents an approximate clinical range of moisture and temperature of air delivered to laryngectomized patients [14]. It shows that typically air (AH: 8 mg H_2O/L, 22 °C/40% RH) is conditioned by a mechanical ventilator to 21 mg H_2O/L AH, 30 °C/70% RH in the upper respiratory tract using a heat and moisture exchanger (HME) and 13 mg H_2O/L AH, 28 °C/50% RH without. Monitoring temperature and humidity in real-time contributes a second safeguard for chronic patients considering the limited lifetime of an HME.

In chronic wound applications, temperature and moisture are important parameters that contribute to wound healing. Armstrong *et al.* conducted a long-term skin (18-month) care study of diabetic foot ulceration of 225 subjects in which subjects were divided into two groups (standard therapy and dermal thermometry). Both groups received regular foot care and footwear, but the dermal thermometry group patients' feet were measured daily using infrared skin thermometry. This study showed that a temperature difference between feet above ~2.2 °C can be a trigger of early detection signs of ulceration [15]. Clinicians also recognise that wound humidity levels play an important role in healing. High humidity levels (over-wet) contribute to maceration while low humidity levels can lead to drying out of the wound [16]. Despite this, there is no definitive range of permitted humidity recommended throughout the wound healing process. Therefore, measurements and quantification of the wound microenvironment in terms of humidity and temperature will help in the understanding of the healing process.

2.2.2 Fibre optic based humidity and temperature sensors

a. Humidity sensors

The most common commercial humidity sensors are electronic sensors and can be classified into either resistive- or capacitive-based sensor. Resistive-based humidity sensors rely on the change in conductivity of the sensing material exposed to moisture. Alternatively, capacitive-based sensors rely on the dielectric changes of a hygroscopic film due to the humidity change. Generally, electronic humidity sensors are low power consumption and inexpensive, although limited by the cross-sensitivities to some chemicals [17]. In some applications regarding clinic treatment, electronic humidity sensors are not recommended. For example, when a patient is in a magnetic resonance imaging (MRI) system that contains high electric/magnetic fields, the electronic devices could fail and there is a burning hazard to the patient. Compared to electronic humidity sensors, an optical fibre sensor (OFS) offers several advantages such as light weight, miniature size, flexibility, simple configuration and immunity to electromagnetic field.

A range of different approaches for optical fibre humidity sensing have been proposed including interferometers [18], evanescent wave interactions [19], in-fibre gratings (Bragg and long period gratings) [20-22], photonic crystal fibres [23] and reflection measurements [24]. Some recent optical fibre humidity sensors are listed in the table 2-1. The operating platform, sensing material, measurement RH range and response time of these proposed optical fibre humidity sensors have been given and compared. Most optical fibre humidity sensors require a hydrophilic material which can interact with water molecules, so that a property of the guided light (e.g. intensity or wavelength) changes with humidity levels. SiO_2 nanoparticles based optical fibre sensors show fast response time and appropriate RH range for measurement [24]. Optical fibre humidity sensors (OFHSs) based side-polished fibre [25, 26] and in-fibre grating, especially long period grating, [27, 28] are fragile due to long sensing region and in a practical application are high-cost, although they offer a wide measurement range and a quick response time.

Table 2- 1 Optical fibre humidity sensor (OFHS) techniques

Year	**Operating platform**	**Sensing material**	**Range**	**Response time**	**Reference**
2017	Side-polished fibre	MoS_2-coated etched single-mode fibre	20-80%	0.066 s	[25]
2016	Side-polished fibre	WS_2(Tungsten disulphide)	35-85%	1 s	[26]
2016	transmission spectrum	rGO (reduced graphene oxide) coated on hollow core fibre	60-90%	5.2 s	[29]
2006	Fluorescence lifetime	Ruthenium-based complex doped PTFE membrane	4-100%	2 min	[30]
2016	Tip based fibre	PAH/SiO_2 NPs	5-95%	1.13 s	[24]
2014	In-fibre grating $\Delta\lambda_B$	Carbon nanotubes (CNT) coated in SMF	20-90%	9.73 min	[31]
2015	In-fibre grating $\Delta\lambda_B$	Polyimide	11-97%	22 min	[28]
2016	Mach-Zehnder Interferometric	Graphene oxide coated on polarization maintaining fibre (PMF)-enlarged waist-PMF	60-77%	-	[32]
2016	Sagnac Interferometric	Non-coated Hi-Bi(high-birefringence) elliptical microfiber Panda fibre	30-95%	60 ms	[33]
2013	Mach-Zehnder Interferometric	Non-coated waist-enlarged tapers (SM–MM–SM)	35-90%	-	[34]
1999	Fabry–Pérot Interferometric	SiO2-Au: PDDA+/PSS-air cavity	11.3%-100%	1.5 s	[35]
2020	Tip based fibre	PAH/SiO2 NPs	25%-95%	-	This work

In this research, considering cost and simplicity of the fabrication process, the reflection sensor has been chosen as the operating platform while a hydrophilic functional film has been used for interaction with humidity. The detail of the humidity sensor fabrication and testing will be described later in Chapter 4.

b. Temperature sensors

Typically, commercial thermometers can be classified into two categories *via* technology: liquid thermometer and electronic thermometer. The conventional liquid-based thermometer normally is a glass tube with a bulb at one end. There is a liquid, usually mercury or coloured alcohol, filling in the bulb. The liquid expands in a uniform manner with the change of temperature. The mercury thermometer has been used in clinical monitoring if protected from the breakage of the glass tube. However, since 2009, Health Protection Agency (HPA) reported that the mercury thermometers could no longer be sold to the general public in the UK as mercury is a toxic heavy metal. In the electronic thermometer category, a thermocouple is the most popular tool in industrial applications. A thermocouple consists of two dissimilar electrical conductors to form an electrical junction, accordingly a thermocouple can be produced in a small size. A temperature-dependent voltage will be generated at the thermocouple terminals due to the thermoelectric effect and this voltage can be used for measuring temperature. Typically, thermocouple consists of two dissimilar metals, in some harsh situations, the tiny thermocouple is normally protected in a steel cover to avoid the damaging from chemicals and moisture.

An optical fibre temperature sensor (OFTS) initially is applied in situations where immunity to electromagnetic interference such as during radio frequency treatment and MRI. However, OFTSs have recently been developed in different temperature measurements such as in a ventilation system for critical care [36] and in an endotracheal tube (ETT) [37] which benefits from its tiny size and robust performance. Currently, OFTSs can be classified by the operating principle: in-fibre Bragg grating (FBG) [38], long period grating [39], temperature dependent fluorescence lifetime [40] and interferometric [41]. The temperature sensitivity of an FBG in the 1550 nm wavelength region is 10 pm/°C and can be used in extreme temperature conditions over the range from cryogenic (-150 °C) to high temperature (1100 °C) [42]. However, the cost of manufacturing and supporting instrumentation of gratings are relatively high, requiring a tuneable laser or high-resolution spectrometer. Moreover, when the gratings are deployed in optical fibre they are affected easily by strain, which means that a temperature measurement grating must be isolated from external strain. In another non-grating temperature optical fibre sensor, Tao *et al*. developed an epoxy-PAH (poly(allylamine hydrochloride)) membrane coated optical fibre temperature sensor. This sensor demonstrated that the light intensity (central wavelength of 505nm) of fluorescence emitted from the coating changed with temperature [43].

Table 2- 2 Optical fibre temperature sensor techniques

Year	**Operating platform**	**Sensing material**	**Range**	**Sensitivity**	**Reference**
2019	Long period grating	-	25-38 °C	460 pm/°C	[44]
2019	Optical fibre Fabry-Pérot interferometer	-	21.7-30 °C	115 pm/°C	[45]
2018	Balloon-shaped bent single-mode	-	20.7-31.7 °C	2.47 nm/°C	[46]
2015	Fibre Bragg grating	-	20-80 °C	27 pm/°C	[47]
2006	Reflection-based with fluorescence	$LiSrAlF_6:Cr^{3+}$	20-50 °C	0.5 µs/°C	[48]
2003	Reflection-based with thermochromic material	Lophine	10-35 °C	0.1 dB/°C	[49]
1999	Reflection-based with thermochromic material	Cobalt chloride	5-30 °C	-	[50]
2020	Reflection-based with thermochromic material	TLC	28-46 °C	4 nm/°C	This work

However, such optical fibre sensors based on the change in light intensity are highly dependent on stability of light sources, low insertion loss connectors and are subject to bending losses. An optical fibre coating with thermochromic material is another option for temperature sensing. Dybko *et al*. developed an optical fibre temperature sensor coating with cobalt chloride, a thermochromic compound, and this sensor showed a significant intensity change (at a wavelength of 660 nm) due to temperature change in range of 10 – 35 °C [51]. The study by Fernandez-Valdiviels *et al*. demonstrated an optical fibre temperature sensor coated with Lophine, another thermochromic material, in temperature measurement from 5 to 85 °C [52]. However, these studies of temperature sensing based on thermochromic material rely on the intensity change also. In this work, a new OFTS associated with thermochromic material has been developed for investigating a new approach wavelength shift-based temperature sensing. The details of fabrication and calibration will be described in Chapters 5 and 6.

2.2.3 Targeted anti-cancer drugs (Dabrafenib) in healthcare

An anti-cancer drug is one type of drug which is effective in the treatment of malignant or cancerous disease [53]. The mitogen-activated protein kinase (MAPK) pathway inhibitor Dabrafenib is one of the most widely used of the new generation of targeted anti-cancer drugs, with demonstrated efficacy in treating patients with melanoma [54] [55]. The use of Dabrafenib was approved in the European Union in August 2013 [56]. Figure 2.1 shows the chemical structure of Dabrafenib.

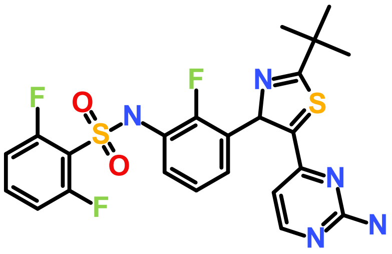

Figure 2. 1 Dabrafenib chemical structure.

Dabrafenib has specific activity against BRAF^{V600}-mutated melanoma cells [57], but although many patients are well-treated with this agent, nearly half of those administered with BRAF inhibitors exhibit progression of disease within ~7 months after treatment starts [55]. Although the mechanisms by which resistance to BRAF inhibitors develop are complex and multifaceted, important contributors include the dosing regime and the duration of exposure, as prolonged dosing below the therapeutic efficacy threshold inherently selects for resistant phenotypes. Since the therapeutic window varies for different patients and indeed across a wide range of therapeutics in addition to Dabrafenib, there is accordingly an urgent need for methods to monitor the dose of drug which the patient receives at the specific site where it acts. In the case of cancers, it is thus critical to measure the concentration of drug not just in the bloodstream overall, but in or near tumours, as these will not be the same over multiple time periods. In addition, it would be highly advantageous if any such measurement could be made in a minimally-invasive manner, and with methods that might be adaptable not just to Dabrafenib and BRAF inhibitors, but also to other drug types for application beyond cancer, such as infection and immunotherapies.

2.2.4 Optical fibre drug detection techniques

Currently, most drugs can be measured in blood or plasma practically using immunoassay or gas-liquid chromatography [58]. Generally, immunoassays are the conventional method due to the ease of operation and small amount of sample required. However, they carry many limitations, such as the interferences from haemoglobin, protein content, endogenous antibodies and structurally similar drugs. On the other hand, chromatography-based methods are still the gold standard for therapeutic drug monitoring (TDM) in clinical laboratories. They provide more advantages, for example, they are relatively free from interference and reduced drug cross reactivity. However, chromatography methods are usually time consuming due to the extensive sample preparation and expensive with high costs of the installation, method validation and personal training [58].

Compared to conventional measurement methods, optical fibre sensors have the potential to be a portable and relatively low-cost device for drug monitoring in clinical treatment. There are several optical fibre based drug sensors as listed in Table 2-3. For example, carbon nanotubes (CNTs) have been demonstrated for sensing Sulfamethaxazole with 0.892 μM limit of detection (LoD) in a cladding removed fibre sensor platform [59].

Table 2- 3 Optical fibre sensors for drug detection

Year	Operating platform	Sensing material	Target drug	LoD	Reference
2018	Evanescent wave fibre	aptamer-based	Cocaine	10.5 μM	[60]
2018	Long period grating	Molecular imprinting in TiO_2 films	Propofol	0.6 μM	[61]
2018	Cladding removed fibre	Carbon nanotubes (CNTs)	Sulfamethaxazole	0.892 μM	[59]
2014	Reflection-based fibre	Molecular imprinted polymers with fluorescein	Cocaine	-	[62]
2014	Long period grating	Molecular imprinted polymers	Vancomycin	1.8 nM	[63]
2020	Long period grating	Molecular imprinted polymers	Dabrafenib	3.3 μM	This work

In recent years, the techniques of molecular imprinting have been adapted beyond their well-established routes to selective separations, and particularly towards some innovative applications in sensing and analysis [64]. Imprinted polymers are increasingly being used as robust and versatile synthetic alternatives to antibodies for sensitive detection of analytes ranging from environmental contaminants through to anti-microbial drugs. However, converting a molecular recognition event into a signal which can be used to report that event has, in the past, been a major difficulty for imprinted polymers, which have often been prepared as monoliths that are difficult to process. Therefore, much recent research in the field of imprinted polymers has been concerned with generating the materials in a format which allows coupling to sensors or detection systems in a simple and rapid way, and in a manner which allows adaptation to multiple sensor formats [65, 66]. For example, a long period grating based molecular imprinting sensor for Vancomycin measurement has demonstrated a LoD of 1.8 nM for Vancomycin [63]. However, to the best of my knowledge, there is currently no optical fibre-based sensor for measuring Dabrafenib. Chapter 7 will describe a molecular imprinting technique applied in the long period grating for Dabrafenib detection.

2.2.5 Immunoglobulin G (IgG) in human body

An antibody, also known as immunoglobulin (Ig), is a large Y-shaped protein synthesized by white blood cells, the B-lymphocytes, that are used by the immune system to neutralize bacteria and viruses [67]. Hence, antibodies are major components of humoral immunity. Each antibody recognizes a unique molecule of antigen via antigen-antibody interaction during immune reaction. Antibodies are important biomarkers in the human body as they participate in the immune response and the concentration level will increase during the pathogen infection. There are five major classes or isotypes of immunoglobulins existing in human blood that are classified according to the type of heavy chain constant region and known as IgG, IgM, IgA, IgD and IgE. Figure 2.2 shows a schematic diagram of the structure and population of these five antibodies.

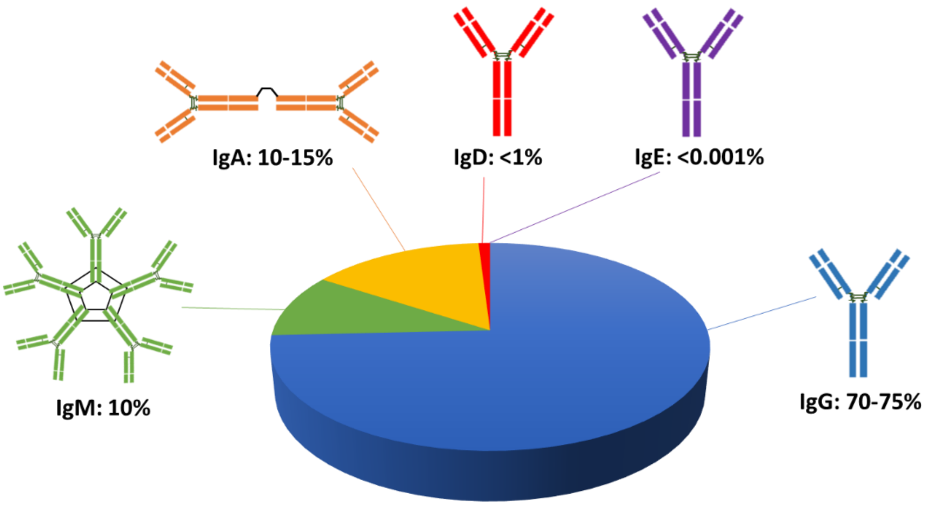

Figure 2. 2 Population of five types of antibodies in human blood [68].

IgM, made up of 5 antibodies, is mainly found in blood and produced for the primary immune response. It is the earliest antibody involved in the course of an infection [69]. IgA is mainly distributed to saliva, nasal and bowel fluid. It plays a significant role in the immune function of mucous membranes. Hence, the amount of IgA generated in mucosal membranes is greater than other isotypes of combined antibody [70]. IgD function has been a puzzle in immunology since its discovery more than fifty years ago [71] since its presence in mammals and possible exception of birds. IgD is present on the surface of B cells and important in the induction of antibody production. In 2009, IgD was found that has ability to bind to basophils and mast cells, activating these cells to generate cytidine to participates in the respiratory immune defence [72]. IgE is a type of antibody that has been found only in mammals. The main function of this type of antibody is immunity to parasites like helminths [73]. IgE is also represented in various allergic diseases such as allergic asthma, allergic rhinitis, food allergies [74]. IgG is the main antibody, representing ~75%, in human body. It should be noted that IgG is the only antibody which can pass through the placenta, accordingly it plays a key role of protection of newborn babies during the first month from birth. IgG also participates in type II and III hypersensitivity reactions. In type II hypersensitivity process, antibodies bind to antigen on the surface of a foreign cell that is perceived by immune system, attributing cellular destruction via membrane attack complex (MAC). On the other hand, antibodies bind to the soluble antigen in type III hypersensitivity. The formed circulating immune complex often deposited in the vessel wall of kidney and joints, causing a local inflammatory reaction [75]. In addition, the concentration level of IgG has clinical value in early stage diagnosis of diseases. For example, nephropathia epidemica (NE) has a rapid IgG response, 100% of patients (198 serum samples) are IgG seropositive by the 6th day in Klaus's study [76]. The different concentration level of IgG has been used for determining the differences between Mikulicz's disease and Sjögren's syndrome. A study showed that the serum IgG is increased in patients with Mikulicz's disease, but not in those with Sjögren's syndrome [77]. In a work by Allan *et al.,* clinicians have frequently taken blood samples from healthy adults and sepsis patients and the serum IgG levels were daily measured using standard lab tests [78]. The results represented positive trend indicating IgG measurement may be significant in sepsis.

2.2.6 Antibody measurement techniques

The conventional method of antibody (or antigen) measuring is based on enzyme-linked immunosorbent assay (ELISA) [79]. Although there are various antigen-antibody interactions used in the ELISA method, an enzyme-labelled antibody (or antigen) is always included. The enzyme activities are demonstrated by using a substrate which changes colour when modified by interacting with enzyme. Subsequently, the formed light absorption is measured and transferred to numeric values for further data analysing. There are four different types of ELISA: direct, indirect, sandwich or competitive ELISA depending on the antigen-antibody combination. Figure 2.3 illustrates an example of sandwich ELISA procedure.

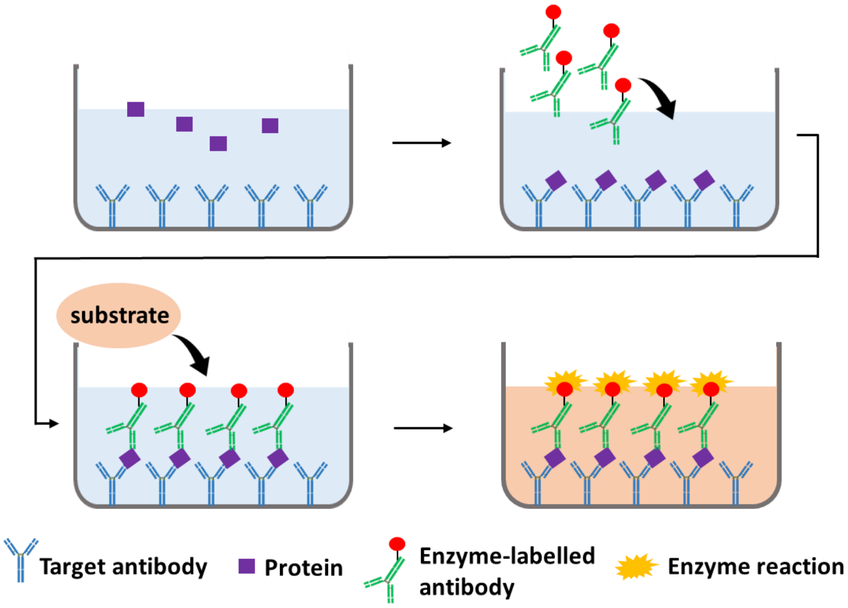

Figure 2. 3 Schematic of a basic sandwich ELISA method.

In the sandwich ELISA method, the target antibody (or antigen) has been immobilised on the surface of microplate wells firstly. Subsequently, these target antibodies are incubated with proteins that have specific binding sites with target antibody and then with another enzyme-labelled antibody. After washing with substrate, the enzyme activity on the surface of microplate well is measured. High sensitivity and specificity are the biggest advantage of using ELISA to recognize antibody or antigen. Typically, a conventional ELISA kit is available in a 96-well plate format, contributing the measurement of multiple samples in one go. Also, the protocols of ELISA are easy to follow. However, ELISA method exhibits the following disadvantages [80]: (1) Tedious procedure and long-time consumption required: the technique normally involves multiple incubations and washing steps. (2) Necessity for centralized laboratory equipment: sophisticated techniques, expensive laboratory equipment and culture media are required, and the bulky equipment causes no chance to be portable. (3) Relatively high sample volume is required (100-200 µL/well and a typical ELISA plate is 9-well based).

To satisfy the need for quick response point of care testing, researchers have focused on the development of distinct protein detection methods and devices, obtaining the low-cost, fast response and portable sensors, which could replace the conventional ELISA method. Optical fibre sensor, due to the tiny size, offers the possibility for minimization of sensing equipment used in the clinics. Recently, there are several optical fibre sensors with distinct operating platform for protein sensing. Table 2-4 lists some optical fibre protein sensor. Most optical fibre protein sensors have been applied in combination of fluorescent sandwich, surface plasmon resonance (SPR) technique. The antigen-antibody reaction or sandwich immunoassay with fluorescein are successfully transferred from ELISA method to optical fibre based antibody measurements [81, 82]. However, the strong antigen-antibody interactions mean that it is currently not possible to re-use the sensor in vivo with the state-of-the-art sensing technologies. Sensors can only be used as a ‘dipstick’ and not a method of continuous monitoring. Therefore, in this research, Chapter 8 will describe the development and initial experiment on peptide applied long period grating optical fibre sensor for IgG detection, which allows initially discovering the reversible measurement for antibody.

Table 2- 4 Optical fibre sensors applied in biological molecules detection

Year	**Operating platform**	**Sensing material**	**Target protein**	**LoD**	**Reference**
2020	Plastic optical fibre	Gold-sputtered	IFX protein	73.5 ng*mL^{-1}	[83]
2019	Tilted fibre Bragg grating	Gold-sputtered	Cytokeratin-17 protein	1 pg*mL^{-1}	[84]
2018	Long period grating	Silica and gold	IgM	15 pg*mm^{-2}	[85]
2016	Long period grating	Silica core gold shell nanoparticles	Streptavidin	19 pg*mm^{-2}	[86]
2016	Plastic optical fibre	Au-based coating	C-reactive protein	0.009 mg*L^{-1}	[87]
2016	Tapered optical fibre	Au-based nanocoating	Streptavidin	271 pM	[88]
1996	Cladding removed fibre	Fluorescent sandwich assay	Protein A	1 ng*mL^{-1}	[81]
1996	Long period grating	Peptide	IgG	16.8 pg*mm^{-2}	This work

2.3 Conclusion

This chapter has presented the introduction of target analytes used in this research. It has introduced state-of-the-art sensing techniques for the detection of Relative Humidity (RH), temperature, drug and antibodies. Typical types of optical fibre sensors in distinct target analytes have been listed. This review supports the aims and objectives of this research.

Chapter 3: Optical fibre sensors introduction

3.1 Introduction

An optical fibre sensor (OFS) offers several advantages such as lightweight, miniature size, flexibility, simple configuration and insensitivity to electromagnetic fields [4]. This chapter introduces light propagation in an optical fibre, optical fibre sensing techniques and the essential components for building an optical fibre sensing system. The sensing platforms used in this project will also be introduced, which include tip-based and long period grating optical fibre sensors. Finally, this chapter will provide a brief overview of the functional film deposition techniques used in this research.

3.2 Optical fibre sensor essentials

3.2.1 Light propagating in an optical fibre

Light is part of the electromagnetic spectrum that includes radio waves, microwaves, infrared radiation, visible light, ultraviolet (UV) "light", x rays and gamma rays [89]. In general, electromagnetic (EM) waves are made up of both oscillating electric (*E*) and magnetic (*H*) field components which are perpendicular to the direction of wave travel, and perpendicular to each other. As Figure 3.1 shows, the two components (electric and magnetic field) are plotted along the x-axis and y-axis, respectively. The z-axis presents the EM wave propagation direction and has the units of length or time. The distance between two adjacent peaks or valleys is the wavelength of λ if z-axis is distance, or the period of T if the z-axis is time. The frequency is defined as:

$$f = \frac{1}{T}, \quad T = \frac{1}{f} \qquad (3-1)$$

The speed of the light (c) in a vacuum is a universal constant, ~$3*10^8$ m/s. The relationship of wavelength (λ), frequency (f) and speed of light (v) in a particular medium is given by:

$$\lambda * f = v \qquad (3-2)$$

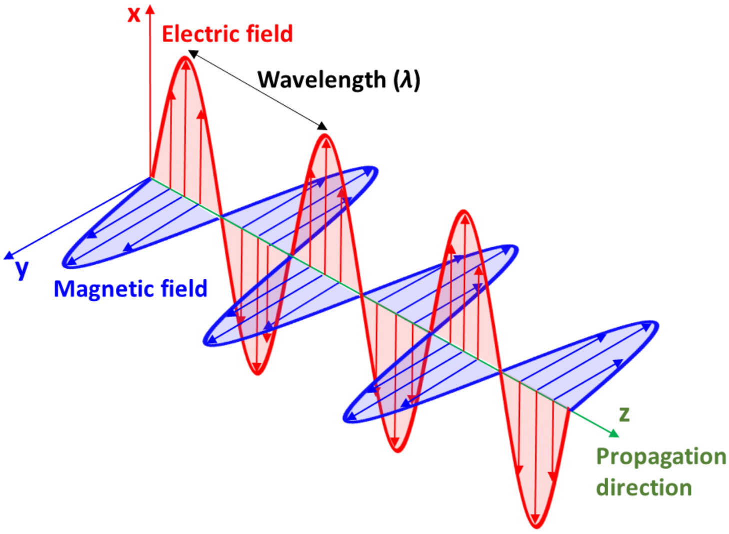

Figure 3. 1 Schematic of an EM wave propagation.

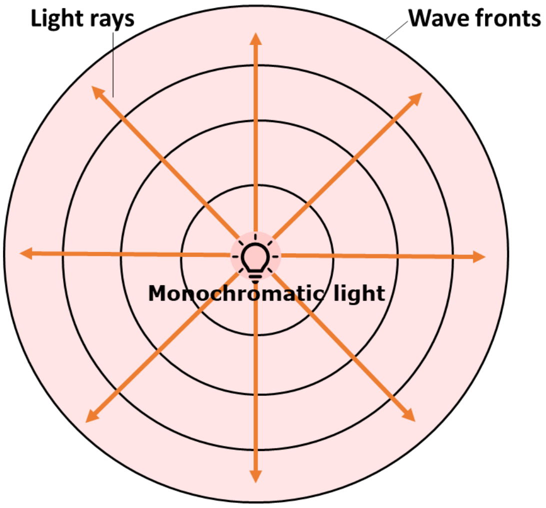

Figure 3. 2 Light rays and wave fronts from a light source.

Light waves are known as transverse waves because they are oscillating perpendicularly to the propagation direction. As Figure 3.2 shows, light radiates from a light source uniformly in all directions. The arrows, known as light rays, drawn from the light source to any point on a transverse wave indicate the direction that the wavefronts are moving. The refractive index (RI) is the ratio of the light speed in vacuum (*c*) to speed in particular material (*v*) and is governed by:

$$n = \frac{c}{v} \qquad (3-3)$$

Combining Equation 3-2 and 3-3, the wavelength (λ) of light in a given material is given by:

$$\lambda = \frac{c}{f * n} \qquad (3-4)$$

Total internal reflection

Figure 3.3 shows a light ray propagating between two mediums that have different refractive indices. Light is incident on the boundary between two different dielectrics following a path from a dielectric with n_1 to another dielectric with n_2 which is less than n_1, the angle of incidence θ_1 is less than refraction θ_2, as shown in Figure 3.3(a).

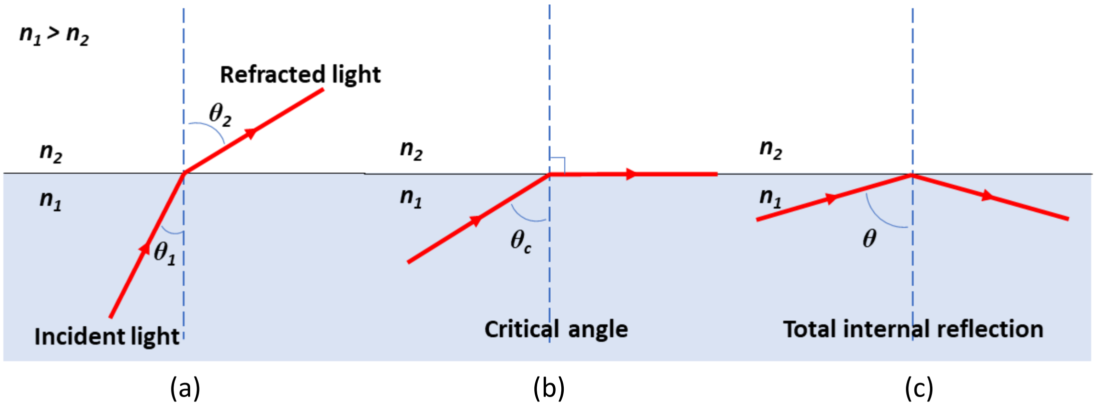

Figure 3. 3 Light incident on the boundary between two media: (a) refraction; (b) critical angle; (c) total internal reflection ($\theta > \theta_c$).

This effect is governed by Snell's law, (Equation 3-5) [90],

$$n_1 sin\theta_1 = n_2 sin\theta_2 \qquad (3-5)$$

When the angle of refraction θ_2 is 90°, a specific angle will be measured between incidence light and the normal at the interface, called the critical angle θ_c, as illustrated in Figure 3.3(b). At this moment, the refracted light is parallel to the boundary between two dielectrics and the value of the critical angle can be calculated by:

$$\theta_c = \sin^{-1}\left(\frac{n_2}{n_1}\right) \qquad (3-6)$$

Accordingly, when the angle of incidence θ is greater than θ_c, the light will be totally internal reflected, as shown in Figure 3.3(c). Under conditions of TIR ($\theta > \theta_c$), an evanescent wave occurs in the immediate vicinity point of the light propagating in the media. In most cases, the decay length of field amplitude of evanescent wave is normally short, hence this field intensity can be detected in the area closes to the interface. This field amplitude of evanescent wave is one of the common sensing principles in the optical fibre sensor. Late, some examples of optical fibre sensor based on evanescent wave will be given in this chapter.

Optical fibres, as a waveguide, retains light in the core of the optical fibre by the phenomenon of total internal reflection [91]. A typical optical fibre structure is shown in Figure 3.4, which includes a fibre core surrounded by a material of lower RI called the cladding layer. Subsequently, the optical fibre is coated with a protective buffer coating, which protects the fibre from mechanical damage.

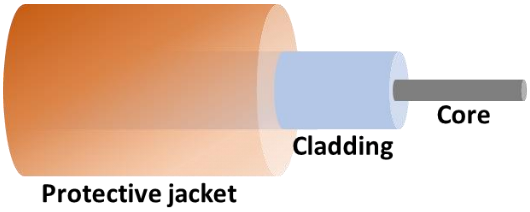

Figure 3. 4 Schematic diagram of a typical optical fibre.

Acceptance angle

Acceptance angle (θ_a) is another parameter of the optical fibre [91]. As Figure 3.5 shows, the acceptance angle (θ_a) is the maximum angle for propagating light with total internal reflection in an optical fibre [91].

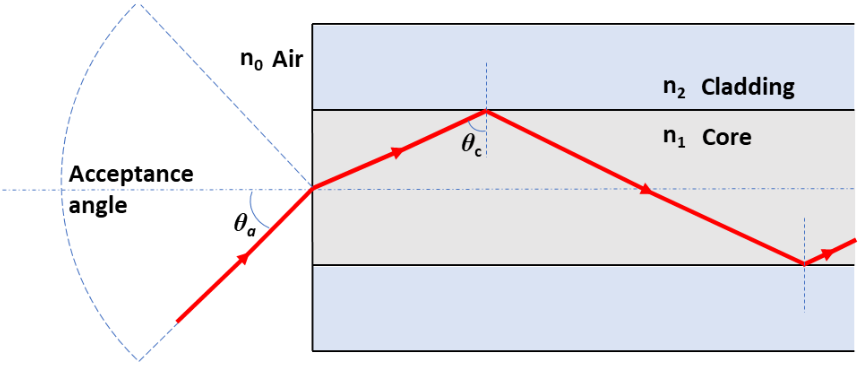

Figure 3. 5 The acceptance angle of an optical fibre.

For example, if the typical optical fibre containing cladding and core is operating in air (index of refraction n_0=1) and using the Snell's law (Equation 3-5):

$$n_0 * \sin\theta_a = n_1 * \sin(90^\circ - \theta_c) \qquad (3-7)$$

According to the basic trigonometrical formula:

$$\mathrm{Sin}(90^\circ - \theta_c) = \cos\theta_c\,; \quad sin^2\theta_c + cos^2\theta_c = 1 \qquad (3-8)$$

Equation 3-7 can be given by:

$$n_0 * \sin\theta_a = n_1 * \sqrt{1 - sin^2\theta_c} \qquad (3-9)$$

Combine Equation 3-6 and 3-9:

$$n_0 * \sin\theta_a = \sqrt{n_1^2 - n_2^2} \qquad (3-10)$$

Numerical aperture

For Equation 3-10, the numerical aperture (*NA*) can also be defined [8].

$$NA = n_0 * \sin\theta_a = \sqrt{n_1^2 - n_2^2} \qquad (3-11)$$

Normally, the NA of single-mode fibre and multi-mode fibre is less and greater than 0.2 respectively. On the other hand, for instance $n_0=1$ and NA=0.2, the acceptance angle (θ_a) is about 11.5°, which means light rays illuminating the fibre end face within ±11.5° can propagate in the fibre core.

Modes in an optical fibre

A set of guided light waves is called the modes of the fibre. These EM waves with same wavelength (same frequency) propagate in the optical fibre with different angles. The normalized frequency, also known as V-number, determines the number of modes supported by an optical fibre, which is a dimensionless quantity. The V-number is defined as [92]:

$$V = \frac{2\pi * a}{\lambda} * NA = \frac{2\pi * a}{\lambda}\sqrt{n_{core}^2 - n_{cladding}^2} \qquad (3-12)$$

where *a* is the radius of the optical fibre and *λ* is the vacuum wavelength. The number of supported modes (*M*) of an optical fibre can be estimated as:

$$M \approx \frac{V^2}{2} \qquad (3-13)$$

As the V-number increases, the number of modes supported by optical fibre increases.

Optical fibre types

In general, optical fibre can be classified into single-mode (mono-mode) and multi-mode fibre. Single-mode fibres (SMF) are commonly made of silica core with a diameter no more than ~10 μm and the cladding can be made of plastic or silica with ~125 μm diameter. There is only one mode propagating in a single-mode fibre because the core size. The normalized frequency (V-number) of single-mode fibre is less than or equal to 2.405. When V ≤ 2.405, single-mode fibres propagate the fundamental mode in the fibre core, high-order modes of light are lost in the cladding. Most of the power is propagated in the cladding of the fibres at low V values (≤ 1).

In terms of multi-mode fibres (MMF), the fibre core and cladding can be made of plastic or silica. The core/cladding diameter of common types of MMF are 50/125 μm and 62.5/125 μm although there are larger-core MMFs with hundreds of micrometres. Such MMFs support hundreds of guided modes transmitted through the large fibre core [8]. Light is easily launched into the optical fibre with a large core and higher *NA*. In addition to applications in communications, optical fibres can as we have seen be used as sensors for many different healthcare parameters.

3.2.2 Optional light sources in optical fibre sensing

There are three main considerations for choosing an appropriate light source in a sensing system: 1) bandwidth (operating wavelength); 2) optical power of the light source and 3) output stability. The operating wavelength of the light source not only should cover the propagating light wavelength transmitted in the optical fibre but needs to match the action wavelength that responds to the designated measurand of the system. Mismatch of the wavelength may cause weak response or unpredictable signal change to the measurand. The optical power also should be considered, for example, in the majority of applications, low optical power could affect the sensitivity or resolution of the sensor due to low signal to noise ratio. However, a powerful light source is not always appropriate. In some sensing situations associated with vulnerable target measured sample [93] or chemicals that photo-bleach [94], the output power of light source should be balanced at an appropriate level. High stability of light source intensity is also important when relating intensity to the measurand.

The common light sources used in this research can be distinguished by operating wavelength or bandwidth. White light (e.g. halogen lamp) is one of the most popular light sources in visible applications, which can cover all the visible range from 380 to 740 nm. Therefore, it is commonly used when monitoring the absorption spectrum of a dye compound [95] or performance of sensor applied with chromic materials [96]. Light emitting diodes (LEDs) are also popular due to low-cost, low power consumption, tiny size and multiple wavelength options from 240 to 900 nm. In contrast to LEDs and halogen lamps that have a relatively wide bandwidth, laser light has a high intensity and low beam divergence, accordingly lasers can be easily coupled into optical fibres compared to LEDs.

3.2.3 Optical detectors used in this research

The last essential component in a typical optical fibre sensing system is a detector that can receive and transform the optical signal into an electrical signal to be processed. The most common detector in an optical fibre sensing system is a photodiode (used in Chapter 4) and spectrometer that uses a charge-coupled device (CCD) detector (used in Chapters 5-8).

A photodiode is a semiconductor device that transforms the energy from light into an electrical current. A photodiode is a p-n junction, when a photon strikes the diode with sufficient energy, an electron-hole pair is created in the junction region. Holes move to the anode and electrons toward the cathode, and a photocurrent is produced. If there is no incident light on the photodiode, a small current is presented, also known as the dark current, which is usually found in the specification sheet of the photodiode. The dark current is mainly produced thermally and it should not be ignored in the situation with low light level [97]. Photodiodes are commonly used in intensity-based optical fibre sensing system, for example Chapter 4, especially in the integrated sensing unit design due to the low-cost and small size. By using a trans-impedance amplifier (see Chapter 4) the photo-current is converted into a voltage.

A CCD is another photo-detector commonly used for optical fibre sensing, especially when monitoring the whole spectrum. Figure 3.6 shows the schematic of a commercial spectrometer that consists of a CCD two-dimensional array that stores charge due to the incident light. In the CCD spectrometer, light from an optical fibre output passes through the slit (2) & optical filter (3) and illuminates the collimating mirror (4) and is reflected to the grating (5) that separates the light into its component wavelengths. After passing through a focusing mirror (6), an optical signal from distinct wavelengths illuminates the detector array (7). Subsequently, the intensity of each wavelength striking the relevant pixel (9), causes each capacitor to accumulate an electric charge that is stored in the well of the CCD. The electric charge is subsequently readout and transformed by the integrated circuit (8) into a voltage signal acquired by software controlled by a PC.

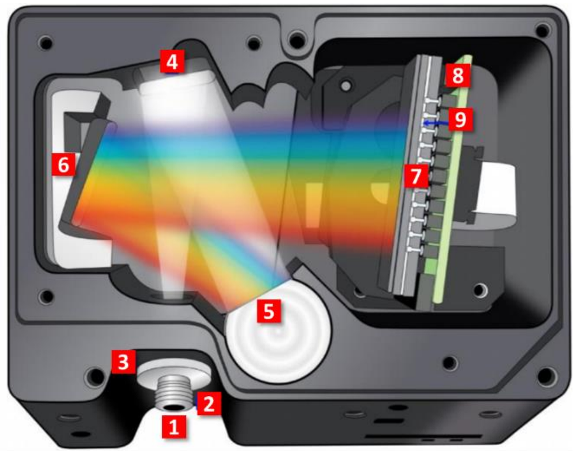

Figure 3. 6 Schematic of CCD spectrometer (the image is from Ocean optics [98]). (1) fibre optic connector, (2) slit, (3) optical filter, (4) collimating mirror, (5) grating, (6) focusing mirror, (7-9) CCD detector.

In contrast to the photodiode, a CCD spectrometer has advantages in optical fibre sensing applications as it provides dynamic monitoring of the whole spectrum and can be used to monitor changes in wavelength, although this type of detector is more expensive than a photodiode.

3.3 Optical fibre sensing classification

The general schematic of an optical fibre sensing system, shown in Figure 3.7, consists of a light source, optical fibre, sensing element and optical detector. Optical fibre sensors commonly can be classified by following three categories: sensing location, operating principle and sensing application [99]. Based on the sensing location, an optical fibre sensor can be divided into either extrinsic or intrinsic [100]. In an intrinsic sensor, measurands interact with the propagating light directly into the optical fibres, causing the optical signal changes of the reflection or transmission of light. On the contrary, the optical fibres simply act as a carrier getting light to and from an external sensing element in the extrinsic sensor [99]. Based on the sensing application, optical fibre sensors can be divided as follows: physical sensors: such as temperature, humidity and stress; chemical sensors: such as for gases, pH, or drugs; biomedical sensors: such as antibodies, proteins or glucose.

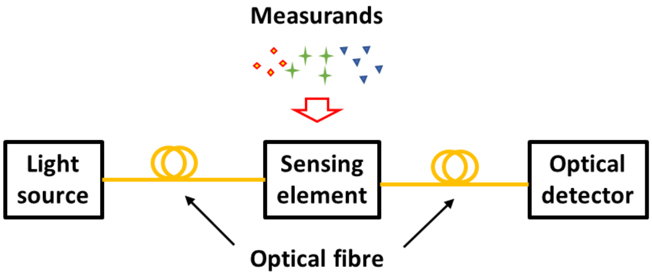

Figure 3. 7 General components of an optical fibre sensing system.

Based on the operating principle, optical fibre sensors can be classified as attenuation-based, absorbance, evanescent wave, grating based or interferometric sensors, as shown in Figure 3.8(a). An attenuation-based OFS is made by using a transducer to convert the measurand into an attenuation within the propagating light signal due to, for instance, a force or bending, as shown in Figure 3.9(a). In general, absorbance-based OFSs rely on specific chemical coating that contains dye compounds that respond within a wavelength range. For example, tetrakis-(4-

sulfophenyl)porphine (TSPP) film illustrates absorbance change at ~700 nm due to ammonia concentration change [101]. Evanescent wave sensors utilize the light in the cladding which leaks from the fibre core. There are a variety of approaches that can provide evanescent wave in the fibre structure, for instance a cladding removed fibre by mechanically stripping or chemically etching, a tapered or U-shape bend optical fibre [102-106]. In most circumstances (and in this thesis), the above types of approach are called intensity-based optical fibre sensors.

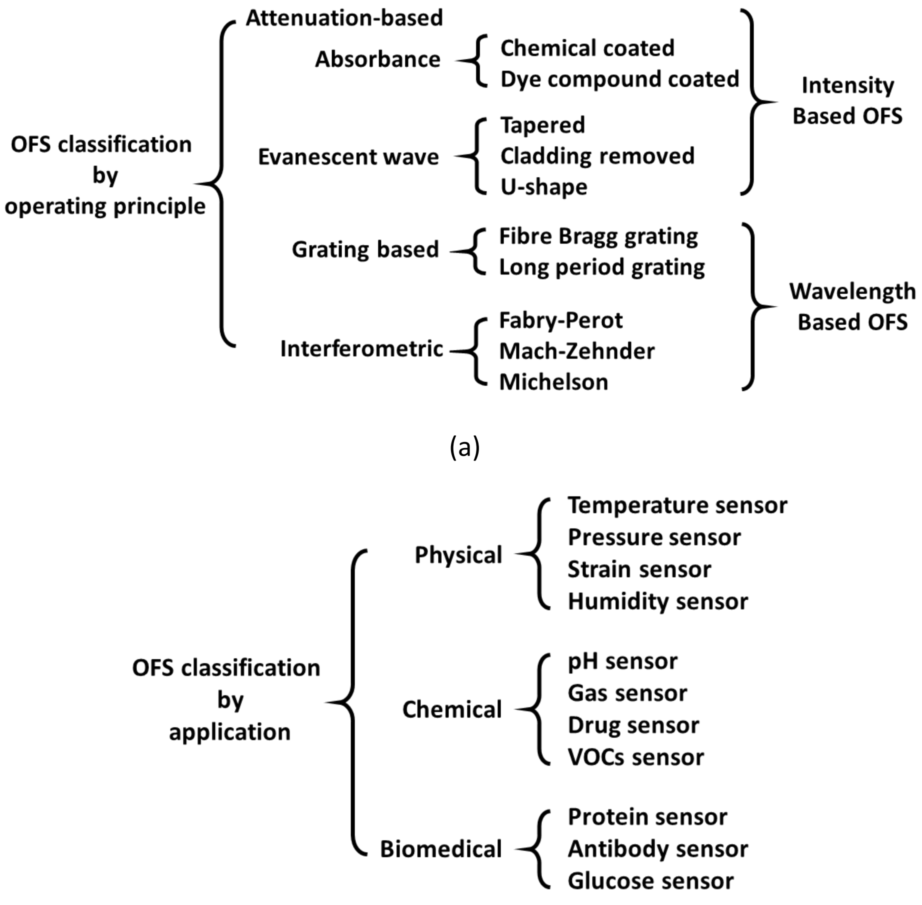

(a)

(b)

Figure 3. 8 General optical fibre sensing system classification by (a) operating principle; (b) application [4].

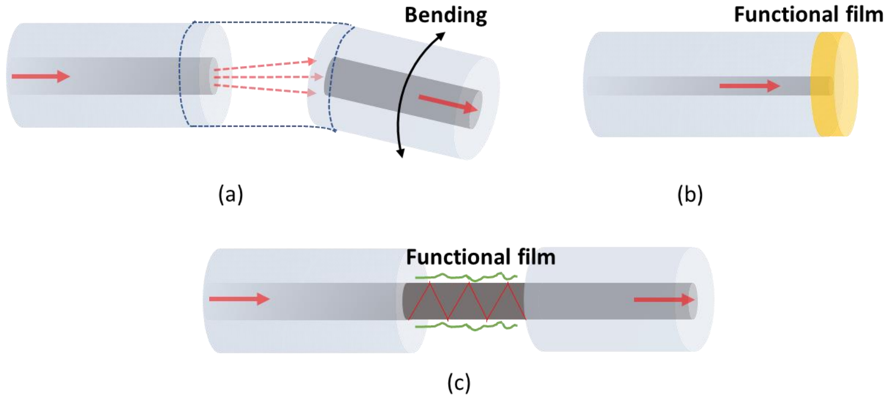

Figure 3. 9 Schematic of (a) attenuation-based bending OFS; (b) absorbance-based OFS; (c) evanescent wave based OFS.

On the other hand, wavelength-based OFSs are commonly classed as grating-based and interferometric OFSs, although some sensing protocols rely on the specific material which can cause wavelength shift due to the chemical properties, for example, chromic materials [2]. In general, a grating in an optical fibre is fabricated by generating a periodic modulation of the RI of the fibre core. The most common and reliable method is exposure to a periodic light pattern from a UV or femtosecond laser [107]. There are two classes of optical fibre gratings: (short period) fibre Bragg gratings (FBG) and long period gratings (LPG). The period of a typical FBG is sub-micron and the in-fibre grating promotes the coupling between the forward propagating mode and a backward propagating mode in the fibre core at a wavelength which satisfies the Bragg condition [108, 109]. Reflected light is in a narrow band of wavelengths back along the fibre while all other wavelengths are transmitted as shown in Figure 3.10. The Bragg wavelength of reflective light is defined by [110]:

$$\lambda_{Bragg} = 2 * n_{eff} * \Lambda \qquad (3-14)$$

where n_{eff} is the effective RI and Λ is the grating period. The FBG is sensitive to the parameters which affect the period of the grating and RI of the fibre. Typically, the FBG sensors have a length of ~5 mm and are commonly used for sensing temperature and strain.

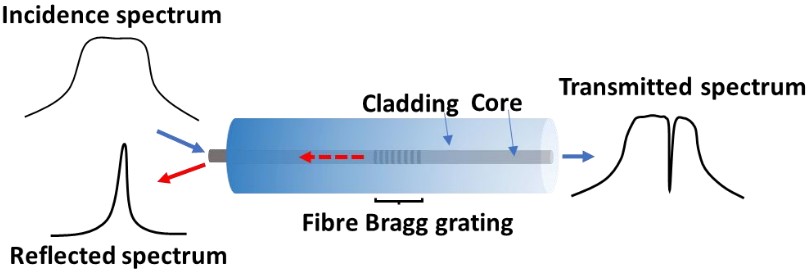

Figure 3. 10 Schematic of a fibre Bragg grating.

Contrary to FBG, LPGs commonly have periods that range from 100 μm to 1 mm and promote coupling between the propagating core mode and discrete forward propagating cladding modes [111]. The transmission spectrum will be significantly influenced by the external surroundings or the local environment as the propagating light involves cladding mode [112]. Therefore, LPG sensors are commonly used for certain measurands which contain temperature, strain, bending and RI changes [113].

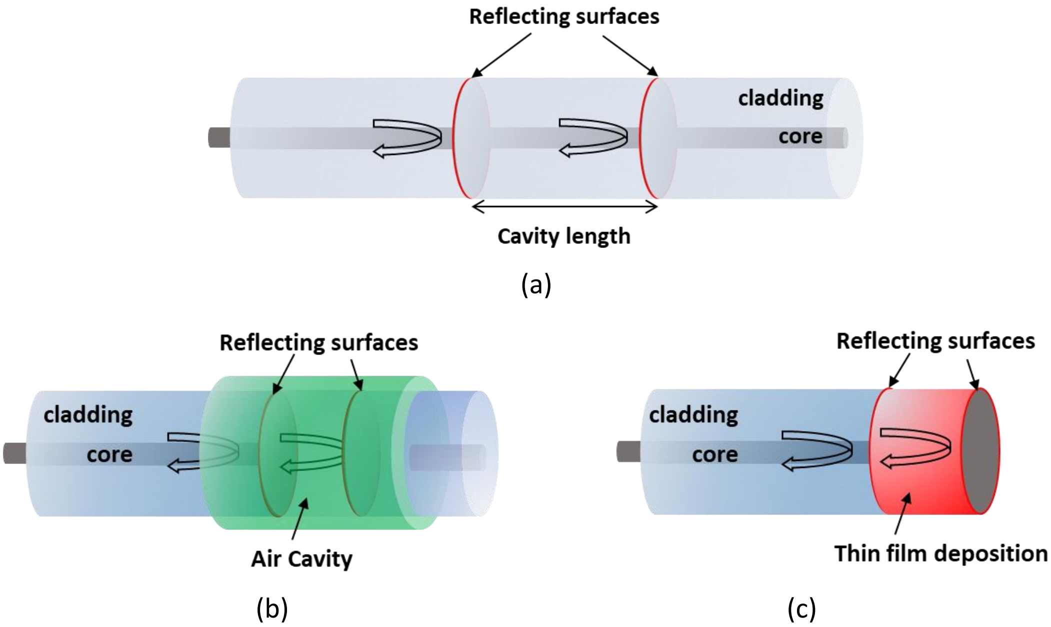

Figure 3. 11 Schematic of Fabry-Perot interferometric optical fibre sensing: (a) intrinsic FPI fabricated by two reflecting components; (b) extrinsic FPI fabricated by an external air cavity; (c) extrinsic FPI fabricated by thin film deposition.

Optical interferometry, another category of OFS, is also a popular platform for sensing development. The operating principle of an optical fibre interferometer is based on the interference between two beams which propagate along distinct optical paths in one or more fibres [114]. The following type of interferometers are used in optical fibre sensors: Fabry-Perot, Mach-Zehnder and Michelson.

The Fabry-Perot interferometer (FPI) consists of two parallel reflecting surfaces. In optical fibres, FPI sensors can be fabricated by generating two reflecting surfaces within or outside a fibre, which can be called intrinsic and extrinsic FPI respectively. A typical intrinsic FPI sensor is shown in Figure 3.11(a), the local intrinsic FP cavity can be formed by distinct methods, for example, chemical etching, fibre Bragg grating and micro machining. However, the high cost fabrication processes have been considered as the main limitation. Compared to the intrinsic FPI, extrinsic FPI is a simpler option for reflecting surface generation. In extrinsic FPI, two reflecting surfaces can be formed by the fibre ends in between the air cavity, shown in Figure 3.11(b), and by the boundaries of fibre-coating and coating-environment, in Figure 3.11(c).

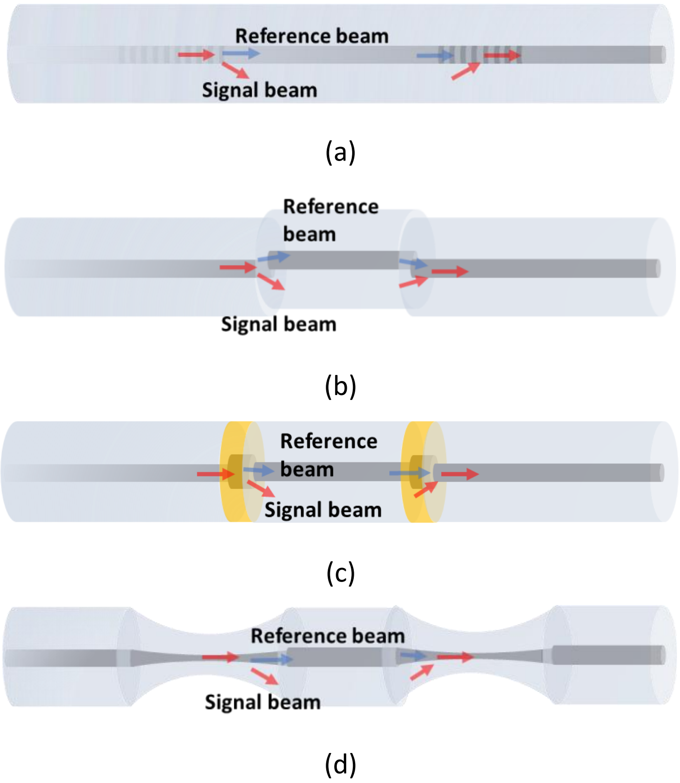

Figure 3. 12 Schematic of Mach-Zehnder interferometric optical fibre sensing using: (a) a pair of LPGs; (b) core mismatch; (c) larger core fibre segment; (d) a pair of tapered fibres.

Mach-Zehnder interferometer (MZI) optical fibre sensors commonly contain two independent arms for propagating light: sensing arm and reference arm. The sensing arm is exposed to the measurands while the reference arm is kept isolated from external variation [114]. The scheme of splitting and re-coupling of the light typically can be obtained by several waveguide schemes in optical fibres as shown in Figure 3.12.

Michelson interferometer (MI) optical fibre sensors can be described as half of MZI configuration. In a typical MI sensor, the propagating light is separated into two paths and then both light paths are reflected by a mirror. For example, shown in Figure 3.13, the coupling of the light can be obtained by an LPG or a waist-enlarged fibre with a mirror coating on the fibre tip. Both configurations have been demonstrated in relative humidity sensing applications [115, 116].

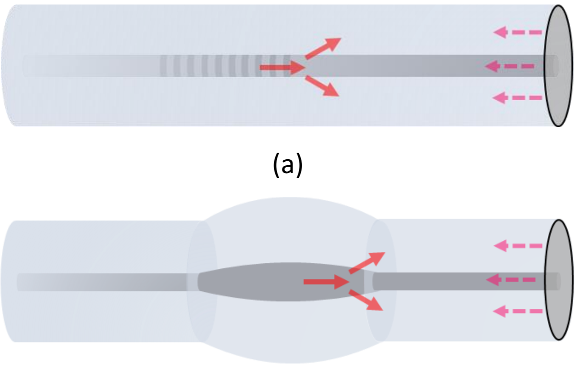

(a)

(b)

Figure 3. 13 Schematic of Michelson interferometric optical fibre sensing using: (a) LPG with a mirror; (b) waist-enlarged fibre with a mirror.

The research in this thesis focuses on the development of reflection-based optical fibre sensors and LPG based sensors. Humidity sensing based on hydrophilic film coating will be discussed in Chapters 4 and 6, temperature sensing based on thermochromic compound coatings will be discussed in Chapters 5 and 6. Dabrafenib, a type of anti-cancer medicine, and antibody measurement based on LPGs will be investigated in Chapters 7 and 8 respectively. The basics of reflection-based and LPG based platforms are covered in the following subsections.

3.4 Sensing platforms used in this research

3.4.1 Reflection-based optical fibre sensing platform

The reflection-based sensing platform can be used to implement several types of OFS, which depend on the fabrication process and properties of the functional film applied on the tip of fibre. The reflection-based sensing platforms used in this work rely on the optical fibre processed with a perpendicular and flat tip surface. Before functionalization, the optical fibre needs to be typically processed with a flat and smooth tip surface with 90° angle, which supplies a maximum reflective light from the end. Fibre cleavers and polishing machines are the common equipment for finishing the tip of optical fibre.

Extrinsic RI-based

As the name implies, an extrinsic RI-based optical fibre sensor relies on the RI change of an extrinsic functional coating on the tip surface. Typically, this type of optical fibre sensor contains at least one reflecting surface situated between optical fibre surface and the thin functional film, as shown in Figure 3.14. In this situation, the single reflection from the surface between fibre and film is dominated due to the aggregation caused rough surface morphology. The reflectance of each surface can be determined by Fresnel's law:

$$R = \frac{(n_1 - n_3)^2}{(n_1 + n_3)^2} \qquad (3-15)$$

where n_1, n_3 are the refractive indices of the fibre core and the functional thin film, respectively.

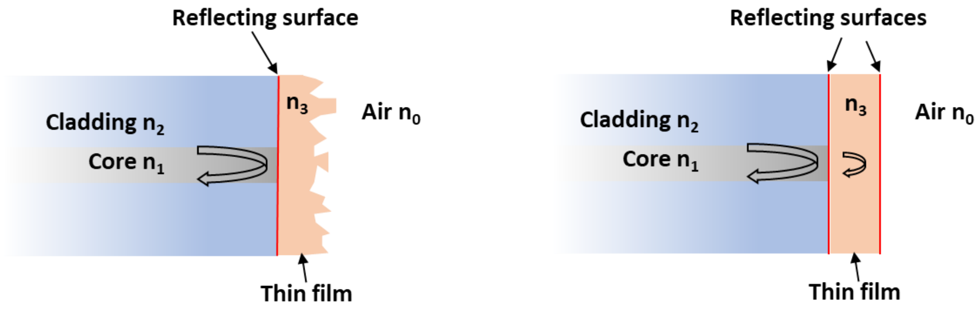

(a) (b)

Figure 3. 14 Schematic of extrinsic RI-based optical fibre sensor with (a) one reflecting surface and (b) two reflecting surfaces.

Two reflecting surfaces exist simultaneously once the second reflecting surface between film and air is generated. Generally, this case is described as an extrinsic FPI sensor (introduced in section 3.3). Typically, the RI of fibre core and cladding is a constant. The RI of the thin functional film relies on the interaction between film and surrounding measurands. The value of n_3 will be changed once the film material interacts with the target analyte through physical adsorption or chemical binding. Accordingly, the reflected light will be changed due to the interaction between film and measurands. The humidity sensor described in this research is based on this principle, Chapter 4 will show more details about the sensor fabrication and testing.

Extrinsic thermochromism-based

The second type of reflection-based optical fibre sensor used in this work relies on the thermochromic property of the coating material. As the name implies, the thermochromic (TC) materials are commonly applied for temperature sensing. In this sensing approach, the TC material changes colour with temperature decrease or increase and an optical fibre is incorporated to capture these optical signal changes. There are a variety of TC materials depending on the thermochromism principle. The two most common approaches are based on leuco dyes and liquid crystals. The principle and application of these TC materials will be discussed in Chapter 5.

For the fibre tip functionalization, dip coating and Layer-by-Layer methods are commonly used in coating a film on the fibre tip. In this work, two dip coating machines have been investigated: dip coating machine with built-in oven for thermochromic material coating; and Layer-by-Layer coating robot for hydrophilic material coating, which will be described in Section 3.5.

3.4.2 Long period grating platform

An LPG couples the light between the propagating core (fundamental) mode and discrete forward propagating cladding modes, as shown in Figure 3.15. The attenuation bands that can be observed in the transmission spectrum of the fibre containing an LPG are due to coupled cladding modes. The central wavelength of the attenuation bands will be influenced by the surrounding environment, such as changes in temperature and surrounding RI [111].

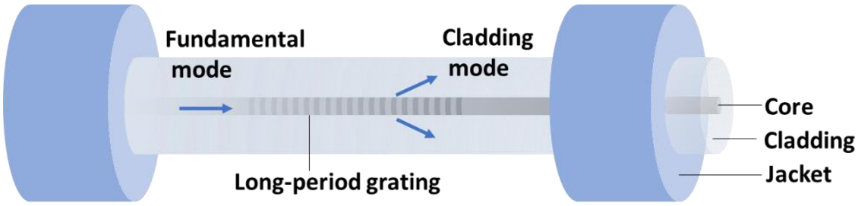

Figure 3. 15 Schematic of long period grating.

LPG fabrication

The LPGs used in this work have been manufactured using a UV laser with a custom-made amplitude mask. The main components used in the fabrication process (Figure 3.16) are: photosensitive optical fibres (PS750, Fibercore); linear stage (M-405.DG, physikinstrumente PI) with V-groove fibre holders for translating the fibre in a perpendicular direction to the laser beam; frequency-quadrupled Nd:YAG UV laser (Photonic Solutions Ltd, Continuum minilite I, operating at wavelength of 266 nm, 100 ns pulse duration, 12 mW power) for side-illuminating the fibre; customized amplitude mask (1Cr18Ni9Ti, Suzhou Sunshine Laser Technology Co., Ltd); CCD spectrometer (HR4000, Ocean Optics); tungsten-halogen light source (HL-2000, Ocean Optics).

In the fabrication process, the buffer jacket of the optical fibre over the proposed LPG section is first removed by a fibre stripper and cleaned by wiping with 2-propanol. The optical fibre is placed on the translation stage and aligned on the V-groove. The amplitude mask is placed in front of the fibre on the stage and facing the UV laser beam. Illumination is adjusted to ensure that the light passes through the mask and strikes the optical fibre. During the fabrication, the stage is moved at a constant velocity at an optimal speed of 0.02 mm/s. Below this speed, the fibre would be broken due to the overloaded strike from the laser, whilst above this, the LPG attenuation band would be too small to be used as a sensor.

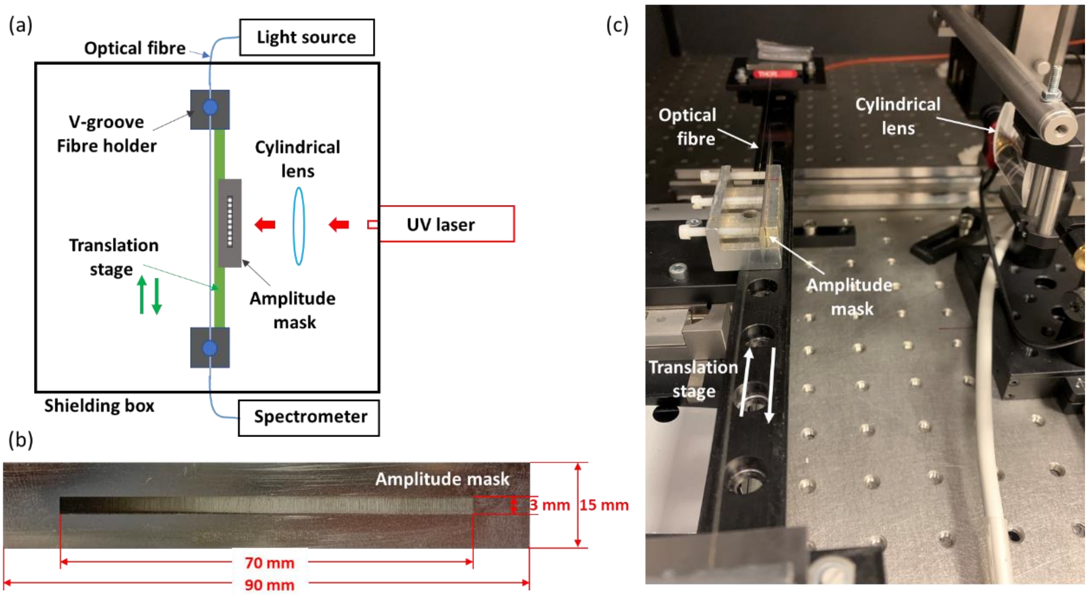

Figure 3. 16 (a) Schematic of long period grating fabrication set-up. (b) Customized steel alloy amplitude mask. (c) Photograph of the fabrication set-up.

LPG theory

The central wavelengths (λ_{cw}) of attenuation bands occur in the transmission spectrum of an LPG can be obtained by [117]:

$$\lambda_{cw} = \left[n_{eff\ core} - n^{i}_{eff\ clad}\right] * \Lambda \qquad (3-16)$$

where the $n_{eff\ core}$ and $n^{i}_{eff\ clad}$ are the effective refractive indices of the fibre core and *i-th* cladding mode [118], respectively, Λ is the grating period. Considering the three layer theory [117], the $n_{eff\ core}$ is determined by the RI of core and cladding and the $n^{i}_{eff\ clad}$ is determined by the RI of core, cladding and the external environment surrounding. Hence, the value of $n^{i}_{eff\ clad}$ can be affected by the RI changes of surrounding media representing a wavelength shift of the attenuation band in the spectrum of LPG. The minimum transmission depth of the attenuation band, T_i, is governed by [111]:

$$T_i = 1 - sin^2(\kappa_i * L) \qquad (3-17)$$

where T_i is the transmission at *i-th* cladding mode, κ_i is coupling coefficient for *the i-th* cladding mode and *L* is the length of LPG.

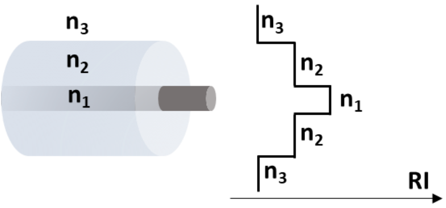

Figure 3. 17 Configuration of three layer theory [117]: n_1, n_2 and n_3 are the RI values of fibre core, cladding and surrounding respectively.

The LPG is sensitive to the surrounding RI, the sensitivity of attenuation band is maximum when the phase matching occurs at the phase matching turning point (PMTP) [119]. The PMTP is defined as a point where the slope of the phase matching changes from positive to negative. The phase match curves, determined by Equation 3-16, from 14th linearly polarized mode (LP_{014}) to LP_{020} are shown in Figure 3.18. For example, a case of LPG with a period ~110 μm, there is an attenuation band at ~700 nm wavelength corresponding to the coupling of LP_{018} and PMTP at ~900 nm wavelength corresponding to the coupling of LP_{019}.

Figure 3.19 explains the evolution of the transmission spectrum of an LPG operating near the PMTP [120]. As Figure 3.19(a) shows, the grating period satisfies the phase matching condition to 18th cladding mode (LP_{018}), but it does not couple to the LP_{019}.

Hence, the resulting transmission spectrum of the LPG is shown in Figure 3.19(b). If there is an increase of effective RI of cladding modes caused by the change in the optical thickness of the coating (product of the RI and geometrical thickness) then the phase matching curve has moved upwards as shown in Figure 3.19(c). The horizontal grating period line is tangential to the phase matching curve at PMTP, resulting in the generation of an attenuation band corresponding to the coupling to the LP_{019} cladding mode and a blue shift at central wavelength of the LP_{018} cladding mode. Further increase of the optical thickness of the coating surrounding LPG causes the coupling to the same cladding mode (for example LP_{019}) at two wavelengths (Figure 3.19(e)). Hence, the attenuation band of LP_{019} cladding mode splits into dual attenuation bands.

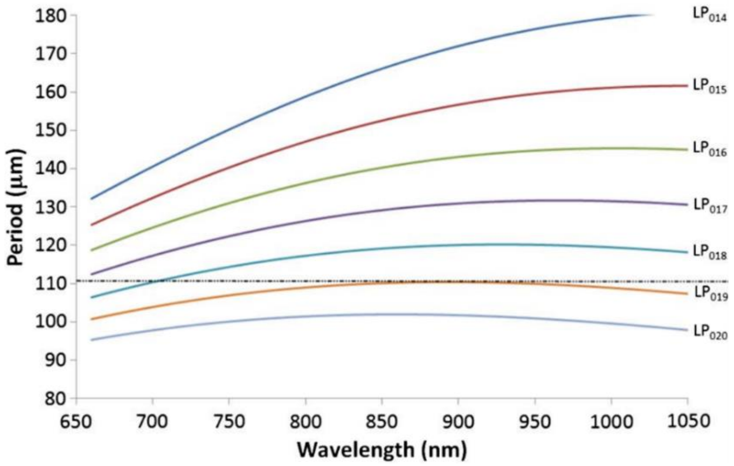

Figure 3. 18 Phase matching curves of 14th to 20th cladding mode [119].

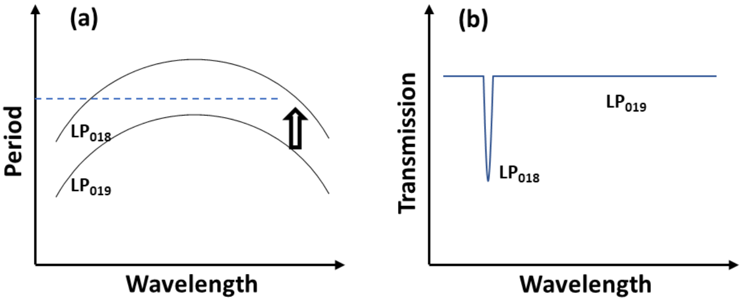

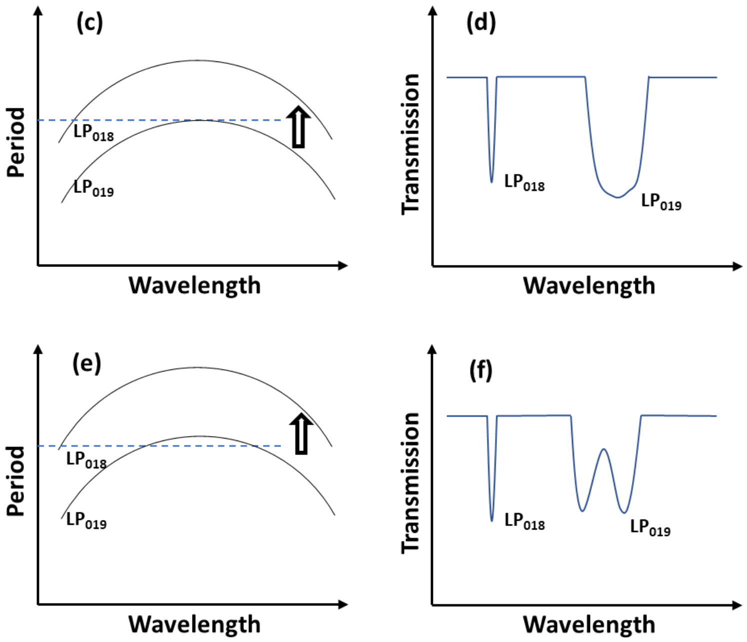

Figure 3. 19 Illustration of transmission spectrum of LPG working near or at PMTP, the arrow presents direction of the shift of phase matching curve at the increase of the effective RI of the cladding mode due to the optical thickness increasing (modified from [120]).

An example shows the transmission spectrum recording of LPG with a period of 111.5 μm after starting fabrication (Figure 3.20) described in section 3.4.2. It shows that the attenuation band of cladding mode LP$_{019}$ starts appearing at a central wavelength of ~820 nm after 12 mm and then the attenuation becomes stronger with increased length (achieved by translating the optical fibre).

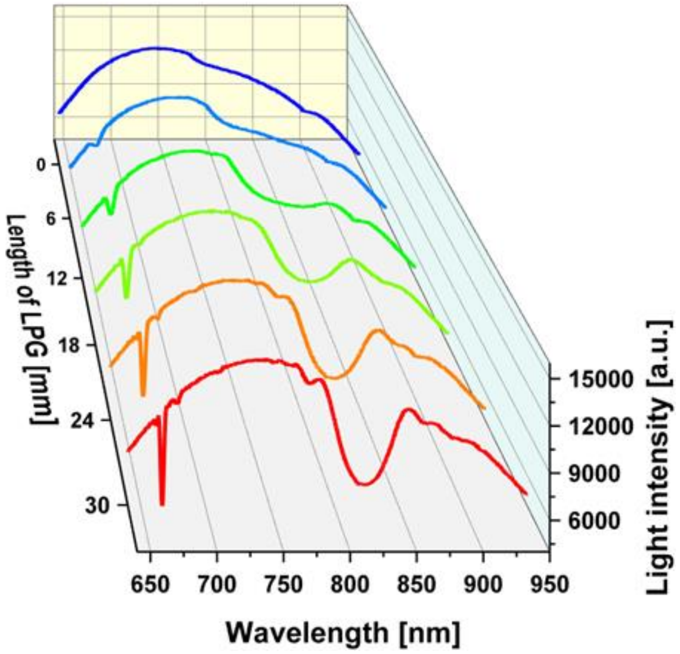

Figure 3. 20 Transmission spectra of LPG with different length from 0 (blue) to 30 mm

(red) during fabrication process.

LPG temperature and surrounding RI sensitivity

The temperature sensitivity of the LPG sensor is related to the period of the grating, the material of optical fibre, and the order of the coupling cladding mode. The temperature sensitivity can be understood by differentiating Equation 3-16 [121]:

$$\frac{d\lambda}{dT}=\frac{d\lambda}{d(\delta n_{eff})}\left[\frac{dn_{eff}}{dT}-\frac{dn_{eff\ clad}^{i}}{dT}\right]+\Lambda\frac{d\lambda}{d\Lambda}\frac{1}{L}\frac{dL}{dT} \qquad (3-18)$$

where λ is the central wavelength of the attenuation band, T is the temperature, n_{eff} is the effective RI value of the fundamental mode propagating in the core, $n^i_{eff\ clad}$ is the effective RI value of the coupling cladding mode, $\delta n_{eff} = n_{eff} - n^i_{eff\ clad}$ and Λ and L is the period and length of the LPG, respectively. The first term of right-hand side of the Equation 3-18 corresponds to the composition material of the fibre. When temperature changes, the differential RI between fibre core and cladding will change. This contribution relies on the material composition of the fibre and the order of the coupling cladding mode. The second term in the equation is attributed to the grating period [111]. In most LPG applications temperature cross-sensitivity needs to be addressed. In laboratory conditions environmental temperature can be controlled but alternatively an additional LPG can be used for temperature compensation [122].

The surrounding RI sensitivity of LPGs derives from the dependence of the phase matching condition on the effective RI of the cladding mode ($n^i_{eff\ clad}$). The effective RI of the cladding mode is dependent on the difference between the RI of cladding and surrounding environment. The central wavelength of the attenuation band thus responses to this RI change. The RI sensitivity reaches to the greatest level when the surrounding RI approaches the RI of cladding [111].

In this research, LPG sensors are fabricated at or near the PMTP to obtain the maximum sensitivity of the attenuation band. The operation of these LPG sensors is based on the measurement of changes in the optical properties (RI) due to interactions between a functional film coated on the LPG region and surrounding analytes. Chapters 7 and 8 will give details about different LPG sensing applications.

3.5 Functional film deposition methods in this research

Bare optical fibres are commonly used for communication applications as they are made of chemically inert material (e.g. silica) which does not interact with individual physical or chemical targets for sensing. With bare optical fibres, some pre-processed sensing platforms such as interferometric and grating based optical fibre sensors would only be used to measure physical parameters, for example, temperature, strain or RI. Hence, functional film coatings that respond to specific targets are required in the majority of chemical and bio-sensing applications. The deposition methods utilised in this research are described in this Section.

3.5.1 Layer-by-Layer technique

The Layer-by-Layer (LbL) technique is a prevalent assembly method for coating functional thin films on substrates (an optical fibre in this research). In the LbL assembly process, charged materials are adsorbed on the optical fibre surface, and after washing, oppositely charged materials are adsorbed on top of the first layer. Hence, a single bilayer with certain thickness is generated through this cyclical process and this can then be repeated until the optimized thickness is achieved [123]. The basic LbL technique can be classified into several categories, as shown in Figure 3.21: (a) spin; (b) electromagnetic; (c) spray; (d) immersive. Spin based LbL assembly method utilizes the common coating technology of spinning a substrate, material 1 and 2 are deposited successively onto the surface. The electromagnetic LbL assembly method is based on coating electrodes in polymer solutions to achieve multiple layers on the substrate. Spray and spin based LbL assembly method is not suitable for use in coating optical fibre sensor compared to other two methods due to area limitation of the surface to be coated.

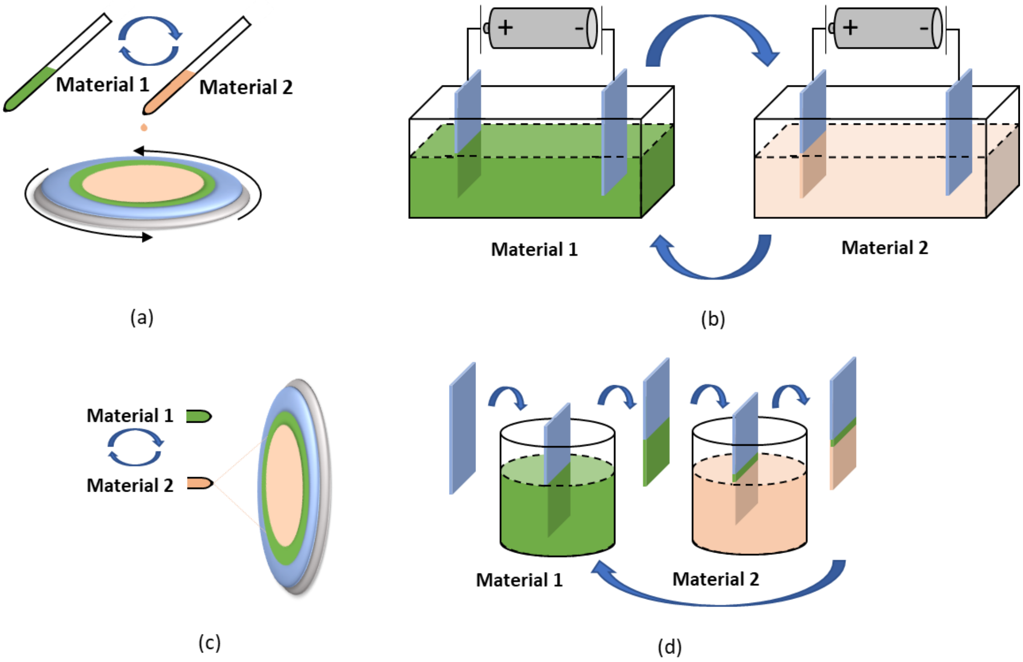

(a)

(b)

(c)

(d)

Figure 3. 21 Layer-by-Layer deposition methods: (a) spin; (b) electromagnetic; (c) spray; (d) immersive coating.

In this research, the LbL deposition method is based on immersive self-assembly due to the limited size of optical fibre and the low processing cost. Considering the coating area is on the fibre tip (except for grating-based OFS) in this research, a custom-made LbL coating robot has been developed for automatic layer deposition. The LbL coating robot consists of two stepper motors with vertical and horizontal direction stages (STANDA, 8MT175-50, Italy), as shown in Figure 3.22, which are controlled by a microcontroller (Arduino Nano, USA) with two stepper motor drivers (A4988, Pololu, USA). During the deposition process, the optical fibre is held in the vertical stage and inserted into or withdrawn from the coating solutions which are held on the horizontal stage.

LbL deposition technique is used for humidity functional film deposition in Chapters 4 and 6, and as part of the functionalization process for LPG antibody sensing in Chapter 8.

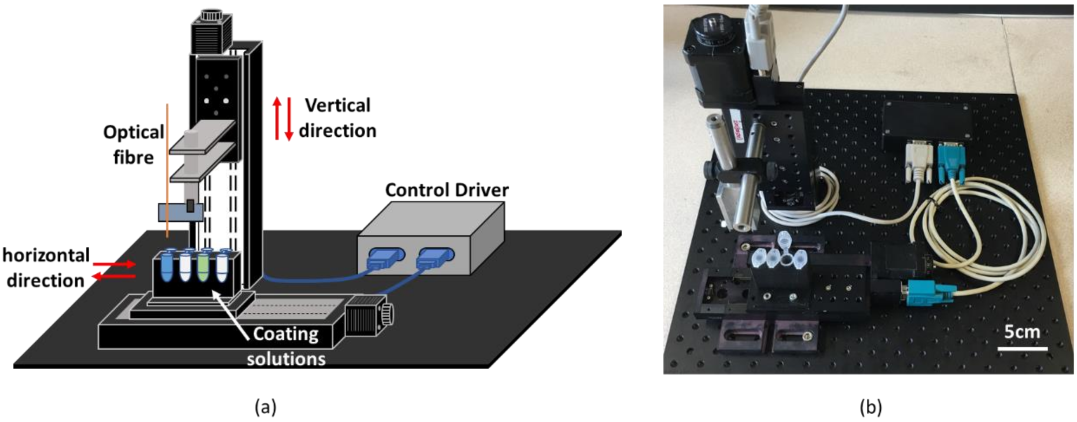

Figure 3. 22 Layer-by-Layer dip coating robot: (a) schematic, (b) photograph.

3.5.2 Molecular imprinting technique

Molecular imprinting is a process of producing a solid or gel with an impression (imprinted polymer) which corresponds to a template molecule [124]. The imprinted polymer (a synthetic receptor) has capacity to bind the target molecule with high affinity and specificity. In recent years, molecular imprinting has been adapted beyond its well-established routes to selective applications, and particularly towards some innovative applications in sensing and analysis [64]. The ability to ‘design-in’ a recognition site for a specific analyte in a synthetic receptor is obviously appealing when compared to raising an antibody for the same target by more conventional methods. However, converting a molecular recognition event into a signal which can be used to report that event has, in the past, been a major difficulty for imprinted polymers, which have often been prepared as monoliths that are difficult to process. Therefore, much recent research in the field of imprinted polymers has been concerned with generating the materials in a format which allows coupling to sensors or detection systems in a simple and rapid way, and in a manner which allows adaptation to multiple sensor formats [125].

The process of molecular imprinting consists of three steps, shown as Figure 3.23. Firstly template-monomer complexes are generated by selecting functional monomers link to the template molecule. A polymerization process is then performed over the complex, which creates a matrix that fits the monomers in a right position binding the target template. The final step is the removal of the template from the cavities to leave the polymer specific for the template [126].

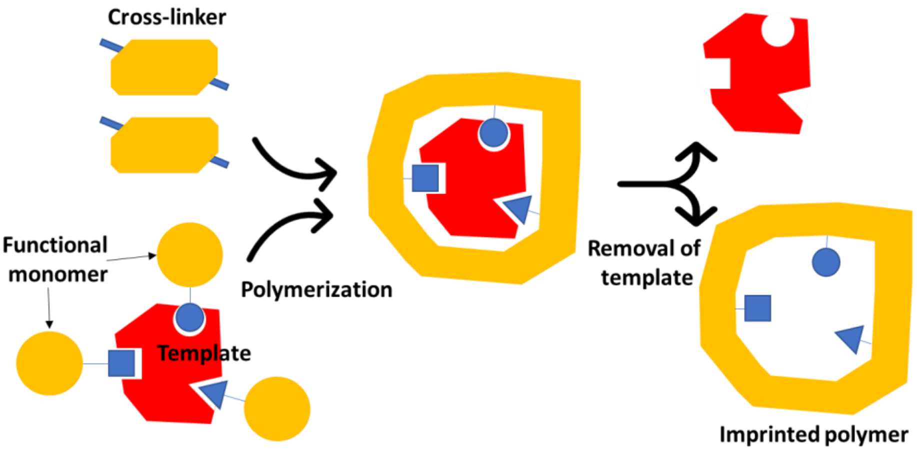

Figure 3. 23 Schematic of the molecular imprinting technique.

There are still some limitations to this prevalent method and the template removal process is challenging, especially for some large molecular template target molecules such as proteins. It must be considered in the compromise between original templates fully removed and damaging of the imprinted polymer. A strong removal process would cause a collapsed cavity and distorted binding sites [127]. Therefore, molecular imprinting method could be an optional approach for the detection of some small molecule analytes like a drug. This method has been used for detecting Dabrafenib, a type of anti-cancer drug, in Chapter 7.

3.6 Conclusions

Optical fibre sensor technology has a wide range of physical, chemical and biomedical sensing applications. Typically, an integrated optical fibre sensing system consists of an optical fibre, light source, sensing element and detector. There are some considerations such as the operating wavelength of all optical devices, input power of the light source and the resolution of the detector when selecting these components for building a system.

Optical fibre sensors can be classified by following the role of application, sensing area or operating principle. In addition, there are a variety of optical fibre sensor configurations for establishing the interaction of light from the sensing element with target measurands. The theory and fabrication of LPG-based platform has been introduced in this chapter.

Two functional film deposition methods have also been introduced. LbL deposition method represents easy-control and low-cost advantages and an automatic coating robot has been developed. The molecular imprinting technique has been shown to supply a high affinity and specificity to target molecules.

Chapter 4: Relative humidity measurement using an optical fibre sensing system

4.1 Introduction

In the previous Chapter, the optical fibre sensing configuration, functional film deposition techniques and the general background information of humidity in health monitoring were described. In this Chapter, optical fibre based relative humidity sensing system has been developed by the combination of a light source, optical fibre coupler, photodiode circuit, microcontroller and optical switch with 2 pairs of sensing probes. Each pair consists of two optical fibres, one has a thin functional film on its tip for measurement of relative humidity whilst the other is a bare fibre deployed as a reference for bending loss compensation.

For the functional film, the response of such sensors depends on the number of bilayers and the optimum number of these layers will be investigated in this Chapter. Fibre bending affects the sensing output of optical fibre sensors and hence bending loss compensation techniques are investigated in this Chapter with a range of bending radii and angles.

The performance of these sensors is explored during a dynamic exercise test on an exercise bike. The robustness of the system to motion artefacts and bending losses is also investigated. Two garments (T-shirts) with well-known and different properties (100% cotton where the material adsorbs moisture and 100% polyester which has known moisture wicking properties) were used in this experiment. These are selected to demonstrate that the properties of the fabric can affect humidity maintenance rather than to demonstrate the well-established differences between a natural and a synthetic garment. The relationship between comfort, performance and humidity has inevitably led to a wide range of different materials being developed by textile and clothing manufacturers [128]. ISO 15496:2018 standard describes a method for testing the water vapour permeability of textiles that are often adopted within the field. Although this is a useful first approach, performed in a controlled environment, the tests are static, conducted on fabric swatches and not on the fully assembled garment or in a real-world environment. There is therefore interest in developing new technology to assess water vapour permeability of fully assembled garments on human subjects in climatic chambers or on the field of play.

Healthy volunteers participated in the cycling test and ethical approval was provided by the Ethics Committee, Faculty of Engineering, University of Nottingham, 26th July 2018 (see Appendix A).

4.2 Methodology

4.2.1 Materials

Potassium hydroxide (KOH), Sodium hydroxide (NaOH), Ethanol and Poly(allylamine hydrochloride) (Mw~58,000, PAH) were purchased from Sigma-Aldrich, UK. Also, Silica Nanoparticles (SiO_2 NPs, diameter 40-50 nm) were purchased from Nissan Chemical, Japan. Finally, deionised water (DI water), having resistivity of 15 MΩ cm, was obtained from a University of Nottingham water purification system (PURELAB Option S/R, ELGA).

4.2.2 Sensing probe fabrication and characterization

All optical fibres used in this work for tip-based sensing have been stripped, cleaned and perpendicular cleaved using optical fibre cleaver (INNO, VF-78, UK). A thin film composed of PAH/SiO_2 NPs was coated on the tip of an optical fibre using the Layer-by-Layer self-assembly technique [129] by using the laboratory designed L-b-L coating robot described in Section 2.3.1.

The fabrication process is shown in Figure 4.1 as follows:

(a) the surface of the fibre tip was firstly immersed into a KOH solution (1 wt% in ethanol/water = 3:2, v/v) for 25 min to hydroxylate the fibre;

(b) after washing with DI water and drying, the fibre was treated with a 0.17 wt% positively charged PAH solution (pH: 10-11) for 15 min;

(c) wash and dry, and the fibre was then immersed into a 5 wt% negatively charged SiO_2 NPs solution for 15 min.

(d) repeat (b) and (c) processes to achieve the required thickness. The coated optical fibre was dried at room temperature in the laboratory for 24 hours before use.

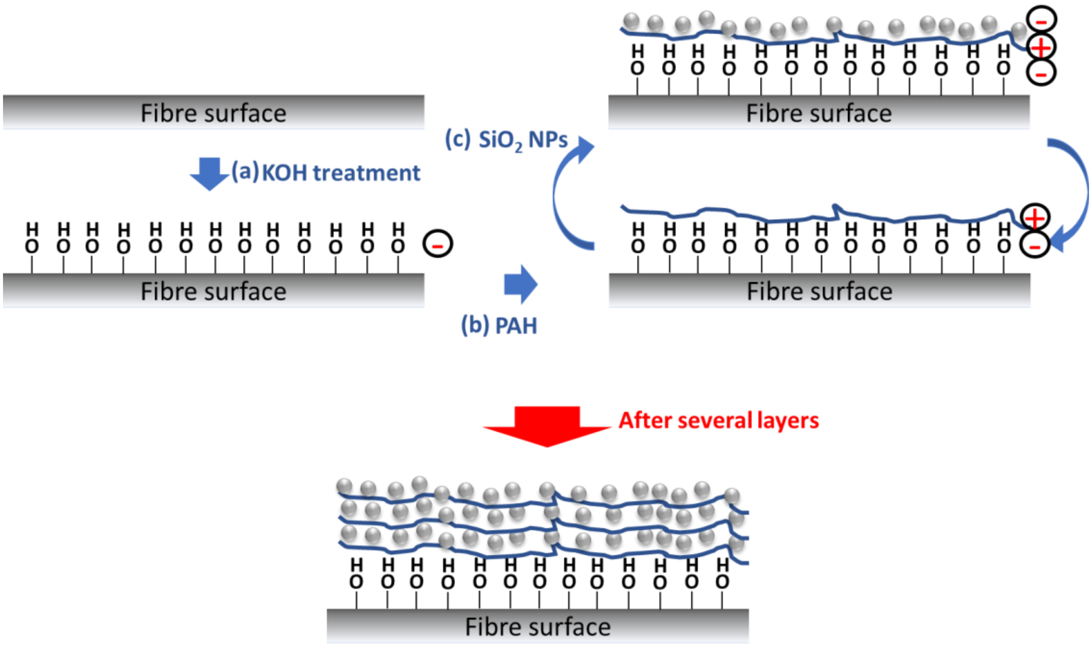

Figure 4. 1 Schematic of layer by layer deposition process of PAH/SiO_2 NPs film on the fibre surface.

Theoretically, the thickness of monolayer equals the diameter of SiO_2 NPs (40-50 nm in this case). For characterising the functionalised fibre, a transmission optical microscope (Olympus, BX50, UK) was used to observe the shape of fibre tip after coating with PAH/SiO_2 NPs film. The morphology of the functionalised fibre tip was studied using a scanning electron microscopy (SEM) (JEOL, JSM-7100F, UK) with 15 keV beam voltage. To obtain a high quality SEM image of the functionalised sensing film, the optical fibre coated with PAH/SiO_2 NPs thin film, followed the procedure described above and was then cut and adhered perpendicular on a dedicated SEM holder as shown in Figure 4.2.

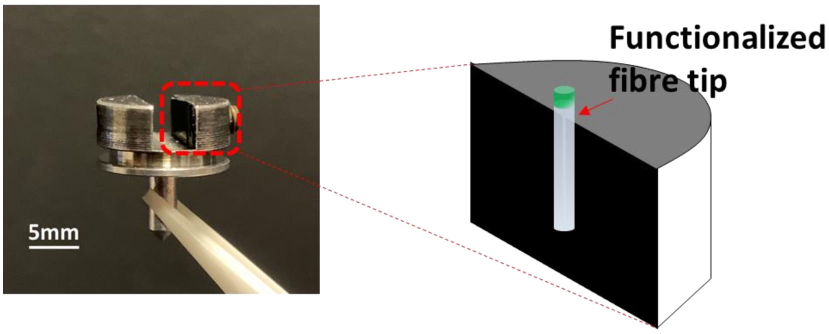

Figure 4. 2 SEM perpendicular holder for observing film on the fibre tip.

4.2.3 Humidity sensing mechanism

After the deposition process, a porous coating containing silica nanoparticles was generated on the tip of fibre, which facilitates adsorption of water molecules through chemisorption and physisorption [130]. The mechanism of water molecule adsorption based on SiO_2 is shown in Figure 4.3. Firstly, (a)-(b) the silica surface facilitates the dissociation of H_2O into a hydroxyl group, which binds to the silicon cation site, and a proton, which binds to an adjacent oxygen anion site. Secondly, (c) the remaining water vapour is physiosorbed with the surface hydroxyl groups through H-bonds (hydrogen-bonds). Once the first physiosorbed layer is formed, (d) the following layers are absorbed through the H-bonds. Finally, water starts to be absorbed into the pores of the coating film [130].

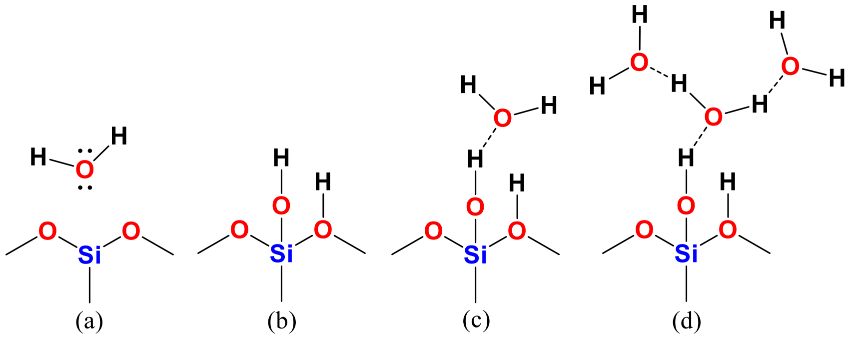

Figure 4. 3 Water vapour adsorption on the silica nanoparticle surface: (a) H_2O molecule close to SiO_2 surface; (b) H_2O dissociation into a -OH group binds to silicon cation site and a hydrogen proton binds to oxygen anion site; (c) and (d) the rest of H_2O were physiosorbed through the hydrogen-bonds (modified from [130]).

In addition, a poly(allylamine hydrochloride) (PAH) layer in the coating film contributes to the adsorption of water molecules due to its hydrophilic property [131]. Therefore, the total reflection intensity due to the Fabry-Perot cavity created by functional film deposition can be explained as follows: 1) two main reflections were generated by two optical interfaces (fibre surface to film and film to air); 2) reflected light changes are due to refraction index (RI) changes of the film; 3) losses are due to light scattering and roughness of the film surface. Once the sensing film is coated on the tip of the optical fibre, the total optical response can be modulated by adsorption and absorption of water molecules by means of changing the effective RI of the film [24].

4.2.4 Sensing system prototype

An optical evaluation system was generated for monitoring target parameters using multiple channels of the optical fibre sensing probe as shown in Figure 4.4. In order to acquire a stable optical baseline signal, a Superluminescent Diode (SLD) (Superlum, SLD-761-HP, UK) with central wavelength of 1550 nm and a full width at half maximum (FWHM) bandwidth of 45nm was used as a light source. The SLD-761-HP combines high spatial coherence and relatively high intensity, where the output power can reach 10 mW which is sufficient for optical signals propagating into the single-mode fibre. An optical switch (Sercalo Microtechnology, SW1*4-9N, Switzerland) containing 4 channels is used to receive the reflected light from each sensing channel, which allows the protocol to achieve multi-port sensing (no more than 4 in this system). Light is emitted from the light source and transmitted through a 1X2 50/50 optical fibre coupler (All4fiber, SPL9-12-5050-NC-FP) to a port of the optical switch. The light then propagates to the tip of the selected optical fibre sensor and its reflected component returns to the switch. The reflected light from the sensing probe is then directed via the coupler to a circuit containing a photodiode (RS, FCI-InGaAs-120L-FC, operating wavelength: 900 -1700 nm, UK) and a transimpedance amplifier (TIA) built using LM358 operational amplifier (op-amp). A micro-controller (Arduino, Uno) with an extra analog-to-digital converter (ADC) breakout (Adafruit, ADS1115, 16 Bit resolution) is utilised. This microcontroller has two functions in the system: (1) to convert the voltage signal into the required parameter (i.e. humidity value); and (2) to control the optical switch.

The prototype demonstrated in this Chapter comprises several components such as an SLD, fibre optic coupler and optical switch that would limit its use to a laboratory-based testing tool. However, for widespread use in wearable sensing, the system could be simplified and reduced in cost. For example, tiny size multiple LEDs and photodiodes could be integrated in a Printed circuit board circuit to replace the bulky SLD and optical switch. The bill of materials for a single channel system with wireless electronics is estimated to be ~€25 with the most significant cost a wireless microcontroller. As with most electronics systems, this cost would reduce with higher volumes.

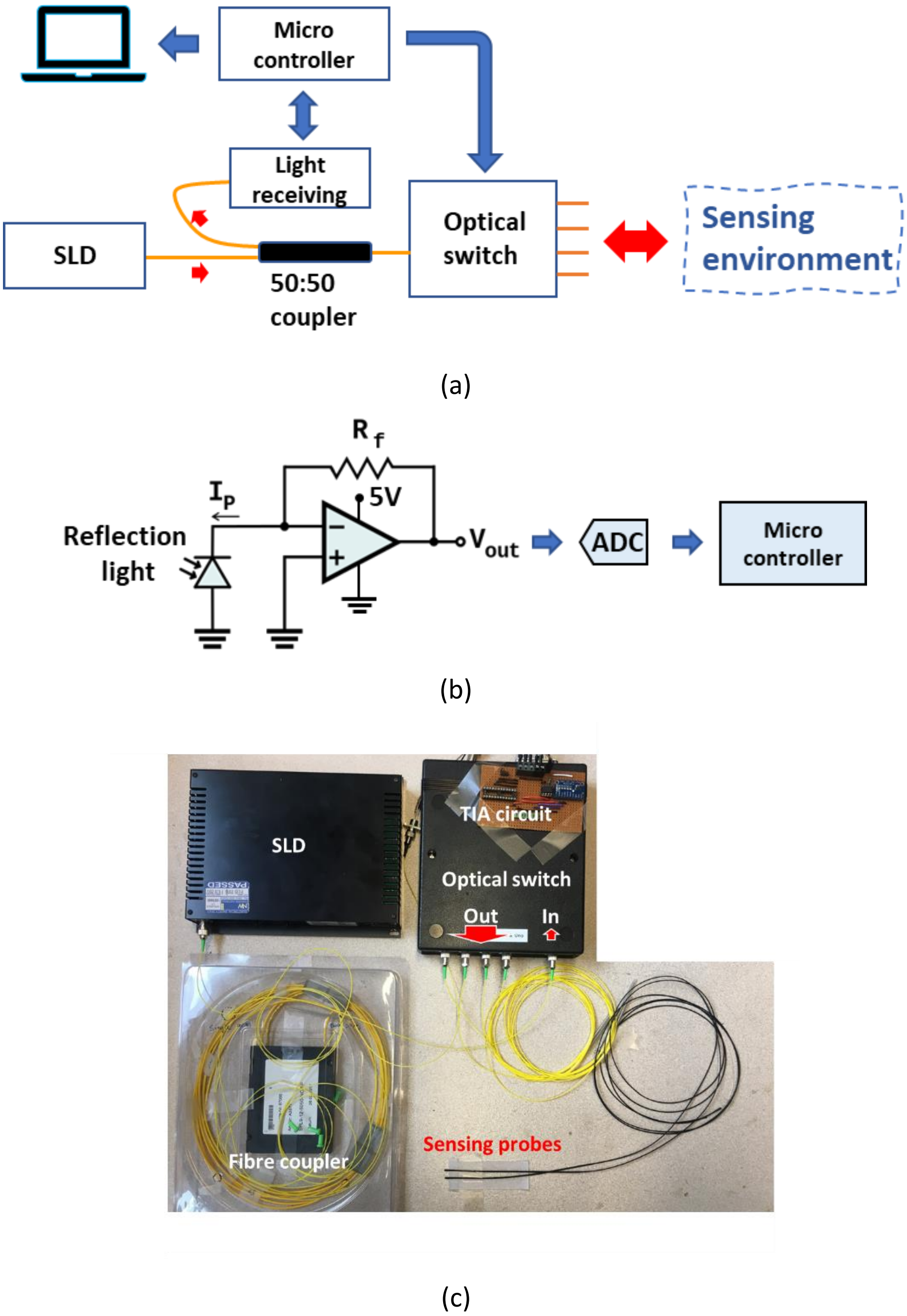

Figure 4. 4 (a) Schematic diagram of sensing system. Light is emitted from the light source (SLD) and through an optical fibre coupler that transmits to a port of the optical switch. The photodiode and transimpedance amplifier convert the reflected light intensity to a voltage which is then converted into a humidity value in the microcontroller and transferred to a PC via USB. (b) TIA photovoltaic mode circuit, ADC and Microcontroller. (c) Complete OFS evaluation system.

As mentioned in the introduction, the effect of fibre bending could be an issue in humidity monitoring during exercise activity. For investigation of bending loss compensation, the proposed sensing probe is composed of two optical fibres (Corning, SMF-28e+, fibre diameter: 242±5 µm, UK). Each probe contains one optical fibre humidity sensor (OFHS) coated PAH/SiO_2 NPs thin film as described in Section 4.2.2 and one bare reference fibre (REF) without any coating for bending loss compensation. Two fibres are tightly surrounded by a 1.5 metre long heat shrink tubing (TE Connectivity Raychem Cable Protection, X4-0.8-0-SP-01-ND, inner diameter (after heating) = 400 µm, UK). In order to protect the fibre tips from mechanical damage, a 2 cm length of 900 µm diameter furcation tube (Thorlabs, FT900Y, UK) is placed surrounding the tip. Two pairs of sensors are used allowing duplex humidity monitoring in this study where one pair consists of a fibre with PAH/SiO_2 NPs thin film and a separate bare reference fibre.

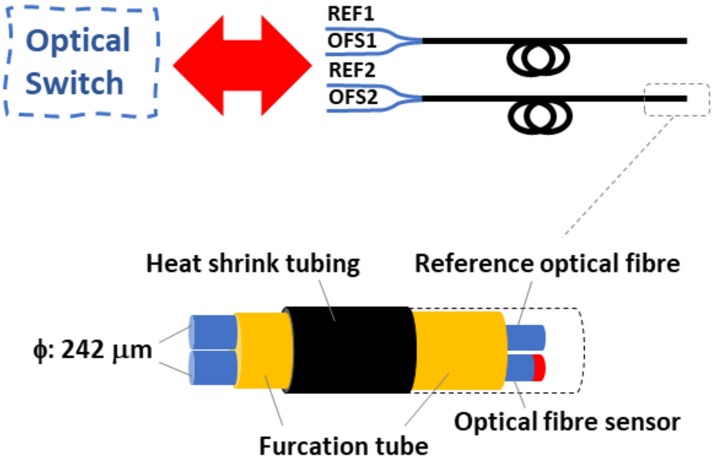

Figure 4. 5 Sensing probes in this project. Two fibres (reference fibre for bending loss compensation and optical fibre humidity sensor) are tightly surrounded by a furcation tube and heat shrink tubing for protecting the tip from mechanical damage. Two pairs of sensors are used allowing duplex humidity monitoring in this study.

4.2.5 Relative humidity sensor calibration and performance

In order to systematically control the humidity change, a climatic chamber (CVMS

Climatic, C-TH40, Bench Top, RH range: 20% RH - 98% RH, humidity fluctuation: ±2.5% RH, temperature range: -20 °C - 180 °C) was used in the calibration process. According to the temperature humidity control range, Figure 4.6(b), the humidity in the climatic chamber should be set in the range from 45 to 98 % RH at ~30 °C. The sensing probe and a commercial capacitive humidity sensor (Bosch, SparkFun BME280 atmospheric sensor breakout, RH range: 0% RH - 100% RH; accuracy tolerance: ±3% RH; hysteresis: ±1% RH and response time: 1 s in the temperature range of -40 °C to 85 °C) were placed 0.5 cm apart inside the climatic chamber.

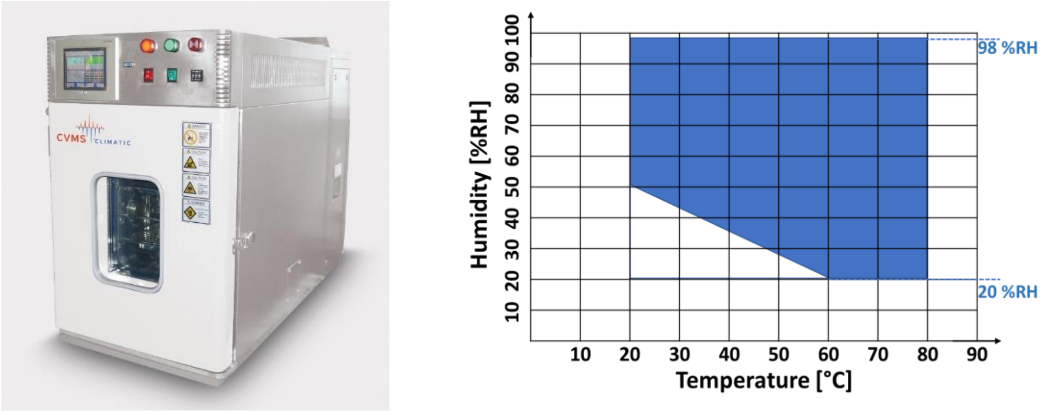

(a) (b)

Figure 4. 6 (a) Climatic chamber used in this work for humidity calibration and performance test of OFHS. (b) The temperature, humidity control range of the climatic chamber.

The sensor response has previously been reported as linear [24, 103] and so the RH was changed from 50% RH to 85% RH and reversed every 10 min with three cycles to obtain the line of best fit. In order to determine the highest sensitivity to RH, functionalised fibres with different numbers of PAH/SiO_2 NPs bilayers were tested.

The RH sensitivity can be obtained using the calibration curve from the above experiment, accordingly the output signal from the sensing probe was confirmed in terms of RH units. In order to verify the repeatability, the calibrated RH OFS and a commercial sensor have been placed in the climatic chamber and humidity was changed from 55% RH to 95% RH and reversed with two cycles.

4.2.6 Evaluation of bending loss compensation

Generally, water vapour does not easily adhere to the smooth tip surface of the uncoated bare fibre, which means that the bare fibre with perpendicular cleaved tip has the potential to be a reference for reducing the bending loss effect. Ideally, under the same bending conditions, the intensity-loss coefficients (α) between two separate optical fibres from one batch are identical [132].

In this work, the intensity changes due to bending of the OFHS is compensated using a reference fibre. We define a term α as a loss of intensity due to an arbitrary bending angle θ normalised by the intensity at a bending angle $\theta = 0$.

$$\alpha = \frac{\Delta I_{ref}}{I_{ref(\theta=0)}} \qquad (4-1)$$

where ΔI_{ref} is the change in intensity between the reference fibre at $\theta = 0$ and at a bending angle θ. $I_{ref}(\theta = 0)$ is the intensity measured from the reference fibre at $\theta = 0$ which can be made before measurements commence. As the (unknown) bending angle θ is the same in both reference and sensing fibres, α is then used to compensate the humidity sensing channel.

$$I_{compensated} = I_{OFS} * (1-\alpha) \qquad (4-2)$$

where I_{OFS} is the intensity measured from the sensing optical fibre.

In order to investigate the bending response, 2 bare fibres surrounded by shrink tubing were bent at different orientations (parallel and perpendicular bending), as shown in Figure 4.7(a), angles (0° – 90° – 180° – 270° – 360° – 0°) and with different bend radii (14 mm, 10 mm, 7.5 mm, 6 mm and 5 mm). Fibres were bent (between the tip and the coupler) over steel cylinders with corresponding diameter to simulate typical movements of the fibre that might occur during exercise.

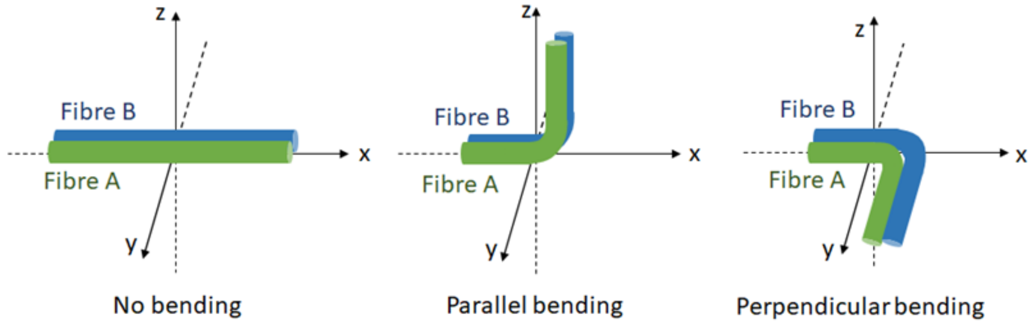

(a)

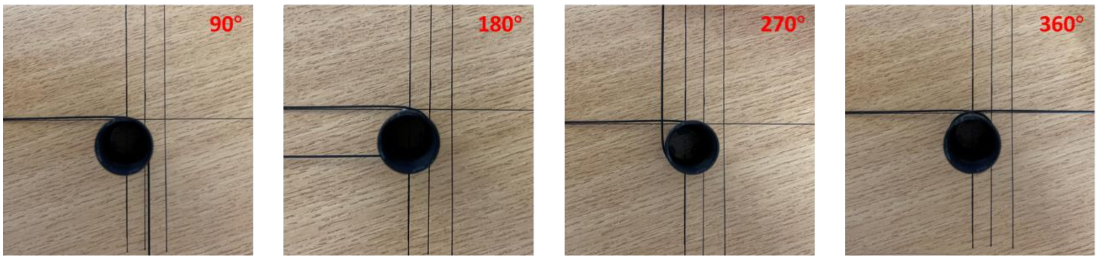

(b)

Figure 4. 7 Bending test with two bare fibres (a) configuration of fibres and different bending orientations (b) configuration showing bending with different angles (90-360°).

4.2.7 Relative humidity measurement during exercise activity

In order to observe the performance in exercise activities of the optical humidity sensing system, a cycling experiment was performed. A total of 9 volunteers (male, weight: 61 - 90 kg, median weight: 71.5 kg, age 23 – 48, median age: 33) participated in the cycling test using an indoor cycle (Domyos, VM590, UK) at room temperature (22 ± 1 °C). Each volunteer wore tightly two sports T-shirts with different materials (100% cotton and 100% polyester) separately for the same cycling test. This experiment aims to demonstrate that the properties of the fabric can affect the humidity generated from a human body and the practical capability of this optical fibre humidity sensing system.

The two cycling tests were separated by 45 mins in order to stabilise the physical condition of volunteers. All the T-shirts were laundered and conditioned in the lab for 24 h before testing. Ethical approval was provided by the Ethics Committee, Faculty of Engineering, University of Nottingham, 26th July 2018.

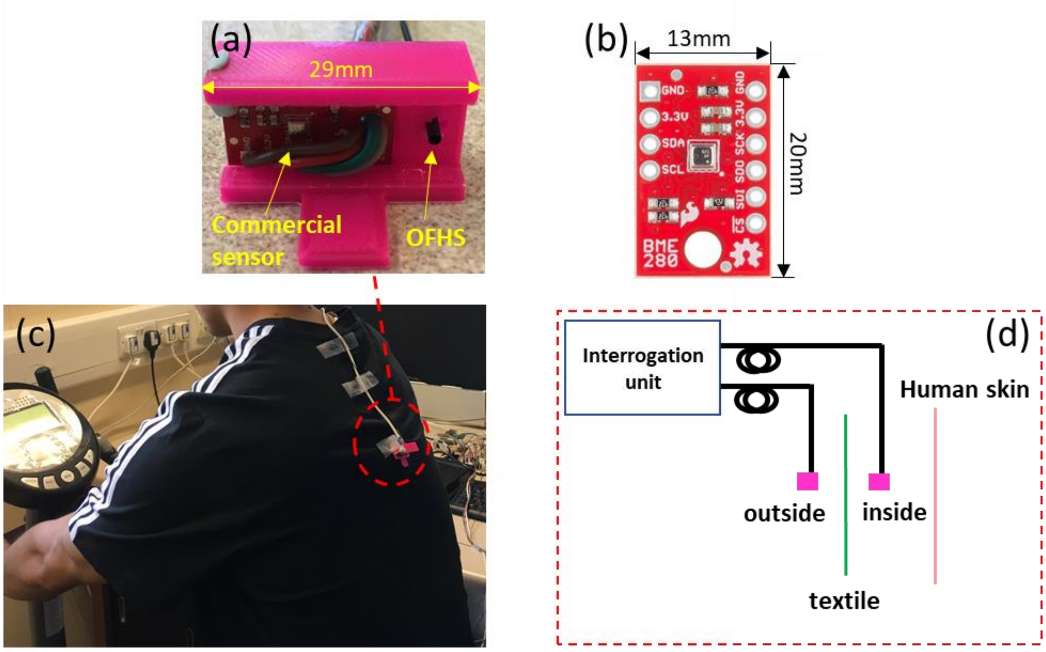

Figure 4. 8 (a) BME280 and OFHS were embedded in a small 3D-printed holder for maintaining the same sensing direction (towards the front in figure(a)). (b) Dimension of BME280 breakout. (c) and (d) humidity measurement in sports activity (cycling), two pairs of sensors (BME280 and OFHS) were placed inside and outside of the garment respectively.

The commercial humidity sensor BME280 from Bosch was also used for calibration of the signals from the designed optical fibre humidity sensor (OFHS). The BME280 and OFHS were embedded in a 3D-printed holder (Figure 4.8(a)) for maintaining the same sensing direction. Two sensing units (OFHS and BME280) were attached in the back area of the sports T-shirt (inside and outside within 0.5 cm distance from each other) by double-sided tape. The cycling protocol is shown in Table 4-1:

Table 4- 1 Protocol for the humidity measurements during cycling

Actions	Time (min) / Velocity (km/h)
Pre-condition by sitting	10 / 0
Pedal	5 / 3.3-3.5
Static position	10 / 0

4.3 Results and discussion

4.3.1 Sensor probe modification

Sensors with 3, 7 and 11 layers were fabricated to help determine the optimum layer thickness. Figure 4.9(a) shows a transmission optical microscope image of the 11 layers of PAH/SiO$_2$ NPs film coated optical fibre, which reveals a relatively smooth fibre tip after coating. The SEM images were taken of the optical fibre tip surface with different magnifications. The uniform attachment and porous morphology of PAH/SiO$_2$ NPs can be easily observed from Figure 4.9(b) and (c). In the SEM image with 100 nm scale bar (Figure 4.9(d)), it can be clearly seen that the SiO$_2$ particles attached on the fibre surface are a consistent size of around 50 nm.

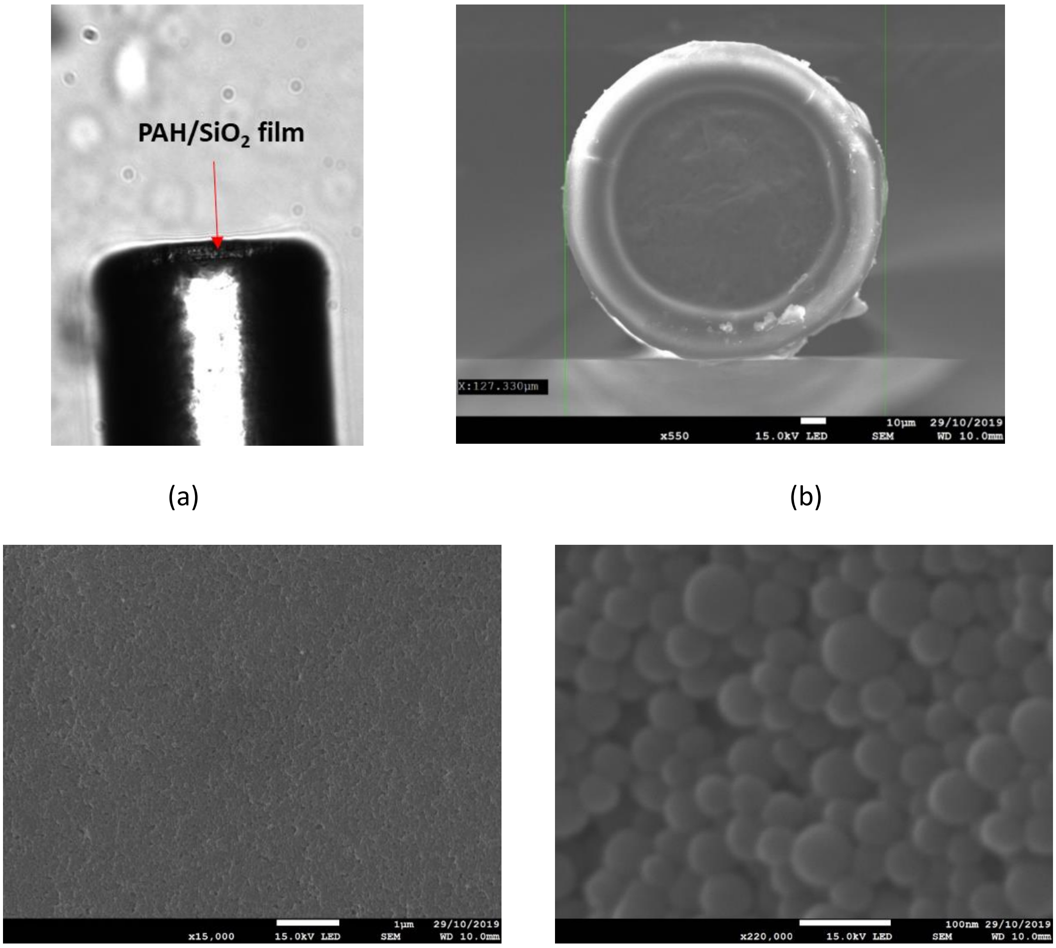

(a) (b)

(c) (d)

Figure 4. 9 (a) Optical microscope images of cleaved fibre after coating with 11 layers of PAH/SiO2 NPs (b) SEM images of PAH/SiO$_2$ NPs film deposited onto a fibre tip with scale bar: 10um, 1um (c) and 100nm (d) labelled at the lower edge of each image.

For the layer by layer technique, the thickness of each layer is approximately equal to the diameter of the SiO2 NPs i.e. a 40-50 nm/monolayer [24], the total estimated thickness of 11 layers sensing film is 440-550 nm.

4.3.2 Relative humidity calibration

The dynamic reflection light response of the OFHS with different bilayers (3, 7 and 11) of PAH/SiO_2 film upon exposure to changing RH in the climatic chamber are shown in Figure 4.10. The RH was changed from 50% RH to 85% RH and reversed every 10 minutes with three cycles to obtain the line of best fit while the temperature is held constant at 30 °C in the climatic chamber for the duration of the experiment.

It should be noted that the OFHS response (blue curve) is broadly repeatable and inversely proportional to the RH change measured by the commercial humidity sensor (black curve). Comparing the dynamic light changes of OFHS with different layers (3, 7 and 11), Figure 4.10 shows that the increase in the geometrical thickness of the porous morphological film leads to a higher sensitivity as more water vapour can be adsorbed. However, thicker films provide less reflected light [24, 133], which can be observed in Figure 4.10. With a thicker film which greater than 11 layers, the intensity signal deceases out of the sensing limitation in a higher humidity level (> 90 %RH). Therefore, to obtain a balance between sensitivity and detected signal level 11 bilayers are utilised in the remaining experiments.

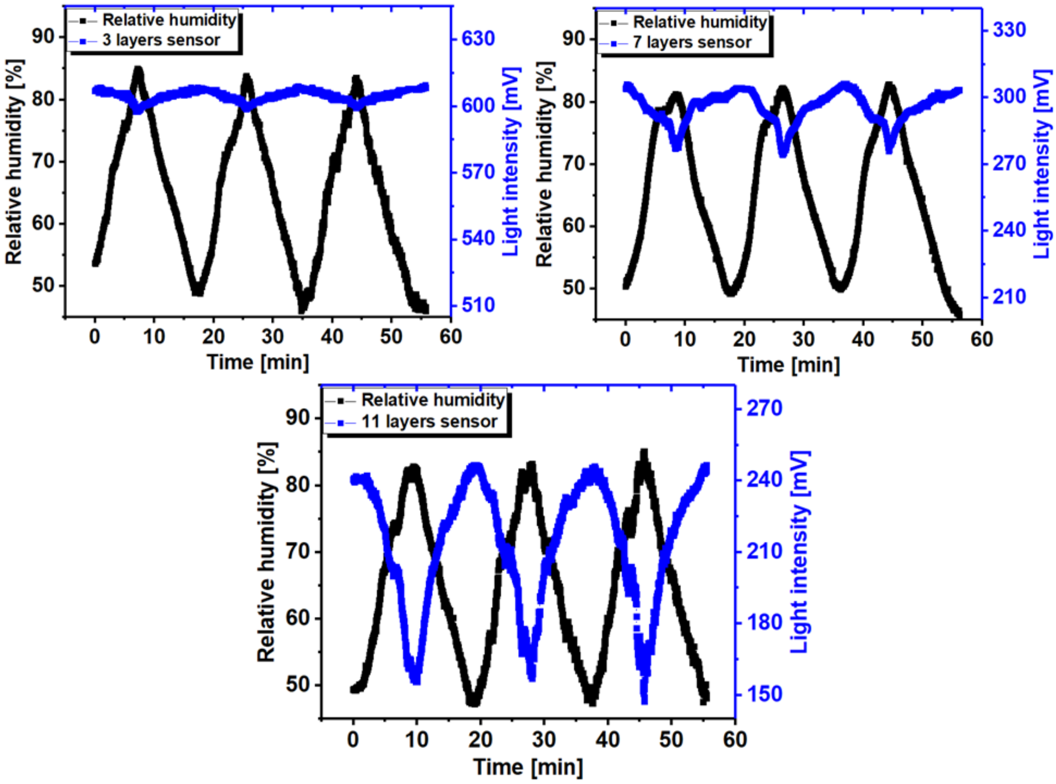

Figure 4. 10 Dynamic light intensity changes of OFHS with different layers (top left: 3 layers, top right: 7 layers, bottom: 11 layers) thin film (blue curve, PAH/SiO_2 NPs) on exposure to a humidity changing environment. The black curve is the RH change measured by the commercial sensor.

The calibration curves for RH measurements with OFHS with 3, 7 and 11 layers of PAH/SiO_2 thin film were shown in Figure 4.11. For all sensors, the light intensity change was observed to exhibit an approximately linear dependence on the change of RH (50 – 80%). It can be observed that, the greater the number of layers, the higher the sensitivity of the OFHS. For the sensor with 3 layers (red line), the sensitivity was 0.40 mV / %RH (R^2=0.95), for 7 layers (dark blue line), the sensitivity was 0.96 mV / %RH (R^2=0.88) and for 11 layers (orange line) the sensitivity increased to 3.02 mV / %RH (R^2=0.96>0.90, linear regression acceptable). The error bars in the Figure 4.11 represent the standard deviation of three repeat cycles, and each standard deviation was calculated using 6 points at relevant RH value.

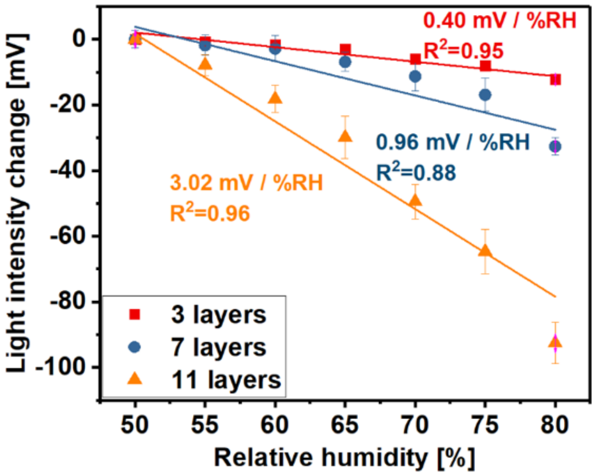

Figure 4. 11 Calibration curves for OFHSs with 3, 7 and 11 layers thin film represent the sensitivity for each case (error bars represent the standard deviation of three repeat cycles). For the purpose of comparison, the Y-axis in the calibration curve shows the differences in reflected light intensity relative to the 50% RH value.

After determining the optimum number of layers, the hysteresis of 11-layers humidity sensor was calculated to be ±1.17% RH. The hysteresis as a performance specification, is defined as the difference between measurements of the humidity increase / decrease branch and the averaged curve of both branches, the sequence 50-85-50% RH is used as shown in Figure 4.12, which was obtained from the dynamic response of the OFHS in RH calibration process [134]. The standard uncertainty for hysteresis is [134], $Max|Y_{upscale} - Y_{downscale}|$ represents the maximum difference between increase and decrease traces:

$$S_{hysteresis} = \frac{Max\left|Y_{upscale} - Y_{downscale}\right|}{\sqrt{3} * sensitivity} \qquad (4-3)$$

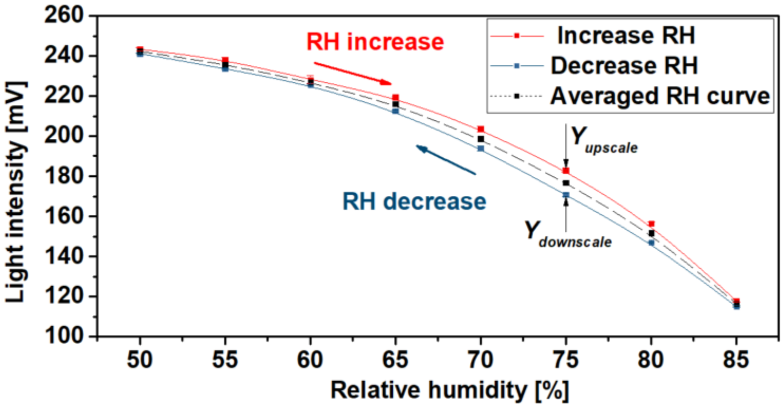

Figure 4. 12 OFHS response when RH is increased and decreased, error bars are smaller than the markers.

After calibration, the RH results obtained from the developed OFHS with 11 layers and commercial sensor can be compared in Figure 4.13. As shown in Figure 4.13(a), the two RH readings provide a similar trace during the two cycles of changing RH (from 60% RH to 92% RH).

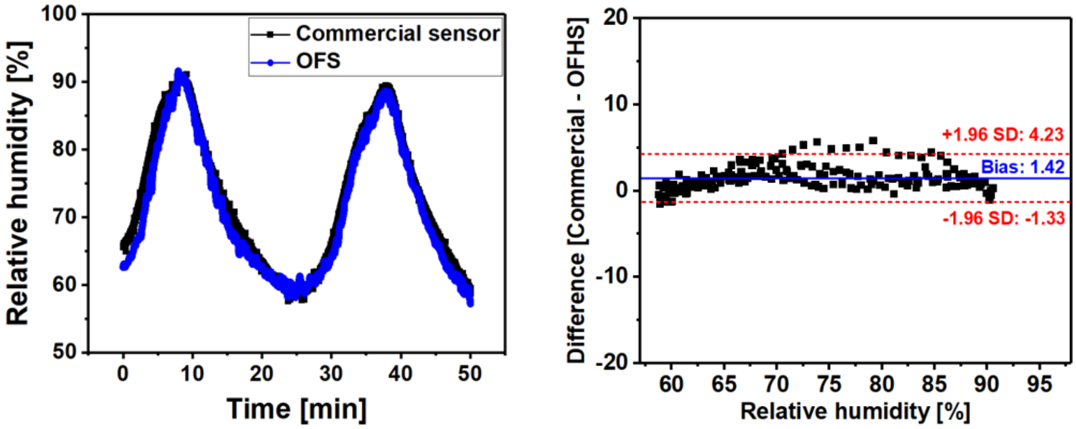

(a) (b)

Figure 4. 13 (a) The RH outputs from the 11 layer sensing probe (blue curve) and commercial sensor (black curve) measured in the climatic chamber. (b) Bland-Altman plot showing the difference between RH measurements from sensing probe and commercial humidity sensor. The x-axis and y-axis show the relative humidity and the difference (Commercial - OFHS) of the RH reading from the two sensors, respectively.

Using Bland-Altman analysis [135], Figure 4.13(b) demonstrates that the difference between the two sensors is similar in the RH range from 60% to 92%, although some excess scatter can be seen at 70-80% RH. In the Bland-Altman plot, setting the response of the BME280 commercial sensor as the reference standard of RH value in x-axis. As can be seen in Figure 4.13(b), the mean and standard deviation of the difference is 1.42% RH and 1.41% RH, respectively. These indicators confirm that OFHS has the potential to monitor RH as a commercial device.

4.3.3 Bending loss compensation

The responses of two identical bare fibres (A and B) bending in two orientations, parallel and perpendicular, over a range of angles (0° – 90° – 180° – 270° – 360° – 0°) around cylinders with different radii (14 mm, 10 mm, 7.5 mm, 6 mm and 5 mm) are illustrated in Figure 4.14(a) and (b). As expected, the light intensity shows a dependence on the bending radius and angle with the response attenuation being larger for smaller radius and greater angle. For both bending orientations, the intensities do not show significant attenuation during the whole experiment when the bending radius is at 14 mm. It should be noted that light intensity reached nearly 0, in 5 mm bending radius, after bending angle 180° and above. Therefore, as long as the bending radius is >=14 mm, there will be no significant light intensity attenuation due to bending losses.

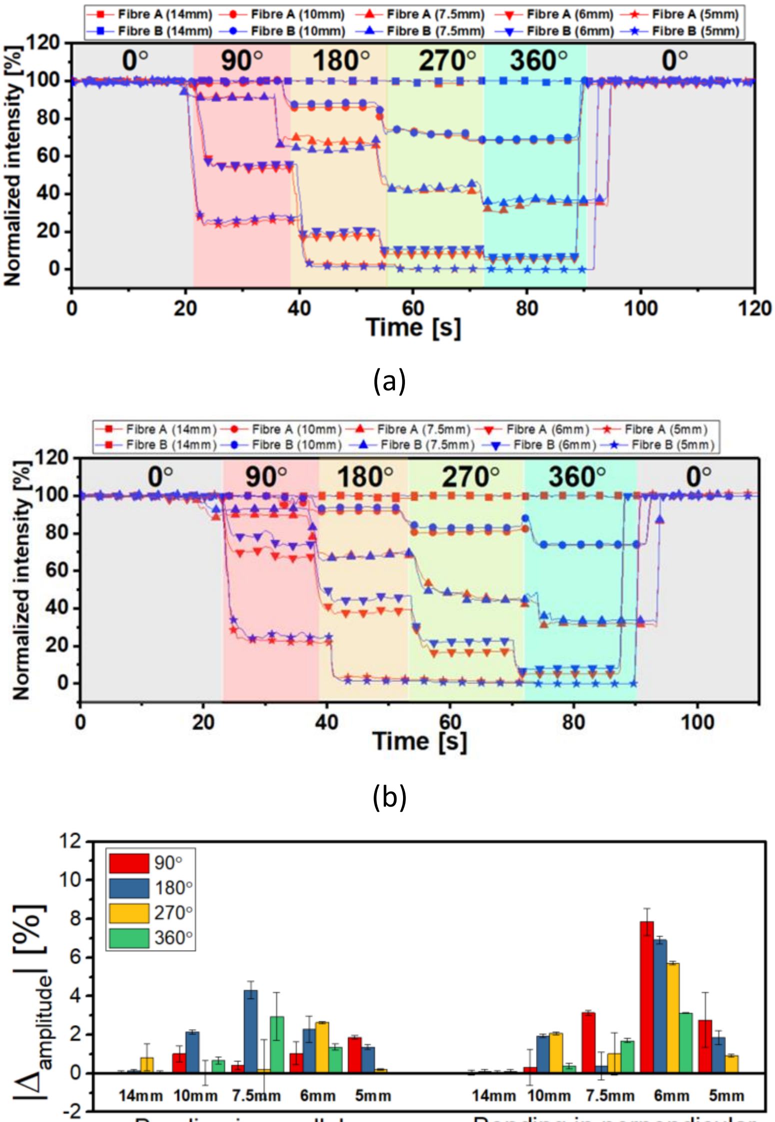

(a)

(b)

(c)

Figure 4. 14 (a) The responses of two identical bare fibres (A and B) bending in parallel over a range of angles around cylinders with different radius (b) bending the A and B fibres perpendicular over a range of angles around cylinders with different radius (c) Summary of % differences in amplitude between fibre A and fibre B.

When the fibres are bent in parallel, as shown in Section 4.2.6 Figure 4.7(a) middle, the bending losses should be the same theoretically. However, when the bend is perpendicular, the bending losses may be different in both fibres due to a slightly different bending radius. In the case with a 5mm bending radius, it reaches the measurement limit of the system after 180° bending angle. A summary of the difference in amplitude between two bare fibres for both bending orientation tests is shown in Figure 4.14(c). The worst case difference in intensity over a wide range of bend angles and radii is ~8% in the perpendicular bending case with the majority of cases less than 3% in both orientations.

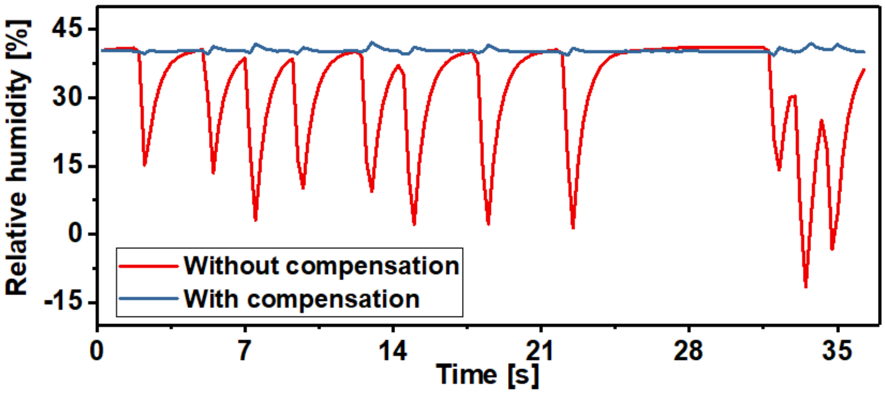

Figure 4. 15 The output from the sensing probe during random bending. The red trace is the RH output without compensation from the reference fibre and the dark blue trace is after compensation using Equations 3.1 and 3.2.

Subsequently, a random bending test was undertaken with a sensing probe contains both OFHS and a reference fibre. Figure 4.15 shows the output of the OFHS sensing probe before (red curve) and after (dark blue curve) compensation from the reference fibre during the random bending test. As can be seen the system is robust to bending motion artefacts due to the intimate inclusion of a reference fibre that compensates for bending losses. There is a small residual signal in the compensated channel in Figure 4.15 as there is a slightly different response in the fibres. This is due to light travelling in slightly different paths depending on the bend orientation of the fibre. However, the reference fibre is uncoated and so should be unaffected by humidity. Although not observed in these experiments, there is potential for the reference signals to be affected by condensation at the fibre tip and so a future design would benefit from a hydrophobic coating on the reference sensor.

4.3.4 Relative humidity measurements

Figure 4.16 shows one of the results of RH measurement from the OFHS and commercial sensor during cycling exercise using an indoor bike (the full set of results are presented in Appendix B). The experiment was described in Section 4.2.7 for demonstrating the practical capability of the OFHS system in determining how the choice of fabric can affect the humidity generated from the human body. In Figure 4.16, the traces of the OFHS show a similar trend to the commercial device, although there was a slight absolute offset difference between the RH reading of the OFHS and commercial sensor in both T-shirts, 100% cotton T-shirt (Figure 4.16(a)) and 100% polyester T-shirt (Figure 4.16(b)). This is likely caused by the measurement position of the OFHS and commercial devices being slightly different i.e. separated by ~0.5 cm.

Cotton is a hydrophilic material and polyester has hydrophobic property [136]. It can be seen from the two graphs that there is a significant difference in RH readings between the cotton and polyester cases. The amplitude of the RH reading has reached a maximum of 73.3% (OFHS) in the cotton case and a maximum of 47.7% (OFHS) in polyester. Moreover, when the volunteer wears a polyester T-shirt the humidity levels recovered much quicker than that in the cotton case when the subject rests.

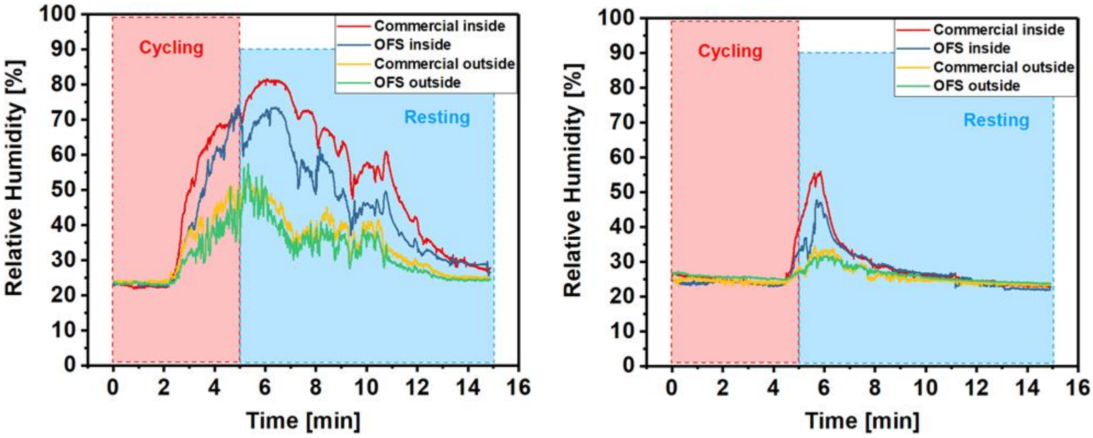

(a) Cotton (b) Polyester

Figure 4. 16 The RH reading from the OFHS sensing probe (inner, blue curve and outer, green curve) and commercial sensor (inner, red curve and outer, yellow curve) measured during the cycling exercise with 100% cotton T-shirt (a) and 100% polyester T-shirt (b) of volunteer 1.

Table 4- 2 Full width at half maximum (FWHM) and Δ_{peak} of the OFHS RH reading under different textile (100% cotton and 100% polyester) for 9 volunteers

Volunteer number	**FWHM (s)**		**Δ_{peak} (RH%)**	
	Cotton	Polyester	Cotton	Polyester
V1	313.8	75.6	23.72	16.23
V2	296.4	181.8	38.38	26.69
V3	354	148.8	28.68	51.75
V4	247.2	168.6	24.01	36.24
V5	580.8	384	30.39	26.56
V6	484.2	334.8	37.66	29.29
V7	577.2	258.6	28.66	21.44
V8	*	407.4	41.42	38.35
V9	314.4	309.6	17.72	9.61

* In the V8 cotton case, the RH did not recover to the half maximum before the end of the experiment due to profuse sweating.

Table 4-2 shows the full width at half maximum (FWHM) of RH measurement curve obtained inside the garment (OFHS), which is calculated by taking the biggest value in each case, and the difference between the RH peak value (Δ_{peak}) of inner and outer sensors from the OFHS for volunteers wearing 100% cotton and 100% polyester T-shirts respectively. As can be seen from Table 4-2, the 100% polyester group has a significantly lower FWHM value (median = 258.6) than the 100% cotton group (median = 334.2), which means the generated humidity is released more quickly in the polyester case. In addition, the majority of Δ_{peak} readings with polyester were smaller than that in the cotton group (median of Δ_{peak} in polyester 26.7 < in cotton 28.7). This confirms the improved performance of polyester as a moisture wicking material [137].

4.4 Conclusion

A new approach to monitor humidity in garments based on optical fibre sensing has been demonstrated. Due to their flexibility and small diameter (smaller than most textile yarns), optical fibre sensors can be easily integrated within textiles, with the potential to form next generation smart garments. They are more unobtrusive than commercial electronic humidity sensors but, for future widespread use, they need to be more competitive on cost.

Eleven-layer PAH/SiO_2 nanoparticle film has been deposited successfully onto the surface of an optical fibre tip, which was used to measure changes in light intensity reflected from the tip of the fibre which are proportional to humidity. Bending losses were partially compensated by including an uncoated reference fibre which enables measurements to be made during exercise.

The response of the sensing system to RH concentration was linear with a sensitivity of 3.02 mV/% (R^2=0.96) when 11 bilayers of PAH/SiO_2 NPs coated on the tip of fibre was used. This was higher than that of 7 (0.96 mV/%, R^2=0.84) and 3 bilayers (0.40 mV/%, R^2=0.93) of PAH/SiO_2 nanoparticles.

Measurements from 9 volunteers during a cycling test demonstrate the capability of the system to measure the effect of textile properties on humidity, with polyester providing improved moisture wicking properties than cotton. The small size and flexibility of the sensors allow them to be easily integrated within garments with negligible effect on the moisture wicking properties and has the potential to be used as a tool for clothing developers designing moisture managing products.

Chapter 5: Investigation of thermochromic material in optical fibre temperature sensing

5.1 Introduction

Chapter 2 described the importance of temperature measurement in a wide range of applications, especially in human health monitoring, along with the state of the art of optical fibre temperature sensors. In this Chapter, optical fibre tip-based temperature sensors coated with thermochromic material films are presented. Two types of thermochromic materials are investigated: one coating material is microencapsulated reversible thermochromic leuco ink (RT-leuco-ink) and the other is thermochromic liquid crystal (TLC).

A spectrometer, light source and fibre coupler operating in the visible wavelength range are used in this work for acquiring the spectral change of optical fibres coated with the proposed thermochromic material. The approach demonstrates the novelty of using thermochromic ink or TLC with spectral properties for sensing temperature. To the best knowledge of the author, this is the first time that combining an optical fibre sensing technique with RT-leuco-ink or TLC for temperature monitoring has been reported in the literature.

Two thermochromic materials are coated on the tip of a fibre through the same dip-coating protocol and each sensor is calibrated using a climatic chamber. In addition to verifying the repeatability of the optical fibre temperature sensors, temperature readings from the fibre temperature sensors and a commercial thermocouple are compared.

5.2 Methodology

5.2.1 Material

Reversible thermochromic ink (RT-leuco-ink) is described via a base colour and a temperature at which the colour starts to change to invisible (intensity change). Blue RT-leuco-ink (temperature point of changing colour: 31 °C) was purchased from Good Life Innovations Ltd, UK and green and magenta RT-leuco-inks (36 °C) were purchased from Matsui Shikiso Chemical Co. Ltd, Japan. Thermochromic liquid crystal (TLC) (R25C5W) was supplied by LCR Hallcrest, UK, which is described via a start colour temperature and the bandwidth (W). The bandwidth is defined as the difference between the start colour and clearing colour temperature.

5.2.2 Reversible thermochromic ink (RT-leuco-ink)

Thermochromic materials have a high potential for mapping or sensing temperature. Microencapsulated RT-leuco-ink with colour reversible thermochromism has been shown to monitor temperature [138, 139]. Microencapsulation technology is commonly applied in applications of such thermochromic material due to there being a barrier generated for protecting the entire system within each microcapsule from unwanted reactions with the surroundings. Generally, the microencapsulated RT-leuco-ink consists of three components:

a. Colour former: the majority of these compounds are electron-donating and halochromic leuco dyes, which change colour when pH is altered such as spiropyrans [140], fluorans and thymolphthalein [139]. The presented colour depends on the chemical properties of the different dyes similar to pH indicators.

b. Colour developer: frequently used developers are weak acids, e.g. bisphenol A and phenols, which allow the reaction with colour formers due to their electron-accepting property [141].

c. Solvent: the compound that acts as the medium allowing interaction between colour former and developer. The relatively low-melting-point of the solvent controls the temperature at which the colour of this RT-leuco-ink begins to change. Esters, acids and alcohols are the preferred choice of solvent [142-144].

As shown in Figure 5.1, the colour changing principle of RT-leuco-ink is based on two competing interactions: the dye-developer and developer–solvent. These interactions are controlled by the melting point temperature of the applied solvent, in this work denoted by activation temperature (T_a). At lower temperatures ($<T_a$), the solvent is in its solid form. In this condition, the interaction between dye and developer prevails and gives the mixture colour. With increasing temperature the solvent melts and another interaction (developer-solvent) becomes dominant. This undermines the dye-developer complexes and the mixture subsequently becomes colourless [144-146].

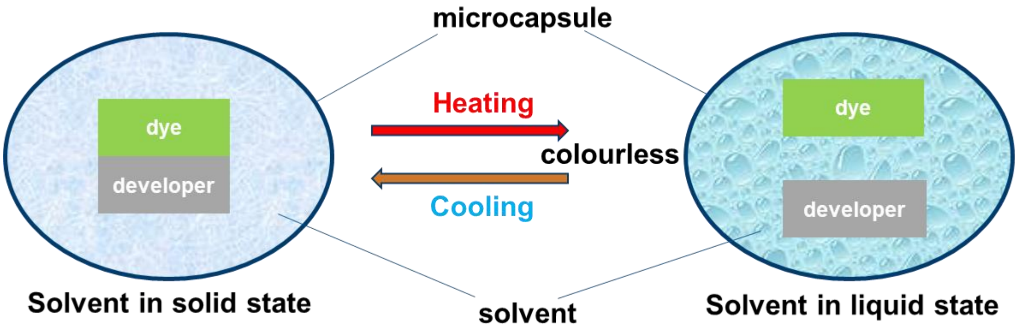

Figure 5. 1 Colour changing principle of microencapsulated RT-leuco-ink.

A variety of activation temperature (T_a) of leuco dye-based RT-leuco-inks are available but most applications are limited to three standard temperatures: 1) cold (~10 °C), 2) Body activated (~31 °C) and 3) warm (~43 °C) [139]. Table 5-1 gives a brief description of RT-leuco-inks used in this work including the activation temperature and colour. Water-based RT-leuco-inks are popularly used for the application on textile, paper or plastics. It is therefore interesting to investigate the RT-leuco inks ability to monitor temperature combined with the advantages offered by optical fibres.

Table 5- 1 RT-leuco-inks used in this work

	Good life Co.	**Matsui Co.**
State/colour	Ink/blue	Ink/green and magenta
Product description	Water based microcapsules	Water based ink microcapsules
T_a(°C)	31	31
Composition	Colour developer: 1-10% non-hazardous components: 90-100%	(developer) Bisphenol A: 4-6% Water and other non-hazardous components: the rest

5.2.3 Thermochromic liquid crystal (TLC)

The thermochromic liquid crystal (TLC) material is a mesophase of matter existing between the solid crystal and liquid state, which was discovered in the 19th century when studying a cholesterol derivative by Reinitzer [147]. When an anisotropic (with long-range crystalline ordered structure) solid crystal is heated to the melting-point, it transforms into an isotropic liquid with no long-range molecular order. However, there are certain substances which do not pass directly from an anisotropic crystalline solid state to an isotropic liquid state, and vice versa. These materials are called liquid crystals since they exist in an intermediate structure with molecular order less than that of the solid crystal state, but more than that of isotropic liquid. Figure 5.2 illustrates that the liquid crystal not only has the fluidity like the liquid state but also retains its orientational order due to the anisotropic property of crystallinity.

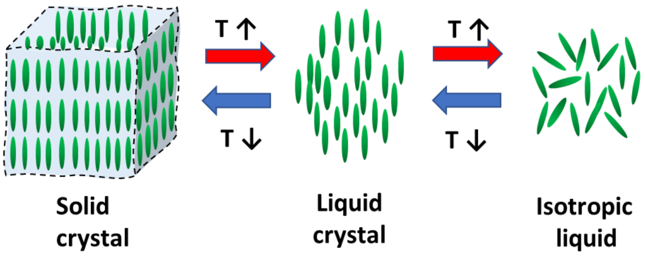

Figure 5. 2 Schematic representation of the phase changes in crystalline.

As shown in Figure 5.3, liquid crystals can be classified into two main groups namely lyotropic and thermotropic liquid crystals. Generally, lyotropic liquid crystals consist of two components: a hydrophilic polar head and a hydrophobic tail. For example, soaps and phospholipids (shown in Figure 5.3) are materials that form lyotropic liquid crystal [148]. Thermotropic liquid crystal is the thermally activated mesophase which results from melting of the crystal solid. According to the structure, thermotropic liquid crystal can be further divided into two distinct types: smectic and nematic [149]. Smectic liquid crystal phase occurs at a relatively lower temperature than nematic phase in the process of melting the solid crystal. Chiral smectic liquid crystals are useful in liquid-crystal display (LCD) technology where they are commonly used in PC and TV monitors [150, 151].

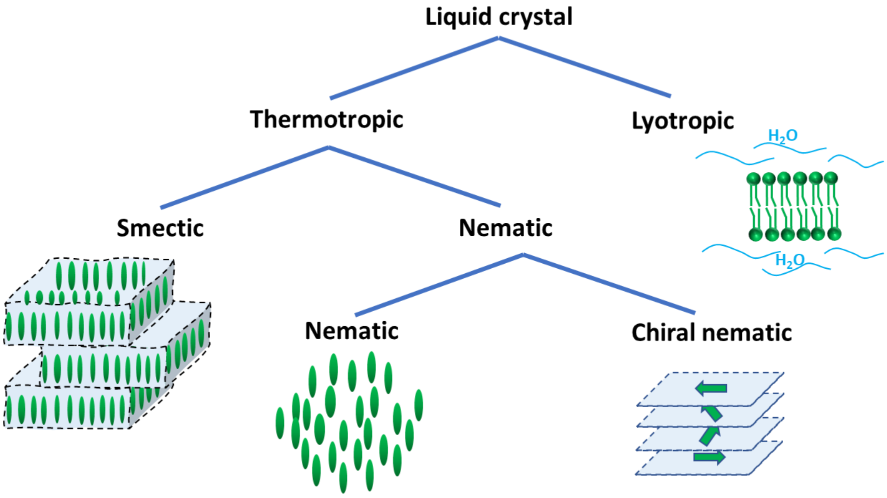

Figure 5. 3 Classification of liquid crystal.

The thermochromic liquid crystal (TLC) investigated in this work is from the chiral nematic (cholesteric) phase of liquid crystal. In this mesophase, the TLC molecules prefer to align parallel to each other due to the strong intermolecular attraction (π – π interactions) [152]. In the chiral nematic phase, as shown in Figure 5.4, the “molecule director” spirals around an helical axis (optical axis) which is perpendicular to every molecule, and the optical properties are symmetric about this axis [153].

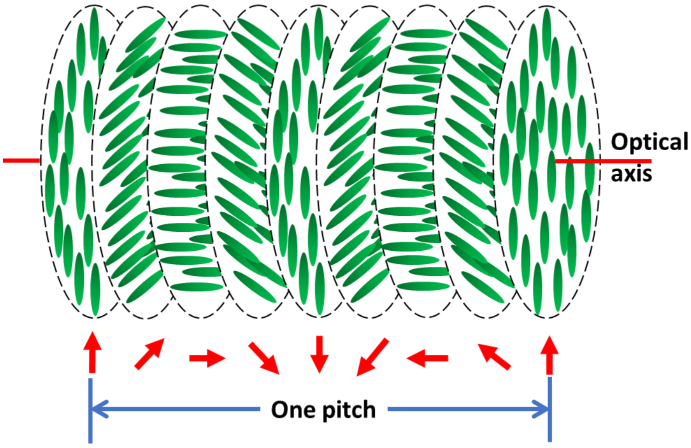

Figure 5. 4 The helical arrangement of molecules in the chiral nematic phase of a liquid crystal – deployed in the thermochromic liquid crystal (TLC).

The resultant helical arrangement of TLC molecules has the ability to selectively reflect light of specific wavelengths (λ_s) [154] satisfying:

$$\lambda_s = \bar{n} \times p \times \cos\theta \qquad (5-1)$$

$$\bar{n} = \frac{(n_o + n_e)}{2} \qquad (5-2)$$

Where θ is the incidence angle of the light; *p* is the helical pitch of the TLC which is defined as the distance it takes the molecule director to rotate 360° in the helix as illustrated in Figure 5.4; n_o and n_e are the ordinary and extraordinary refractive indices, respectively.

Thermal energy increases the molecule temperature of the TLC [155]: the director angle changes more rapidly, the pitch becomes shorter, causing the wavelength of the selective reflection peak to shift to the blue region. Alternatively, the wavelength of the selective reflection peak is longer with a temperature decrease [153]. The difference from RT-leuco-ink is that TLC produces a variety of different colour transitions with temperature changes due to the different mechanism, which represents the wavelength shift of the selective peak at different temperature.

The TLC materials used in this work are purchased from Hallcrest company and packaged by isolating in a microcapsule for protecting the TLC mixture and acquiring a longer lifetime. Unsealed (without microencapsulating) TLC films can maintain function from a matter of hours to a few days, depending on usage, however, the lifetimes of microencapsulated TLC films can be around 6 months [156]. The microencapsulation process of TLC is called “coacervation in liquid suspending media” [149] and it is divided into three steps: 1) initial suspension of dispersed droplets of liquid crystal material in a solution of the wall polymer, called Oil-in-Water; 2) then the wall polymer is induced to separate as a liquid phase by adding another polymer that has a relatively higher solubility in the same solvent; 3) subsequently, the Polymer-Polymer Incompatibility [157] process causes the first polymer that has lower solubility to start combining to a continuous coating around each liquid crystal droplet individually. Eventually, a hard microcapsule wall is generated, and the diameters of microcapsule are generally in microns level, for example the size of TLC microcapsule used in this work is ~10microns [156].

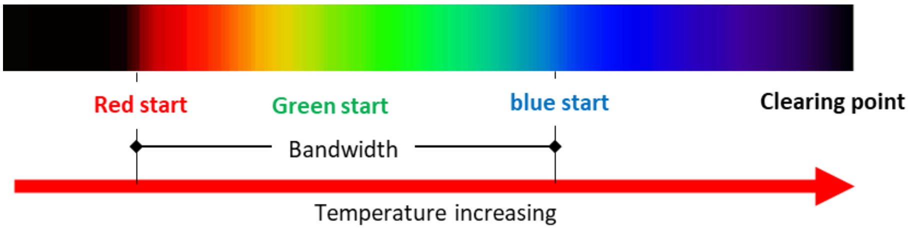

Figure 5. 5 Colour changes of TLC material due to temperature [156].

The TLC used in this work are supplied by LCR Hallcrest, which turns from colourless to red firstly at a certain temperature. As the temperature increases, it changes to other colours in the sequence, yellow – green – blue – violet, before turning colourless again at a specific higher temperature due to the distinct types of TLC (Table 5-2) as Figure 5.5 shown. These colour changes are reversible with a temperature decrease.

Table 5- 2 Colour table of TLC products from LCR Hallcrest [156]

TLC types	**Red start/ °C**	**Green start/ °C**	**Blue start/ °C**	**Clearing point/ °C**	**Bandwidth/ °C**
R20C5W	20.0	21.0	25.0	41.0	5.0
R25C5W	25.0	26.0	30.0	44.0	5.0
R30C5W	30.0	31.0	35.0	46.0	5.0
R35C1W	35.0	35.2	36.0	49.0	1.0
R35C5W	35.0	36.0	40.0	49.0	5.0
R40C5W	40.0	41.0	45.0	52.0	5.0

LCR Hallcrest supply distinct TLC types, shown in Table 5-2, with various turning colour temperature points. The R25C5W type of TLC was chosen due to its suitable colour change which covers the human body temperature. Although the bandwidth is 5 °C through the datasheet, we have proven the spectrum change can be detected until the clearing point later in Section 5.3.1 & 5.3.2. Therefore, acceptable monitoring temperature of R25C5W can be extended from 25 to 44 °C, which covers the majority of health monitoring applications.

5.2.4 Temperature sensor fabrication and characterisation

The temperature sensing films (RT-leuco-ink and TLC) were coated on a perpendicularly cleaved multimode optical fibre tip (pigtail easy-strip 62.5/125 µm ST, A1082, All4fiber) using the dip coating machine as shown in Figure 5.6. The reason for using multimode fibre as the transducer is that the larger diameter core of multi-mode optical fibres allows the collection of a larger amount of light as well as allowing the illumination of an increased number of microencapsulated particles.

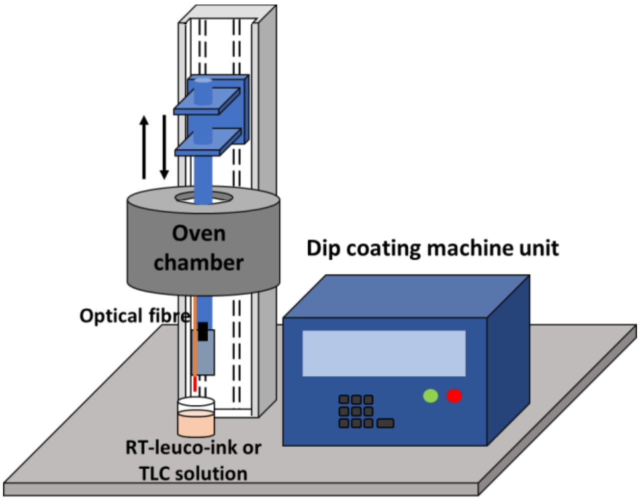

Figure 5. 6 Sensor fabrication set-up.

In the fabrication set-up, the dip coating machine (HO-TH-02, HOLMARC, India) with an in-built oven chamber was used. The temperature sensing solutions are coated on the fibre tip with 6mm/s of withdrawing velocity with dip coating for consistency. Subsequently, the coated fibre was placed into the oven at 60 °C for 1 hour for drying the film completely.

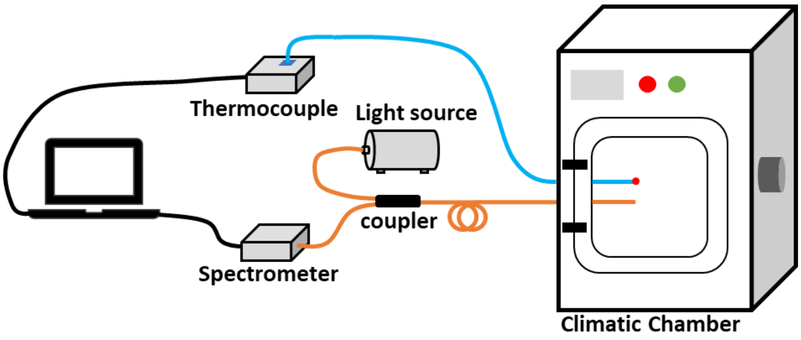

Figure 5. 7 Characterisation experimental set-up of temperature OFS.

A halogen light source (HL-2000, Ocean Optics, UK) illuminates the fibre tip through a 2 x 1 50%/50% multimode fibre coupler (Newport, F-CPL-M12855, UK), and the spectrum of an optical fibre sensor recorded at ambient temperature (~20 °C) and a relatively higher temperature using a heat gun (~40 °C) was captured by the spectrometer (USB2000+, Ocean Optics, UK) through an operating software (SpectraSuite, Ocean Optics, UK) for a quick preliminary spectra checking. Then, a climatic chamber (CVMS Climatic, Benchtop C-TH40, UK) which can set the temperature from -20 °C to 180 °C (fluctuation: ±0.5 °C) was used for further characterisation, allowing a controlled change of temperature – see Figure 5.7. A type K thermocouple with data logger (Pico technology, USB TC-08 thermocouple data logger, UK) was placed inside the chamber as a temperature reference. Light from a halogen source (HL-2000, Ocean Optics, UK) is coupled into the 2x1 fibre coupler (Newport, F-CPL-M12855, UK).

For temperature calibration of the proposed sensors, the chamber temperature was set to increase and decrease gradually in range of 20-40 °C for blue RT-leuco-ink, 20-44 °C for green and magenta RT-leuco-ink and 22-46 °C for TLC, while the relative humidity was set at a constant level (55% RH). In all experiments, the reflection spectra of the OFS and temperature reading of the thermocouple were recorded simultaneously with the same frequency (1 Hz). In order to generate the linear fitting curve, each calibration point takes the average of each stabilized step (120 seconds) obtained from dynamic calibration change and the error bar is the standard deviation of each step. Also, the hysteresis can be calculated by Equation 4-3 described in Chapter 4.

5.3 Results and discussion

5.3.1 Qualitative material characterisation

a. RT-leuco-ink

Figure 5.8 shows the spectra of the optical fibre tip with distinct RT-leuco-inks. In the absorption spectra, three ambient temperature absorption peaks appear at wavelengths of 600 nm, 640 nm and 530 nm for blue, green and magenta ink coating respectively. The peaks respond concordantly to the change of temperature, which undergo a decrease in absorbance value at higher temperature (~40 °C). Therefore, the intensity changes of the spectra can be used for the temperature measurement and the signal using the intensities at the peak wavelengths would be the beneficial for the measurement since they would offer a higher sensitivity to temperature due to the largest spectral intensity change.

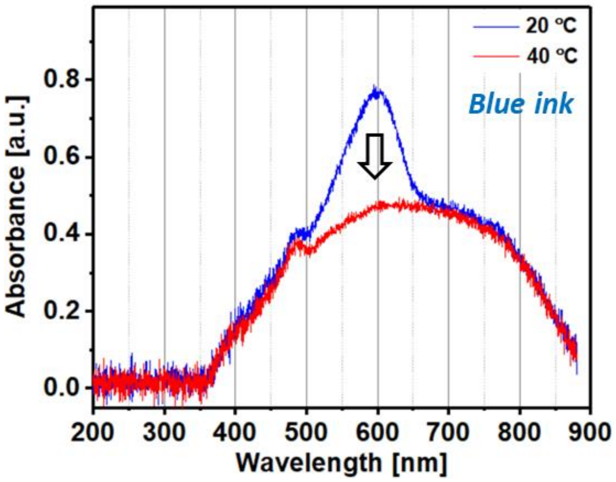

(a)

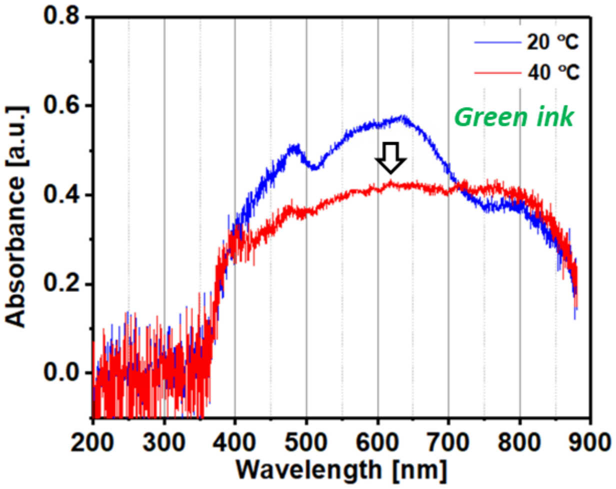

(b)

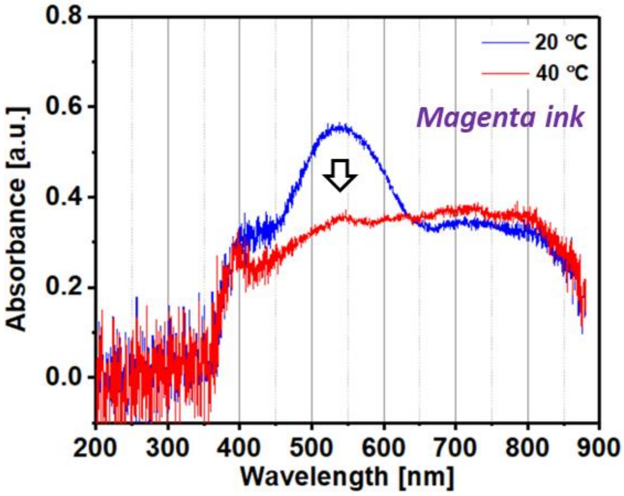

(c)

Figure 5. 8 Reflection spectra of optical fibre temperature sensor coated with (a) blue RT-leuco-ink, (b) green RT-leuco-ink and (c) magenta RT-leuco-ink.

b. Thermochromic liquid crystal

The reflection spectra of an optical fibre temperature sensor coated with TLC film is shown in Figure 5.9, no specific peak exists at 22 °C (black trace), and with temperature increasing, the wavelength of a specific peak appears and moves to a lower wavelength (532 nm at 28 °C (blue trace) and 446 nm at 46 °C (red line)). Therefore, the temperature change can be monitored by the wavelength shift of the specific peak, which is different with temperature OFS coated with RT-leuco-ink which uses intensity change at a specific wavelength. Using a wavelength tracking strategy could potentially be more robust as it would have less bending interference when compared to an intensity-based sensor.

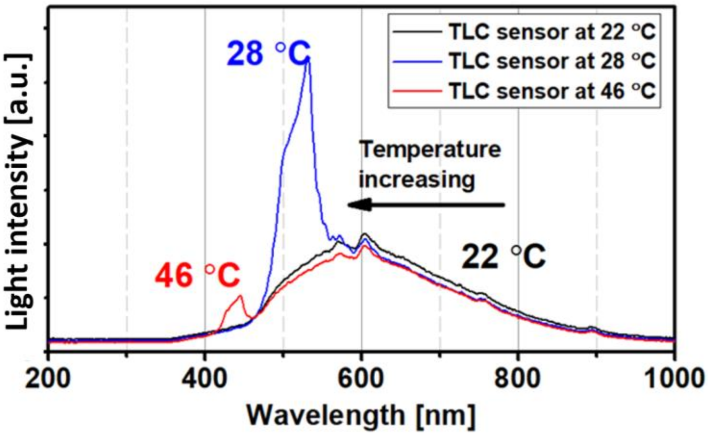

Figure 5. 9 The changing of reflection spectrum of optical fibre temperature sensor coated with TLC material at different temperatures in the chamber.

5.3.2 Temperature calibration

a. RT-leuco-ink

The responses in the reflection spectra of the optical fibre temperature sensor modified with blue RT-leuco-ink film, upon exposure to a range of temperatures in the climatic chamber are shown in Figure 5.10(a). The intensity of the reflected light (at λ = 600 nm) changes in accordance with the temperature change measured from the thermocouple described in Section 5.2.4. The reflection (at λ = 600 nm) of the OFS increases as the temperature increases from 20 to 40 °C. It can be initially verified that the effective temperature measuring range is from 22 to 32 °C.

Figure 5.10(b) represents the dynamic intensity change at 600nm wavelength, for a gradual temperature increase and decrease between 20 °C and 40 °C. With the temperature increase, the optical signal gradually saturates when the temperature exceeds 36 °C. Oppositely, the light intensity starts to show a decreasing trend when the temperature drops to 28 °C. The activation temperature (T_a) of blue RT-leuco-ink is 31 °C specified by the manufacturer, which is located between these two temperatures. Each point in the Figure 5.10(c) is from the average of 120 seconds in each stabilized step obtained from Figure 5.10(b) and the error bar (too small to observe) is the standard deviation of each step and max SD is 0.1 and 0.29 % for increasing and decreasing. The sensitivity is 5.03 %/°C (R^2=0.99) or 3.67 %/°C (R^2=0.94) with temperature increase and decrease, respectively, and the final sensitivity (the average of both) is 4.35 %/°C.

As can be seen there was a significant hysteresis present in the calibration curve of Figure 5.10(c). The hysteresis is calculated to be ±3.18 °C through the Equation 4-3 described in Chapter 4.

The hysteresis as a performance specification, is defined as the difference between measurements of the temperature increase and decrease branch as shown in Figure 5.10(c), which was obtained from the dynamic response of the OFS in the temperature calibration process [134]. This large hysteresis loop might be an obstacle of an optical fibre temperature sensor using this blue film.

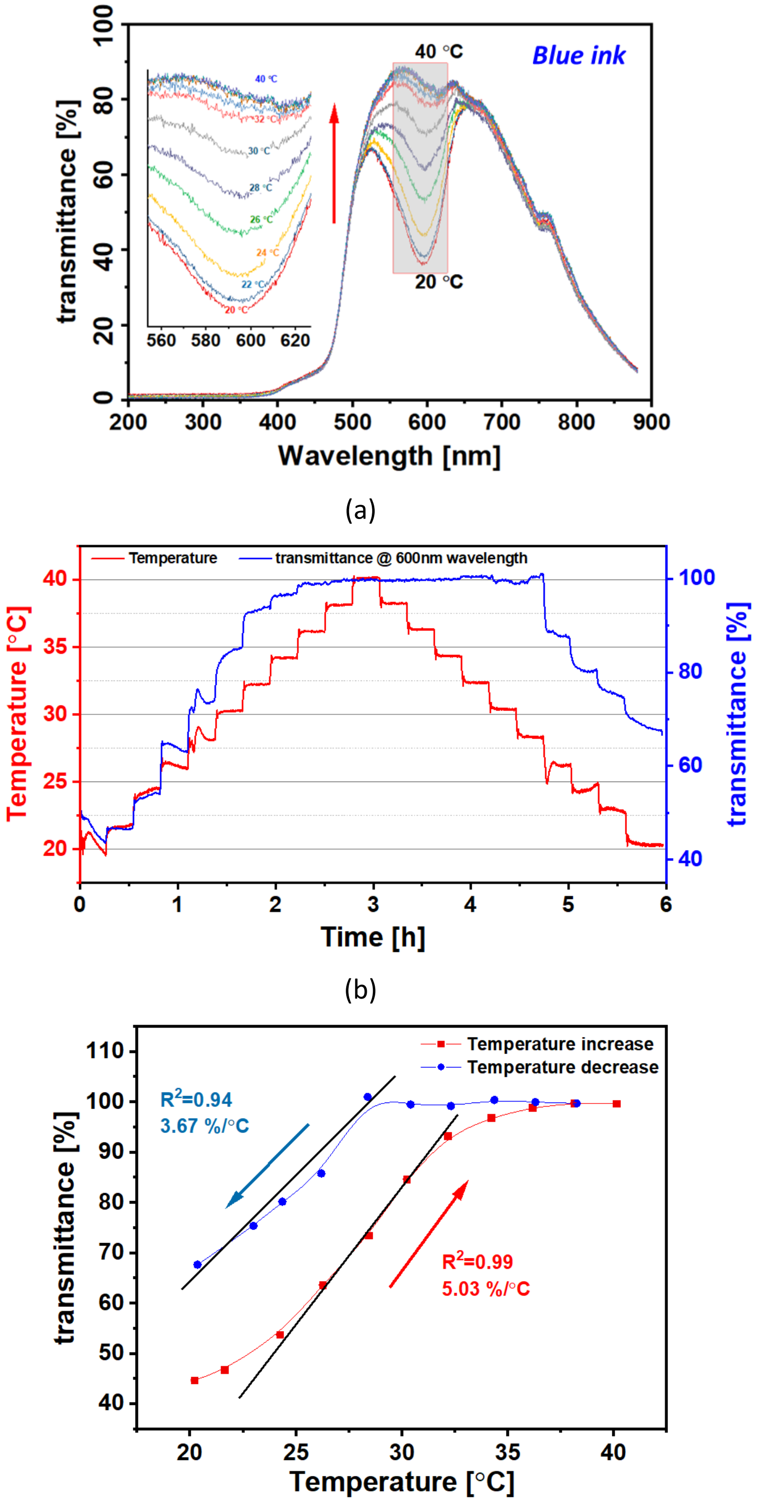

(a)

(b)

(c)

Figure 5. 10 (a) Reflection spectra of optical fibre temperature sensor coated with RT-leuco-ink blue ink film at different temperatures. (b) The dynamic response of the intensity at 600 nm wavelength with changing temperature for calibration in the climatic chamber. (c) The temperature calibration curve, the error bar is smaller than the marker.

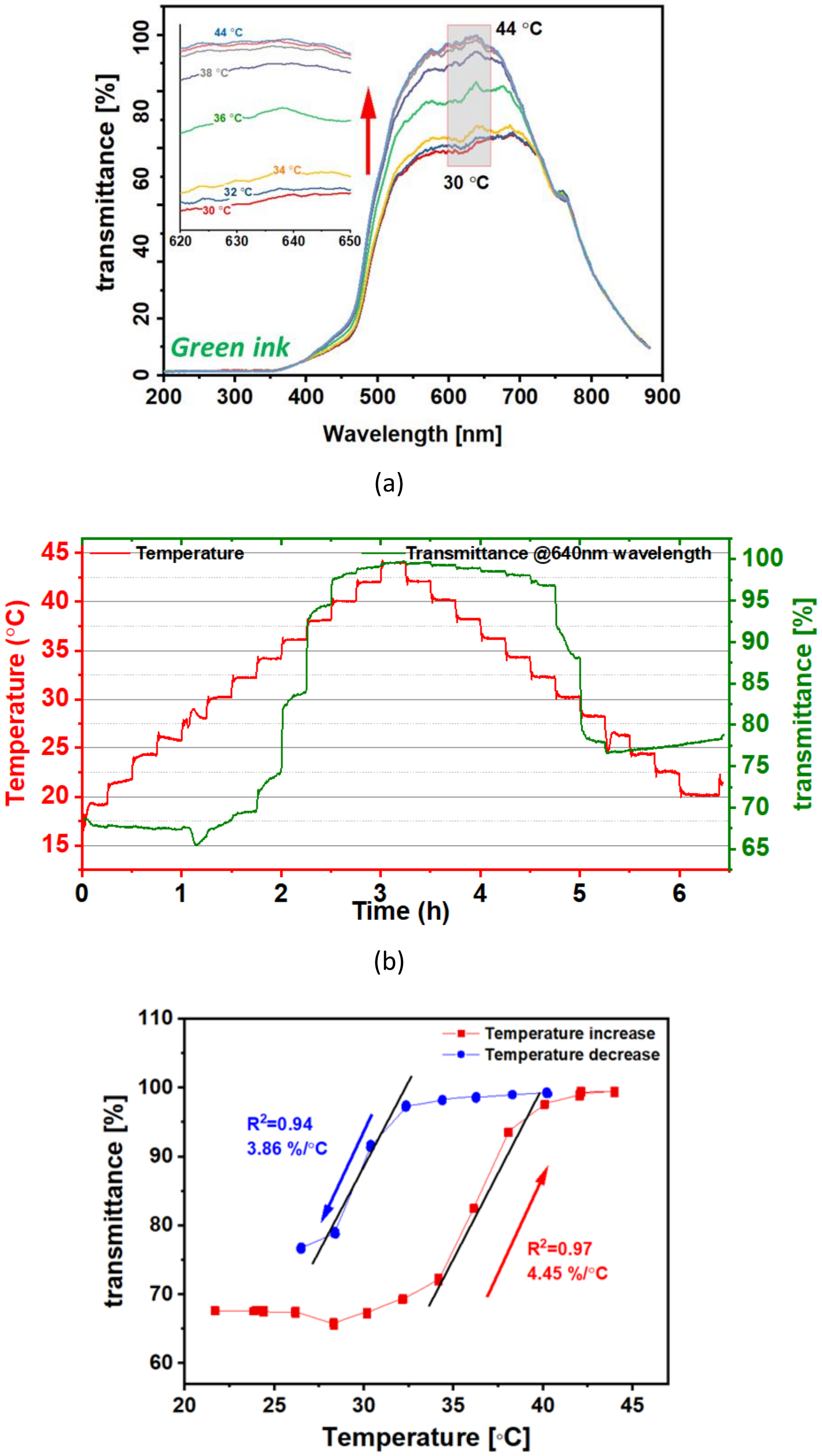

(a)

(b)

(c)

Figure 5. 11 (a) Reflection spectra of optical fibre temperature sensor coated with RT-leuco-ink green ink film from Matsui at different temperatures. (b) The dynamic response of the intensity at 600 nm wavelength with changing temperature for calibration in the climatic chamber. (c) The temperature calibration curve, the error bar is smaller than the marker.

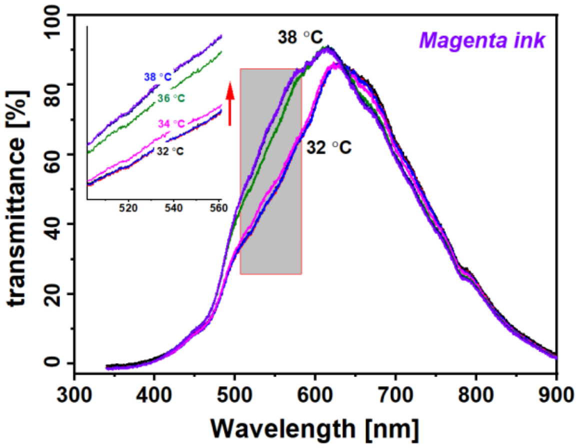

(a)

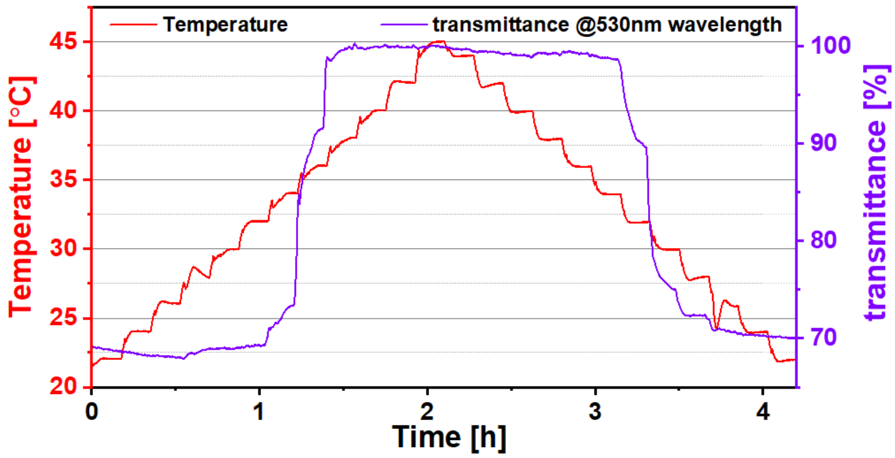

(b)

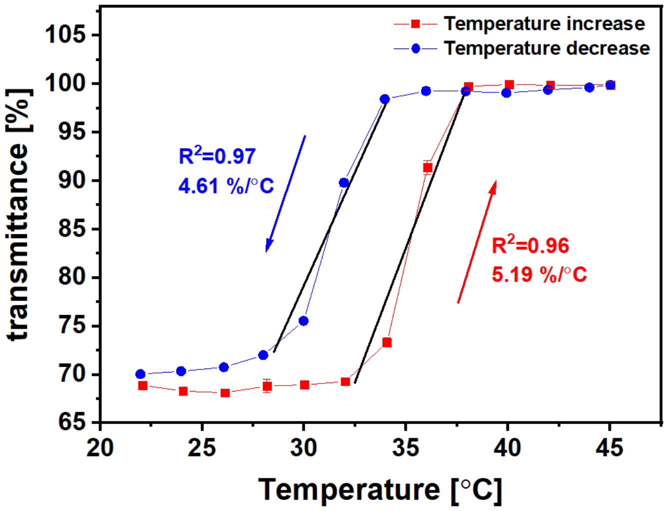

(c)

Figure 5. 12 (a) Reflection spectra of optical fibre temperature sensor coated with RT-leuco-ink magenta ink film from Matsui at different temperature. (b) The dynamic response of the intensity at 530 nm wavelength with changing temperature for calibration in the climatic chamber. (c) The temperature calibration curve.

The green and magenta ink from Matsui company coated optical fibre temperature sensors have been investigated and compared to the previous blue ink from Good life Co. Figure 5.11(a) and 5.12(a) shows the spectral responses of the sensor coated with green and magenta ink film in the climatic chamber with different temperature respectively. The intensity of the reflected light (λ = 640 nm (green) & 530 nm (magenta)) increases with the temperature increase and is compared to that measured by a thermocouple. Subsequently, Figure 5.11(b) and 5.12(b) illustrate the dynamic intensity changes at 640 nm (green) and 530 nm (magenta) wavelength with temperature increasing and decreasing gradually between 20 °C and 44 °C in the calibration process. The calibration curves are illustrated in Figure 5.11(c) and 5.12(c), the points are the average of each stabilized step obtained from the dynamic changes (Figure 5.11(b) and 5.12(b)). The error bar is the standard deviation of each step, max SD are 0.32&0.35 and 0.74&0.42 % for increasing and decreasing process of green and magenta, respectively. The sensitivity is 4.45 %/°C (R^2=0.97) or 3.86 %/°C (R^2=0.94) for green ink and 5.19 %/°C (R^2=0.96) or 4.61 %/°C (R^2=0.97) for magenta ink with temperature increase and decrease, respectively, and the final sensitivity (the average of both) is 4.16 %/°C and 4.90 %/°C for green and magenta ink. It is also noticeable that hysteresis exists in the green and magenta ink cases (as well as the blue at +/- 3.18 °C), which are calculated to be ±2.09 °C for green and ±1.54 °C for magenta.

In summary, these RT-leuco-ink coated OFSs respond monotonically well to temperature but present high hysteresis, ±3.18 °C for blue ink, ±2.09 °C for green ink and ±1.54 °C for magenta ink, attributed to the interactions with lower crystallinity between developer and solvent in the RT-leuco-ink [139, 145].

b. Thermochromic liquid crystal

Another thermochromic material, TLC, has a different thermochromism principle described in Section 5.2.3 and illustrates multi-colour change with distinct temperature. This can be observed by this time using wavelength shifting of a specific peak in the reflection spectrum of the optical fibre coated with TLC. Figure 5.13(a) shows the reflection spectra changes of a TLC coated temperature sensor in temperature range of 22 – 48 °C. No selective reflection peak exists at 22 °C, and with temperature increasing, the selective reflection peak appears and moves to the lower wavelength region. It should be noted that the wavelength of the reflection peak illustrates a large shift from 830 to 570nm (~260nm wide) as temperature increases from 23.75 to 25.83 °C (~2 °C difference). On the other hand, the peak wavelength becomes very sensitive to temperature between 23.75 and 25.83 °C, which might contribute to a stability issue of the optical signal. However, the wavelength shift displays a relatively regular change when the temperature is above 28 °C and covers the temperature range of human core and skin surface (31 – 37 °C) [158] in the majority of health monitoring applications.

Figure 5.13(b) represents the calibration curve of the developed TLC sensor by dynamically tracking of the wavelength shift (black curve) with temperature increasing and decreasing (red curve) gradually between 28 °C and 46 °C. The wavelength shift was calculated by recording the position of selected peak in the spectrum. This preliminary data shows robust performance compared to the previous optical fibre temperature sensor with RT-leuco-ink coatings. There is no significant hysteresis (±0.07 °C) appearing in the calibration curve, shown in Figure 5.13(c), and each point is the average of each stabilized step (120 seconds) obtained from Figure 5.13(b) and the error bar is the standard deviation of each step and max SD is 0.74 and 0.16 nm for increasing and decreasing. The wavelength shift shows linear correlation (R^2 =0.985, 0.973) to the temperature which has the sensitivity of 4.52 nm/°C (temperature increasing), 4.60 nm/°C (temperature decreasing), respectively. It can be noted that the linear fitting curve of temperature increase and decrease is consistent, which indicates that the TLC OFS has a high accuracy for temperature sensing in the range of 28 – 46 °C. The overall temperature sensitivity obtained by taking the average of the above values is 4.56 nm/°C.

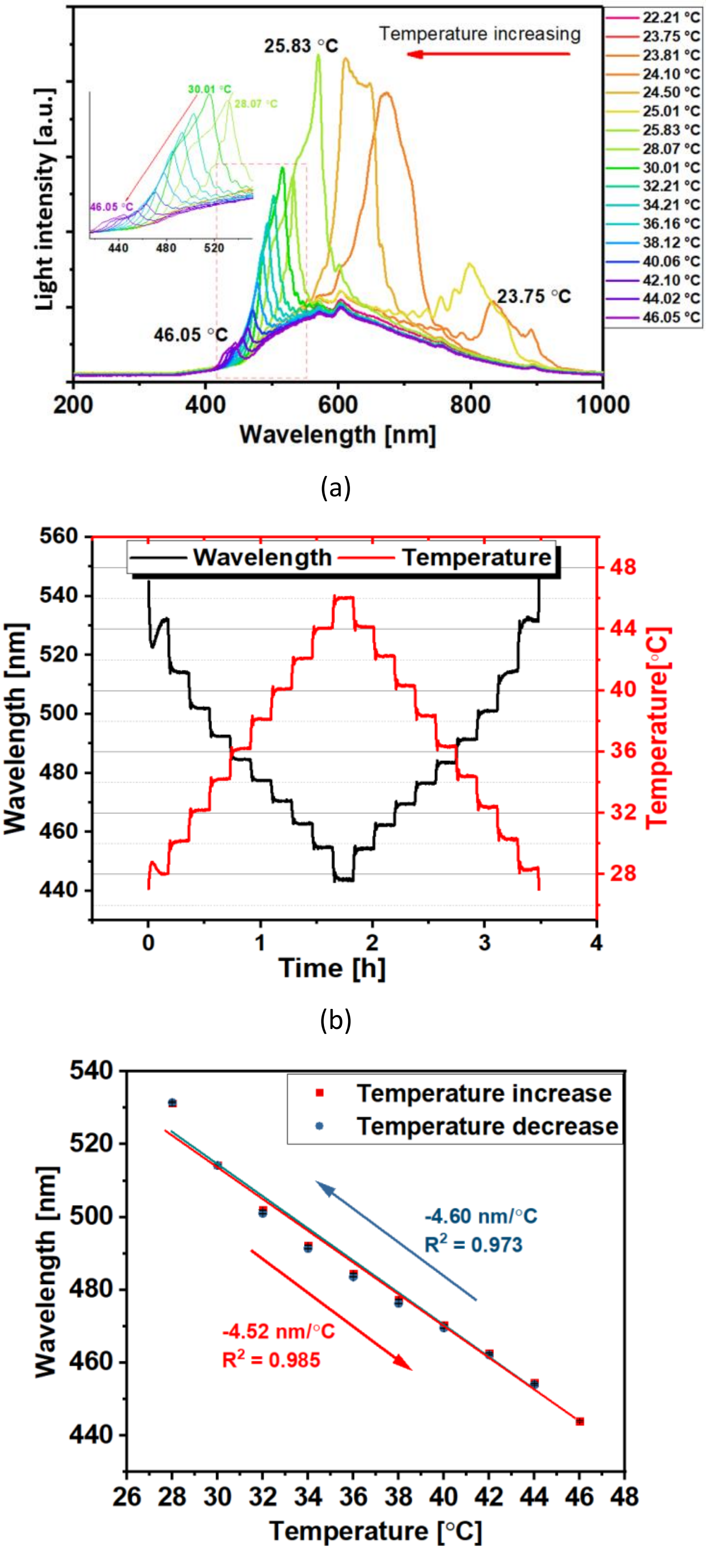

(a)

(b)

(c)

Figure 5. 13 (a) Reflection spectra of TLC coated optical fibre temperature sensor with different temperatures. (b) The dynamic response of wavelength shift of selective reflection peak to temperature calibration in the climatic chamber. (c) The temperature calibration curve.

5.3.3 Temperature test optical fibre sensor

For verifying the repeatability of the TLC OFS for the temperature measurement, 10 TLC OFSs are fabricated simultaneously using the same processing set-up. Subsequently, these 10 sensors are calibrated in the climatic chamber. The calibration curves of 10 TLC OFSs are illustrated in Figure 5.14, the linear fitting curve of each sensor is almost identical. The average sensitivity to temperature was obtained by taking the average of the sensitivities of these ten TLC OFSs, which is 4.29 ±0.06 nm/°C.

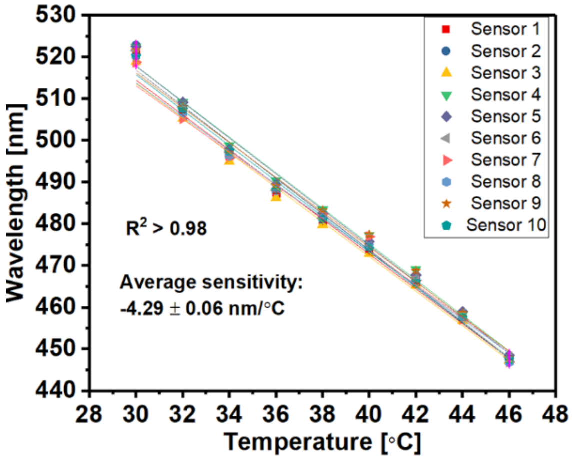

Figure 5. 14 Calibration curves of 10 TLC OFSs in climatic chamber, the error bars are smaller than the markers.

After calibration, the temperature reading of TLC OFS is converted from wavelength to degrees in Celsius. These calibrated TLC OFSs were tested in a climatic chamber with a commercial thermocouple for two test days. The results obtained from the developed TLC OFSs and thermocouple can be compared through Bland-Altman plots [135] – see Figure 5.15. Using Bland-Altman analysis, Figure 5.15(a) for test day1 and (b) for test day2 demonstrates that the difference between the two sensors is similar (P-value = 0.875 > 0.05) in the temperature range from 30 to 46 °C. In the Bland-Altman plot, setting the response of commercial thermocouple as the reference standard of temperature value in x-axis. As can be seen in Figure 5.15, the bias and standard deviation of the difference in test day1 and test day2 is -0.040 °C with STD: 0.278 °C and -0.168 °C with STD: 0.299 °C, respectively. These indicators confirm that TLC OFS has the potential to monitor temperature as a commercial device.

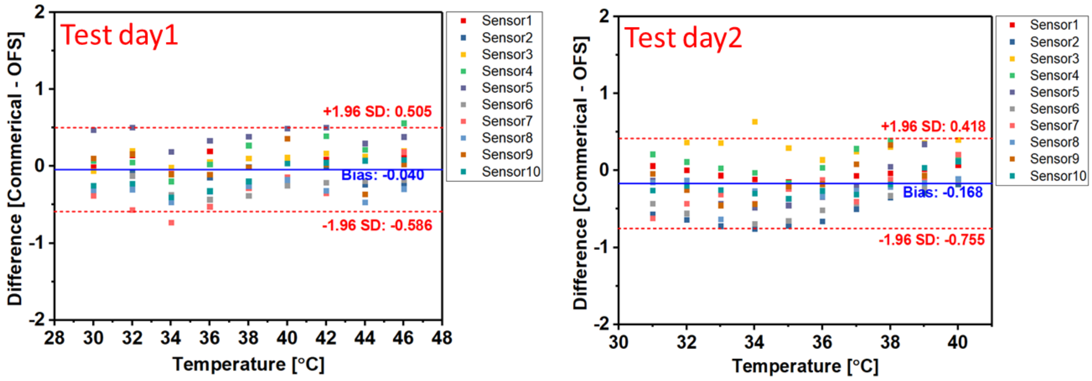

(a) (b)

Figure 5. 15 Bland-Altman plot showing the difference between temperature measurements from 10 TLC OFSs and commercial thermocouple. The x-axis and y-axis show the temperature and the difference (Commercial - OFS) of the temperature reading from the two devices, respectively. (a) test day1 and (b) test day2.

5.4 Conclusion

Two novel approaches, consisting of the use of different thermochromic materials for the fabrication of optical fibre temperature sensors have been demonstrated. Due to their visualized thermochromism in the appropriate temperature range and low cost, the microencapsulated reversible thermochromic leuco ink (RT-leuco-ink) and microencapsulated thermochromic liquid crystal (TLC) have the potential to be a reasonable coating film for optical fibre temperature sensing. Three RT-leuco-ink films have been deposited successfully onto the surface of an optical fibre tip, which respond to temperature with changes in the intensity of the reflected light, but all present high hysteresis, ±3.18 °C for blue ink, ±2.09 °C for green ink and ±1.54 °C for magenta ink. Therefore, this approach of using RT-leuco-ink is not suitable for continuous temperature monitoring due to the large hysteresis exhibited.

The alternative material was TLC which also demonstrates multi-colour changing at different temperatures. After successful coating a TLC film on the tip of the optical fibre, the selective peak appears in the reflection spectrum and it shifts to the blue region with temperature increase. In temperature calibration, the response of TLC OFS to temperature was linear with a sensitivity of 4.52 nm/°C (R^2 =0.985) when temperature increases and 4.60 nm/°C (R^2=0.973) when temperature decreases from 28 – 46 °C. Importantly however, no significant hysteresis appears in these TLC coated optical fibre temperature sensors.

Ten TLC OFSs were fabricated simultaneously using the same set-up. The coincidental calibration curves successfully verify the repeatability of the TLC coating approach. The Bland-Altman plots also demonstrate that the difference between thermocouple and these calibrated TLC temperature OFSs are similar (P-value > 0.05) in the temperature range from 30 – 46 °C. It is therefore proposed that the small size and straightforward fabrication of these TLC sensors allow them to be used as a temperature sensing probe for many health monitoring applications.

Chapter 6: Tip-based hybrid optical fibre sensor for simultaneous humidity and temperature measurement

6.1 Introduction

This Chapter describes a novel hybrid sensor for simultaneously monitoring relative humidity (RH) and temperature. This is achieved by coating a humidity sensitive film (PAH/SiO_2) and a thermochromic liquid crystal (TLC) film for temperature measurement on the same tip of a multi-mode optical fibre Y-type coupler. These sensing films were thoroughly investigated in Chapters 4 and 5. According to the theory of these functional films, the intensity change in the reflection spectrum indicates the relative humidity response for PAH/SiO_2 coating while the wavelength position of a selective reflection peak represents the distinct temperature level for the TLC film. To the author's knowledge, it is the first attempt to combine these two different functional films coated on one single optical fibre. The performance of this hybrid sensor is evaluated by using an optical system consisting of a spectrometer, light source and fibre coupler operating in the visible range. In this Chapter, the response & recovery time, sensitivity, repeatability and crosstalk of the proposed sensor is demonstrated using a climatic chamber and two commercial sensors for temperature and relative humidity reference. Temperature and RH can be combined to provide a measurement of absolute humidity which will also be calculated in this Chapter. This is potentially useful in clinical applications such as monitoring the range of moisture & air temperature delivered to laryngectomized patients [14] and those patients with respiratory problems [12, 13]. Other applications and the importance of this development were described in Section 2.2 in Chapter 2.

6.2 Methodology

6.2.1 Materials

Ethanol, Poly(allylamine hydrochloride) (Mw ~58,000, PAH), Potassium hydroxide (KOH) and Sodium hydroxide (NaOH) were purchased from Sigma-Aldrich, UK. Silica Nanoparticles (SiO_2 NPs, diameter 40-50nm) were purchased from Nissan Chemical, Japan. Thermochromic liquid crystal (TLC, R25C5W) was supplied by LCR Hallcrest, UK. Deionised water (DI-water), having resistivity of 18.2 Megaohm-m, was obtained from a water purification system (PURELAB Option S/R, ELGA). Optical fibre (multimode, pigtail easy-strip 62.8/125 µm ST, A1082) was purchased from All4fiber.

6.2.2 Sensing probe fabrication

The RH sensing film (PAH/SiO_2) was coated on the multimode optical fibre tip using the layer-by-layer technique. The coating step is as follows: (i) KOH solution (Ethanol: DI-water = 3:2) treatment for 30 min to obtain a hydroxylated surface; (ii) after washing and drying, immerse the fibre into the positively charged PAH solution (0.17 wt%, pH=11) for 12 min; (iii) wash and dry, and immerse the fibre in the negatively charged SiO_2 NPs solution for 12 min; (iv) repeat (ii) and (iii) steps to obtain multilayers of PAH/SiO_2 film. In order to obtain a uniform film of NPs, a custom-made coating machine has been assembled by two motorised linear stages (STANDA, 8MT175-50, Italy), as shown in Figure 6.1. Subsequently, the temperature sensing film was coated with TLC by using a dip coating machine (HO-TH-02, HOLMARC, India). After the coating process, the functionalized fibre was placed into an oven at 60 °C for 1 hour for drying the film completely.

The mechanism of the functional films used for humidity (PAH/SiO_2) and temperature (TLC) sensing were thoroughly described in Chapter 4 and Chapter 5, respectively. In this hybrid sensing protocol, the temperature sensing element used is the TLC film. When thermal energy increases the molecular temperature of the TLC [155]: i.e. the director angle changes more rapidly, the pitch becomes shorter, causing the wavelength of the selective reflection peak to shift to the blue region. Vice versa occurs with a temperature decrease, where the wavelength shifts are longer (i.e. a shift towards the red wavelength) [153].

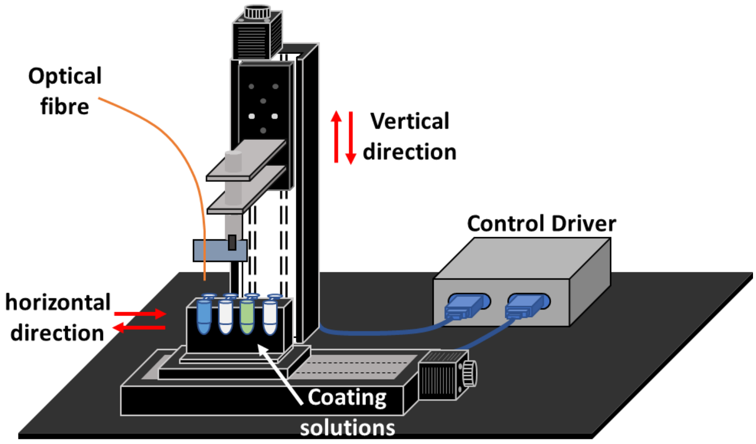

(a)

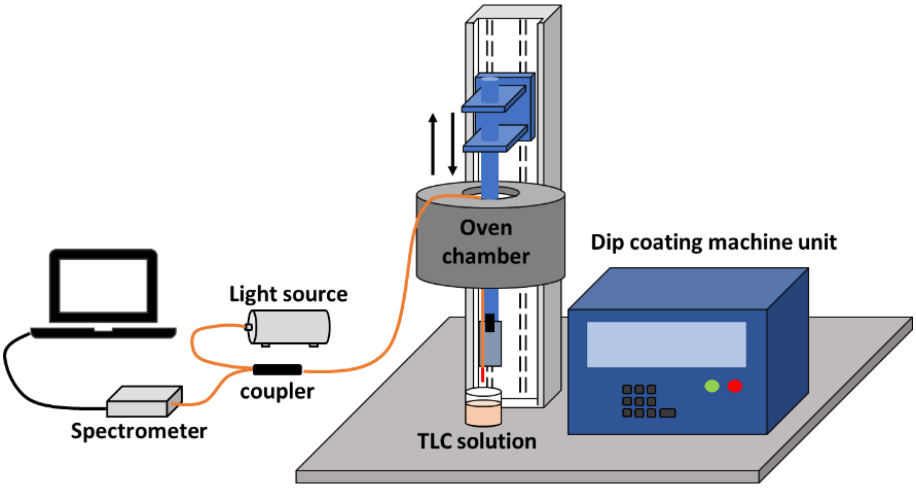

(b)

Figure 6. 1 (a) Custom made coating machine for layer-by-layer self-assembly which has two motorised linear stages (STANDA, 8MT175-50, Italy). (b) Dip coating set-up, the dip coating machine (HO-TH-02, HOLMARC, India) with an in-built oven chamber was used, the reflection spectrum was monitored by a spectrometer (USB2000, Ocean Optics, UK).

The sensing of humidity is determined by PAH/SiO_2 NPs film which has a porous morphology structure, and the hydrophilic property of the PAH layer contributes to adsorb water molecules. Once the sensing film is coated on the tip of the optical fibre, different levels of atmospheric humidity lead to a change of RI of the optical fibre tip with PAH/SiO_2 film [159].

According to the optical signal change, described in the previous two chapters, it is expected for the response of humidity and temperature to be represented in the same spectrum as intensity and wavelength shift change, respectively. The crosstalk of both measuring parameters will be investigated and calibration will be undertaken if required.

6.2.3 Experimental set-up

The climatic chamber (CVMS Climatic, Benchtop C-TH40, UK) described in Chapter 4 and 5 which allows setting the RH in the range from 20% RH to 98% RH (±2.5% RH) and temperature from -20 °C to 180 °C (fluctuation: ±0.5 °C) was used in the experiments. A type K thermocouple with data logger (Pico technology, USB TC-08 thermocouple data logger, UK) and a commercial capacitive humidity sensor (SparkFun BME280, Bosch, GER, RH range: 0% RH - 100% RH, accuracy ±3% RH in the temperature range of -40 °C to 85 °C) were placed inside the chamber for temperature and humidity reading. Light from a halogen source (HL-2000, Ocean Optics, UK) is coupled into a 3dB 2x1 fibre coupler (Newport, F-CPL-M12855, UK). The reflected light from the tip of the fibre is measured by a spectrometer (USB2000+, Ocean Optics, UK).

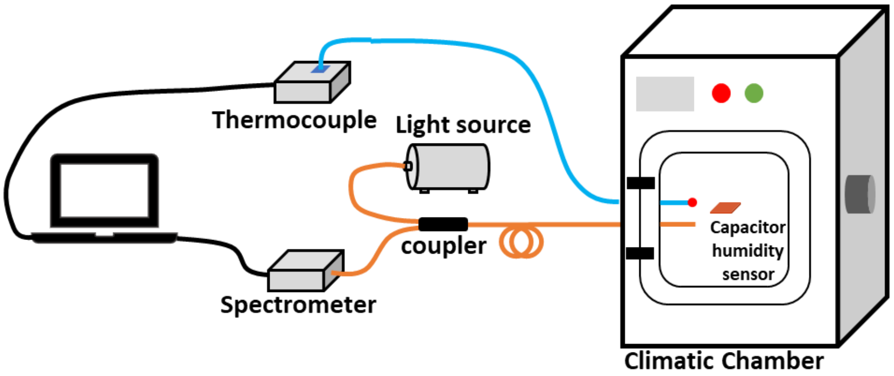

Figure 6. 2 Experimental set-up for the calibration, humidity and temperature measurement of OFS; a commercial capacitive humidity sensor (BME280) and a thermocouple (Pico technology, USB TC-08, UK) were placed inside the climatic chamber (Benchtop C-TH40, UK), the spectrometer (USB2000, Ocean Optics, UK) is connected to a PC to monitor the reflectance spectrum.

6.2.5 Sensor characterization and measurements

The morphology of the PAH/SiO_2 film and the TLC film coating on the fibre tip were studied using scanning electron microscopy (JEOL, JSM-7100F, UK).

Response and recovery time of the OFS were investigated by using the set-up in Figure 6.2. Firstly, the climatic chamber was set at a constant temperature and humidity level. Then the prepared OFS and commercial sensors are inserted into the chamber until all signals stabilize. Finally, the sensors are withdrawn into ambient conditions to observe how rapidly the signal recovers to a stable level. The response and recovery times are measured as the time between 10% - 90% of signal change.

For humidity calibration, the RH was changed from 90% RH to 55% RH and reversed every 15 min with three cycles at a constant temperature of 32 °C. The reflection spectra of OFS, RH and temperature readings of the commercial sensors were recorded simultaneously with the same frequency (1 Hz). The humidity crosstalk of temperature sensing can be investigated in the meantime.

For temperature calibration, the chamber temperature is increased gradually from

28 °C to 46 °C and back, while the relative humidity was set at a constant 55%. The reflection spectra of the OFS, temperature and humidity reading of the thermocouple and humidity commercial sensor were recorded simultaneously with the same frequency (1 Hz). The temperature crosstalk of humidity sensing can be investigated in the meantime.

For assessment of the OFS repeatability to temperature, the latter was increased from 30 °C to 37 °C (common temperature range of human body) and reversed back to 30 °C with 10 cycles while relative humidity was set at a constant 55%.

Finally, in order to investigate the OFS performance under the changing of both temperature and humidity simultaneously, the environmental chamber temperature and humidity was set to ramp up and down three times (30 °C & 55% RH to 37 °C & 90% RH, respectively) and was held for 10mins in each step. The reflection spectra, temperature and humidity readings from the commercial logger were recorded simultaneously. The absolute humidity (AH) with units of mg H_2O/L can be calculated from these two parameters [160]:

$$AH = \frac{M_{H_2O} * RH * P_{ws}}{R * T};\ \ P_{ws}(T) = 6.112 * e^{\frac{17.67*T}{243.5+T}} \qquad (6-1)$$

where M_{H2O} is the molar mass of H_2O (18.02 g/mol), R is the gas constant which is 8.314 J/mol*K, RH and T are relative humidity and temperature value in units of % and K, respectively, $P_{ws}(T)$ is the saturation vapour pressure as a function of temperature [160]. These values are then substituted into Equation (6-1) to obtain the Absolute Humidity (AH):

$$AH = \frac{2.1674 * RH * 6.112 * e^{\frac{17.67*T}{243.5+T}}}{273.15 + T} \qquad (6-2)$$

Where T is the temperature in degrees Kevin.

6.3 Results and discussion

6.3.1 Hybrid sensor modification

Figure 6.3(a) illustrates the sensor probe structure. Figure 6.3(b) and (c) show the SEM image of the optical fibre surface coated PAH/SiO_2 only and with TLC film, respectively. It can be seen that the PAH/SiO_2 film presents a uniform and porous morphology. Although the TLC film is thick, shown in Figure 6.3(c), the water vapour is able to pass through the TLC and interact with inner humidity sensing layer. The humidity response in the spectrum changing will be shown in section 6.3.3. As described in Chapter 5, the TLC material is packaged by isolating in microcapsules for protecting and the diameters are generally in microns level. Each of those micro-mounds on the fibre surface shown in the SEM image is a single TLC micro-capsule. The reflection spectra in Figure 6.3(d) show the spectral changes before and after coating with humidity and temperature functional films. It can be seen that there has been marked drops of the whole spectrum after coating with each functional film due to the increasing RI of the film during the coating process based on the Fresnel equation [159]. After coating with TLC, a selective reflection peak appears at ~500 nm at 32 °C environmental temperature compared with the spectra before coating with TLC at the same temperature condition [161].

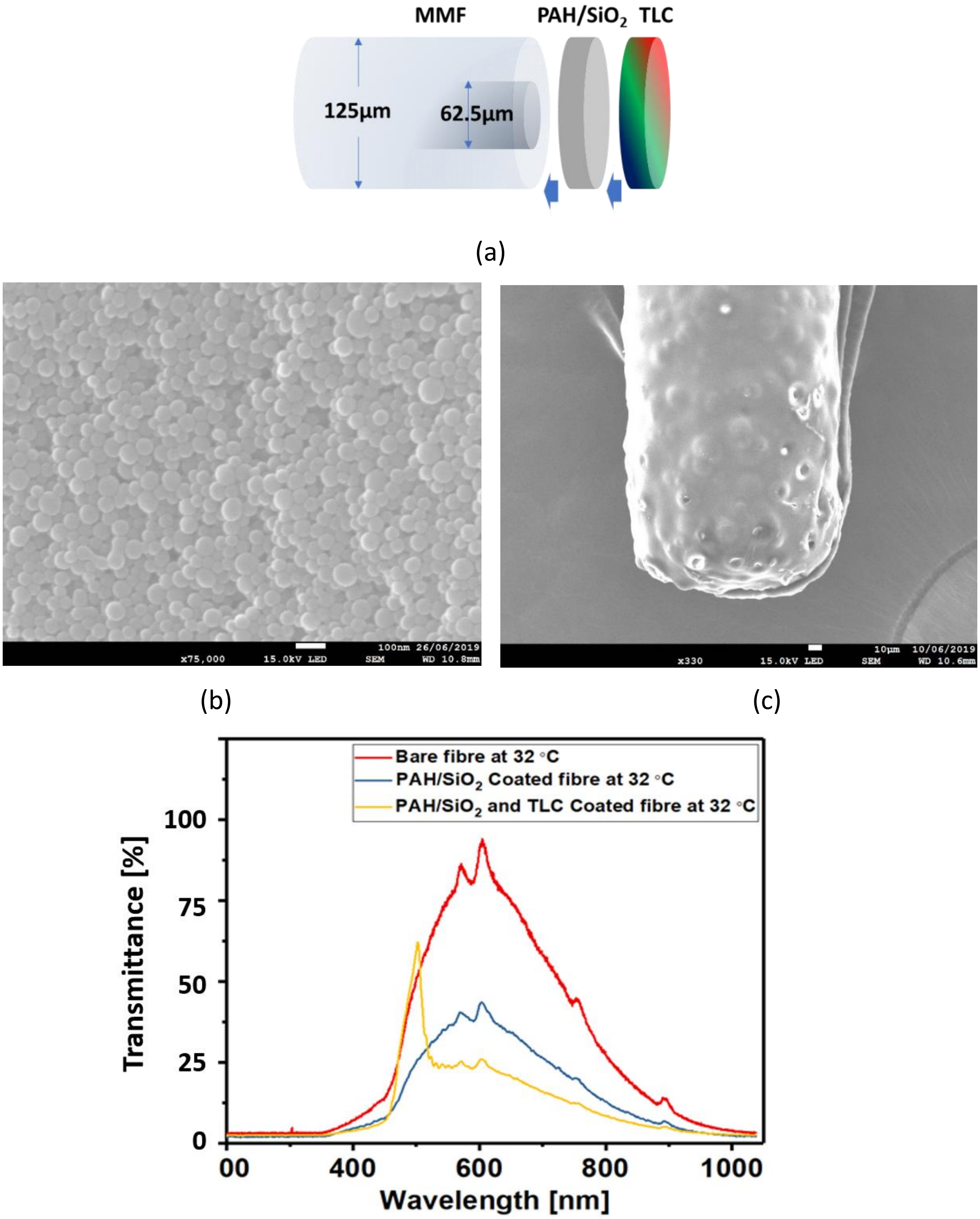

(d)

Figure 6. 3 (a) Hybrid sensor structure (MMF- multimode fibre: 62.5 µm of core diameter, TLC- thermochromic liquid crystal). (b) SEM image of PAH/SiO$_2$ film coating on the fibre surface (scale bar = 100 nm). (c) SEM image of optical fibre tip coated with PAH/SiO$_2$ & TLC film (scale bar = 10 µm). (d) Reflection spectra of bare OFS, after coating with PAH/SiO$_2$ film and TLC at 32 °C.

6.3.2 Response and recovery time of hybrid OFS

Figure 6.4(a) and (b) show the response and recovery times of the OFS with temperature and humidity measurement, respectively, compared with a thermocouple and a commercial humidity sensor as the reference. The response and recovery times are measured as the time between 10% - 90% of signal change for increase and decrease of signals respectively.

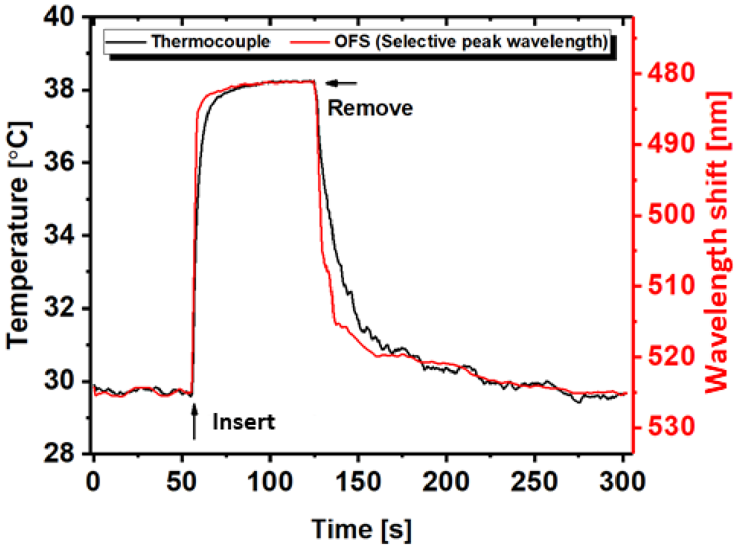

(a)

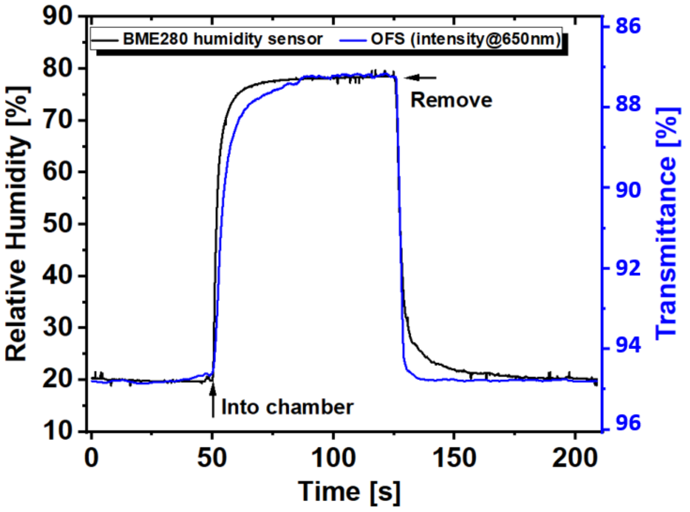

(b)

Figure 6. 4 (a) Response and recovery times of OFS for temperature measurement; (b) Response and recovery times of OFS for humidity measurement (BME280 – commercial humidity sensor)

In the temperature measurement, for OFS, the response and recovery time is calculated as 3.1 s and 57.3 s, for the thermocouple, the response and recovery time is 8.5 s and 59.1 s, respectively between 30 – 38 °C. In the humidity measurements, for the OFS, the response and recovery time is calculated as 13.2 s and 2.6 s whilst for the commercial humidity sensor the response and recovery time is 6.7 s and 8.9 s, respectively between 20 – 80% RH. In a humid case, the vapour molecule interacting with the SiO_2 film first needs to pass through the TLC film, which may cause a slightly longer response time. The optical signal recovers back once there is a dissociation of water vapour with SiO_2 surface, therefore, the RH recovery time is shorter than response time.

6.3.3 Humidity measurements using OFS

Figure 6.5(a) shows the reflection spectrum change of the OFS at a constant temperature (32 °C) with different humidity levels, 55% and 90%, respectively. It should be noted that there is a significant intensity change of the whole spectrum during the increase of humidity, meanwhile, the selective reflection peak of the TLC sensor remains at the same wavelength (~501 nm) indicating the position of the peak is not affected by humidity. This phenomenon offers initial confidence in the investigation of humidity crosstalk for the spectral signal due to temperature. Figure 6.5(b) illustrates the intensity change at a wavelength of 650 nm in comparison with the RH readings from the BME280 commercial humidity sensor against time. The OFS response (black trace) correlates with the change of RH (blue trace) and the reversibility to RH can be observed from the dynamic intensity change graph. In the RH calibration curve, Figure 6.5(c), the response of the OFS shows a linear relationship (R^2 =0.973) to the RH change with a sensitivity of -0.43 %/RH% (@650nm) in the range of 55-90%. The error bars in the calibration curve represent the standard deviation of three repeat cycles, and each standard deviation is calculated using 6 points at relevant RH values obtained from figure 6.5(b).

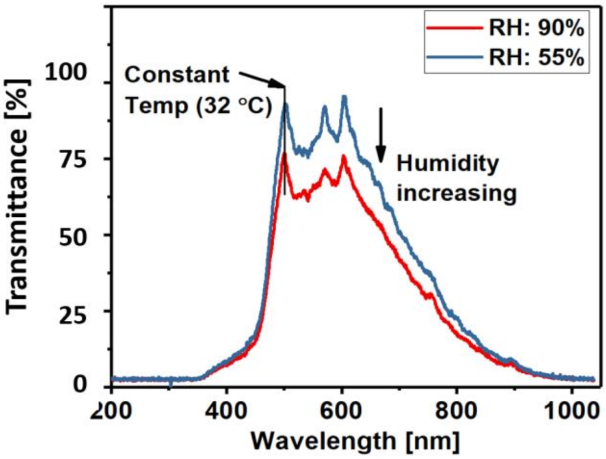

(a)

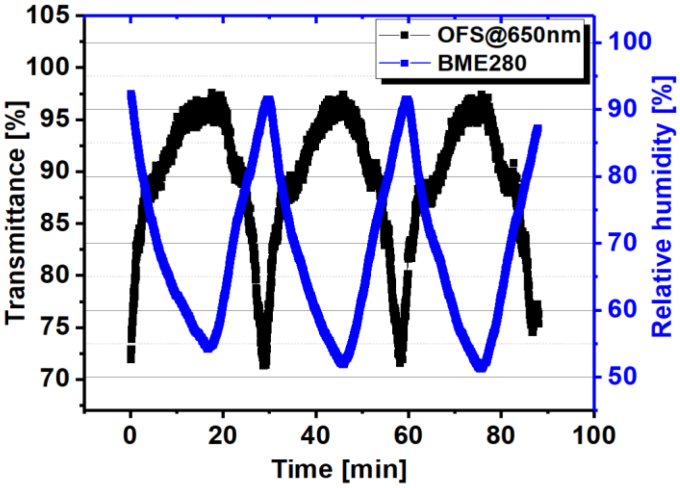

(b)

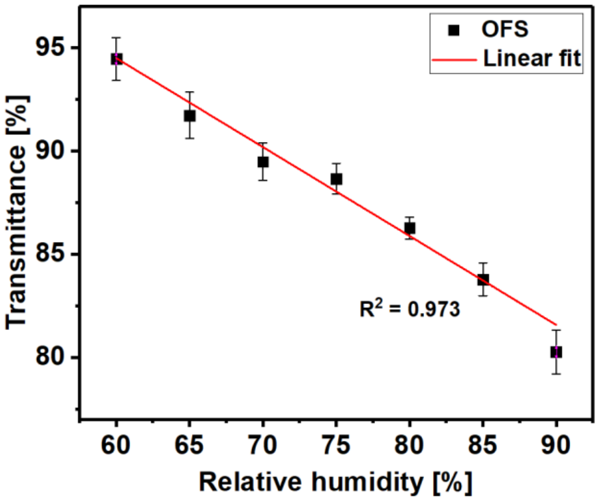

(c)

Figure 6. 5 (a) Reflection spectrum of OFS in 90% RH and 55% RH at constant temperature (32 °C). (b) The dynamic light intensity response at 650nm wavelength of OFS in comparison to RH readings from a commercial humidity sensor. (c) The RH calibration curve of OFS (error bars represent the standard deviation of three repeat cycles).

Figure 6.6 shows the humidity cross-sensitivity evaluation of wavelength position of the selective peak of the proposed hybrid sensor, the temperature was controlled at 32 °C while the humidity decreases. With a 7 %RH change of humidity, the wavelength of the selective peak and the temperature fluctuates at a stable level, 507±0.3 nm for wavelength and 32.3 °C for temperature, respectively. This relatively stable reflection value demonstrates that the selective peak wavelength has a negligible cross-sensitivity to humidity.

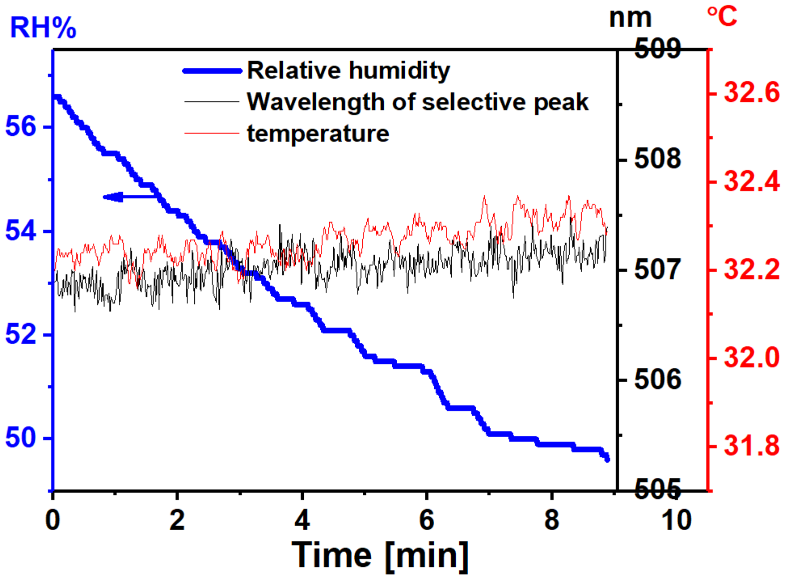

Figure 6. 6 Humidity crosstalk evaluation of temperature sensing film: blue, red and black trace represents relative humidity, temperature and wavelength shift of selective peak, respectively.

6.3.4 Temperature measurements by using OFS

In order to investigate the shelf-life reliability of the OFS, the same OFS has been recalibrated after 20 days. Figure 6.7(a) represents the dynamic wavelength shift with temperature increasing and decreasing gradually between 28 °C and 46 °C on the 1st and 20th day, respectively. This preliminary data shows robust performance. The temperature calibration curves of two test days are shown in Figure 6.7(b), each point is the average of each stabilized step obtained from Figure 6.7(a) and the error bar is the standard deviation of each step.

The wavelength shift shows linear correlation (R^2 =0.995, 0.992, 0.996, 0.990) to the temperature which has the sensitivity of 4.02 nm/°C (temperature increasing), 3.99 nm/°C (temperature decreasing) on the first calibration day and 3.81 nm/°C (temperature increasing), 4.07 nm/°C (temperature decreasing) on the 20th calibration day, respectively.

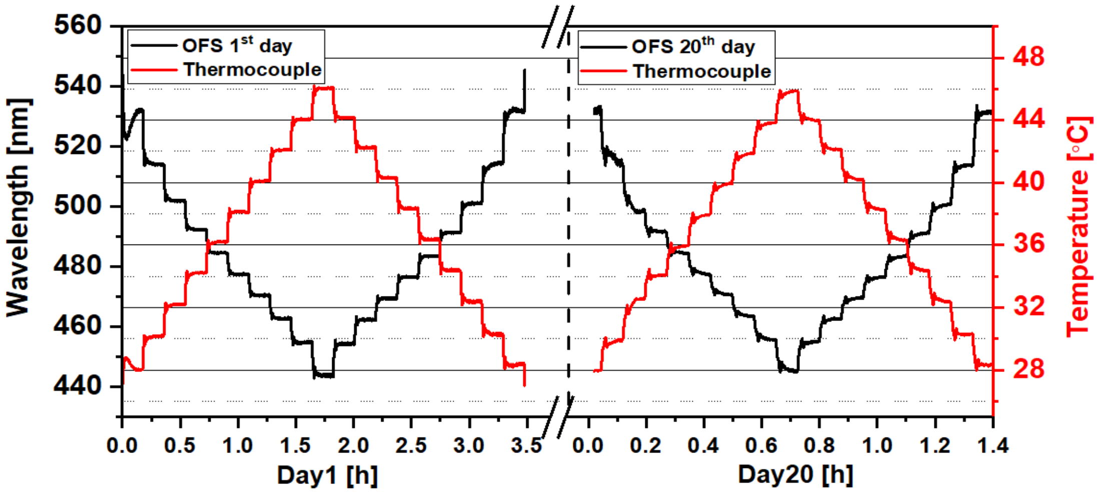

(a)

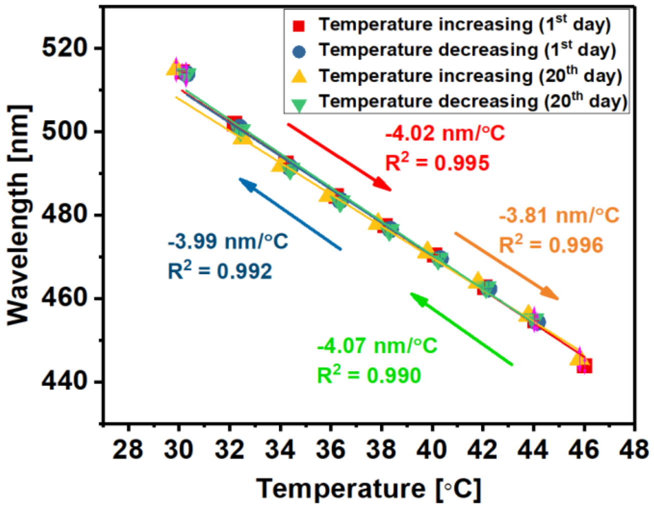

(b)

Figure 6. 7 (a) The dynamic response of wavelength shift for selective reflection peak with changing temperature in the climatic chamber on the 1st and 20th calibration day. (c) The temperature calibration curves of OFS for 1st and 20th test day, the error bar is smaller than the marker.

The overall temperature sensitivity obtained by taking the average of the above values is 3.97 nm/°C. It can be noted that the linear fitting curve of each test is almost coincidental, which indicates that the OFS has a long lifetime and high accuracy for temperature sensing in the range of 28 – 46 °C.

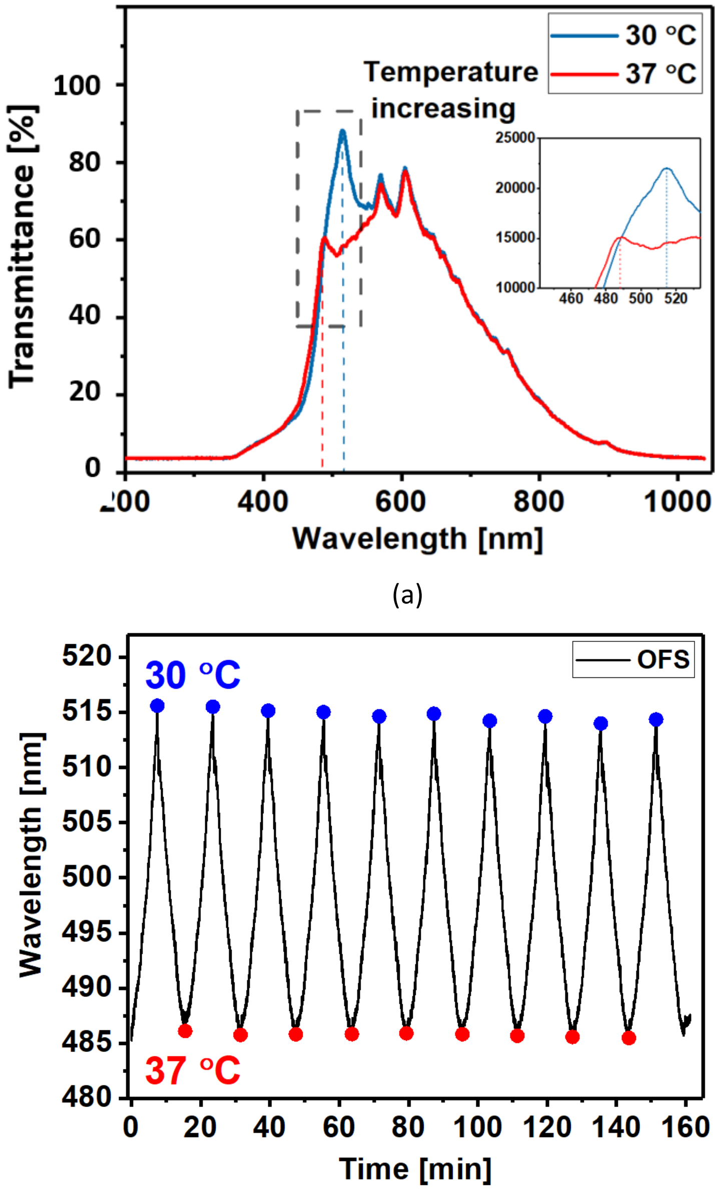

(a)

(b)

Figure 6. 8 (a) The reflection spectrum of OFS at different temperature (blue line for 30 °C and red line for 37 °C) at constant humidity level of 50 RH%, inset shows region around the selective peak. (b) The wavelength shift of the selective reflection peak under alternating temperature between 30 and 37 °C.

To further illustrate the repeatability of the prepared OFS, Figure 6.8 shows the spectrum and the wavelength of the selective reflection peak change as the temperature alternates between 30 and 37 °C for 10 repeats at a constant level of humidity. The selective reflection peak moved from around 515 nm (30 °C) to 485 nm (37 °C) as shown in Figure 6.8(a).

In addition, the intensity of the remaining spectrum (apart from the selective peak) remains at the same level, including the intensity at 650 nm wavelength, during the temperature measurement except for the region of the selective peak. This means the intensity change at most wavelengths is not affected by the temperature change in the range of 30-37 °C.

As shown in Figure 6.8(b), the wavelength value in 30 °C and 37 °C environment tends to be a constant during the 10 thermal cycles, which indicates the performance of the OFS to temperature sensing is stable and repeatable within the tested temperature range.

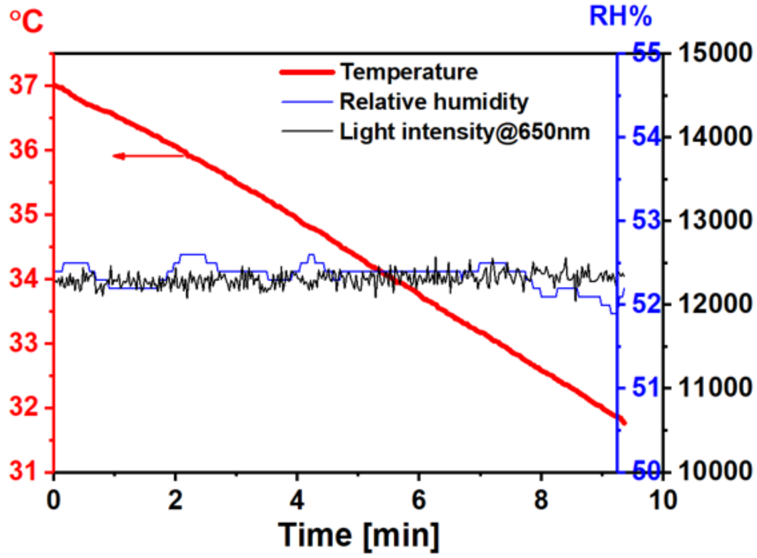

Figure 6. 9 Temperature crosstalk evaluation of humidity sensing film: red, blue and black trace represents temperature, relative humidity and intensity change at 650 nm wavelength, respectively.

Figure 6.9 illustrates the temperature cross-sensitivity evaluation for the light intensity at a wavelength of 650 nm (indicating relative humidity) of the proposed hybrid sensor, setting the temperature decreasing while the humidity remains at a relative stable level. It can be noted that the light intensity(@650 nm) and the humidity value fluctuates at a stable level when the temperature decreasing. This relatively stable reflection value indicates the light intensity(@650 nm) has a negligible cross-sensitivity to temperature.

6.3.5 Simultaneous temperature and humidity measurement

To further illustrate the performance of the prepared sensor, the temperature and RH are modified simultaneously (30 °C to 37 °C and 55 RH% to 90 RH%) in the climatic chamber while monitoring the spectral change of the OFS. According to the previous results, the wavelength shift of the selective reflection peak indicates the temperature change and the intensity (@650 nm) indicates the humidity change. The selective reflection peak position has been tracked by using the *findpeak* function in MATLAB. The dynamic change of spectra with temperature and RH increasing simultaneously is shown in Figure 6.10(a), the selective peak moves left and the whole spectrum falls with temperature and RH increase, respectively. Figure 6.10(b) also shows the spectrum change of the sensor in different temperature & RH environments (low: 30 °C and 55 RH%, high: 37 °C and 90 RH%).

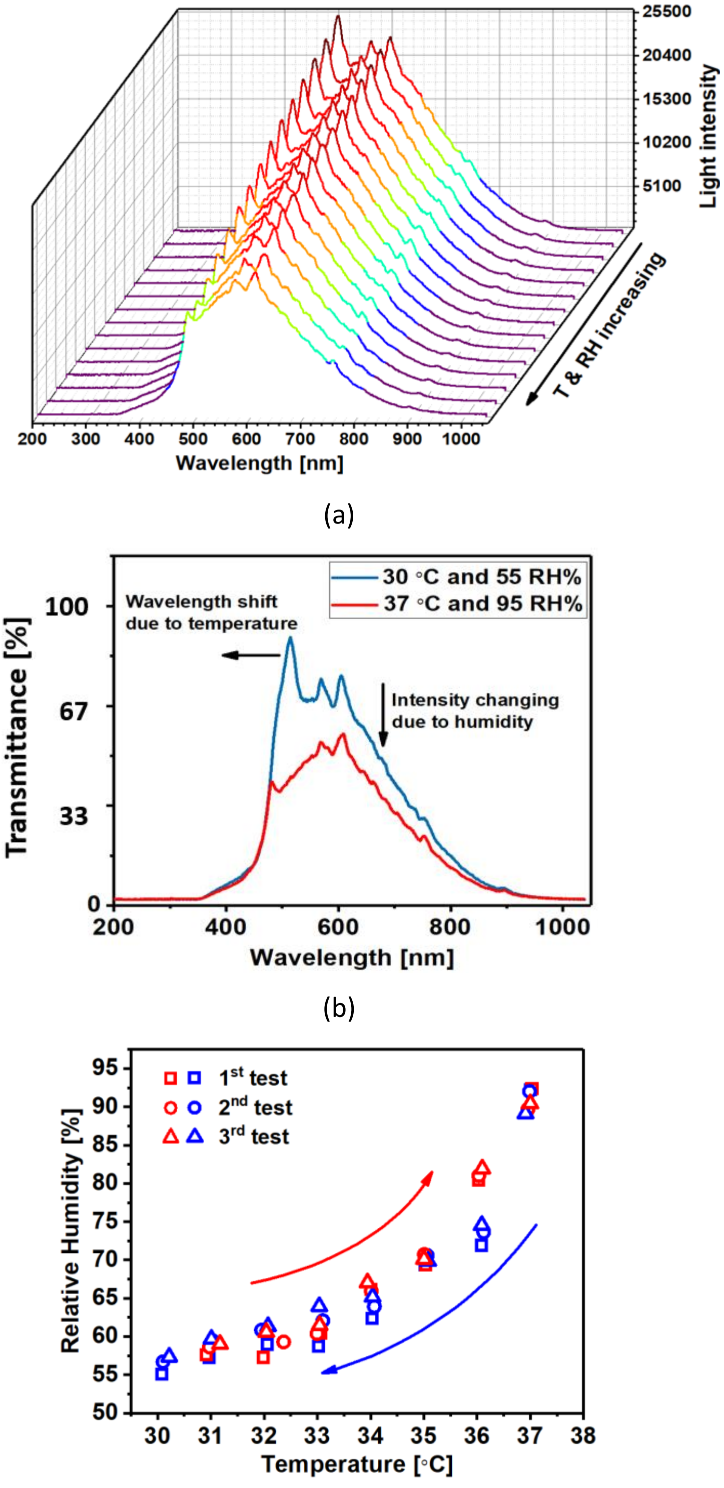

Figure 6. 10 (a) The spectrum changes with temperature and RH increasing simultaneously. (b) The reflection spectrum in low (blue curve) and high (red curve) temperature & RH environment, the wavelength shift and intensity change due to temperature and RH, respectively. (c) Hybrid sensor response for changing RH and temperature simultaneously, square, circle and triangle represent 1st, 2nd and 3rd test, red and blue for increasing and decreasing process respectively.

Once the RH and temperature tests were performed, and sensitivities were obtained, the response from the sensor can be translated into a RH and temperature reading. As shown in Figure 6.10(c), the experimental results are repeatable in environments of 55 %RH & 30 °C to 90 %RH & 37 °C. The absolute humidity (AH) change, as shown in Figure 6.11, was calculated from the temperature and RH values using equation (2).

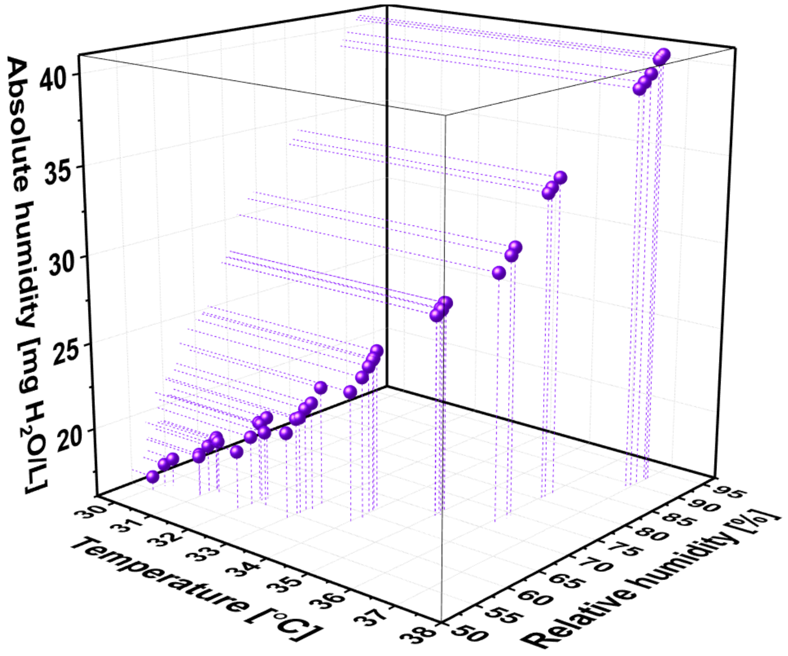

Figure 6. 11 Absolute humidity calculated from the simultaneous temperature and RH measurements, in the ranges of 30-37 °C and 55-90%, respectively.

The state of the art in hybrid optical fibre sensors for humidity and temperature sensing is presented in Table 6-1. It can be seen that our current hybrid sensor exhibits a higher sensitivity to temperature (3.97 nm/°C), although it cannot be directly compared to the RH sensitivity due to the different response units (intensity base in this work). The temperature measuring range of the proposed sensor is narrower compared with other types of sensor in the table, which is 28-46 °C, however, it is ideally suited to many healthcare applications. The cost of using an OFS based on gratings is much higher than reflection type optical fibre sensors, thus, the proposed sensor has the potential for widespread use. Moreover, the proposed hybrid sensor is able to measure at a single sensing point for RH and temperature, which allows sensor to operate in a confined environment, compared to other types of optical fibre sensors.

Table 6- 1 Comparison of different RH and temperature optical fibre sensors. '-' indicates the information is not provided in the cited work

Optical fibre sensor structure	*RH sensitivity & range*	*Temperature sensitivity & range*	*Sensing region*	*Response time*	*Ref*
Array of LPGs	0.53 nm/RH% (35-98%)	0.46 nm/°C (25-38 °C)	6 cm	RH: - T: -	[162]
Functional tip & FBG	- (11-97%)	0.01 nm/°C (10-85 °C)	5 mm + fibre tip(Ø:125 µm)	RH: <1.5 s T: -	[163]
Partially-coated LPG	0.063 nm/RH% (20-80%)	0.41 nm/°C (25-85 °C)	6 cm	RH: - T: -	[164]
Polymer fibre FBG	0.007 nm/RH% (10-90%)	0.03 nm/°C (20-100 °C)	2 mm	RH: - T: -	[165]
Suspended-core fibre	-	0.01 nm/°C (20-1100 °C)	Fibre tip (only temperature)	T: -	[166]
Hybrid functional tip	0.43 %/RH% (55-90%)	3.97 nm/°C (28-46 °C)	One fibre tip (Ø:125 µm)	RH: 13.2 s T: 3.1 s	This work

6.4 Conclusion

A novel optical fibre hybrid sensor for monitoring relative humidity and temperature was developed by coating the tip of a single optical fibre with PAH/SiO_2 for relative humidity, and a thermochromic liquid crystal for temperature. The reflected intensity changes in response to the RI change of the PAH/SiO_2 film when absorbing water molecules at different RH. The signal response to RH was linear (R^2 =0.973) with a sensitivity of 0.43 %/RH% in the RH range of 55% to 90%. The selective reflection peak showed the sensitivity to temperature and a linear relationship (R^2 =0.993) between peak wavelength shift and temperature with a sensitivity of 3.97 nm/°C over the temperature range of 28 – 46 °C. Moreover, the proposed sensor shows no significant crosstalk between each of the sensing parameters, with a response time of 3.1 s temperature (30 – 38 °C) and 13.2 s for relative humidity (20 – 80 %).

In addition, the simultaneous RH and temperature measurement is repeatable over several cycles and several shelf-life days, indicating that the proposed sensor has the potential for measuring absolute humidity to generate additional information in clinical applications. In comparison to grating based optical fibre sensors the proposed sensor is low-cost with a simple manufacturing process which has the potential to find widespread use in healthcare applications.

Considering the temperature and humidity measurement range in the majority of clinical applications mentioned in the Chapter 2, the proposed optical fibre sensor has potential to be used in some specific clinical situation, considering the suitable measurement range of temperature (28 – 46 °C) and humidity (20 – 90%). For example, in the chronic wound healing process, a temperature difference between feet above ~2.2 °C can be a trigger of early detection signs of ulceration, meantime wound humidity levels play an important role in healing.

Chapter 7: Dabrafenib detection by using a surface polymer imprinted long period grating

7.1 Introduction

Dabrafenib is one of the most widely used of the new generation of targeted anti-cancer drugs. However, its therapeutic window varies for different patients and so there is an unmet need for methods to monitor the dose of a drug which the patient receives. In this Chapter, a novel sensor based on an optical fibre long period grating (LPG) modified with a molecular imprinted polymer (MIP) has been developed with the ultimate aim of achieving minimally invasive measurements of Dabrafenib concentration *in vivo*. As discussed in Chapter 3, the significant advantages of LPG optical fibre sensors over other types such as tapered, intensity based and multimode interferometers are their mechanical robustness and wavelength encoded sensor output making them ideal candidates for practical biomedical applications [4].

The aims of this study is to evaluate if molecularly imprinted polymers could be prepared on LPG surfaces to generate cavities with selective binding properties for target templates [124], and with the ability to transduce a signal from the binding events via a wavelength shift under conditions relevant to clinical monitoring. The molecular imprinting process will be carried out on a methacryloylalkoxysilane-functionalised fibre in the presence of Dabrafenib and an analogue, 2-aminoquinoline (2-AQ). The bulk RI influence is tested by comparing a bare LPG with functionalised LPG in different solvents. Moreover, the selectivity of the Dabrafenib MIP LPG sensor is investigated by comparing the response of bare LPG, the functionalised LPG to Dabrafenib and 2-AQ in different concentration of Dabrafenib and 2-AQ in PBS solution. In addition to verifying the performance of the prepared Dabrafenib molecularly imprinted polymer (DAB MIP) sensor under more clinically relevant conditions, measurements are conducted to detect Dabrafenib and 2-AQ in

Fetal bovine serum (FBS).

7.2 Methodology

7.2.1 Materials

Sulphuric acid, Hydrogen peroxide solution (30 wt% in H_2O), 3-(Trimethoxysilyl) propyl methacrylate (TMSPMA), Methanol, Acetic acid, Chloroform ($CHCl_3$), 2,2-Dimethoxy-2-phenylacetophenone (DMPA), Ethylene glycol dimethacrylate (EGDMA), Poly(ethylene glycol) methacrylate (M_n = 500 $g{\cdot}mol^{-1}$, PEGMA), Methacrylic acid (MAA), 2-Aminoquinoline (2-AQ), Fetal bovine serum (FBS) were purchased from Sigma-Aldrich, UK. Dimethyl sulfoxide (DMSO) was purchased from Honeywell, UK. Dabrafenib was purchased from Adooq bioscience, USA. All the chemicals were of analytical grade and used without further purification. Deionised water (DI-water) was obtained from water purification system (PURELAB Option S/R, ELGA). Phosphate buffered saline (PBS) was freshly prepared by dissolving PBS tablets (Oxoid, UK) in DI-water, which comprised Sodium chloride (8.0 $mg{\cdot}mL^{-1}$), Potassium chloride (0.2 $mg{\cdot}mL^{-1}$), Disodium hydrogen phosphate (1.15 $mg{\cdot}mL^{-1}$), Potassium dihydrogen phosphate (0.2 $mg{\cdot}mL^{-1}$), pH 7.3 ± 0.2, at 25 °C.

7.2.2 LPG fabrication

The LPG used in this chapter is generated through the LPG fabrication process method described in Chapter 3. An LPG of length 30 mm and with a grating period of 112 µm was fabricated in boron-germanium co-doped optical fibre (Fibrecore PS750, Ø core/cladding: 4.4/125 µm, single-mode with cut-off wavelength of 670 nm) using a custom made amplitude mask and side-illuminating the optical fibre by the output from a ultraviolet radiation (operating at wavelength of 266 nm, 100 ns pulse duration, 12 mW power) of a frequency-quadrupled Nd:YAG laser. During the fabrication process, light is launched through the fibre and the transmitted spectrum recorded at a 1 Hz sampling frequency. The LPG period was selected for operating at or near the phase matching turning point (PMTP), which ensures the highest sensitivity [167].

7.2.3 Design of a molecular imprinted polymer surface on an LPG

An imprinting approach based on the key functionality in the analyte of interest, Dabrafenib, i.e. the 2-aminopyrimidine ring, was developed which is expected to bind strongly to methacrylic acid, one of the most utilised monomers for molecular imprinting. The sensors are intended for use in aqueous conditions, thus in addition to methacrylic acid as the functional binding monomer, we included the water-soluble monomer poly(ethyleneglycol) methacrylate (PEGMA), in order to swell the MIP matrix in contact with serum, and allow easier access of the drug molecules into the recognition sites. In addition, PEGMA was included because of its strong enthalpic binding to water and entropic resistance to compression, helping to provide a barrier to adsorption of proteins, predominantly albumin, which otherwise cause fouling of materials in contact with serum components. Owing to the cost and potency of Dabrafenib, the initial fibre-coating and imprinting protocols was optimised using 2-aminoquinoline as an inexpensive analogue of Dabrafenib, with 2-aminopyridine functionality to serve as a model for imprinting the 2-aminopyrimidine region of Dabrafenib (Figure 7.1).

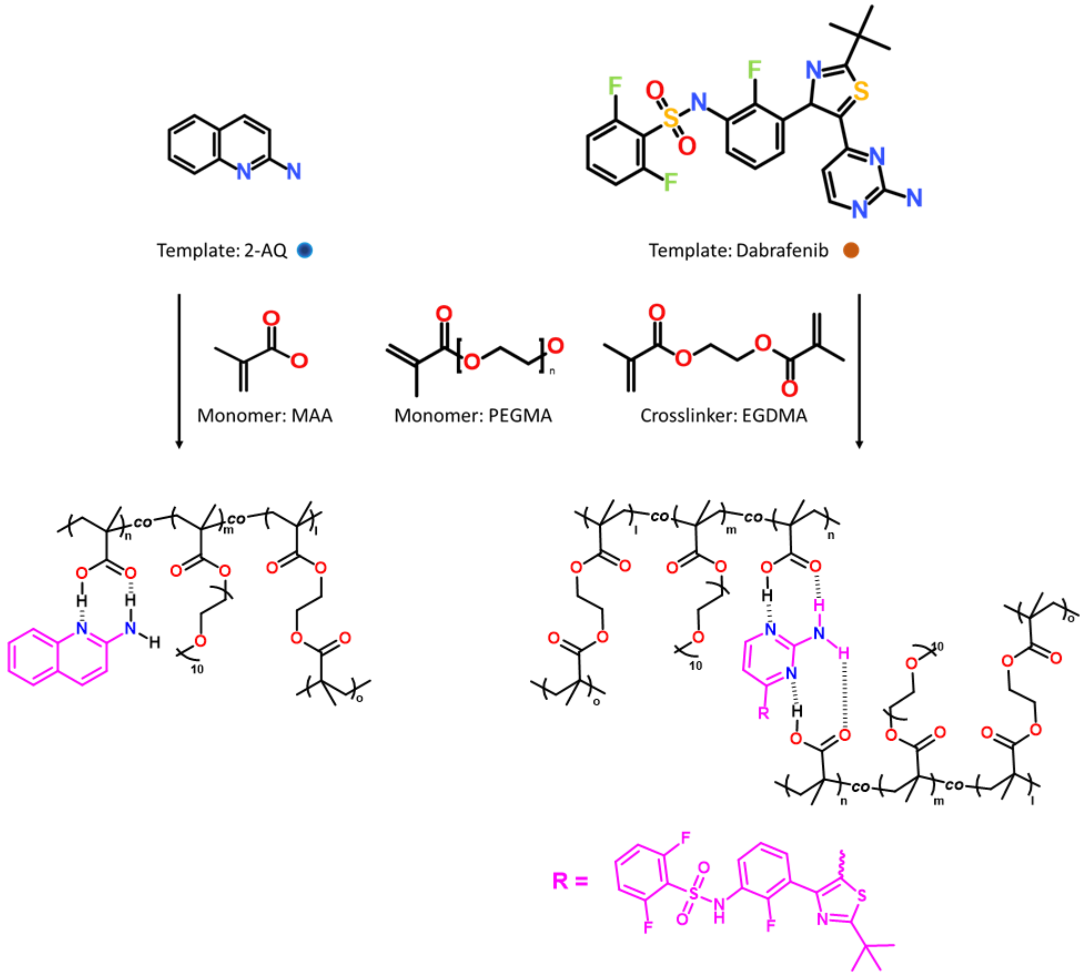

Figure 7. 1 Schematic of potential binding modes for imprinting of 2-aminoquinoline (2-AQ) and Dabrafenib.

7.2.4 Imprinted LPG sensor preparation and characterization

Piranha solution is prepared by slowly adding 30% hydrogen peroxide into sulfuric acid as 1:3 (v/v) [168]. The region of the optical fibre containing the LPG is initially treated with Piranha solution for 30 mins. After washing with deionized water (15 MΩ cm) and drying with a stream of N_2 gas, the LPG is then modified by silanizing in a 5% solution of 3-(trimethoxysilyl) propyl methacrylate in acidified methanol/H_2O (95/5, v/v) for 1 h [124]. The fibre is then washed with methanol and water repeatedly in an ultrasonic bath. The pre-polymerization solution is prepared by dissolving Dabrafenib

(10.4 mg, 20 µmol), MAA (5.2 µL, 61.7 µmol), EGDMA (79.2 µL, 420 µmol) and PEGMA (6.5 µL, 14.3 µmol) and DMPA (20 mg, 78.1 µmol) in 1 mL chloroform. Subsequently, the mixture is sonicated for 10 min and degassed by bubbling with N_2 for 20min. The fibre is immersed into the freshly prepared pre-polymerization solution. The fibre is then withdrawn and exposed to UV irradiation (XX-15 Bench Lamp Fixture, 365 nm) for 5 h and left at room temperature overnight. Finally, the MIP coated LPG sensor is washed with a solution of methanol/chloroform (50/50, v/v), pH=3.5) and dried under a stream of N_2 gas.

2-AQ MIP sensors (Dabrafenib analogue) are fabricated as these provided a cost-effective means of optimizing sensor parameters and also enabled rapid evaluation of any cross sensitivity of the Dabrafenib MIP sensors. These are prepared under identical conditions using the same methodology but with the following polymerization mixture: 2-AQ (14.4 mg, 100 µmol) MAA (17.2 µL, 204 µmol), EGDMA (396 µL, 2.1 mmol) and PEGMA (65.4 µL, 143 µmol) and DMPA (20 mg, 78.1 µmol).

Fourier transform infrared spectrometry (FTIR) is performed using a Cary 630 spectrometer (UK) with wavenumber accuracy of 0.05 cm^{-1}. Measurements are performed at 25 °C, with 64 scans per sample, after subtracting a background spectrum measured over an average of 16 scans between 4000 – 650 cm^{-1}. The spectra from the LPG are measured using a CCD spectrometer (Ocean Optics, HR4000, UK) with 0.11 nm wavelength accuracy and a tungsten-halogen light source (Ocean Optics, HL-2000, UK).

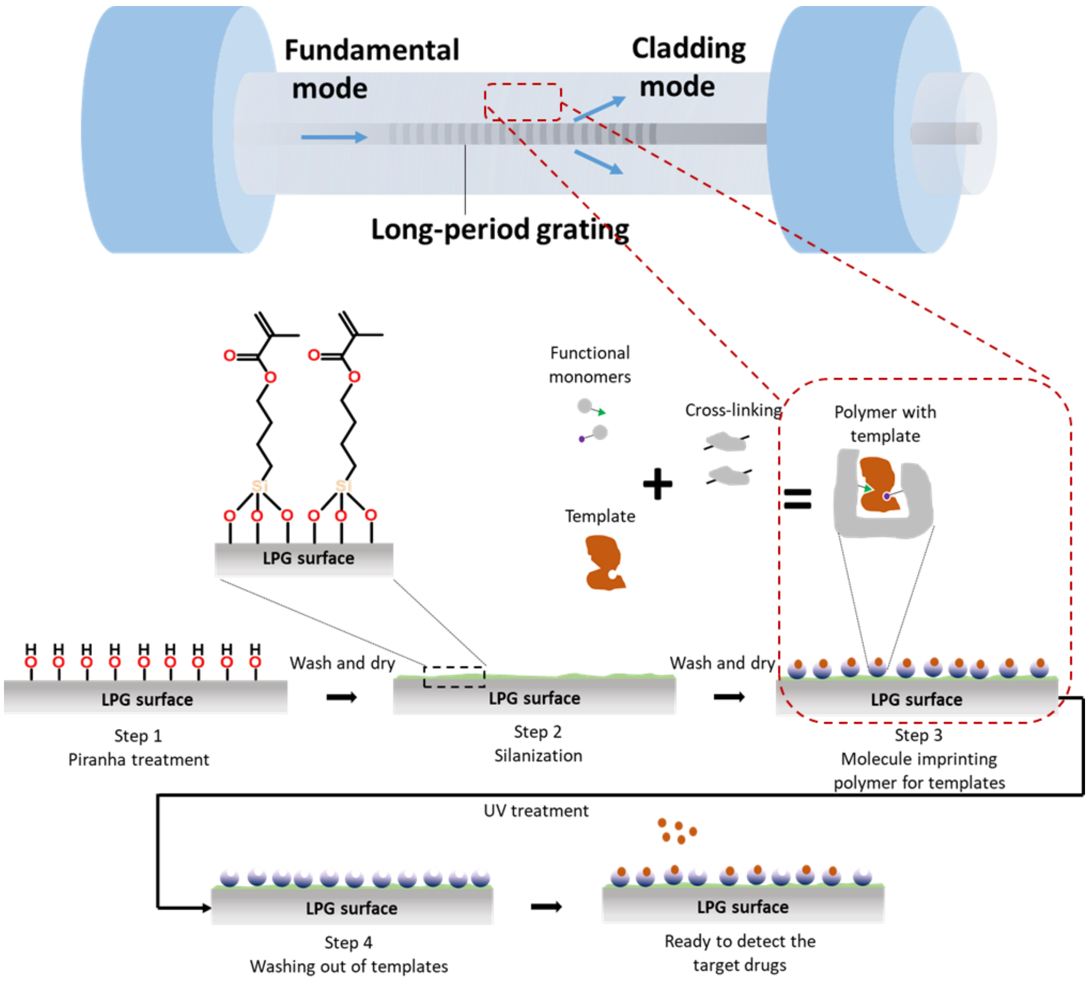

Figure 7. 2 Schematic of the format and functionalisation of LPG sensors.

7.2.5 Measurements of template binding specificity

The bulk RI of different solvents can be a confounding issue for measurement of the LPG response in liquid [126]. Accordingly, the responses of the bare LPG and MIP functionalized LPG in different buffer solutions were evaluated, with transmission spectra of two LPGs, before and after functionalization, being measured after immersion into DI-water, PBS and FBS, respectively.

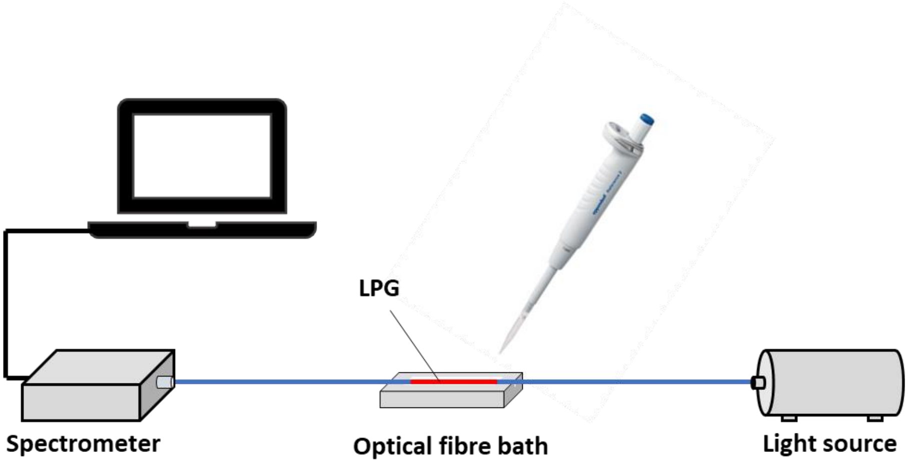

Figure 7. 3 Experimental set-up of measurement using LPG in transmission mode, a pipette used for changing solutions.

The behaviour of a non-imprinted LPG (NIP LPG) sensor was investigated by comparing the response of the 2-AQ imprinted LPG with the non-imprinted LPG. After fabrication, the two LPGs were immersed in 2-AQ solutions varying in concentration from 1.0-6.6 mg·mL^{-1} and the LPG response measured by recording the wavelength shift over these concentrations.

Similarly, the Dabrafenib molecularly imprinted polymer sensor (DAB MIP sensor) was exposed to variable concentrations of Dabrafenib (in PBS) by immersion into 0-1.0 mg·mL^{-1} of Dabrafenib until the measured signal does not change with further addition of the analyte. These ranges were chosen as the clinically observed concentration for a dose of 150 mg/kg twice daily is ~2 µM (1.0 mg·mL^{-1}) [169]. In order to investigate cross sensitivity, the DAB MIP sensor was also exposed to varying concentrations of the 2-AQ analogue.

After each exposure, the sensor was washed with acidified water with methanol/chloroform (1:1) to remove the Dabrafenib adsorbed to the MIPs, followed by thorough rinsing with DI-water and drying with N_2. The transmission spectrum of the LPG sensor was acquired and recorded during the whole measurement using the CCD spectrometer (HR4000, Ocean Optics, UK) set-up as shown in Figure 7.3 with a sampling frequency of 1 Hz. A Teflon LPG bath with the dimension of 55×5×4 mm (L*W*D) was used for setting the LPG region in relevant solvent. The wavelength shifts of the attenuation band of the PMTP were tracked from the recorded spectra. For the binding selectivity experiments, the DAB MIP sensor was exposed to 2-AQ (in PBS) with increasing concentrations up to 1 mg·mL^{-1} and the bare LPG and 2-AQ MIP sensors were tested by exposure to variable concentrations of Dabrafenib (in PBS) and 2-AQ (in PBS) respectively.

7.2.6 Detection of Dabrafenib in serum

In order to mimic more closely conditions likely to be encountered *in vivo*, the DAB MIP sensor was tested by exposure to Dabrafenib in FBS at drug concentrations up to 750 µg·mL^{-1} and 2-AQ in serum with concentration up to 500 µg·mL^{-1}. All experiments were conducted at 20 °C in a temperature regulated laboratory to reduce the known effects of temperature cross-sensitivity on LPGs. The LoD is estimated as LoD=3*σ/S, where σ is the standard deviation of the measured signal and S is the sensitivity of the sensor derived from the calibration curve [170]. In all experiments, the reflection spectra of the OFS and temperature reading of the thermocouple were recorded simultaneously with the same frequency (1 Hz).

7.3 Results and discussion

7.3.1 Characterisation and fabrication of Imprinted LPG sensor

The first step in the process is to functionalise the LPG surfaces with methacrylate functionality in order to form a reactive substrate for subsequent covalent anchoring of the MIP matrix. Cleaning of the LPG was performed using Piranha solution and multiple washing steps with deionised water prior to drying. The fibres are then reacted with 3-(trimethoxysilyl) propyl methacrylate (TMSPMA) and allowed to dry. ATR (attenuated total reflectance) FTIR spectra of the bare and silanized glass substrate (Figure 7.4) are recorded to confirm success of the silanization process. There is a weak attenuation band from υ(O-H) stretches between 3200 and 3700 cm^{-1} on the silanized glass due to residual free hydroxyl groups, but also bands present at ~ 3000 cm^{-1} and 1720 cm^{-1}, in the case of silanized glass due to υ(C-H) and υ(C=O ester) contributions, respectively.

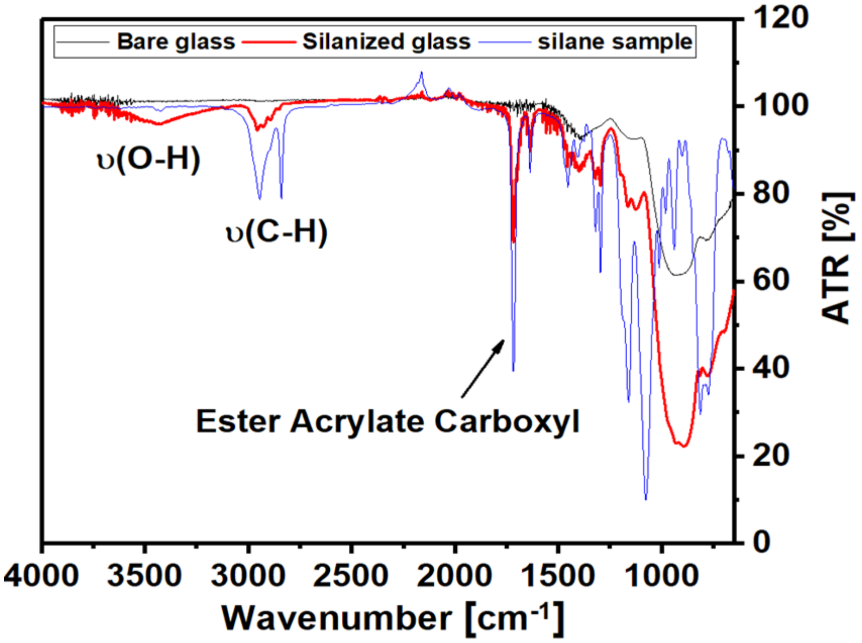

Figure 7. 4 ATR-FTIR spectra of bare glass (black), silanized glass (red) and silane liquid sample of TMSPMA (blue).

The transmission spectra are measured in air after each deposition process and normalised by taking an automatic baseline for each spectrum using MATLAB software. It should be noted that all drug concentration measurements were made relative to this baseline and so the absolute position does not affect the measurement. A simulation software for optical grating evaluation, called *OptiGrating*, is used for verifying the LPG fabrication result. Table 7-1 shows the input setting parameters of optical fibre PS 750 for the simulation of the transmission spectrum of LPG based on *OptiGrating 4.2.2.* The positions of the experimentally measured attenuation bands of an uncoated LPG (LP_{019} = 663.5 nm, LP_{020} = 819.7 nm) are slightly different to those obtained using simulation with *OptiGrating 4.2.2* (LP_{019} = 655 nm, LP_{020} = 830 nm) as the spectra shown in Figure 7.5(a). This may be attributed to the deviation of the real fibre RI value from the optical fibre datasheet values or uncertainties in the LPG fabrication process (error in length or period). As shown in Figure 7.5(b), after methacryloylsilanization (blue curve), there is a blue shift of linearly polarised (LP) mode LP_{020} resonance, and the appearance of a dual attenuation band for LP_{020} mode resonance, which are characteristic of a thin film deposited onto the cladding of the LPG [126, 171]. It should be noted that further blue shifts of LP_{019} mode resonance and development of the dual attenuation band for LP_{020} resonance are observed, after the template imprinting stage (green trace shown in Figure 7.5(b)), indicating successful coating of a MIP layer onto the LPG surface.

Table 7- 1 Input parameters of PS 750 optical fibre

Fibre type	PS750
RI of fibre core	1.4583
RI of fibre cladding	1.4533
RI of surrounding	1
Radius of fibre core (um)	2.21
Radius of fibre cladding (um)	62.6

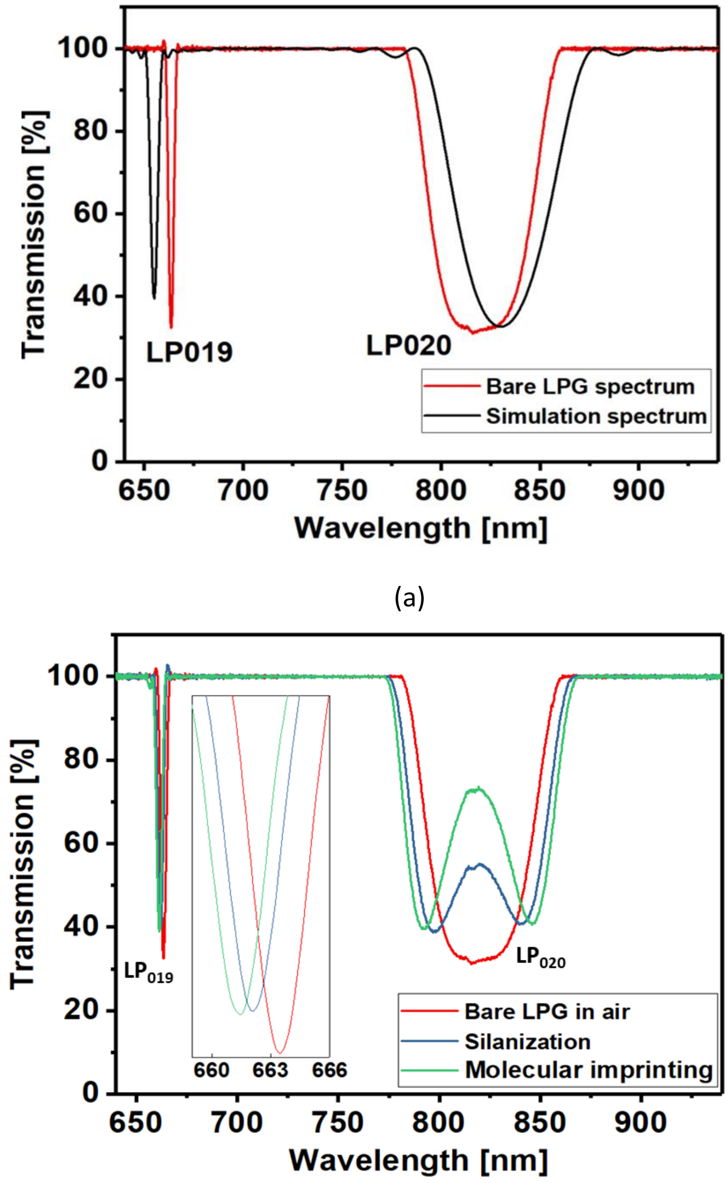

(a)

(b)

Figure 7. 5 (a) Spectral comparison of simulation (*OptiGrating 4.2.2*) and experiment. (b) Transmission spectra of the deposition of MIP LPG sensor.

7.3.2 Bulk RI evaluation & behaviour of non-imprinted LPG sensor investigation

The effects on the bulk RI of the fibres in response to immersion in solutions and assay media are evaluated and shown in Figure 7.6. In the Figure, each column shows the wavelength shift of the trough position for the LP_{020} mode resonance left band, as the solution in which the fibres were immersed was switched from DI-water to the assay solvent. These data indicate there are changes in the resonances of ~0.2 nm and ~1.5 nm in PBS and FBS, respectively, both in the bare LPG and Dabrafenib MIP LPG (DAB MIP LPG) case. Higher response for both functionalised and non-functionalised sensors in FBS as compared to PBS is most plausibly due to the higher RI of the FBS. The RI values of DI-water, PBS and FBS are 1.3331, 1.3350 and 1.3464 respectively measured by digital refractometer (Reichert, Brix/RI-Chek, Japan). The predicted wavelength shifts of bare LPG were calculated as 0.44 nm and 3.29 nm in PBS and FBS by using simulation with *OptiGrating 4.2.2* after the RI values are measured. The difference compared to measured wavelength shift could be affected by the material property difference of optical fibre and the mechanical error during LPG fabrication. However, in the experimental results, the response of the MIP LPG is in agreement with that of the bare LPG within the range of error bars, demonstrating that the MIP LPG was not adversely affected by any non-specific interaction with the salts in PBS and additional proteins in FBS in this case.

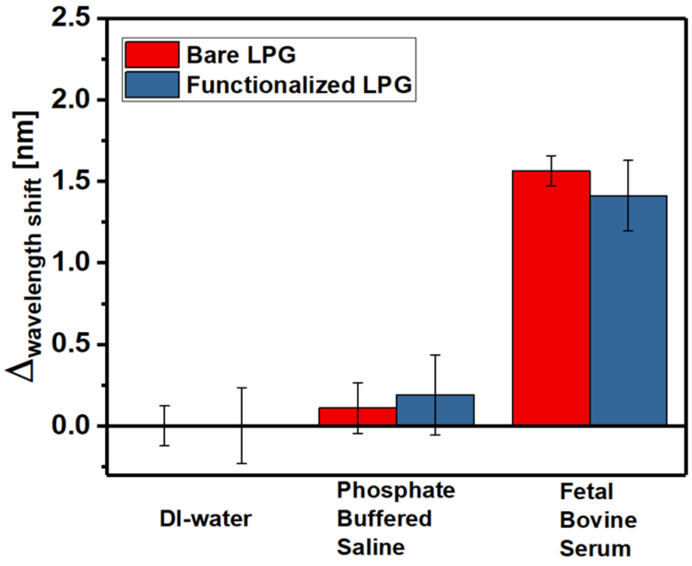

Figure 7. 6 Comparison of the response between bare and Dabrafenib MIP coated LPG in different solvents, DI-water, PBS and FBS, error bars represent standard deviation.

The performance of the two sensor fibres is investigated by comparing the response to the Dabrafenib analogue 2-AQ of an LPG polymer imprinted with 2-AQ (2-AQ MIP LPG) and a non-imprinted polymer LPG (NIP LPG). The imprinted LPG was fabricated by following the steps in section 7.2.4 whereas the NIP LPG was made with the identical protocol but without adding the template. After fabrication, the two LPGs are immersed in the same concentration of 2-AQ solution (e.g. 1 mg·mL^{-1} in PBS) firstly and the LPG response is monitored after increasing the 2-AQ concentration to a higher level (e.g. 6.6 mg·mL^{-1} in PBS).

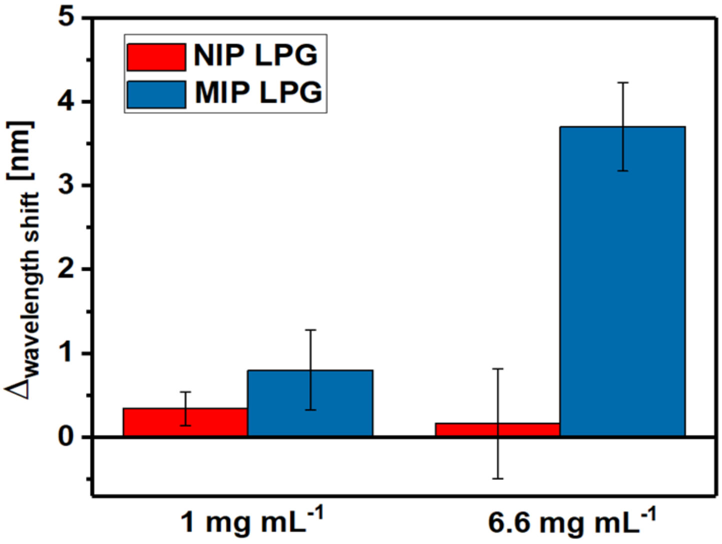

Figure 7. 7 Non-imprinted LPG and 2-AQ tests of imprinted LPG in different concentration of the template (2-AQ). Error bars represent standard deviation.

Figure 7.7 shows the results comparing the optical response of the LPG fibres of the MIP and NIP sensors. The separations of the LP_{020} resonance dual band for each sensor is measured in DI-water and at two different concentrations of template solution (2-AQ in this case). It is seen that the MIP sensor exhibited a wavelength shift of 0.80 and 3.7 nm for 1 mg·mL^{-1} and 6.6 mg·mL^{-1} concentration of 2-AQ solution, respectively. In contrast, the response of the NIP sensor does not significantly change over the different concentrations of target 2-AQ analyte (0.34 and 0.16 nm for 1 mg·mL^{-1} and 6.6 mg·mL^{-1} of 2-AQ solution) in LP_{020} dual band separation (Figure 7.7). These results suggest that there is higher affinity for the analyte in the MIP sensor compared to the NIP sensor, confirming the presence of selective binding sites for 2-AQ as a consequence of the imprinting process in the MIP and induction of molecular recognition in this system.

7.3.3 Selectivity of Dabrafenib MIP LPG sensor

The MIP LPG sensor is subsequently exposed to increasing concentrations of Dabrafenib in PBS solution. As shown in Figure 7.8(a), with the increase in target analyte concentration, the LP_{020} resonance dual-band (L-LP_{020} and R-LP_{020}) becomes broader and there is a blue shift for the LP_{019} resonance band indicating RI increase during the binding process. The dynamic wavelength shift for the separation of dual-band in Figure 7.8(b) demonstrated an increase in the amount of Dabrafenib bound to the DAB MIP sensor surface, which exhibits wavelength shifts of 0.31, 0.88, 1.26, 3.30, 6.33 and 13.40 nm for the 10, 50, 100, 250, 500 and 1000 µg·mL^{-1} Dabrafenib concentrations, respectively. The data for washing steps are excluded. The 'spikes' in the figures could be related to the tension of the liquid as they exist a short period of time once the solution is added in the LPG bath cell. Therefore, a suitable period needed to allow the optical signal reaches a stable plateau. In contrast, the response of DAB MIP sensor has not shown a significant change over the different concentrations of 2-AQ in PBS solution in LP_{020} dual band separation (Figure 7.8(c)). In order to verify further the selectivity of the proposed DAB MIP sensor, 2-AQ MIP sensor and bare LPG is tested with different concentrations of Dabrafenib and 2-AQ solution in PBS. For the 2-AQ MIP sensor measurements, shown in Figure 7.8(d) and (e), the responses are calculated by taking the average of the signal remaining at a constant level in each concentration, showing wavelength shifts of 0.14, 0.22, 0.30, 0.39 and 0.69 nm for the 62.5, 125, 250, 500 and 1000 µg·mL^{-1} 2-AQ concentrations and 0.06, 0.28, 0.49 and 0.59 nm for the 125, 250, 500 and 1000 μg·mL^{-1} Dabrafenib concentrations, respectively. In addition, the LP$_{020}$ dual band response in the bare LPG case (Figure 7.8(f)) and (Figure 7.8(g)) do not show a significant wavelength shift with increasing concentrations of target templates, as expected. Figure 7.8(h) depicts the total sensitivity comparison between bare LPG, 2-AQ and DAB MIP LPG, indicating that the DAB MIP sensor demonstrated selectivity and good sensitivity to Dabrafenib. The linear fitting curve represented in the Figure 7.8(h), demonstrating the linear response to Dabrafenib with a sensitivity of 13.2 pm/(μg·mL^{-1}) (R^2=0.998).

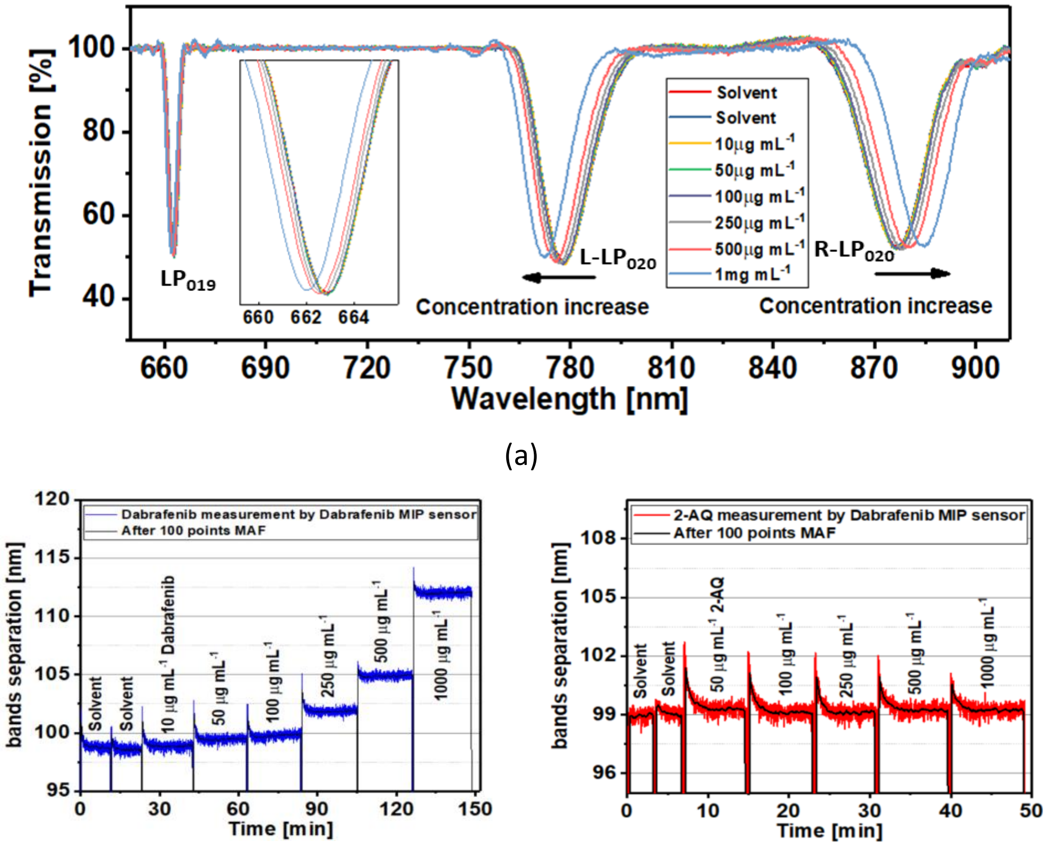

(a)

(b)

(c)

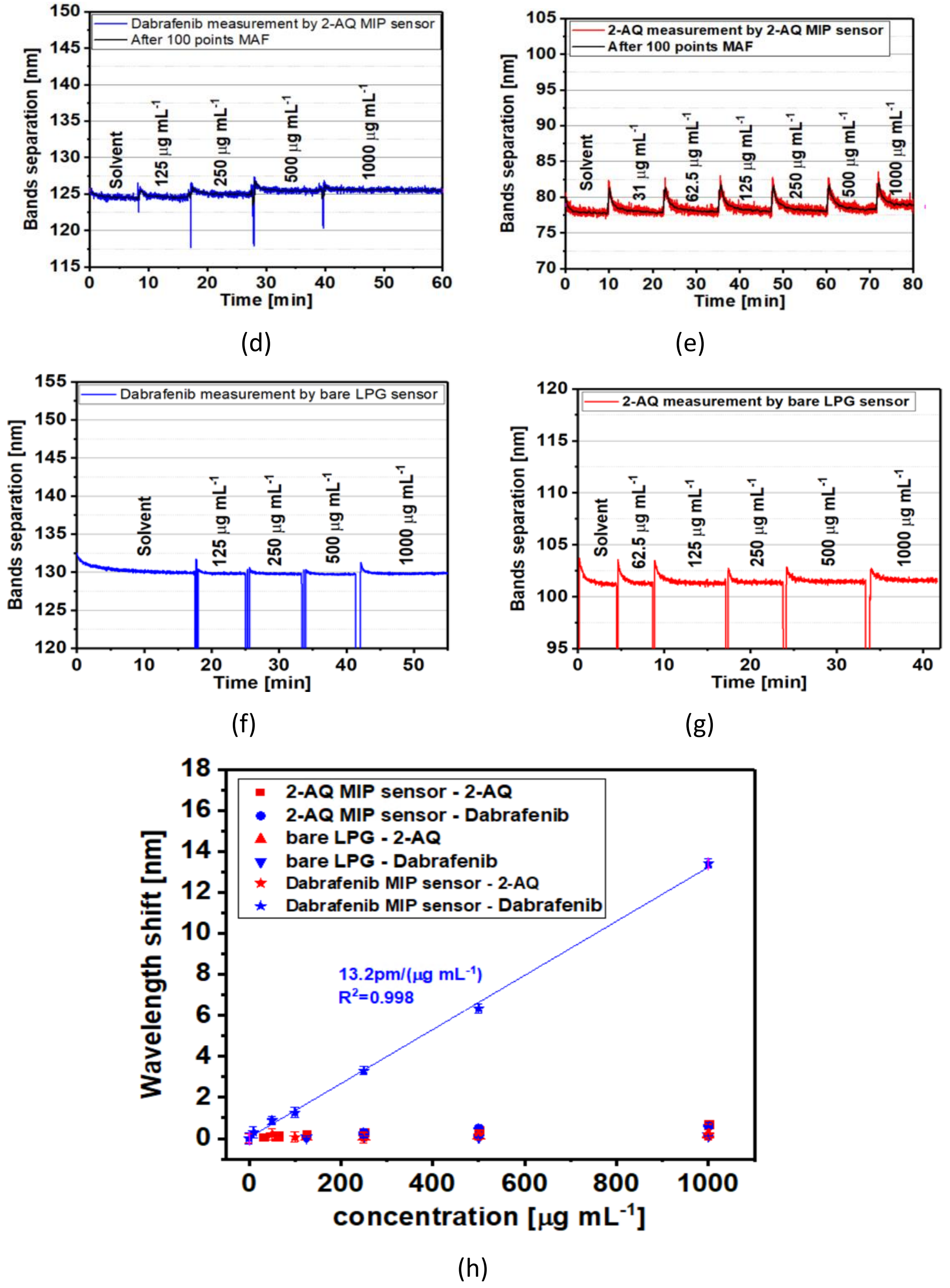

Figure 7. 8 (a) Transmission spectra of DAB MIP sensor with different concentrations of Dabrafenib in PBS solution. The dynamic change of LP_{020} band separation for DAB MIP sensor is shown in (b) Dabrafenib and (c) 2-AQ measurement. (d) and (e) represent Dabrafenib and 2-AQ measurement using 2-AQ MIP. (f) and (g) is Dabrafenib and 2-AQ measurement using bare LPG. (h) Selectivity and sensitivity comparison for the sensors (error bars are the standard deviation of each measurement).

7.3.4 Dabrafenib measurement in serum

To evaluate the performance of the prepared DAB MIP sensor under more clinically relevant conditions, measurements are conducted of Dabrafenib and 2-AQ in Fetal bovine serum (FBS). In Figure 7.9(a), it can be seen that the LP_{020} band separation changes during the whole Dabrafenib measurement, which exhibited wavelength shifts of 0.25, 0.76, 1.63, 2.62, 4.77, 7.97 and 11.87 nm for the 10, 20, 50, 100, 250, 500 and 750 μg·mL^{-1} Dabrafenib concentrations in FBS, respectively. For comparison, the DAB MIP sensor is also exposed to a range of concentrations of 2-AQ in FBS, Figure 7.9(b), and the wavelength shifts changed by 1.26 nm at a concentration of 2-AQ of 500 μg·mL^{-1}. This response of the Dabrafenib sensor to 2-AQ was also apparent in PBS as well, indicating a small amount of non-specific association of 2-AQ with the DAB MIP. This was not unexpected considering the designed structural similarities, but this binding was much less than Dabrafenib at all concentrations. Overall, the DAB MIP fibres exhibited sensitivities in serum to Dabrafenib and 2-AQ of 15.2 pm/(μg·mL^{-1}) (R^2=0.992) and 2.5 pm/(μg·mL^{-1}) (R^2=0.994), respectively.

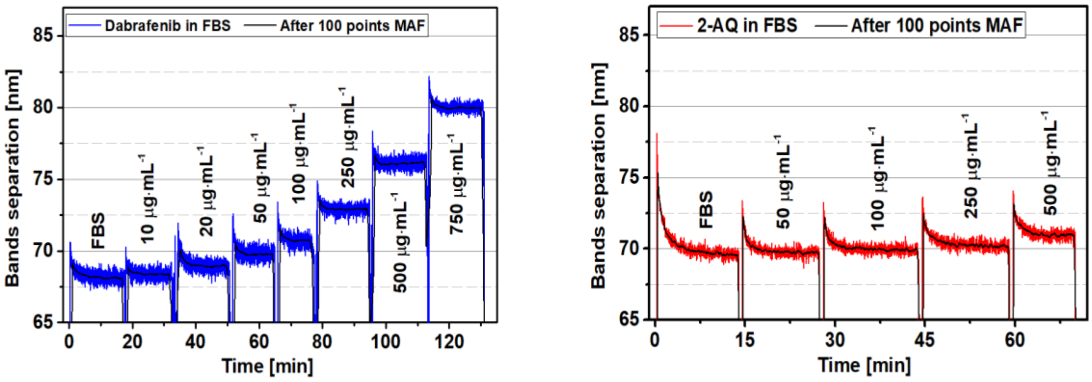

(a) (b)

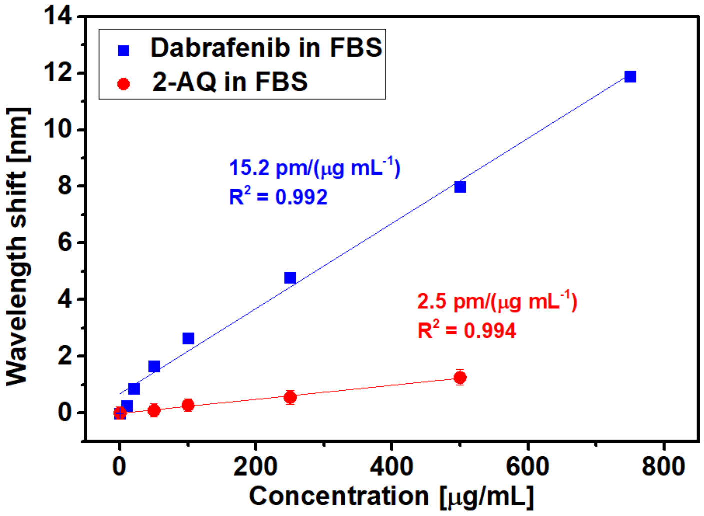

(c)

Figure 7. 9 The dynamic change of LP_{020} band separation for Dabrafenib MIP LPG sensor is shown in (a) Dabrafenib and (b) 2-AQ measurement; (c) sensitivities comparison for the sensor in Dabrafenib and 2-AQ measurement.

Clinically relevant ranges of Dabrafenib in plasma are approximately 6 μg·mL^{-1} [172] and based on the LoD from the raw data (74.4 μg·mL^{-1}) our sensor currently falls outside this range. Estimation of the LoD calculation depends on the sensitivity of the sensor and the noise level of the data (Section 7.2.6). Some simple signal processing can reduce the noise levels and the estimated LoD. For example, applying a Moving Average Filter (MAF) in the time domain with a 20 or 100 data points calculation window can be used to reduce the noise (σ) from 320 pm to 57.9 pm (20 pts) or 8.66 pm (100 pts), respectively. Subsequently, the estimated LoD is reduced from 74.4 to 11.4 (20 pts) or 1.71 μg·mL^{-1} (100 pts). Translation of the technology *in vivo* will require measurements to be made at body temperature, which is higher than the ambient temperature used here. However, it should be noted that high stability against non-physiological conditions such as high temperature is one of the advantages of MIPs [173, 174]. Furthermore, a study by Svenson *et al.* demonstrated that the molecularly imprinted MAA & EGDMA polymers, monomer and cross-linker also used in this work, have been shown to be able to withstand exposure to temperatures of up to 150 °C without loss of affinity for their template [175]. Therefore, the MIP in this work should be able to operate in ~36 °C (*in vivo* temperature). This will be investigated in more detail as the technology is translated to *in vivo* applications.

7.4 Conclusion

An LPG optical fibre-based sensor modified with a molecularly imprinted polymer film for Dabrafenib detection has been introduced. The sensor demonstrated high sensitivity in serum of 15.2 pm/(μg·mL^{-1}) (R^2=0.992) when exposed to varying concentrations of Dabrafenib in serum. In principle, the LoD could be further reduced to 1.71 μg·mL^{-1} with additional signal processing, which is well within the range required clinically. The selectivity of the proposed sensor was also investigated by comparing the response of the functionalised LPG to Dabrafenib and a structurally similar compound, 2-AQ. The DAB MIP sensor shows a weak sensitivity to 2-AQ (2.5 pm/(μg·mL^{-1}) (R^2=0.994)) in serum as compared to Dabrafenib (15.2 pm/(μg·mL^{-1})). In addition, the response of LPG functionalised with non-imprinting molecularly imprinted polymer to both Dabrafenib and structurally similar compound, 2-AQ was negligible indicating low non-specific binding.

Considering the optimized LoD (1.71 μg·mL^{-1}) and high sensitivity (15.2 pm/(μg·mL^{-1}))., it is possible to turn this Dabrafenib sensor into a clinically useful tool. The sensor has the potential to be a probe for drug concentration test in blood or tumour sample.

Chapter 8: LPG based antibody measurement with flow system

8.1 Introduction

Antibodies are the important biomarkers in several medical applications such as disease diagnosis and therapy [176]. Background details about antibodies and relevant applications have been described in Chapter 2. Antibody-antigen interaction is the most common principle applied in antibodies detection approaches. Previous work by our research group developed a LPG-based antibody biosensor modified with silica core – gold shell nanoparticles for IgM detection [177]. The sensor demonstrated a sensitivity of 11 nm/(ng/mm^2) and a LoD of 15 pg/mm^2 in IgM measurement. However, the reversibility of the sensor has not been investigated. While point of care optical fibre 'dipsticks' such as this are useful for one-off measurements, they cannot be re-used for measuring antibody in distinct levels. This is due to the strong antibody-antigen interactions which means that binding does not reverse when the antibody concentration reduces. The aims of this Chapter are to investigate the feasibility of developing a reversible optical fibre immunosensor, which would have great potential for continuous monitoring applications. For instance, in response to treating an infection of a critically ill patient, for example sepsis, antibodies levels might rise [78]. In a work by Allan *et al,* clinicians have frequently taken blood samples from healthy adults and sepsis patients and the serum IgG levels were daily measured using standard lab tests [78]. The results represented positive trend indicating IgG measurement may be significant in sepsis. Compared to conventional antibodies level detection method, it would be useful to monitor antibody levels continuously by a new sensing approach, which allows reducing the workload of medical staff and supplies relative higher precise dynamic extent of antibodies.

In this Chapter, a novel LPG is coated with a IgG-binding peptide that has previously been isolated from a phage-displayed random peptide library [178, 179]. In phage display technique, the randomized amino acid sequences are fused to filamentous phage envelope proteins through genetic engineering of the phage genome. A phage display library allows screening of a larger number of peptides simultaneously to identify high-affinity ligands to a specific target such as immunoglobulin protein [180]. This type of peptide can be used to bind antibodies in an optical fibre immunosensor, while allowing the peptide-antibody affinity to be fine-tuned by modification of the peptide’s amino acid sequence. This work will demonstrate a method of controlling the binding affinity so that the non-covalent bonds can be broken relatively, for example using an elution acidic buffer. The LPG is fabricated using the method described in Chapter 3 and is coated with peptide on the fibre surface. Subsequently, the bulk RI influence is tested by comparing a bare LPG response with that of a functionalised LPG in different solvents. Moreover, the selectivity of the peptide coated LPG sensor is investigated by comparing the response of a bare LPG, the functionalised LPG to IgG and IgM antibodies in different concentrations in PBS solution. In the previous research [177], measurement was undertaken in an open bath into which the optical fibre was positioned. In this case, a microfluidic channel is designed and developed for use with the optical fibre sensor. The performance of this system is investigated by a basic RI measurement with a bare LPG.

So far, the work in this Chapter is incomplete due to the lab closures in the period of the COVID-19 pandemic. Figure 8.1 illustrates the overall plan, reversibility is generally manifested in the process of measurement. A reversible sensor can continually monitor the increase and decrease of the analyte concentration. For comparison, reversibility of peptide coated sensors would be investigated after acquiring at least two different amino acid sequence peptide functionalised LPG sensors. Therefore, the rest of characterisation and experiments with extra peptides will be done in the future.

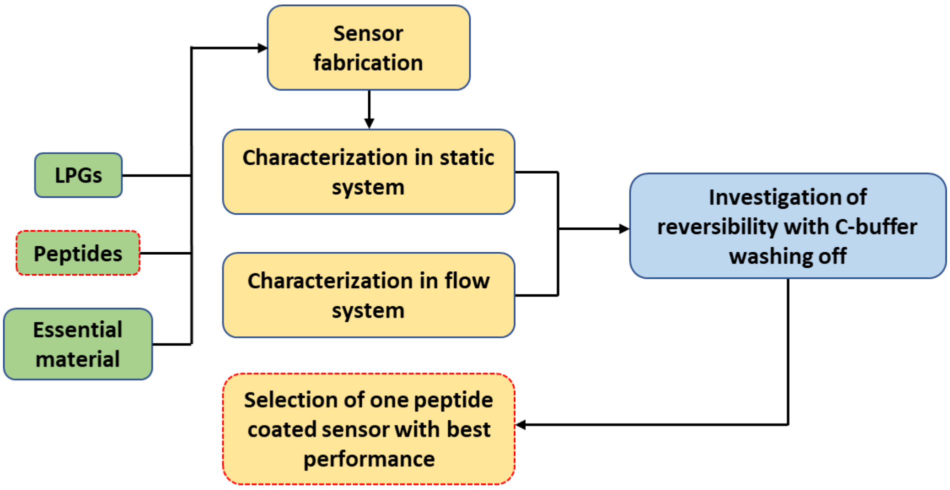

Figure 8. 1 Flow chart of the overall plan for reversible optical fibre immunosensor development.

8.2 Methodology

8.2.1 Material

IgG (Immunoglobulin G from human serum), Potassium hydroxide (KOH), Sodium hydroxide (NaOH), Ethanol, Poly(allylamine hydrochloride) (Mw~58,000, PAH), (3-Aminopropyl) triethoxysilane (APTES), Sodium citrate, Gold (III) chloride trihydrate ($HAuCl_4 \cdot 3H_2O$), Cysteamine, 2-(N-Morpholino)ethanesulfonic acid hydrate (MES hydrate), *N*-(3-Dimethylaminopropyl)-*N*′-ethylcarbodiimide hydrochloride (EDC) and Citrate acid were purchased from Sigma-Aldrich, UK. Silica Nanoparticles (SiO_2 NPs, diameter 90-100nm) were purchased from Nissan Chemical, Japan. Deionised water (DI water), having resistivity of 15 MΩ cm, was obtained from a water purification system (PURELAB Option S/R, ELGA). All the chemicals were of analytical grade and used without further purification. Phosphate buffered saline (PBS) was freshly prepared by dissolving PBS tablets (Oxoid, UK) in DI-water, which comprised Sodium chloride (8.0 $mg \cdot mL^{-1}$), Potassium chloride (0.2 $mg \cdot mL^{-1}$), Disodium hydrogen phosphate (DSP) (1.15 $mg \cdot mL^{-1}$), Potassium dihydrogen phosphate (KDP) (0.2 $mg \cdot mL^{-1}$), pH 7.3 ± 0.2, at 25 °C. IgG-binding Peptide was supplied by the Department of Life

Sciences at the University of Nottingham. Silicone elastomer (Sylgard 184) was purchased from Dow, Japan.

8.2.2 Gold nanoparticles synthesis

Gold nanoparticles were synthesized via the protocol described by Turkevich et al. [181]. 1 mM $HAuCl_4{\cdot}3H_2O$ stock solution was prepared in DI-water initially. 90 mL DI-water and 10 mL of 1 mM $HAuCl_4{\cdot}3H_2O$ stock solution were mixed in a beaker and heated on heating plate until it began to boil. Subsequently, 1 mL of 34 mM (1% w/v in DI-water) sodium citrate trihydrate solution was added to the mixture solution. The Gold NPs size is stable if the molar ratio of sodium citrate to $HAuCl_4$ is above 3 (~3.4 in this work) [182, 183]. Heating continued for around 10-15 mins until the colour of mixture turned from transparent (Figure 8.2(a)) to red wine (Figure 8.2(d)). Then the gold nanoparticles solution was removed from the heating plate for cooling down naturally to room temperature.

For characterization, Gold NPs were coated on a glass substrate functionalised with APTES. The glass surface was then studied using scanning electron microscopy (SEM) (JEOL, JSM-7100F, UK).

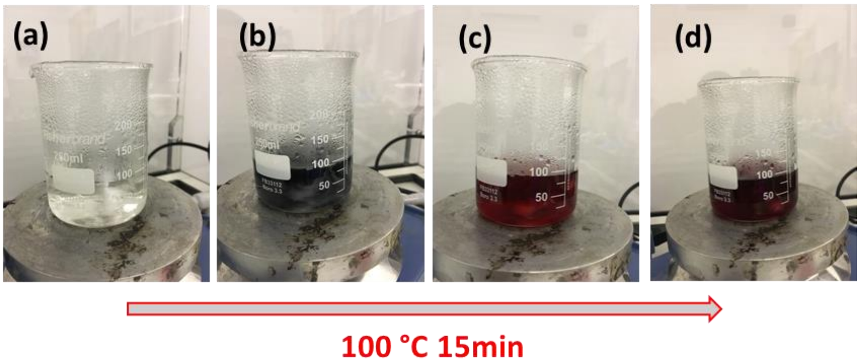

Figure 8. 2 Progress of Gold NPs synthesis, the mixture solution is boiled, the colour of the solution turns from (a) transparent to (b) grey, (c) red and (d) red wine finally.

8.2.3 Antibody-binding peptide

A peptide is a short chain of between two and fifty amino acids. The amino acids in a peptide are connected by peptide bonds to one another in a sequence. Figure 8.3 illustrates the binding of IgG with IgG-Fc affinitive peptide. The binding site positioned on Fc-domain of immunoglobulin G is reported to be exposed, adaptive and permitted to the interaction with distinct molecules [180]. Two consensus binding sites exist on the IgG Fc region, the hinge proximal region of the CH2 domain and the junction of the CH2 and CH3 domains [184]. The IgG-binding peptide used in this work has previously been isolated from a phage-displayed random peptide library [178, 179]. In phage display technique, the randomized amino acid sequences are fused to filamentous phage envelope proteins through genetic engineering of the phage genome. Phage display library allows screening of a larger number of peptides simultaneously to identify high-affinity ligands to a specific target such as immunoglobulin protein [180].

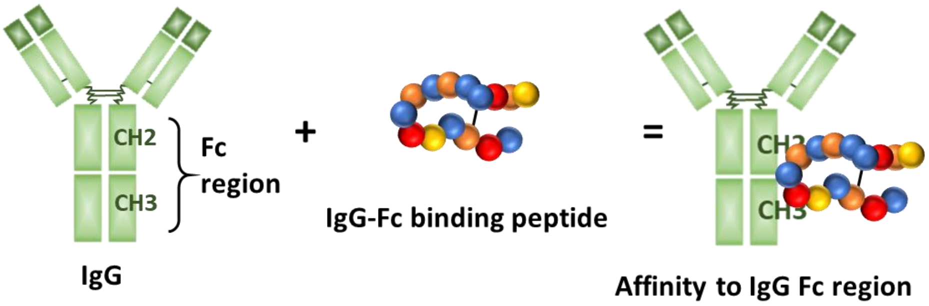

Figure 8. 3 Schematic of binding between IgG-Fc affinitive peptide and IgG.

This type of peptide can be used to bind antibodies while allowing the peptide-antibody affinity to be fine-tuned by modification of the peptide’s amino acid sequence toward the consensus binding sites on Fc region of IgG. For each peptide, there is an elution pH existing for breaking the bind between peptide and antibody. For example, in a study by Dinon *et al.*, elution of the bound antibody from the peptide is achieved by using 0.1 M acetate buffer (pH = 4) [185] and another study using sodium chloride solution at 6.0 pH as elution buffer [186].

8.2.4 LPG fabrication and modification

The LPG was fabricated through the same method described in Section 7.2.2 in Chapter 7 with a length of 30 mm and grating period of 111.5 µm. The LPG was written in boron-germanium co-doped optical fibre (Fibrecore PS750, Ø: 250 µm, single-mode with cut-off wavelength of 670 nm). The LPG period was selected for operating at or near the phase matching turning point (PMTP), which ensures the highest sensitivity [167].

The region of the optical fibre containing the LPG was hydroxylated with 1 wt% ethanolic KOH solution (ethanol/water=3:2. v/v) to functionalise the surface with -OH groups for 20 min. After washing with deionized water and drying with a stream of N_2 gas, the LPG was then subsequently immersed into positively charged Poly(allylamine hydrochloride) solution (PAH 0.17 wt%, pH=10-11 in DI-water) and negatively charged SiO_2 NPs solution (5 wt%) (particle size: 90-100 nm) for 15 min immersion respectively. The LPG was washed and dried in between each immersion. This Layer-by-Layer coating process was repeated three times for increasing the interaction area with gold NPs in further functionalization [120].

Subsequently, the LPG coated with PAH/SiO_2 NPs was immersed into an APTES solution (2 % v/v in ethanol) for 20 min to lay an amine group (-NH_2) on the surface and followed by subsequently being rinsed thrice with distilled water and ethanol to remove the abundant APTES from the surface. The washed LPG was annealed for 1 hour at 120 °C in an oven to remove the water molecules attached on the surface and to form siloxane bonds. The LPG was then immersed into the prepared gold NPs solution for 45 min, then washing and drying. After modified with gold NPs, the LPG was immersed into 0.1 M cysteamine solution in ethanol for 30 min to obtain amine group terminations on the gold surface.

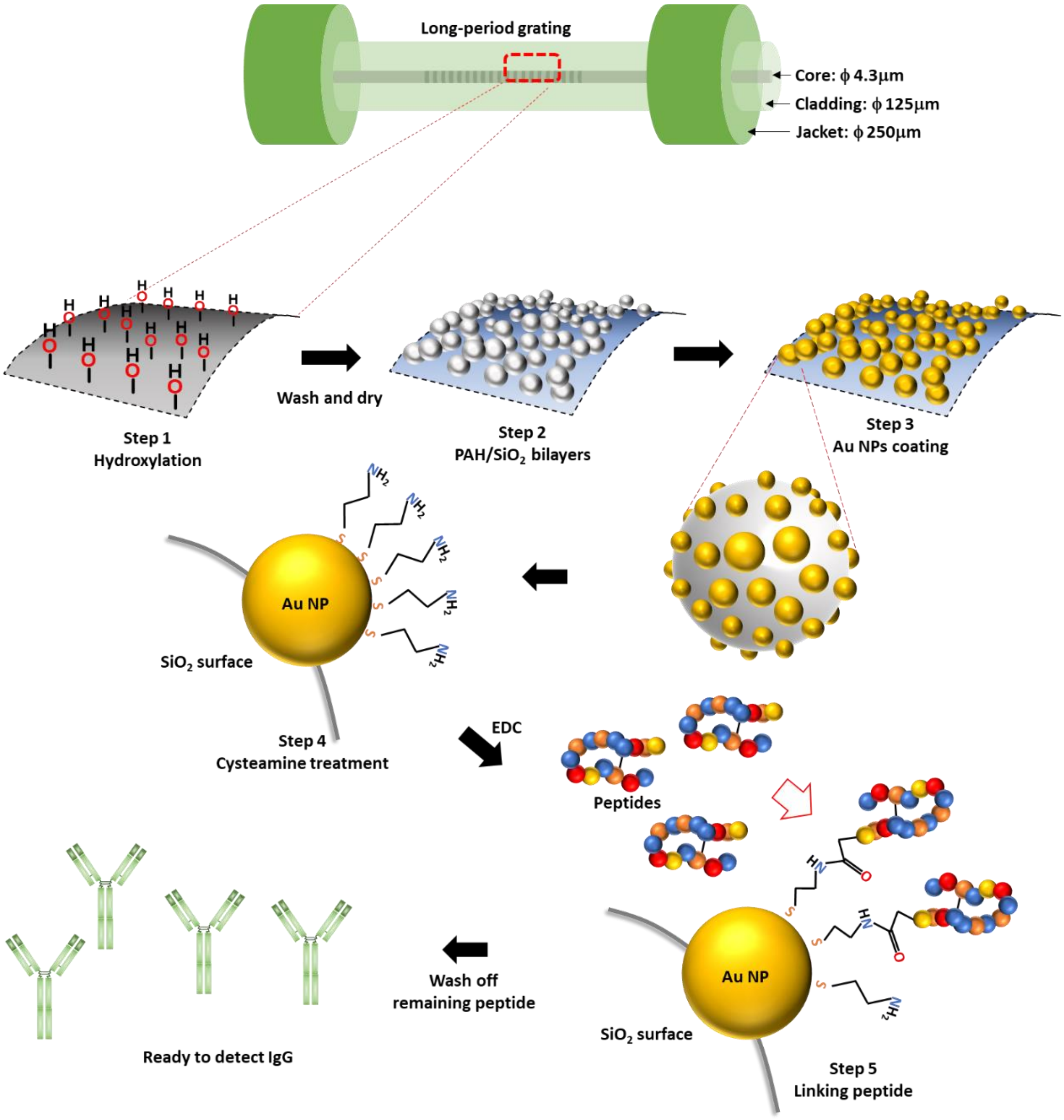

Figure 8. 4 Schematic of linkage approach for IgG-binding peptide onto LPG surface.

For linking peptide with the amine group terminated LPG, the water soluble carbodiimide EDC (*N*-(3-Dimethylaminopropyl)-*N'*-ethylcarbodiimide hydrochloride) was used as it can activate carboxylate (in peptide) to create a highly reactive intermediate ester. This ester can then couple to amines to generate stable binding in-between peptide and cysteamine as illustrated in Figure 8.4 and the LPG can be used to measure antibody (IgG).

For characterization, SEM (JEOL, JSM-7100F, UK) was used to study the surface structure of functionalized LPG.

8.2.4 IgG sensor characterisations

After fabrication, the characterisations of IgG sensor have been investigated. Firstly, the bulk RI of different solvents can be a confounding issue for measurement of the LPG response in liquid [126]. Accordingly, the responses of the bare LPG and functionalized LPG in different buffer solutions were evaluated, with transmission spectra of two LPGs, before and after functionalization, being measured after immersion into DI-water, PBS and Citrate buffer respectively.

A spectrometer sensing system was used to monitoring the LPG spectral change during the sensor fabrication and measurements as shown in Figure 8.5. This system consists of a Halogen light source (HL-2000, Ocean Optics, UK), CCD spectrometer (HR4000, Ocean Optics, UK) and a Teflon LPG bath with the dimension of 55*5*4 mm (L*W*D) for setting the LPG region in the relevant solvent. All experiments were conducted at 20 °C in a temperature regulated laboratory to reduce the effects of temperature cross-sensitivity.

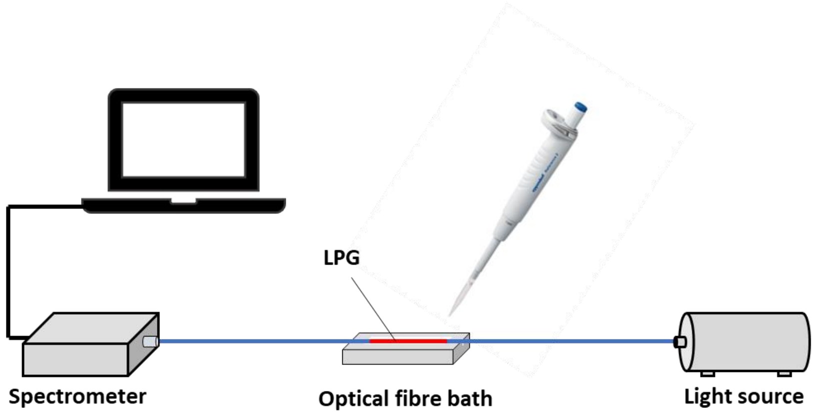

Figure 8. 5 Experimental set-up of measurement using LPG for transmission mode.

The IgG selectivity for the LPG sensor was investigated by comparing the response of the proposed LPG sensor with a bare LPG. After fabrication, the two LPGs were immersed into IgG and IgM solutions with same concentration and the LPG response measured by recording the wavelength shift over these solutions.

The IgG antibodies from human serum were suspended into PBS buffer (0.14 M NaCl, 2.68 mM KCl, 8.10 mM DSP and 1.47 mM KDP, pH=7.3) at a concentration range from 31.2 μg·mL^{-1} (200 nM) to 500 μg·mL^{-1} (3.3 μM). The functionalized LPG sensor was immersed in distinct concentrations of IgG solution. After each exposure, the sensor was washed with a citrate buffer (elution C-buffer) (0.1 M Citric acid and 0.1 M Sodium citrate, pH=6.2) to remove the unbound IgG antibodies and accelerate the dissociation of bound antibodies, followed by thorough rinsing with PBS solution and drying with N_2. The transmission spectrum of the LPG sensor was acquired and recorded using the spectrometer set-up shown in Figure 8.5 with a sampling frequency of 1 Hz. The wavelength shifts of the attenuation band of the PMTP were tracked from the recorded spectra.

In order to investigate the reversibility of antibodies measurement, the peptide functionalized LPG sensor was exposed to constant concentration of IgG by repeated immersion into 3.3 μM IgG solution. After each immersion, C-buffer was used to wash off the remaining antibodies.

8.2.5 LPG protein sensor parameters

Protein binding to the surface of an LPG sensor is typically simulated by using the Langmuir isotherm theory [187]:

$$a = \frac{MkC}{1 + kC} \qquad (8-1)$$

where a is the amount of protein adsorbed, *k* is the equilibrium binding constant, *M* is the adsorption maximum and *C* is the concentration of the protein solution.

It can be assumed that the wavelength shift of the LPG sensor is proportional to the protein adsorption. The Equation 8-1 can be transformed as:

$$\Delta\lambda = \Delta\lambda_{max}\left(\frac{kC}{1+kC}\right) \qquad (8-2)$$

where $\Delta\lambda$ is the wavelength shift of the attenuation band of the LPG response to the RI change associated with the protein adsorption on the LPG surface and $\Delta\lambda_{max}$ is the maximum change of the wavelength shift due to the complete formation of protein on the self-assembled LPG surface. Subsequently, in order to estimate the parameters $\Delta\lambda_{max}$, the Langmuir isotherm is linearized by using the reciprocal [188, 189], as shown below:

$$\frac{C}{\Delta\lambda} = \frac{1}{\Delta\lambda_{max}k} + \left(\frac{1}{\Delta\lambda_{max}}\right)C \qquad (8-3)$$

Accordingly, the sensitivity (*S*) of the protein detection LPG sensor can be given by [190]:

$$S = \frac{\Delta\lambda_{max}}{\sigma_{max}}\ ,\ \ \sigma_{max} = \frac{M}{N_A * P^2} \qquad (8-4)$$

where σ_{max} is the surface density of protein immobilised onto the LPG surface when all the capture sites are occupied, *M* is molecular mass of IgG (150 kDa, 150000 g*mol^{-1}), *P* is average length (IgG: ~14 nm) [191] and N_A = 6.0221 1023 mol^{-1} as Avogadro's number. The theoretical LoD for the LPG sensor can be estimated [190]:

$$LoD = \frac{R}{S} \qquad (8-5)$$

where *R* is the resolution of the spectrometer using in this work (0.11 nm) and *S* is the sensitivity calculated with Equation 8-4.

8.2.6 Microfluidic measurement system set-up

As part of the development process a microfluidic design has been developed to test optical fibre sensors in a flow system. Originally the measurement chamber was an open bath into which the optical fibre was positioned (Figure 8.5), however, in the new design, the fibre is completely enclosed in a microfluidic chamber. In order to standardise conditions for flow of liquid over the sensor, new microfluidic chamber was designed and produced using 3D-printed moulds and Polydimethylsiloxane elastomer (PDMS). The dimensions of the 3D-printed moulds are shown in Figure 8.6(a). The PDMS microfluidic cell for hosting LPG is fabricated by casting silicone elastomer (Sylgard® 184) into the proposed 3D-printed mould and curing in an oven for 1 h at 100 °C or in ambient temperature (~20 °C) for two days. The elastomer microfluidic cell before and after demoulding is shown in Figure 8.6(b), the lid of the cell has two tubing ports in end of the micro-channel for entry and exit of the fluid flow. The approximate volume of the micro-channel can be estimated as 88 μL ($0.75^2 \times \pi \times 50(mm^3)$).

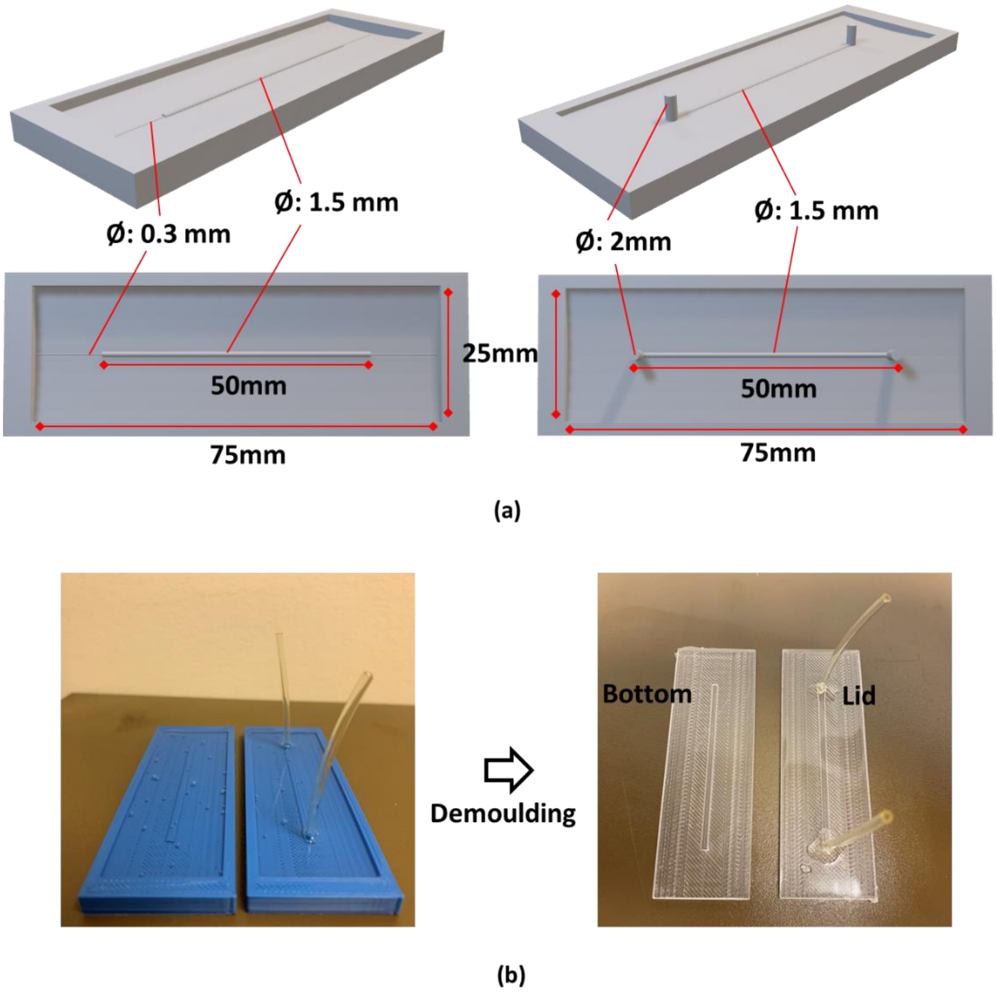

Figure 8. 6 (a) the 3D-printing structures of the microfluidic chamber mounds with dimensions. (b) Elastomer microfluidic cell before and after demoulding, two tubes allow fluid flow to enter and exit.

The set-up of the microfluidic measurement system is shown in Figure 8.7, the functionalized LPG lays in the micro channel assembled by two parts with inner diameter of ~1.5 mm which allows liquid to flow through. A peristaltic pump circulates sample solution to the flow cell with constant minimum flow rate (0.8 mL/hr). Meanwhile, the spectral change of the LPG was recorded by the spectrometer.

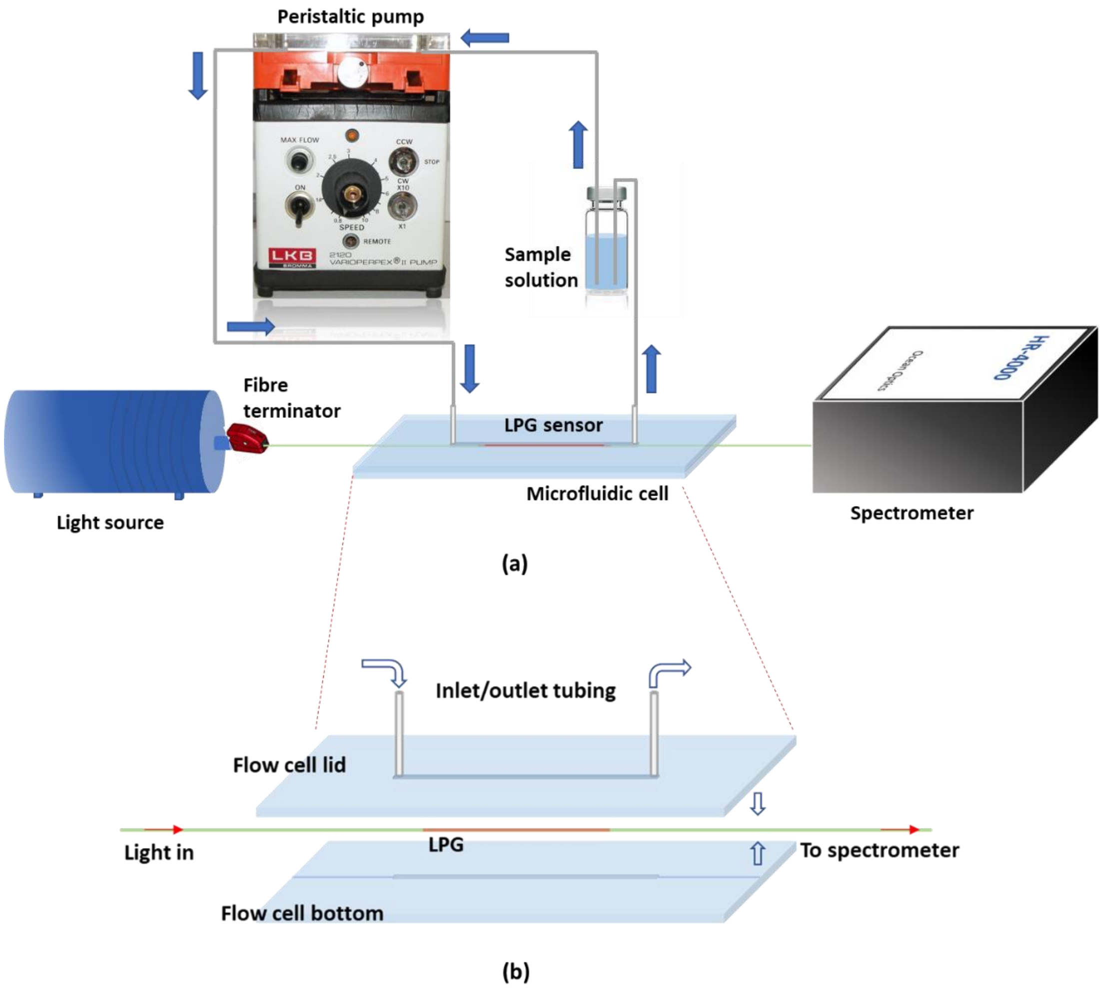

Figure 8. 7 (a) Schematic of microfluidic measurement system set-up. (b) Sandwich structure of laying LPG in the microfluidic chamber.

8.2.7 Measurements based on microfluidic system

In order to investigate the performance of the microfluidic system, an initial test of RI measurements with a bare LPG was undertaken using the proposed microfluidic system shown in Figure 8.7(a). The RI liquid media were prepared by mixing isopropyl alcohol (IPA) with DI-water in different volume ratio. The RI value of each IPA solution was measured three times by using a digital refractometer (Digital Brix/RI-Chek, 13940000, ReiChert) in advance.

The IgG antibodies measurements can be conducted by using the microfluidic system. The peptide functionalized LPG sensor was set in the microfluidic chamber as shown in Figure 8.7(a). The PBS solution, C-buffer solution and distinct concentrations of IgG antibodies solution were prepared in advance. These solutions were circulated into the micro chamber in which the LPG sensor lays following the sequence of PBS – IgG – C-buffer. The flow rate should be set at a constant value, minimum flow rate in this work (0.8mL/hr). The transmission spectrum of the LPG sensor was acquired and recorded with a sampling frequency of 1 Hz and the wavelength shifts of the attenuation band of the PMTP was tracked. All experiments were conducted at 20 °C in a temperature regulated laboratory to reduce the effects of temperature cross-sensitivity.

8.3 Results and discussion

8.3.1 LPG sensor modification

The synthesised Au NPs were initially coated on an APTES functionalised glass substrate for characterisation by SEM. The majority of Au NPs adhere to the glass surface uniformly although some aggregations can be seen in Figure 8.8(a)). The spherical shape of Au NPs can be observed in the zoom-in SEM image (Figure 8.8(b)) and the particle size also can be estimated by taking an average of measured values in Figure 8.8(b) (~19.2±2 nm). The uniform particle size and successful coating process provide confidence in coating Au NPs on the surface of the LPG.

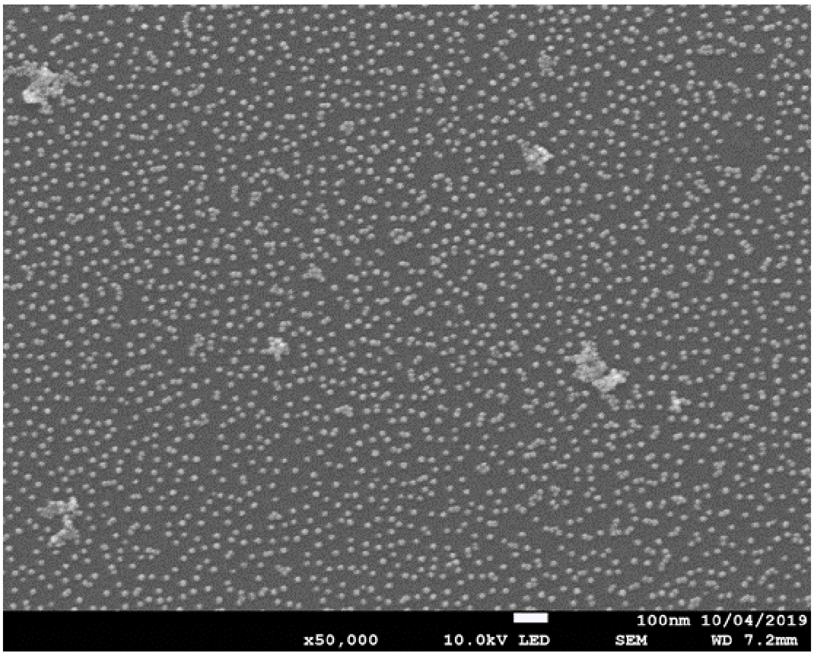

(a)

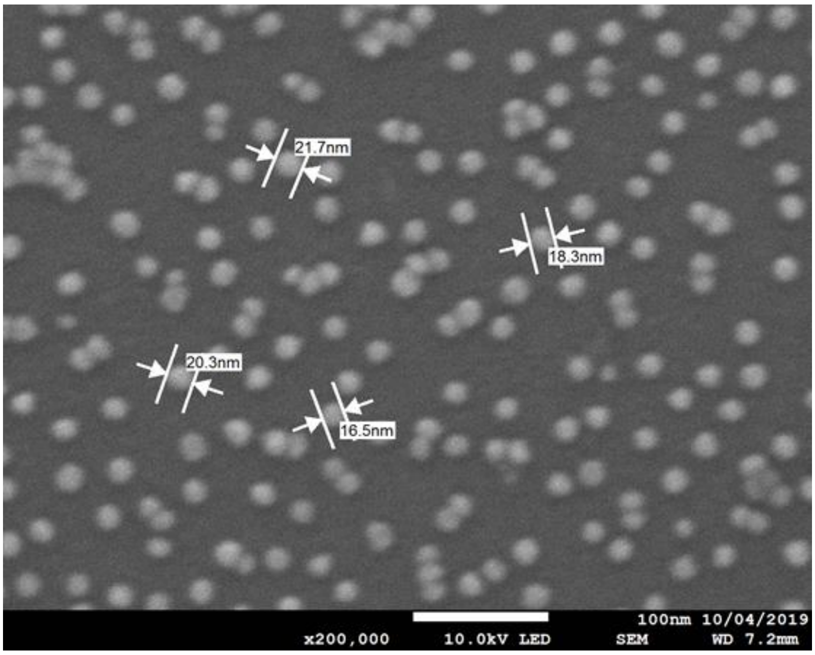

(b)

Figure 8. 8 SEM images of Au NPs coated on the substrate with magnification (scale bar: 100nm) (a) ×50,000 and (b) ×200,000.

The functional film deposition process was monitored using the set-up described in Section 8.2.4. The transmission spectra are measured in air after each deposition process and normalised by taking an automatic baseline for each spectrum using

MATLAB software. It should be noted that all protein concentration measurements were made relative to this baseline and so the absolute position does not affect the measurement. As shown in Figure 8.9(a), after coating with SiO_2 NPs (red curve), there is a blue shift of linearly polarised (LP) mode LP_{019} resonance, and the appearance of a dual attenuation band for LP_{020} mode resonance, which are characteristic of a thin film deposited onto the cladding of the LPG [126, 171].

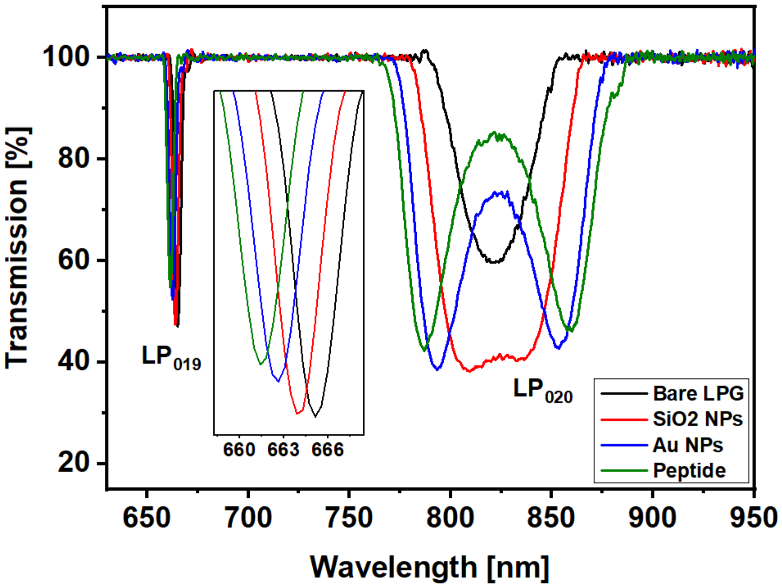

(a)

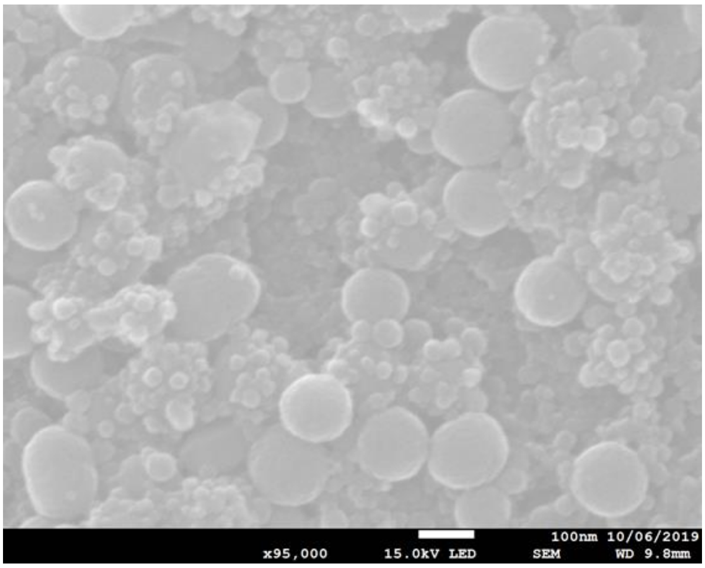

(b)

Figure 8. 9 (a) Transmission spectra of LPG in air after each deposition. The wavelength of attenuation band at LP_{019} shifts to the blue region with each deposition process and a dual attenuation band appears at LP_{020} resonance. (b) SEM image of peptide functionalised LPG surface (scale bar = 100 nm).

It should be noted that further blue shifts of LP_{019} mode resonance and development of the dual attenuation band for LP_{020} resonance are observed, after Au NPs and peptide layer deposition (blue and green trace shown in Figure 8.9(a)), indicating successful coating of peptide onto the LPG surface. Figure 8.9(b) illustrates the SEM image of functionalised LPG surface, peptides cannot be seen through SEM. It can be seen that the majority of SiO_2 NPs (~100 nm diameter) are surrounded by Au NPs. The gold shell structure supplies more binding sites for peptide onto gold surface compared to the flat surface.

8.3.2 Bulk RI evaluation & selectivity investigation

The effects on the bulk RI of the fibres in response to immersion in solutions and assay media are shown in Figure 8.10. In the Figure 8.10, each column shows the wavelength shift of the LP_{020} mode resonance band, as the solution in which the fibres were immersed was switched from DI-water to the assay solvent. These data indicate that there are changes in the resonances of ~1.4 nm and ~5 nm in PBS and C-Buffer, respectively, both in the PAH/SiO_2 coated LPG and functionalized LPG case. Higher response for both functionalised and PAH/SiO_2 coated LPG in C-Buffer as compared to PBS is most plausibly due to the higher RI of the C-Buffer. The RI values of DI-water, PBS and C-Buffer is 1.3331, 1.3362 and 1.3382 respectively measured by digital refractometer (Reichert, Brix/RI-Chek, Japan). It should be noted that the responses in bare LPG are smaller than that in the above two cases, ~0.6 nm and ~1.8 nm in PBS and C-Buffer. The predicted wavelength shifts of bare LPG were calculated as 0.6 nm and 1.3 nm in PBS and C-Buffer by using simulation with *OptiGrating 4.2.2* after the RI values are measured. The difference compared to measured wavelength shift could be affected by the material property difference of optical fibre and the mechanical error during LPG fabrication. The pH-sensitive property of PAH polymer layer may cause a different response in LPG with and without PAH layer [192, 193]. The pH of PBS and C-Buffer is 7.2 and 6.2 respectively measured by the digital pH meter (HI98103, Hanna, UK). The response of the functionalized LPG is in agreement with that of the PAH/SiO_2 coated LPG within the range of error bars, demonstrating that the functionalized LPG was not adversely affected by any non-specific interaction within the PBS and C-Buffer in this case.

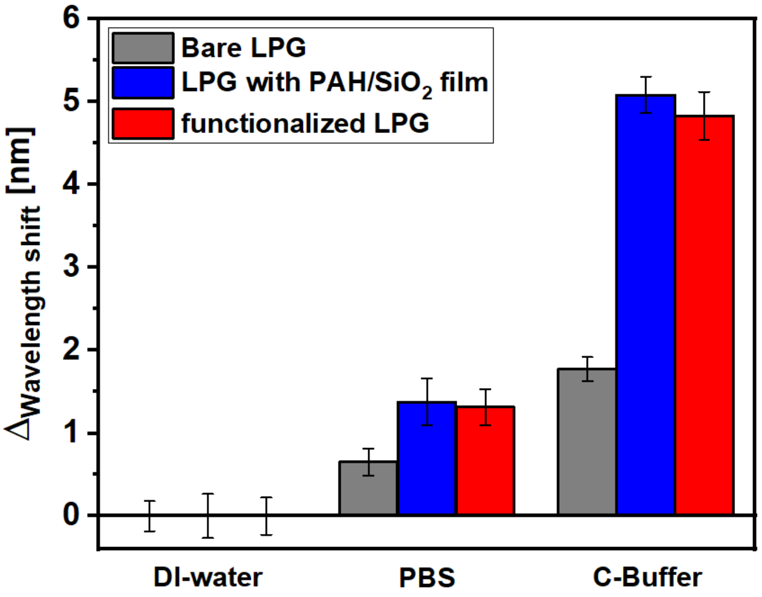

Figure 8. 10 Comparison of the response between bare, PAH/SiO_2 coated and functionalized LPG in different solvents, DI-water, PBS and C-Buffer, error bars represent standard deviation.

In order to verify the selectivity, peptide coated LPG sensor and bare LPG are tested with different concentrations of IgG and IgM solution in PBS. In Figure 8.11, each column shows the wavelength shift of the LP_{020} mode resonance band, as the solution in which the two LPGs were immersed was switched from pure PBS (no IgG or IgM) to distinct concentrations of IgG and IgM solution in PBS. For the bare LPG measurements (grey columns in Figure 8.11), the responses are calculated by taking the average of the signal remaining at a constant level in each concentration, showing wavelength shifts of 0.38 and 0.56 nm for the 400 and 800 nM of IgM concentrations and 0.54 and 0.70 nm for the 400 and 800nM of IgG concentrations, respectively. In contrast, the response of PAH/SiO_2 coated (blue columns) and IgG specific peptide coated LPG (red columns) sensors have shown similar signal changes over the different concentrations of IgM in PBS solution in LP_{020} dual band separation (Figure 8.11), 1.13&1.21 and 1.25&1.36 for 400 and 800 nM of IgM concentrations, which indicates the cross sensitivity to IgM is low. The difference between the bare LPG and PAH/SiO_2 coated LPGs is attributed to the higher RI sensitivity of PAH/SiO_2 coated LPG. For PAH/SiO2 coating, the response to IgM is larger as compared to IgG could be due to the molecular size of IgM is larger than IgG. In addition, the IgG measurements in the PAH/SiO_2 coated LPG has not shown a significant wavelength shift with increasing concentrations, whilst the functionalized LPG demonstrates 2.20 and 3.36 nm for 400 and 800 nM of IgG concentrations, indicating the selectivity to IgG.

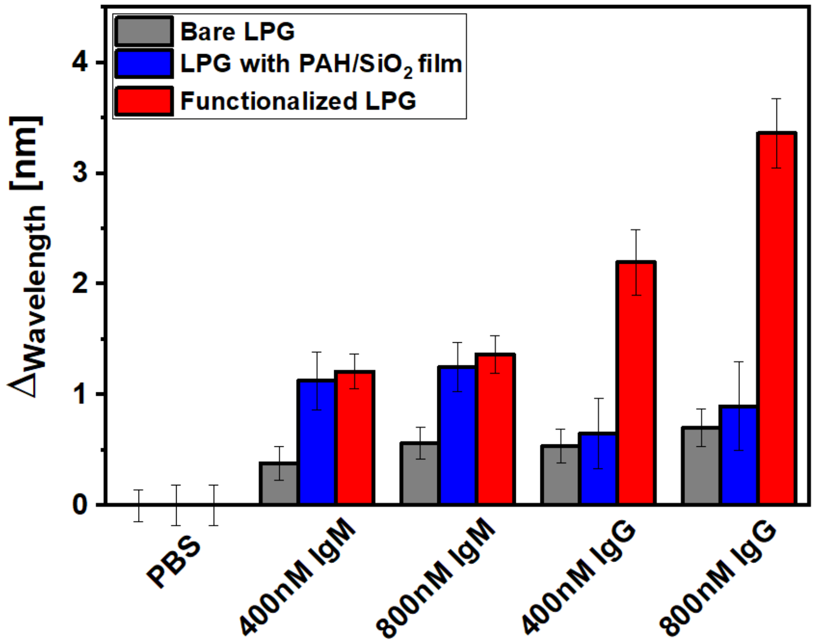

Figure 8. 11 Comparison of the response between bare and functionalized LPG in different concentrations of IgM and IgG solution (0 nM, 400 nM and 800 nM) in PBS.

8.3.3 Sensitivity to IgG antibody investigation

The peptide functionalised LPG sensor is subsequently exposed to increasing concentrations of IgG in PBS solution from 200 nM (31.2 μg*mL^{-1}) to 6.6 μM (1 mg*mL^{-1}) using the measurement set-up shown in Figure 8.5. As shown in Figure

8.12(a), with the increase in target analyte concentration, the LP_{020} resonance dual-band (L-LP_{020} and R-LP_{020} in Figure 8.12(b)&(c)) becomes broader and there is a blue shift for the LP_{019} resonance band indicating RI increase during the binding process. The dynamic wavelength shift for the separation of dual-band in Figure 8.12(d) demonstrated an increase in the amount of IgG bound to the peptide coated sensor surface, which exhibits wavelength shifts of 0.77, 2.04, 3.24, 4.36, 5.28 and 6.85 nm for the 200, 400, 800, 1600, 3300 and 6600 nM IgG concentrations in PBS, respectively. A Moving Average Filter (MAF) in the time domain with a 100 data points calculation window is applied in order to reduce the noise as the red trace shows in Figure 8.12(d). The data for washing steps are excluded. The responses in Figure 8.12(e) are calculated by taking the average of the signal remaining at a constant level in each concentration. The fit of the Langmuir isotherm (Equation 8-2) for the adsorption of IgG is presented as the red trace in Figure 8.12(e). Figure 8.12(f) show the linearization of Langmuir isotherm using Equation 8-3 in order to estimate the equilibrium binding constant (k) and the maximum wavelength shift ($\Delta\lambda_{max}$).

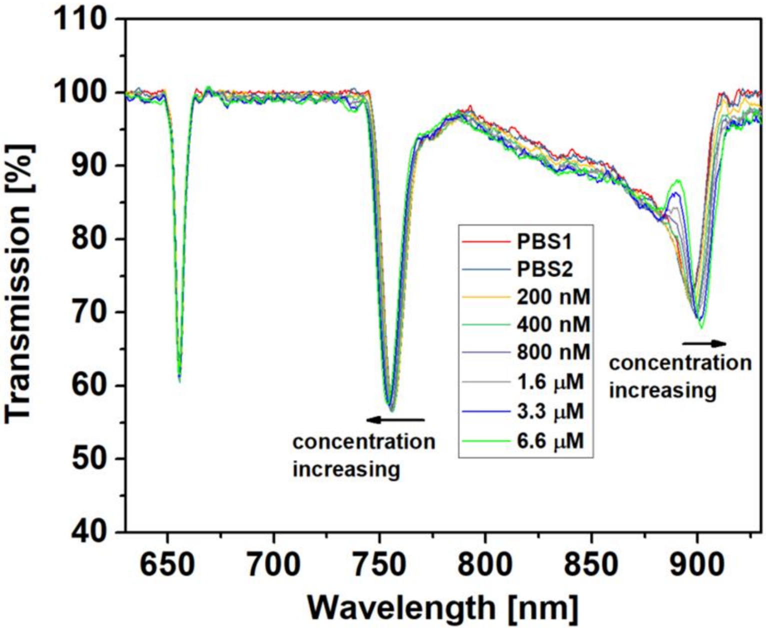

(a)

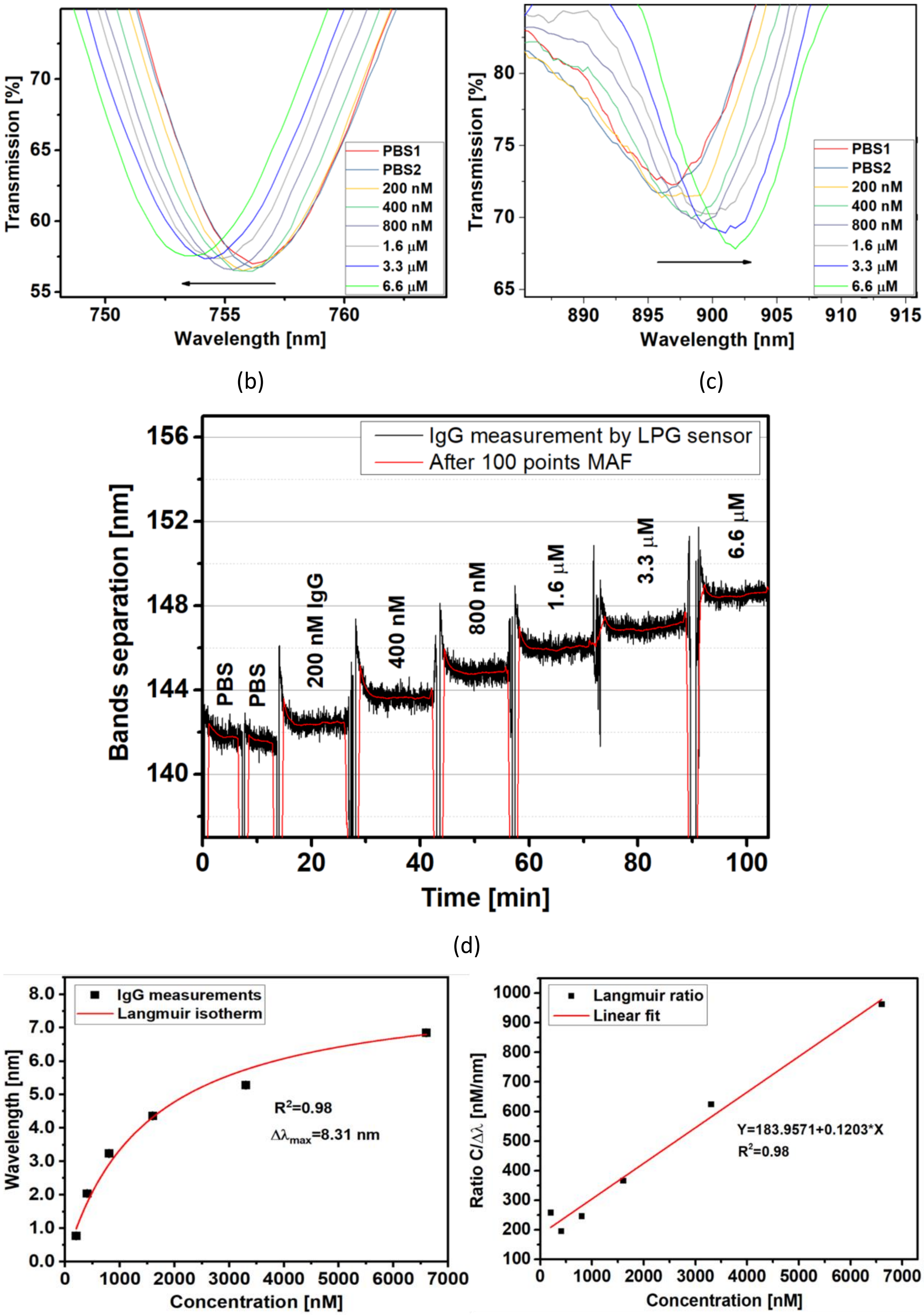

(b) (c)

(d)

(e) (f)

Figure 8. 12 (a) Transmission spectra of peptide coated LPG sensor with different concentrations of IgG in PBS solution. (b) and (c) represent the wavelength shift of L-LP_{020} and R-LP_{020}. (d) The dynamic change of LP_{020} band separation for LPG sensor in different concentrations of IgG. (e) Langmuir isotherm fit of data from (d) (error bars are the standard deviation of each measurement and smaller than the points). (f) Linearization of Langmuir isotherm using Equation 8-3.

The estimated *$\Delta\lambda_{max}$* value can be calculated by comparing the adjusted linear equation (shown as inset in the Figure 8.11(f)) with Equation 8-3:

$$\frac{1}{\Delta\lambda_{max}} = 0.1203 \rightarrow \Delta\lambda_{max} = 8.31\, nm$$

The Langmuir isotherm curve can be plotted using these parameters in Equation 8-2 and the correlation coefficient is $R^2=0.98$ compared to experimental data. Subsequently, considering the molecular mass (*M*), average length (*P*) of IgG as *M*=150,000 g*mol^{-1}, *P*=14 nm [191, 194] and N_A is Avogadro's number. The theoretical surface density (σ_{max}) of protein immobilised onto the LPG surface is:

$$\sigma_{max} = \frac{M_{IgG}}{N_A \cdot P_{IgG}^2} = \frac{150000}{(6.0221 \times 10^{23}) \cdot (1.4 \times 10^{-8})^2} = 1.27\, ng/mm^2$$

accordingly, the sensitivity and the LOD of this peptide LPG sensor can be calculated by Equation 8-4 & 8-5: $S = \Delta\lambda_{max}/\sigma_{max}$ = 8.31/1.27 = 6.55 nm/(ng/mm^2) , *LOD = R/S* = 0.11/6.55 = 16.8 pg/mm^2.

In order to investigate the reversibility, the proposed peptide coated LPG sensor was tested by cyclically exposing to PBS, constant concentration of IgG solution and C-Buffer 4 times. Figure 8.13 illustrates the dynamic response of band separation, the parts with grey, green or cyan colour are LP_{020} band separation response of LPG sensor in PBS, IgG or C-buffer respectively. In each measurement cycle, a significant association process appears when sensor is immersed into IgG solution. Subsequently, the IgG attached LPG sensor is immersed in C-Buffer for dissociation process. The binding between IgG antibody and peptide is broken due to the weak acidity of C-Buffer. As can be seen from Figure 8.13, after the sensor was immersed in C-Buffer, the signal nearly recovers to the level where the sensor was immersed in PBS solution at the beginning of the test. In order to quantify the signal response of the four times exposure to IgG, the wavelength shift from PBS to 3.3 μM IgG solution has been calculated as 5.94, 5.30, 4.56 and 3.35 nm respectively. There is an overall decrease in the response with repeated exposure of the sensor to IgG, which illustrates the partial capability of the sensor to be reused using the original peptide. Alteration of the peptide sequence to give reduced affinity to IgG is expected to enhance the reversibility of the interaction. Also, the 'spikes' in the figure could be related to the tension of the liquid as they exist a short period of time once the solution is added in the LPG bath cell, which might be a disturbing factor for observation of the LPG response, especially in the association process. However, this factor may be eliminated by setting the LPG fibre in an enclosed flow chamber completely and flowing the solvent all the time.

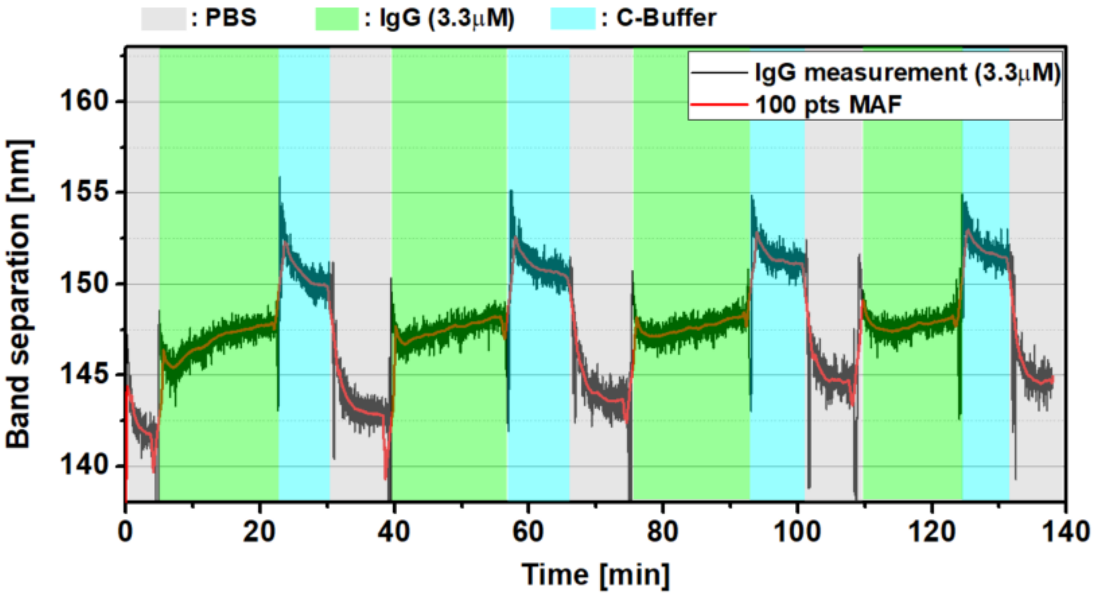

Figure 8. 13 The dynamic change of band separation for LPG sensor with association and dissociation details in constant IgG concentration level (3.3 μM).

8.3.4 Preliminary RI test of bare LPG using microfluidic system

An initial RI test of bare LPG has been undertaken using the microfluidic system described in Section 8.2.6 for verifying the reliability of LPG performance in this system. Using the set-up shown in Figure 8.7(a), the LPG lays in the micro channel assembled by two parts of PDMS cell which allows liquid to flow through. A peristaltic pump circulates RI solution to the flow cell. Meanwhile, the spectral change of the

LPG was recorded by the spectrometer. The RI liquid media were prepared by mixing isopropyl alcohol (IPA) with DI-water in different volume ratio. The RI value of each IPA solution is 1.3327, 1.3397, 1.3474, 1.3649, 1.3717 and 1.3770 for IPA ratio 0, 10, 20, 50, 70 100% in DI-water measured by digital refractometer (Digital Brix/RI-Chek, 13940000, ReiChert). As shown in Figure 8.14(a), with the increase in RI value of IPA solution, the LP_{020} resonance dual-band becomes broader. The dynamic wavelength shift and calibration curve for the separation of LP_{020} resonance in Figure 8.14(b)&(c) demonstrate the linear response with sensitivity of 355 nm/RIU (R^2=0.997) to RI in range of 1.3327-1.3770 operating in the flow system.

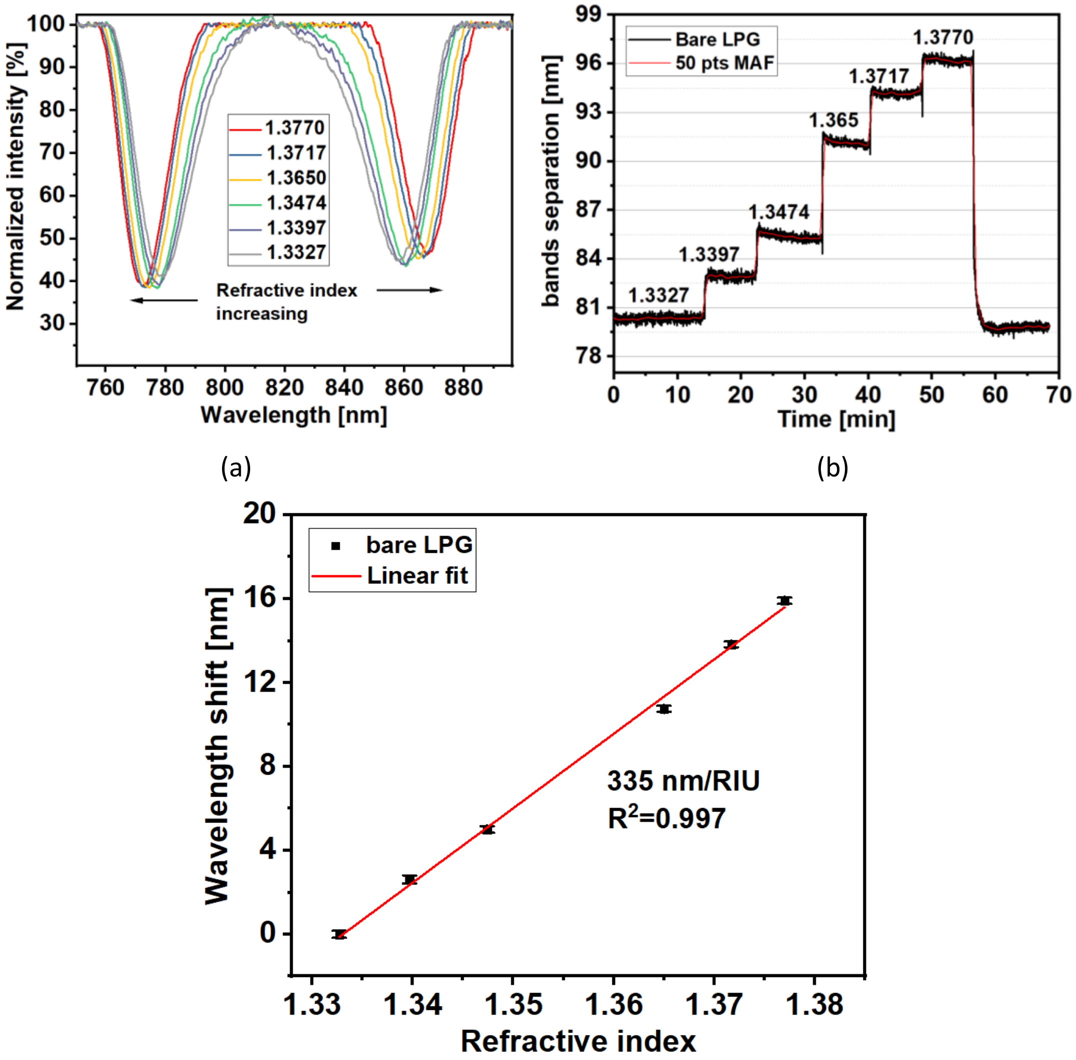

(a)

(b)

(c)

Figure 8. 14 (a) Transmission spectra of bare LPG with different RI value solution. (b) The dynamic change of LP_{020} band separation. (c) RI measurement calibration curve of LPG in flow system.

8.3.5 IgG measurements using the microfluidic system

The functionalized LPG sensor is tested in the flow system by circulating the 640 nM IgG concentration in PBS solution once the reliable performance of the system was verified. Figure 8.15 illustrates the dynamic response of the LPG sensor. As expected, the signal does not show the 'spikes' when flowing solution is switched from PBS to IgG. Accordingly, a clear association process of IgG binding on the surface of sensor can be observed. In addition, the appearance of signal jumps when C-Buffer is circulated in the flow cell is due to the pH-sensitive PAH layer in the functional film. The pH value of PBS (7.2) and C-Buffer (6.2) has been mentioned before in the Section 8.3.2.

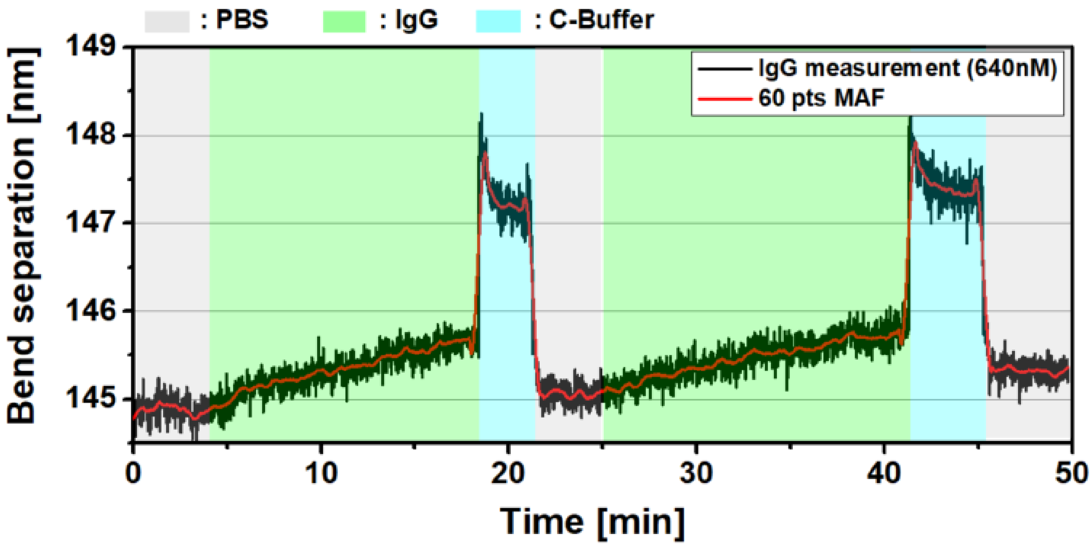

Figure 8. 15 The dynamic change of band separation for LPG sensor IgG measurements in the flow system.

8.4 Conclusion

A new LPG optical fibre-based sensor modified with an IgG-binding peptide for IgG antibody detection has been demonstrated. Strong antibody-antigen interactions mean that it is currently not possible to continuously use the sensor *in vivo* with the state-of-the-art sensing technologies. The IgG-binding peptide supplies a controllable binding affinity compared to antibody-antigen interaction due to the non-covalent bonds of the peptide's amino acid, which allows us to develop a reversible optical fibre immunosensor.

The antibody binding data of the proposed LPG sensor fits the Langmuir isotherm and the sensor demonstrated high sensitivity of 6.55 nm/(ng/mm^2) with a detection limit of 16.8 pg/mm^2 for the detection of IgG antibody. The peptide coated LPG sensor has shown a low cross-sensitivity to IgM by comparing the response of the bare, PAH/SiO_2 coated and functionalised LPG to IgG and another antibody IgM. The partial reversibility of the sensor has been demonstrated by an overall decrease in the response with repeated exposure of the sensor to IgG. In theory, the peptide-antibody affinity can be finely tuned by modification of the sequence of peptide's amino acid. Distinct peptides with different amino acid sequence will be tested in future research work.

A microfluidic system has been developed for standardising conditions for flow of liquid over the sensor. The performance of the LPG operating in this system has been investigated by an initial RI measurement. In addition, the clear association process of binding antibody has been observed using the system.

Due to time limitations and COVID restrictions the work in the topic of this Chapter has only been carried out partially. The overall plan, referred to in the introduction (Figure 8.1), involves the rest of the characterisation and experiments with extra peptides that will be completed in future work however, the preliminary results indicated here show great promise.

Chapter 9: Conclusions

9.1 Conclusions

The implementation of optical fibre sensing technology in physical and biochemical health monitoring applications through the investigation and development of optical fibre sensors to measure humidity, temperature, anti-cancer drug and antibody has been explored.

A new approach to monitor humidity in garments based on optical fibre sensing have been presented. The fabrication of the chosen optical fibre humidity sensor was described. Eleven-layer PAH/SiO_2 nanoparticle film has been deposited successfully onto the surface of an optical fibre tip, which was used to measure changes in light intensity reflected from the tip of the fibre which are proportional to humidity. Bending losses were partially compensated by including an uncoated reference fibre which enables measurements to be made during exercise. The response of the sensing system to RH concentration was linear with a sensitivity of 3.02 mV/% (R^2=0.96). Measurements from 9 volunteers during a cycling test demonstrate the capability of the system to measure the effect of textile properties on humidity, with polyester providing improved moisture wicking properties than cotton. The small size and flexibility of the sensors allow them to be easily integrated within garments with negligible effect on the moisture wicking properties and has the potential to be used as a tool for clothing developers designing moisture managing products.

In the case of optical fibre sensor for temperature measurements, there were two approaches, consisting of the different thermochromic materials applied onto optical fibres have been explored. Due to their visualized thermochromism in the appropriate temperature range and low cost, the microencapsulated RT-leuco-ink and TLC have the potential to be a reasonable coating film for optical fibre temperature sensing. The results obtained from three RT-leuco-ink films present however, high hysteresis, ±3.18 °C for blue ink, ±2.09 °C for green ink and ±1.54 °C for magenta ink. Therefore, this approach is not suitable for continuous temperature monitoring. However, the TLC material coated optical fibre temperature sensor demonstrates multi-colour changing at different temperatures with no significant hysteresis. The calibration results of TLC coated sensor present a reliable and linear response and the sensitivity is 4.52 nm/°C (R^2 =0.985) with temperature increases and 4.60 nm/°C (R^2=0.973) with temperature decreases, respectively in range of 28 – 46 °C. In addition, the coincidental calibration curves from ten TLC coated sensors successfully verified the repeatability of the TLC coating approach. It is proposed that the small size and straightforward fabrication of these TLC sensors allow them to be used as a temperature sensing probe for many health monitoring applications.

A novel optical fibre hybrid sensor for monitoring relative humidity and temperature was developed and explored. The hybrid sensor was fabricated by coating the tip of a single optical fibre with PAH/SiO_2 for relative humidity, and a thermochromic liquid crystal for temperature. In the measurement, the intensity changes from the reflection spectrum in response to the RI change of the PAH/SiO_2 film that absorbs water molecules at different RH. The signal response to RH was linear (R^2 =0.973) with a sensitivity of 0.43 %/RH% in the RH range of 55% to 90%. The selective reflection peak showed the sensitivity to temperature and a linear relationship (R^2 =0.993) between peak wavelength shift and temperature with a sensitivity of 3.97 nm/°C over the temperature range of 28 – 46 °C. The sensor shows the low crosstalk between each of the sensing parameters, with a response time of 3.1s temperature (30 – 38 °C) and 13.2 s for relative humidity (20 – 80 %).

In addition, a new approach for anti-cancer drug (Dabrafenib) detection was demonstrated using a long period grating optical fibre sensor functionalised with a molecularly imprinted polymer. This novel sensor demonstrated high sensitivity in serum of 15.2 pm/(μg·mL^{-1}) (R^2=0.993) with a LoD of 1.71 μg·mL^{-1} when exposed to varying concentrations of Dabrafenib in serum, which is well within the range required clinically. Also, the sensor shows a weak sensitivity to 2-AQ (2.5 pm/(μg·mL^{-1})) in serum as compared to Dabrafenib (15.2 pm/(μg·mL^{-1})), indicating the promising selectivity to Dabrafenib.

A new LPG optical fibre-based sensor modified with an IgG-binding peptide for IgG antibody detection has been demonstrated. The IgG-binding peptide supplies a controllable binding affinity compared to antibody-antigen interaction due to the non-covalent bonds of the peptide's amino acid, which allows the development of a reversible optical fibre immunosensor. The antibody binding data of the proposed LPG sensor fits the Langmuir isotherm and the sensor demonstrated high sensitivity of 6.55 nm/(ng/mm^2) with a detection limit of 16.8 pg/mm^2 for the detection of IgG antibody. Besides, this peptide coated LPG sensor showed a low cross-sensitivity to IgM by comparing the response of the bare and functionalised LPG to IgG and another antibody IgM. A microfluidic system has been developed for standardising conditions for flow of liquid over the sensor. The partial reversibility of the sensor has been demonstrated by an overall decrease in the response with repeated exposure of the sensor to IgG. The peptide-antibody affinity can be finely tuned by modification of the sequence of peptide's amino acid. Distinct peptides with different amino acid sequence will be tested in the future research work. Overall, the work in this chapter has been done partially and the rest of characterisation and experiments with extra peptides will be done in the future.

9.2 Future work

The work presented in this PhD thesis provides key preliminary results from the development of optical fibre sensors for humidity, temperature, Dabrafenib and protein measurements in the laboratory. Although the results are promising there are some limitations of this research requiring further investigations in order to improve the performance of such sensors and turn them into useful clinic-ready healthcare tools for example:

i) in the case of hydrophilic film (PAH/SiO_2 NPs) coated humidity optical fibre sensor, to the sensor itself, different size of nanoparticles would affect the sensing performance due to the possible changes in the surface coverage and film thickness, accordingly the humidity sensitivity or response time could be influenced as well. Another improvement will focus on the optimization and minimization of the electronic unit. In order to minimize the unit, the current SLD light source and the extra ADC circuit board can be replaced by components can be integrated such as LED and ADC circuit, respectively. Moreover, the extent of the humidity detectable range will be investigated by allowing measurement in a clinically useful range in different applications. For example, a study by Engebretsen *et al*. demonstrated the effect of humidity level on human skin barrier function and dermatitis by placing skin in dry (RH < 10%), normal (RH 40 - 70%) and humid conditions (RH > 80%) [195].

ii) in the case of the temperature optical fibre sensor coated with TLC, future work will focus on deploying the sensor in a possible healthcare application as the proposed temperature sensor has only been characterized in the laboratory. Considering the detectable temperature range of the sensor (28 – 46 °C), the possible clinic application would be related to monitoring temperature on the skin of human or in-vivo situation for post-operative pneumonia.

iii) regarding the hybrid optical fibre sensor for temperature and humidity measurement, improvements can be implemented by applying this hybrid sensor in the suitable applications, for example, moisture and temperature monitoring in the facemask, contributing to health monitoring in upper respiratory pathway [196]. Alternatively, considering wound healing, there is no definitive range of permitted humidity recommended throughout the healing process [197]. Therefore, measurements and quantification of the wound microenvironment in terms of humidity and temperature using the proposed sensor may be beneficial for understanding the healing process. Moreover, the biocompatibility test (10993) of the sensing film and optical fibre itself should be approved if the proposed sensor will be applied in the clinic study.

iv) for the reported Dabrafenib LPG sensor, future work will involve development of the sensor into a minimally invasive tool for measurement at a tumour site. The sensor will be inserted into the cultured 3D spheroids cells carried with different concentration of Dabrafenib. Correlations between drug concentration and extent of response will be determined in the tumour sites. In this step, the crosstalk to other possible analytes such as small molecular protein in tumour site cell tissue should be investigated. In addition, the compensation of temperature affect should be considered when the sensor is used in-vivo. Using an LPG array, one for compensation and another for analyte measurement, will be investigated for turning the sensor into clinically useful tool.

v) so far, the work in Chapter 8 is incomplete due to the lab closures in the period of COVID-19 pandemic. Future work (outside of this thesis) will involve investigation of peptides (consists of different amino acid sequence) coated LPG IgG sensors and repeat the characterization experiments such as sensitivity, selectivity and reversibility investigation for these sensors. A performance comparison summary, including reversibility and selectivity, of using different peptides coated LPG IgG sensor will be generated once all experiments have been done. Moreover, the possible impacts from the current microfluidic system will be considered. For example, the circulating flow rate of the peristaltic pump would affect the association and dissociation between functional surface on the LPG and antibodies. The flow cell mode of unsuitable material may capture an immeasurable amount of antibodies on the roughness surface, which can cause the incorrected output.

In closing the journey of the exploration of fibre optic sensors for healthcare applications has been a most wonderful experience and one that the author has been delighted to be a part of.

References

[1] C. He *et al.*, "Real-Time Humidity Measurement during Sports Activity using Optical Fibre Sensing," *Sensors*, vol. 20, no. 7, p. 1904, 2020.

[2] C. He, S. Korposh, R. Correia, B. Hayes-Gill, and S. Morgan, "Optical fibre temperature sensor based on thermochromic liquid crystal," in *Seventh European Workshop on Optical Fibre Sensors*, 2019, vol. 11199, p. 1119908: International Society for Optics and Photonics.

[3] C. He *et al.*, "Surface polymer imprinted optical fibre sensor for dose detection of dabrafenib," *Analyst,* vol. 145, pp. 4504-4511, 2020.

[4] R. Correia, S. James, S. Lee, S. Morgan, and S. Korposh, "Biomedical application of optical fibre sensors," *Journal of Optics,* vol. 20, no. 7, p. 073003, 2018.

[5] A. V. Arundel, E. M. Sterling, J. H. Biggin, and T. D. Sterling, "Indirect health effects of relative humidity in indoor environments," *Environmental health perspectives,* vol. 65, pp. 351-361, 1986.

[6] C. L. Lim, C. Byrne, and J. K. Lee, "Human thermoregulation and measurement of body temperature in exercise and clinical settings," *Annals Academy of Medicine Singapore,* vol. 37, no. 4, p. 347, 2008.

[7] M. Shelly, G. Lloyd, and G. Park, "A review of the mechanisms and methods of humidification of inspired gases," *Intensive care medicine,* vol. 14, no. 1, pp. 1-9, 1988.

[8] K. Thyagarajan and A. Ghatak, *Fiber optic essentials*. John Wiley & Sons, 2007.

[9] R. J. Maughan, H. Otani, and P. Watson, "Influence of relative humidity on prolonged exercise capacity in a warm environment," *European journal of applied physiology,* vol. 112, no. 6, pp. 2313-2321, 2012.

[10] S. Jing, B. Li, M. Tan, and H. Liu, "Impact of relative humidity on thermal comfort in a warm environment," *Indoor and Built Environment,* vol. 22, no. 4, pp. 598-607, 2013.

[11] J. K. Zuur, S. H. Muller, A. Vincent, M. Sinaasappel, F. H. De Jongh, and F. J. Hilgers, "Assessment of tracheal temperature and humidity in laryngectomized individuals and the influence of a heat and moisture exchanger on tracheal climate," *Head & Neck: Journal for the Sciences and Specialties of the Head and Neck,* vol. 30, no. 8, pp. 1072-1082, 2008.

[12] G. Thiéry *et al.*, "Heat and moisture exchangers in mechanically ventilated intensive care unit patients: a plea for an independent assessment of their performance," *Critical care medicine,* vol. 31, no. 3, pp. 699-704, 2003.

[13] N. K. Nakagawa *et al.*, "Effects of a heat and moisture exchanger and a heated humidifier on respiratory mucus in patients undergoing mechanical ventilation," *Critical care medicine,* vol. 28, no. 2, pp. 312-317, 2000.

[14] J. Zuur, S. Muller, F. H. de Jongh, N. Van Zandwijk, and F. Hilgers, "The physiological rationale of heat and moisture exchangers in post-laryngectomy pulmonary rehabilitation: a review," *European Archives of Oto-Rhino-Laryngology and Head & Neck,* vol. 263, no. 1, pp. 1-8, 2006.

[15] D. G. Armstrong, K. Holtz-Neiderer, C. Wendel, M. J. Mohler, H. R. Kimbriel,

and L. A. Lavery, "Skin temperature monitoring reduces the risk for diabetic foot ulceration in high-risk patients," *The American journal of medicine,* vol. 120, no. 12, pp. 1042-1046, 2007.

[16] T. R. Dargaville, B. L. Farrugia, J. A. Broadbent, S. Pace, Z. Upton, and N. H. Voelcker, "Sensors and imaging for wound healing: a review," *Biosensors and Bioelectronics,* vol. 41, pp. 30-42, 2013.

[17] T. Yeo, T. Sun, and K. Grattan, "Fibre-optic sensor technologies for humidity and moisture measurement," *Sensors and Actuators A: Physical,* vol. 144, no. 2, pp. 280-295, 2008.

[18] D. Lopez-Torres *et al.*, "Photonic crystal fiber interferometer coated with a PAH/PAA nanolayer as humidity sensor," *Sensors and Actuators B: Chemical,* vol. 242, pp. 1065-1072, 2017.

[19] D. Lopez-Torres *et al.*, "Enhancing sensitivity of photonic crystal fiber interferometric humidity sensor by the thickness of SnO2 thin films," *Sensors and Actuators B: Chemical,* vol. 251, pp. 1059-1067, 2017.

[20] Y. Wang *et al.*, "Fiber optic relative humidity sensor based on the tilted fiber Bragg grating coated with graphene oxide," *Applied Physics Letters,* vol. 109, no. 3, p. 031107, 2016.

[21] B. Gu, M. Yin, A. P. Zhang, J. Qian, and S. He, "Optical fiber relative humidity sensor based on FBG incorporated thin-core fiber modal interferometer," *Optics express,* vol. 19, no. 5, pp. 4140-4146, 2011.

[22] Y. Liu, L. Wang, M. Zhang, D. Tu, X. Mao, and Y. Liao, "Long-period grating relative humidity sensor with hydrogel coating," *IEEE Photonics Technology Letters,* vol. 19, no. 12, pp. 880-882, 2007.

[23] W. C. Wong, C. C. Chan, L. H. Chen, T. Li, K. X. Lee, and K. C. Leong, "Polyvinyl alcohol coated photonic crystal optical fiber sensor for humidity measurement," *Sensors and Actuators B: Chemical,* vol. 174, pp. 563-569, 2012.

[24] F. U. Hernandez *et al.*, "Characterization and use of a fiber optic sensor based on PAH/SiO 2 film for humidity sensing in ventilator care equipment," *IEEE Transactions on Biomedical Engineering,* vol. 63, no. 9, pp. 1985-1992, 2016.

[25] D. Li *et al.*, "Molybdenum disulfide nanosheets deposited on polished optical fiber for humidity sensing and human breath monitoring," vol. 25, no. 23, pp. 28407-28416, 2017.

[26] Y. Luo *et al.*, "Tungsten disulfide (WS 2) based all-fiber-optic humidity sensor," vol. 24, no. 8, pp. 8956-8966, 2016.

[27] C. Bariain, I. R. Matías, F. J. Arregui, M. J. S. Lopez-Amo, and A. B. Chemical, "Optical fiber humidity sensor based on a tapered fiber coated with agarose gel," vol. 69, no. 1-2, pp. 127-131, 2000.

[28] Y. Lin, Y. Gong, Y. Wu, and H. J. P. s. Wu, "Polyimide-coated fiber Bragg grating for relative humidity sensing," vol. 5, no. 1, pp. 60-66, 2015.

[29] R. Gao *et al.*, "Humidity sensor based on power leakage at resonance wavelengths of a hollow core fiber coated with reduced graphene oxide," vol. 222, pp. 618-624, 2016.

[30] M. Bedoya, M. T. Díez, M. C. Moreno-Bondi, G. J. S. Orellana, and A. B. Chemical, "Humidity sensing with a luminescent Ru (II) complex and phase-sensitive detection," vol. 113, no. 2, pp. 573-581, 2006.

[31] B. N. Shivananju *et al.*, "Highly sensitive carbon nanotubes coated etched fiber bragg grating sensor for humidity sensing," vol. 14, no. 8, pp. 2615-2619, 2014.

[32] Y. Wang, C. Shen, W. Lou, F. J. S. Shentu, and A. B. Chemical, "Polarization-dependent humidity sensor based on an in-fiber Mach-Zehnder interferometer coated with graphene oxide," vol. 234, pp. 503-509, 2016.

[33] L.-P. Sun, J. Li, L. Jin, Y. Ran, B.-O. J. S. Guan, and A. B. Chemical, "High-birefringence microfiber Sagnac interferometer based humidity sensor," vol. 231, pp. 696-700, 2016.

[34] M. Shao, X. Qiao, H. Fu, Y. Liu, X. Zhao, and N. J. O. C. Yao, "High sensitivity refractive index sensing of Mach–Zehnder interferometer based on multimode fiber core sandwiched between two waist-enlarged fiber tapers," vol. 311, pp. 359-363, 2013.

[35] F. J. Arregui, Y. Liu, I. R. Matias, R. O. J. S. Claus, and A. B. Chemical, "Optical fiber humidity sensor using a nano Fabry–Perot cavity formed by the ionic self-assembly method," vol. 59, no. 1, pp. 54-59, 1999.

[36] F. Hernandez *et al.*, "Simultaneous temperature and humidity measurements in a mechanical ventilator using an optical fibre sensor," in *Sixth European Workshop on Optical Fibre Sensors*, 2016, vol. 9916, p. 99160C: International Society for Optics and Photonics.

[37] R. Correia *et al.*, "Highly sensitive contact pressure measurements using FBG patch in endotracheal tube cuff," in *Sixth European Workshop on Optical Fibre Sensors*, 2016, vol. 9916, p. 99161F: International Society for Optics and Photonics.

[38] D. Tosi, E. G. Macchi, and A. Cigada, "Fiber-optic temperature and pressure sensors applied to radiofrequency thermal ablation in liver phantom: methodology and experimental measurements," *Journal of Sensors,* vol. 2015, p. 22, 2015.

[39] S. Khaliq, S. W. James, and R. P. Tatam, "Enhanced sensitivity fibre optic long period grating temperature sensor," *Measurement Science and Technology,* vol. 13, no. 5, p. 792, 2002.

[40] Y. Zhao, M.-Q. Chen, R.-Q. Lv, P. Wang, and X. Feng, "Small and practical optical fiber fluorescence temperature sensor," *IEEE Transactions on Instrumentation and Measurement,* vol. 65, no. 10, pp. 2406-2411, 2016.

[41] R. Flores, R. Janeiro, and J. Viegas, "Optical fibre Fabry-Pérot interferometer based on inline microcavities for salinity and temperature sensing," *Scientific reports,* vol. 9, no. 1, pp. 1-9, 2019.

[42] B. Zhang and M. Kahrizi, "High-temperature resistance fiber Bragg grating temperature sensor fabrication," *IEEE sensors journal,* vol. 7, no. 4, pp. 586-591, 2007.

[43] S. Tao and A. Jayaprakash, "A fiber optic temperature sensor with an epoxy-glue membrane as a temperature indicator," *Sensors and Actuators B: Chemical,* vol. 119, no. 2, pp. 615-620, 2006.

[44] J. Hromadka *et al.*, "Simultaneous in situ temperature and relative humidity monitoring in mechanical ventilators using an array of functionalised optical fibre long period grating sensors," vol. 286, pp. 306-314, 2019.

[45] R. Flores, R. Janeiro, and J. J. S. r. Viegas, "Optical fibre Fabry-Pérot interferometer based on inline microcavities for salinity and temperature

sensing," vol. 9, no. 1, pp. 1-9, 2019.

[46] K. Tian *et al.*, "A high sensitivity temperature sensor based on balloon-shaped bent SMF structure with its original polymer coating," vol. 29, no. 8, p. 085104, 2018.

[47] L. Alwis, T. Sun, and K. T. Grattan, "Characterization of a polyimide-coated humidity sensor in a hybrid fibre grating configuration," in *24th International Conference on Optical Fibre Sensors*, 2015, vol. 9634, p. 963462: International Society for Optics and Photonics.

[48] J. Wu, Y. Wang, and W. Liu, "A fluorescence optic-fiber temperature sensor based on crystal LiSrAlF6: Cr3+," in *Third International Symposium on Precision Mechanical Measurements*, 2006, vol. 6280, p. 62801I: International Society for Optics and Photonics.

[49] C. Fernandez-Valdivielso, E. Egozkue, I. Matıas, F. Arregui, C. J. S. Bariain, and A. B. Chemical, "Experimental study of a thermochromic material based optical fiber sensor for monitoring the temperature of the water in several applications," vol. 91, no. 1-3, pp. 231-240, 2003.

[50] A. Dybko, W. Wroblewski, E. Rożniecka, J. Maciejewski, Z. J. S. Brzozka, and A. A. Physical, "Comparison of two thermochromic solutions for fibre optic temperature probes," vol. 76, no. 1-3, pp. 203-207, 1999.

[51] A. Dybko, W. Wroblewski, E. Rożniecka, J. Maciejewski, and Z. Brzozka, "Comparison of two thermochromic solutions for fibre optic temperature probes," *Sensors and Actuators A: Physical,* vol. 76, no. 1-3, pp. 203-207, 1999.

[52] C. Fernandez-Valdivielso, E. Egozkue, I. Matıas, F. Arregui, and C. Bariain, "Experimental study of a thermochromic material based optical fiber sensor for monitoring the temperature of the water in several applications," *Sensors and Actuators B: Chemical,* vol. 91, no. 1-3, pp. 231-240, 2003.

[53] C. G. Tocchetti *et al.*, "From molecular mechanisms to clinical management of antineoplastic drug-induced cardiovascular toxicity: a translational overview," vol. 30, no. 18, pp. 2110-2153, 2019.

[54] G. S. Falchook *et al.*, "Dabrafenib in patients with melanoma, untreated brain metastases, and other solid tumours: a phase 1 dose-escalation trial," *The Lancet,* vol. 379, no. 9829, pp. 1893-1901, 2012.

[55] A. Hauschild *et al.*, "Dabrafenib in BRAF-mutated metastatic melanoma: a multicentre, open-label, phase 3 randomised controlled trial," *The Lancet,* vol. 380, no. 9839, pp. 358-365, 2012.

[56] E. M. A. (EMA). (2013). *Tafinlar EPAR*. Available: https://www.ema.europa.eu/en/medicines/human/EPAR/tafinlar

[57] S. J. Welsh and P. G. Corrie, "Management of BRAF and MEK inhibitor toxicities in patients with metastatic melanoma," *Therapeutic advances in medical oncology,* vol. 7, no. 2, pp. 122-136, 2015.

[58] A. Jaworska, S. Fornasaro, V. Sergo, and A. Bonifacio, "Potential of surface enhanced Raman spectroscopy (SERS) in therapeutic drug monitoring (TDM). A critical review," *Biosensors,* vol. 6, no. 3, p. 47, 2016.

[59] A. Pathak, S. Parveen, and B. D. Gupta, "Fibre optic SPR sensor using functionalized CNTs for the detection of SMX: comparison with enzymatic approach," *Plasmonics,* vol. 13, no. 1, pp. 189-202, 2018.

[60] Y. Qiu, Y. Tang, B. Li, and M. J. R. S. o. s. He, "Rapid detection of cocaine using

aptamer-based biosensor on an evanescent wave fibre platform," vol. 5, no. 10, p. 180821, 2018.

[61] F. Hernandez *et al.*, "Propofol Detection Using Optical Fibre Long Period Grating Sensors with Molecularly Imprinted Host-Guest Binding Sites in TiO2 Films," in *Optical Fiber Sensors*, 2018, p. TuE72: Optical Society of America.

[62] S. P. Wren, T. H. Nguyen, P. Gascoine, R. Lacey, T. Sun, and K. T. Grattan, "Preparation of novel optical fibre-based Cocaine sensors using a molecular imprinted polymer approach," *Sensors and Actuators B: Chemical,* vol. 193, pp. 35-41, 2014.

[63] S. Korposh *et al.*, "Selective vancomycin detection using optical fibre long period gratings functionalised with molecularly imprinted polymer nanoparticles," vol. 139, no. 9, pp. 2229-2236, 2014.

[64] S.-W. Lee, S. Korposh, R. Selyanchyn, and T. Kunitake, "Fundamentals and perspectives of molecular imprinting in sensor applications," *Handbook of Molecular Imprinting: Advanced Sensor Applications,* pp. 3-45, 2012.

[65] O. S. Ahmad, T. S. Bedwell, C. Esen, A. Garcia-Cruz, and S. A. J. T. i. b. Piletsky, "Molecularly imprinted polymers in electrochemical and optical sensors," vol. 37, no. 3, pp. 294-309, 2019.

[66] Y. Saylan, S. Akgönüllü, H. Yavuz, S. Ünal, and A. J. S. Denizli, "Molecularly imprinted polymer based sensors for medical applications," vol. 19, no. 6, p. 1279, 2019.

[67] S. Fox, *Human physiology*. McGraw-Hill Education, 2015.

[68] J. M. Woof and D. R. Burton, "Human antibody–Fc receptor interactions illuminated by crystal structures," *Nature Reviews Immunology,* vol. 4, no. 2, pp. 89-99, 2004.

[69] J. S. Fellah, M. V. Wiles, J. Charlemagne, and J. Schwager, "Evolution of vertebrate IgM: complete amino acid sequence of the constant region of Ambystoma mexicanum μ chain deduced from cDNA sequence," *European journal of immunology,* vol. 22, no. 10, pp. 2595-2601, 1992.

[70] S. Fagarasan and T. Honjo, "Intestinal IgA synthesis: regulation of front-line body defences," *Nature Reviews Immunology,* vol. 3, no. 1, pp. 63-72, 2003.

[71] D. S. Rowe and J. L. Fahey, "A new class of human immunoglobulins: I. A unique myeloma protein," *The Journal of experimental medicine,* vol. 121, no. 1, pp. 171-184, 1965.

[72] K. Chen *et al.*, "Immunoglobulin D enhances immune surveillance by activating antimicrobial, proinflammatory and B cell–stimulating programs in basophils," *Nature immunology,* vol. 10, no. 8, pp. 889-898, 2009.

[73] K. J. Erb, "Helminths, allergic disorders and IgE-mediated immune responses: where do we stand?," *European journal of immunology,* vol. 37, no. 5, pp. 1170-1173, 2007.

[74] H. J. Gould *et al.*, "The biology of IGE and the basis of allergic disease," *Annual review of immunology,* vol. 21, no. 1, pp. 579-628, 2003.

[75] V. Kumar, A. Abbas, and J. Aster, "Hypersensitivity: Immunologically mediated tissue injury. Robbins and Cotran Pathologic Basis of Disease," ed: Elsevier Health Sciences, 2014.

[76] K. Hedman, A. Vaheri, and M. Brummer-Korvenkontio, "Rapid diagnosis of hantavirus disease with an IgG-avidity assay," *The Lancet,* vol. 338, no. 8779,

pp. 1353-1356, 1991.

[77] M. Yamamoto *et al.*, "Elevated IgG4 concentrations in serum of patients with Mikulicz's disease," *Scandinavian journal of rheumatology,* vol. 33, no. 6, pp. 432-433, 2004.

[78] E. Allan, I. R. Poxton, and G. R. Barclay, "Anti-bacteroides lipopolysaccharide IgG levels in healthy adults and sepsis patients," *FEMS Immunology & Medical Microbiology,* vol. 11, no. 1, pp. 5-12, 1995.

[79] D. S. Song *et al.*, "Evaluation of a competitive ELISA for antibody detection against avian influenza virus," *Journal of veterinary science,* vol. 10, no. 4, pp. 323-329, 2009.

[80] S. Sakamoto *et al.*, "Enzyme-linked immunosorbent assay for the quantitative/qualitative analysis of plant secondary metabolites," *Journal of natural medicines,* vol. 72, no. 1, pp. 32-42, 2018.

[81] Y. Hsin Chang, T. C. Chang, E.-F. Kao, C. J. B. Chou, biotechnology,, and biochemistry, "Detection of protein A produced by Staphylococcus aureus with a fiber-optic-based biosensor," vol. 60, no. 10, pp. 1571-1574, 1996.

[82] P. S. Pidenko, A. A. Shuvalov, A. A. Zanishevskaya, and N. A. Burmistrova, "Detection of antigen-antibody interactions in microstructured optical fibers," in *Saratov Fall Meeting 2019: Optical and Nano-Technologies for Biology and Medicine*, 2020, vol. 11457, p. 114571J: International Society for Optics and Photonics.

[83] L. Zeni *et al.*, "A portable optical-fibre-based surface plasmon resonance biosensor for the detection of therapeutic antibodies in human serum," *Scientific reports* vol. 10, no. 1, pp. 1-9, 2020.

[84] M. Loyez, M. Lobry, R. Wattiez, and C. J. S. Caucheteur, "Optical fiber gratings immunoassays," *Sensors,* vol. 19, no. 11, p. 2595, 2019.

[85] L. Liu *et al.*, "Highly sensitive label-free antibody detection using a long period fibre grating sensor," *Sensors and Actuators B: Chemical,* vol. 271, pp. 24-32, 2018.

[86] L. Marques *et al.*, "Highly sensitive optical fibre long period grating biosensor anchored with silica core gold shell nanoparticles," *Biosensors and Bioelectronics,* vol. 75, pp. 222-231, 2016.

[87] A. Aray *et al.*, "SPR-based plastic optical fibre biosensor for the detection of C-reactive protein in serum," *Journal of biophotonics,* vol. 9, no. 10, pp. 1077-1084, 2016.

[88] A. Urrutia *et al.*, "Novel highly sensitive protein sensors based on tapered optical fibres modified with Au-based nanocoatings," *Journal of Sensors,* vol. 2016, p. 11, 2016.

[89] S. Sankaran and R. Ehsani, "Introduction to the electromagnetic spectrum," in *Imaging with Electromagnetic Spectrum*: Springer, 2014, pp. 1-15.

[90] N. Bloembergen and P. Pershan, "Light waves at the boundary of nonlinear media," *Physical review,* vol. 128, no. 2, p. 606, 1962.

[91] J. M. Senior and M. Y. Jamro, *Optical fiber communications: principles and practice*. Pearson Education, 2009.

[92] G. Keiser, *Optical fiber communications*. McGraw-Hill Science, Engineering & Mathematics, 1983.

[93] J. H. Stockley *et al.*, "Surpassing light-induced cell damage in vitro with novel

cell culture media," *Scientific reports,* vol. 7, no. 1, pp. 1-11, 2017.

[94] E. K. Yeow, S. M. Melnikov, T. D. Bell, F. C. De Schryver, and J. Hofkens, "Characterizing the fluorescence intermittency and photobleaching kinetics of dye molecules immobilized on a glass surface," *The Journal of Physical Chemistry A,* vol. 110, no. 5, pp. 1726-1734, 2006.

[95] J. W. Parker *et al.*, "Fiber-optic sensors for pH and carbon dioxide using a self-referencing dye," *Analytical chemistry,* vol. 65, no. 17, pp. 2329-2334, 1993.

[96] N. Díaz-Herrera, M. Navarrete, O. Esteban, and A. González-Cano, "A fibre-optic temperature sensor based on the deposition of a thermochromic material on an adiabatic taper," *Measurement Science and Technology,* vol. 15, no. 2, p. 353, 2003.

[97] F. Tavernier and M. Steyaert, *High-speed optical receivers with integrated photodiode in nanoscale CMOS*. Springer Science & Business Media, 2011.

[98] *Flame User Guide - Spectrecology*. Available: https://www.spectrecology.com/wp-content/uploads/2015/12/Flame-Manual.pdf

[99] K. Fidanboylu and H. Efendioglu, "Fiber optic sensors and their applications," in *5th International Advanced Technologies Symposium (IATS'09)*, 2009, vol. 6, pp. 2-3.

[100] S. Korposh, S. James, R. Tatam, and S. Lee, "Fibre-optic chemical sensor approaches based on nanoassembled thin films: A challenge to future sensor technology," *Current Developments in Optical Fiber Technology,* pp. 237-264, 2013.

[101] T. Wang, W. Yasukochi, S. Korposh, S. W. James, R. P. Tatam, and S.-W. Lee, "A long period grating optical fiber sensor with nano-assembled porphyrin layers for detecting ammonia gas," *Sensors and Actuators B: Chemical,* vol. 228, pp. 573-580, 2016.

[102] C. Zamarreño, S. Lopez, M. Hernaez, I. Del Villar, I. Matias, and F. Arregui, "Resonance-based refractometric response of cladding-removed optical fibers with sputtered indium tin oxide coatings," *Sensors and Actuators B: Chemical,* vol. 175, pp. 106-110, 2012.

[103] D. Gomez, S. P. Morgan, B. R. Hayes-Gill, R. G. Correia, and S. Korposh, "Polymeric optical fibre sensor coated by SiO2 nanoparticles for humidity sensing in the skin microenvironment," *Sensors and Actuators B: Chemical,* vol. 254, pp. 887-895, 2018.

[104] F. Surre *et al.*, "U-bend fibre optic pH sensors using layer-by-layer electrostatic self-assembly technique," in *Journal of Physics: Conference Series*, 2009, vol. 178, no. 1, p. 012046: IOP Publishing.

[105] S. Korposh, H. Okuda, T. Wang, S. James, and S.-W. Lee, "U-shaped evanescent wave optical fibre sensor based on a porphyrin anchored nanoassembled thin film for high sensitivity ammonia detection," in *Fifth Asia-Pacific Optical Sensors Conference*, 2015, vol. 9655, p. 965518: International Society for Optics and Photonics.

[106] M. Xu, L. Dong, L. Reekie, J. Tucknott, and J. Cruz, "Temperature-independent strain sensor using a chirped Bragg grating in a tapered optical fibre," *Electronics Letters,* vol. 31, no. 10, pp. 823-825, 1995.

[107] R. Kashyap, *Fiber bragg gratings*. Academic press, 2009.

[108] M. Bass and E. W. Van Stryland, *Fiber Optics Handbook: fiber, devices, and systems for optical communications* (no. Sirsi) i9780071386234). Optical Society of America., 2002.

[109] C. Massaroni, M. A. Caponero, R. D'Amato, D. Lo Presti, and E. Schena, "Fiber Bragg grating measuring system for simultaneous monitoring of temperature and humidity in mechanical ventilation," *Sensors,* vol. 17, no. 4, p. 749, 2017.

[110] Y.-J. Rao, "In-fibre Bragg grating sensors," *Measurement science and technology,* vol. 8, no. 4, p. 355, 1997.

[111] S. W. James and R. P. Tatam, "Optical fibre long-period grating sensors: characteristics and application," *Measurement science and technology,* vol. 14, no. 5, p. R49, 2003.

[112] L. Zhang, W. Zhang, I. Bennion, S. Yin, P. Ruffin, and T. Francis, "In-fiber grating optic sensors," *Fiber optic sensors,* pp. 109-162, 2008.

[113] O. Frazão, L. Ferreira, F. Araújo, and J. Santos, "Applications of fiber optic grating technology to multi-parameter measurement," *Fiber and integrated optics,* vol. 24, no. 3-4, pp. 227-244, 2005.

[114] B. H. Lee *et al.*, "Interferometric fiber optic sensors," *sensors,* vol. 12, no. 3, pp. 2467-2486, 2012.

[115] L. Alwis, T. Sun, and K. Grattan, "Fibre optic long period grating-based humidity sensor probe using a Michelson interferometric arrangement," *Sensors and Actuators B: Chemical,* vol. 178, pp. 694-699, 2013.

[116] P. Hu, X. Dong, K. Ni, L. H. Chen, W. C. Wong, and C. C. Chan, "Sensitivity-enhanced Michelson interferometric humidity sensor with waist-enlarged fiber bitaper," *Sensors and Actuators B: Chemical,* vol. 194, pp. 180-184, 2014.

[117] T. Erdogan, "Cladding-mode resonances in short-and long-period fiber grating filters," *JOSA A,* vol. 14, no. 8, pp. 1760-1773, 1997.

[118] H. J. Patrick, A. D. Kersey, and F. Bucholtz, "Analysis of the response of long period fiber gratings to external index of refraction," *Journal of lightwave technology,* vol. 16, no. 9, p. 1606, 1998.

[119] R. Y. Wong, E. Chehura, S. E. Staines, S. W. James, and R. P. Tatam, "Fabrication of fiber optic long period gratings operating at the phase matching turning point using an ultraviolet laser," *Applied Optics,* vol. 53, no. 21, pp. 4669-4674, 2014.

[120] L. Marques *et al.*, "Highly sensitive optical fibre long period grating biosensor anchored with silica core gold shell nanoparticles," *Biosensors and Bioelectronics,* vol. 75, pp. 222-231, 2016.

[121] V. Bhatia *et al.*, "Temperature-insensitive and strain-insensitive long-period grating sensors for smart structures," *Optical Engineering,* vol. 36, no. 7, pp. 1872-1877, 1997.

[122] J. Hromadka *et al.*, "Multi-parameter measurements using optical fibre long period gratings for indoor air quality monitoring," *Sensors and Actuators B: Chemical,* vol. 244, pp. 217-225, 2017.

[123] J. J. Richardson, M. Björnmalm, and F. Caruso, "Technology-driven layer-by-layer assembly of nanofilms," *Science,* vol. 348, no. 6233, 2015.

[124] L. Chen, X. Wang, W. Lu, X. Wu, and J. Li, "Molecular imprinting: perspectives and applications," *Chemical Society Reviews,* vol. 45, no. 8, pp. 2137-2211, 2016.

[125] O. S. Ahmad, T. S. Bedwell, C. Esen, A. Garcia-Cruz, and S. A. Piletsky, "Molecularly imprinted polymers in electrochemical and optical sensors," *Trends in biotechnology,* vol. 37, no. 3, pp. 294-309, 2019.

[126] S. Korposh *et al.*, "Selective vancomycin detection using optical fibre long period gratings functionalised with molecularly imprinted polymer nanoparticles," *Analyst,* vol. 139, no. 9, pp. 2229-2236, 2014.

[127] R. A. Lorenzo, A. M. Carro, C. Alvarez-Lorenzo, and A. Concheiro, "To remove or not to remove? The challenge of extracting the template to make the cavities available in molecularly imprinted polymers (MIPs)," *International journal of molecular sciences,* vol. 12, no. 7, pp. 4327-4347, 2011.

[128] C. Sun, J. S.-c. Au, J. Fan, and R. Zheng, "Novel ventilation design of combining spacer and mesh structure in sports T-shirt significantly improves thermal comfort," *Applied ergonomics,* vol. 48, pp. 138-147, 2015.

[129] S. Korposh, T. Wang, S. James, R. Tatam, and S.-W. Lee, "Pronounced aromatic carboxylic acid detection using a layer-by-layer mesoporous coating on optical fibre long period grating," *Sensors and Actuators B: Chemical,* vol. 173, pp. 300-309, 2012.

[130] A. Plante, B. Holcombe, and L. Stephens, "Fiber hygroscopicity and perceptions of dampness: part I: subjective trials," *Textile Research Journal,* vol. 65, no. 5, pp. 293-298, 1995.

[131] A. Schulze *et al.*, "Permanent surface modification by electron-beam-induced grafting of hydrophilic polymers to PVDF membranes," *Rsc Advances,* vol. 3, no. 44, pp. 22518-22526, 2013.

[132] D. Marcuse, "Curvature loss formula for optical fibers," *JOSA,* vol. 66, no. 3, pp. 216-220, 1976.

[133] F. J. Arregui, I. R. Matias, Y. Liu, K. M. Lenahan, and R. O. Claus, "Optical fiber nanometer-scale Fabry–Perot interferometer formed by the ionic self-assembly monolayer process," *Optics Letters,* vol. 24, no. 9, pp. 596-598, 1999.

[134] C. Kuyatt, "Determining and Reporting Measurement Uncertainties," 1995: Recommended Practice RP-12, National Conference of Standards Laboratories.

[135] N. E. Breslow, "Lessons in biostatistics," *Past, Present, and Future of Statistical Science,* pp. 335-347, 2014.

[136] M. Raccuglia, C. Heyde, A. Lloyd, S. Hodder, and G. Havenith, "Spatial and temporal migration of sweat: from skin to clothing," *European journal of applied physiology,* vol. 118, no. 10, pp. 2155-2169, 2018.

[137] C. Callewaert, E. De Maeseneire, F.-M. Kerckhof, A. Verliefde, T. Van de Wiele, and N. Boon, "Microbial odor profile of polyester and cotton clothes after a fitness session," *Applied and environmental microbiology,* vol. 80, no. 21, pp. 6611-6619, 2014.

[138] O. Panák, M. Držková, and M. Kaplanová, "Insight into the evaluation of colour changes of leuco dye based thermochromic systems as a function of temperature," *Dyes and Pigments,* vol. 120, pp. 279-287, 2015.

[139] R. Kulčar, M. Friškovec, N. Hauptman, A. Vesel, and M. K. Gunde, "Colorimetric properties of reversible thermochromic printing inks," *Dyes and pigments,* vol. 86, no. 3, pp. 271-277, 2010.

[140] M. Chowdhury, M. Joshi, and B. Butola, "Photochromic and thermochromic

colorants in textile applications," *Journal of Engineered Fibers and Fabrics,* vol. 9, no. 1, pp. 107-123, 2014.

[141] D. C. MacLaren and M. A. White, "Dye–developer interactions in the crystal violet lactone–lauryl gallate binary system: implications for thermochromism," *Journal of Materials Chemistry,* vol. 13, no. 7, pp. 1695-1700, 2003.

[142] C. Zhu and A. Wu, "Studies on the synthesis and thermochromic properties of crystal violet lactone and its reversible thermochromic complexes," *Thermochimica acta,* vol. 425, no. 1-2, pp. 7-12, 2005.

[143] D. MacLaren and M. A. White, "Design rules for reversible thermochromic mixtures," *Journal of Materials Science,* vol. 40, no. 3, pp. 669-676, 2005.

[144] D. C. MacLaren and M. A. White, "Competition between dye–developer and solvent–developer interactions in a reversible thermochromic system," *Journal of Materials Chemistry,* vol. 13, no. 7, pp. 1701-1704, 2003.

[145] M. Hajzeri, K. Bašnec, M. Bele, and M. K. Gunde, "Influence of developer on structural, optical and thermal properties of a benzofluoran-based thermochromic composite," *Dyes and Pigments,* vol. 113, pp. 754-762, 2015.

[146] S. M. Burkinshaw, J. Griffiths, and A. D. Towns, "Reversibly thermochromic systems based on pH-sensitive functional dyes," *Journal of materials chemistry,* vol. 8, no. 12, pp. 2677-2683, 1998.

[147] F. Reinitzer, "Beiträge zur kenntniss des cholesterins," *Monatshefte für Chemie,* vol. 9, no. 1, pp. 421-441, 1888.

[148] S. T. Hyde, "Identification of lyotropic liquid crystalline mesophases," *Handbook of applied surface and colloid chemistry,* vol. 2, pp. 299-332, 2001.

[149] M. Parsley, "The Hallcrest handbook of thermochromic liquid crystal technology," *Hallcrest, Glenview,* 1991.

[150] S. Kuniyasu *et al.*, "The strength of rubbing worked on polyimide films for aligning nematic and chiral smectic liquid crystals: controlling pretilt angles and some electrooptic performances of LCDs," *Japanese journal of applied physics,* vol. 27, no. 5R, p. 827, 1988.

[151] P.-G. De Gennes and J. Prost, "The physics of liquid crystals," vol. 83: Oxford university press, 1993.

[152] J.-G. An, S. Hina, Y. Yang, M. Xue, and Y. Liu, "Characterization of liquid crystals: a literature review," *Reviews on Advanced Materials Science,* vol. 44, no. 4, 2016.

[153] I. Sage, "Thermochromic liquid crystals," *Liquid crystals,* vol. 38, no. 11-12, pp. 1551-1561, 2011.

[154] R. Alben, "Theory of the Change in Cholesteric Pitch Near Cholesteric-Smectic Phase Transitions," *Molecular Crystals and Liquid Crystals,* vol. 20, no. 3-4, pp. 231-238, 1973.

[155] P. P. Gaikwad and M. T. Desai, "Liquid crystalline phase and its Pharma application," *International journal of Pharma Research and Review,* vol. 2, no. 12, pp. 40-52, 2013.

[156] L. Hallcrest, "TLC Products for Use in Research and Testing Applications," *LCR Hallcrest Research & Testing Products, Rev,* vol. 1, pp. 1-18, 2019.

[157] S. Krause, "Polymer–polymer compatibility," in *Polymer blends*: Elsevier, 1978, pp. 15-113.

[158] T. Tamura, M. Huang, and T. Togawa, "Current developments in wearable thermometers," *Advanced Biomedical Engineering,* vol. 7, pp. 88-99, 2018.

[159] C. He *et al.*, "Real-Time Humidity Measurement during Sports Activity using Optical Fibre Sensing," *Sensors,* vol. 20, no. 7, p. 1904, 2020.

[160] D. Bolton, "The computation of equivalent potential temperature," *Monthly weather review,* vol. 108, no. 7, pp. 1046-1053, 1980.

[161] L. Van Der Werff *et al.*, "Thermochromic composite fibres containing liquid crystals formed via melt extrusion," *Journal of Materials Science,* vol. 48, no. 14, pp. 5005-5011, 2013.

[162] J. Hromadka *et al.*, "Simultaneous in situ temperature and relative humidity monitoring in mechanical ventilators using an array of functionalised optical fibre long period grating sensors," *Sensors and Actuators B: Chemical,* vol. 286, pp. 306-314, 2019.

[163] F. J. Arregui, I. R. Matías, K. L. Cooper, and R. O. Claus, "Simultaneous measurement of humidity and temperature by combining a reflective intensity-based optical fiber sensor and a fiber Bragg grating," *IEEE Sensors Journal,* vol. 2, no. 5, pp. 482-487, 2002.

[164] A. Urrutia, J. Goicoechea, A. L. Ricchiuti, D. Barrera, S. Sales, and F. J. Arregui, "Simultaneous measurement of humidity and temperature based on a partially coated optical fiber long period grating," *Sensors and Actuators B: Chemical,* vol. 227, pp. 135-141, 2016.

[165] G. Woyessa, A. Fasano, C. Markos, H. K. Rasmussen, and O. Bang, "Low loss polycarbonate polymer optical fiber for high temperature FBG humidity sensing," *IEEE Photonics Technology Letters,* vol. 29, no. 7, pp. 575-578, 2017.

[166] L. V. Nguyen, S. C. Warren-Smith, H. Ebendorff-Heidepriem, and T. M. Monro, "Interferometric high temperature sensor using suspended-core optical fibers," *Opt Express,* vol. 24, no. 8, pp. 8967-77, Apr 18 2016.

[167] S. W. James and R. P. Tatam, "Fibre optic sensors with nano-structured coatings," *Journal of Optics A: Pure and Applied Optics,* vol. 8, no. 7, p. S430, 2006.

[168] K. Subramani, "Fabrication of hydrogel micropatterns by soft photolithography," in *Emerging Nanotechnologies for Manufacturing*: Elsevier, 2015, pp. 279-293.

[169] K. T. Flaherty *et al.*, "Combined BRAF and MEK inhibition in melanoma with BRAF V600 mutations," *New England Journal of Medicine,* vol. 367, no. 18, pp. 1694-1703, 2012.

[170] L. Liu, S. P. Morgan, R. Correia, S.-W. Lee, and S. Korposh, "Multi-Parameter Optical Fiber Sensing of Gaseous Ammonia and Carbon Dioxide," *Journal of Lightwave Technology,* vol. 38, no. 7, pp. 2037-2045, 2019.

[171] A. Cusano *et al.*, "Cladding mode reorganization in high-refractive-index-coated long-period gratings: effects on the refractive-index sensitivity," *Optics letters,* vol. 30, no. 19, pp. 2536-2538, 2005.

[172] N. Yamazaki *et al.*, "Phase 1/2 study assessing the safety and efficacy of dabrafenib and trametinib combination therapy in Japanese patients with BRAF V600 mutation-positive advanced cutaneous melanoma," *The Journal of dermatology,* vol. 45, no. 4, pp. 397-407, 2018.

[173] D. Refaat *et al.*, "Strategies for Molecular Imprinting and the Evolution of MIP

Nanoparticles as Plastic Antibodies—Synthesis and Applications," *International Journal of Molecular Sciences,* vol. 20, no. 24, p. 6304, 2019.
[174] W. J. Cheong, S. H. Yang, and F. Ali, "Molecular imprinted polymers for separation science: A review of reviews," *Journal of separation science,* vol. 36, no. 3, pp. 609-628, 2013.
[175] J. Svenson and I. A. Nicholls, "On the thermal and chemical stability of molecularly imprinted polymers," *Analytica Chimica Acta,* vol. 435, no. 1, pp. 19-24, 2001.
[176] B. A. Jonsson, C. H. Lindh, and H. Welinder, "Haemoglobin adducts and specific immunoglobulin G in humans as biomarkers of exposure to hexahydrophthalic anhydride," *Biomarkers,* vol. 2, no. 4, pp. 239-246, 1997.
[177] L. Liu *et al.*, "Highly sensitive label-free antibody detection using a long period fibre grating sensor," *Sensors and Actuators B: Chemical,* vol. 271, pp. 24-32, 2018.
[178] A. W. Tarr *et al.*, "Naturally occurring antibodies that recognize linear epitopes in the amino terminus of the hepatitis C virus E2 protein confer noninterfering, additive neutralization," vol. 86, no. 5, pp. 2739-2749, 2012.
[179] A. R. Hakami, J. K. Ball, and A. W. Tarr, "Non-ionic detergents facilitate non-specific binding of M13 bacteriophage to polystyrene surfaces," *Journal of virological methods,* vol. 221, pp. 1-8, 2015.
[180] W. Choe, T. A. Durgannavar, and S. J. J. M. Chung, "Fc-binding ligands of immunoglobulin G: an overview of high affinity proteins and peptides," *Materials,* vol. 9, no. 12, p. 994, 2016.
[181] J. Turkevich, P. C. Stevenson, and J. Hillier, "A study of the nucleation and growth processes in the synthesis of colloidal gold," *Discussions of the Faraday Society,* vol. 11, pp. 55-75, 1951.
[182] J. Dong, P. L. Carpinone, G. Pyrgiotakis, P. Demokritou, and B. M. Moudgil, "Synthesis of precision gold nanoparticles using Turkevich method," *KONA Powder and Particle Journal,* vol. 37, pp. 224-232, 2020.
[183] M. Wuithschick *et al.*, "Turkevich in new robes: key questions answered for the most common gold nanoparticle synthesis," *ACS nano,* vol. 9, no. 7, pp. 7052-7071, 2015.
[184] R. Nezlin and V. J. A. i. i. Ghetie, "Interactions of immunoglobulins outside the antigen-combining site," vol. 82, pp. 155-215, 2004.
[185] F. Dinon *et al.*, "Structural refinement of protein A mimetic peptide," *Journal of Molecular Recognition,* vol. 24, no. 6, pp. 1087-1094, 2011.
[186] W.-W. Zhao, F.-F. Liu, Q.-H. Shi, X.-Y. Dong, and Y. J. B. e. j. Sun, "Biomimetic design of affinity peptide ligands for human IgG based on protein A-IgG complex," *Biochemical engineering journal,* vol. 88, pp. 1-11, 2014.
[187] D. G. Kinniburgh, "General purpose adsorption isotherms," *Environmental science & technology,* vol. 20, no. 9, pp. 895-904, 1986.
[188] S. Maguis *et al.*, "Biofunctionalized tilted Fiber Bragg Gratings for label-free immunosensing," *Optics Express,* vol. 16, no. 23, pp. 19049-19062, 2008.
[189] J. Tellinghuisen, "The least-squares analysis of data from binding and enzyme kinetics studies: weights, bias, and confidence intervals in usual and unusual situations," *Methods in enzymology,* vol. 467, pp. 499-529, 2009.
[190] C. A. Barrios *et al.*, "Label-free optical biosensing with slot-waveguides,"

Optics letters, vol. 33, no. 7, pp. 708-710, 2008.

[191] J. Yang, M. Mayer, J. K. Kriebel, P. Garstecki, and G. M. Whitesides, "Self-assembled aggregates of IgGs as templates for the growth of clusters of gold nanoparticles," *Angewandte Chemie International Edition,* vol. 43, no. 12, pp. 1555-1558, 2004.

[192] C. R. Zamarreño, J. Bravo, J. Goicoechea, I. Matias, and F. Arregui, "Response time enhancement of pH sensing films by means of hydrophilic nanostructured coatings," *Sensors and Actuators B: Chemical,* vol. 128, no. 1, pp. 138-144, 2007.

[193] G. Kocak, C. Tuncer, and V. Bütün, "pH-Responsive polymers," *Polymer Chemistry,* vol. 8, no. 1, pp. 144-176, 2017.

[194] L. Chen *et al.*, "Label-free fiber-optic interferometric immunosensors based on waist-enlarged fusion taper," *Sensors and Actuators B: Chemical,* vol. 178, pp. 176-184, 2013.

[195] K. Engebretsen, J. Johansen, S. Kezic, A. Linneberg, J. J. J. o. t. E. A. o. D. Thyssen, and Venereology, "The effect of environmental humidity and temperature on skin barrier function and dermatitis," vol. 30, no. 2, pp. 223-249, 2016.

[196] T. M. Mäkinen *et al.*, "Cold temperature and low humidity are associated with increased occurrence of respiratory tract infections," vol. 103, no. 3, pp. 456-462, 2009.

[197] T. R. Dargaville *et al.*, "Sensors and imaging for wound healing: a review," vol. 41, pp. 30-42, 2013.

Appendix A: Experiment ethics approval

Appendix

Ethics Committee Reviewer Decision

This form must be completed by each reviewer. Each application will be reviewed by two members of the ethics committee. Reviews may be completed electronically and sent to the Faculty ethics administrator (Jo Deeley) from a University of Nottingham email address or may be completed in paper form and delivered to the Faculty of Engineering Research Office.

Applicant full name …………………Chenyang He………

Reviewed by:

Name …DE13…………………………………………

Signature (paper based only)……………………………………………………………

Date ……20 June 2018……………………………………

☐ Approval awarded - no changes required

■ Approval awarded - subject to required changes (see comments below)

☐ Approval pending - further information & resubmission required (see comments)

☐ Approval declined – reasons given below

Comments:

Please make it clear that the photo you take will not be of the participants' bare back and will be of the placement on the back through the shirt.

Please note:

1. The approval only covers the participants and trials specified on the form and further approval must be requested for any repetition or extension to the investigation.
2. The approval covers the ethical requirements for the techniques and procedures described in the protocol but does not replace a safety or risk assessment.
3. Approval is not intended to convey any judgement on the quality of the research, experimental design or techniques.
4. Normally, all queries raised by reviewers should be addressed. In the case of conflicting or incomplete views, the ethics committee chair will review the comments and relay these to the applicant via email. All email correspondence related to the application must be copied to the Faculty research ethics administrator.

Any problems which arise during the course of the investigation must be reported to the Faculty Research Ethics Committee

Brief description of the study design

Title of the study: Monitoring of humidity of human body by using optical fibre sensor

In this study, the experimental target is relative humidity (RH) from human body. Relative humidity is described as a percentage of maximum saturated capacity of water vapour in a gas express. Humidity is one of the important parameters of human body, especially in the healthcare and clinic case. Humidity of human body can be detected from different parts. For example, in this study, monitoring relative humidity from skin during exercise.

This study developed an optical fibre sensor system (one optical fibre humidity sensor and one reference fibre which reduces the bending loss) for recording humidity. The optical fibre humidity sensor is on the tip of optical fibre and coated by a specific film (PAH/SiO_2 nanoparticles) which is no more than 2µm of thickness. Light from a laser diode illuminates the fibre tip and the reflected light (proportional to humidity) is detected.

20 healthy volunteers will be recruited primarily from the Optics and Photonics research group including researchers/PhD students. In the experiment, a standard digital camera will be used to photograph the position of the sensors. Optical fibre humidity sensor and reference fibre will be sited on volunteers' skin e.g. the middle of back, chest and armpit. The optical fibre humidity sensor is used to measure humidity from skin and reference fibre is used to reduce the bending loss simultaneously. The experiment should last approximately 30 minutes for each participant.

The optical fibre humidity sensor will be stitched or taped on a shirt. The sensing film will be covered by a heat and moisture exchange material, so it is not directly contact with skin. Volunteers will be required to put on the shirt by themselves to avoid embarrassment.

At the beginning, all participants will be required to sit quietly for 5 minutes and during this time the setup of experiment will be done. Then, volunteers are asked to do cycling exercise with low speed for 3 minutes by using indoor cycle exercise bike and keep cycling with high speed for 3 minutes and back to low speed cycling for 3 minutes. After 9 minutes cycling, volunteers are required to have a rest for 5 minutes. And repeat last 9 minutes cycling exercise and have a rest for 5 minutes. The humidity from volunteers' body will be recording during the experiment.

After the experiment, the data from two fibres are analysed by MATLAB to acquire the value of relative humidity during the exercise experiment.

Appendix

The University of Nottingham
UNITED KINGDOM · CHINA · MALAYSIA

Monitoring of humidity of human body by using optical fibre sensor

Participant Information Sheet

You are invited to take part in a study which will detect humidity from human body by using optical fibre sensor. Before you decide whether to take part it is important for you to understand why the research is being done and what it will involve. If you would like more information or have any questions please contact Chenyang He (Henry) eexch9@nottingham.ac.uk or Prof Steve Morgan steve.morgan@nottingham.ac.uk .

Background

Humidity monitoring is widely used in healthcare. This study focusses on monitoring humidity from human body during exercise. On the wounded skin, humidity is one of the important parameters for monitoring wound healing. Since humidity monitoring is very helpful in medical and healthcare areas, an optical fibre humidity sensor that allows continuous monitoring would have clear benefits.

Who are the participants?

Up to 20 healthy volunteers will be recruited primarily from the Optics and Photonics Research Group including researchers/PhD students.

Procedure

At the beginning, you will be asked to sit quietly for 5 minutes and during this time the setup of experiment will be done. In the study, a standard digital camera will be used to take a photograph of the placement of sensor on your back through the shirt (you can refuse without giving a reason). Then, volunteers are asked to do cycling exercise with low speed for 3 minutes by using indoor cycle exercise bike and keep cycling with high speed for 3 minutes and back to low speed cycling for 3 minutes. After 9 minutes cycling, volunteers are required to have a rest for 5 minutes. And repeat last 9 minutes cycling exercise and have a rest for 5 minutes. The humidity from your body will be recording during the experiment. The study should last approximately 30 minutes for each participant. If you feel any discomfort you should inform the researcher who will stop the study.

Part 2: Further Information

1. Do I have to take part?

No. Participation in the study is entirely voluntary; it is up to you to decide whether or not to take part. If you do decide to take part, you will be given this Participation Information Sheet to keep and be asked to complete a consent form. However, even if you complete the consent form you are still free to withdraw at any time and without giving a reason.

2. What will happen to me if I take part?

You will be asked to read through the Participant Information Sheet and then asked to complete the Participant Consent Form.

3. What will happen if I do not want to carry on with the study?

You can withdraw from the study at any time without having to provide a reason. If you do withdraw information that can be attributed to you will not be used in our analysis.

4. Will I be paid?

No. There is no reward for this research.

5. Will my taking part in this study be kept confidential?

Yes. All information which is collected about you during the course of the research will be kept strictly confidential and our procedures for handling, processing, storage and destruction of your data are compliant with the Data Protection Act 1998. The data including humidity signals and photographs will be retained for 7 years following any publication, after this time it will be destroyed. All of the data will be stored on password protected computers in the research laboratory of the Optics and Photonic Research Group. Only members of the research group will have access to the data. It is not possible to identify any individuals because any data will be published anonymously.

6. What will happen to the results of the research study?

The results will be used in project reports and in journal publications. The data and pictures will be used anonymously.

7. Who has reviewed the study?

The study has been approved by the University of Nottingham, Faculty of Engineering Ethical Review Committee.

Appendix

The University of Nottingham
UNITED KINGDOM · CHINA · MALAYSIA

Monitoring of humidity of human body by using optical fibre sensor

Consent form

Experiment for the study of humidity monitoring

I confirm that I have read the information sheet and have had the opportunity to ask questions. ☐

I understand that the collected data will be used for journal publications. ☐

I understand that I am free to withdraw at any time and that in this case any information collected will be destroyed and not used. ☐

I understand that all personal information collected during the study will be kept strictly confidential and only anonymised data will be published. ☐

I agree to take part in the above study. ☐

I am fit and healthy, and capable of conducting physical exercise (periods of low and high speed cycling) as required by the study. ☐

Print Name ....

Signature ....

Date ....

Appendix B: Humidity measurement volunteer results

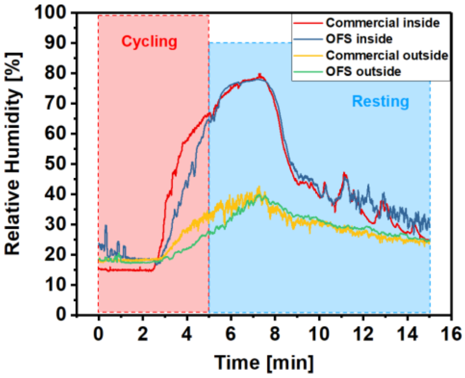

(a)

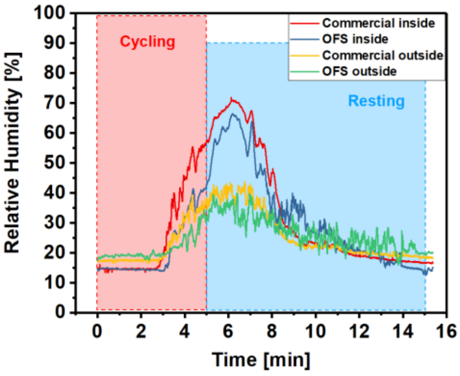

(b)

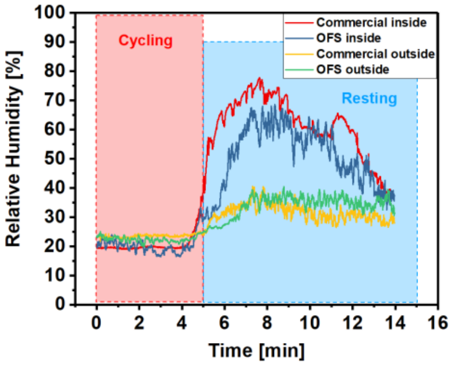

(c)

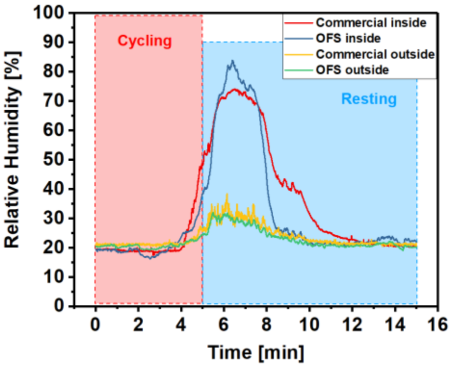

(d)

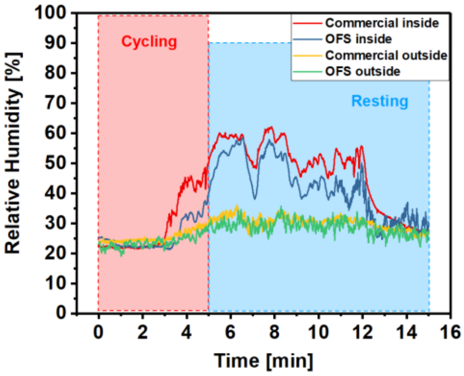

(e)

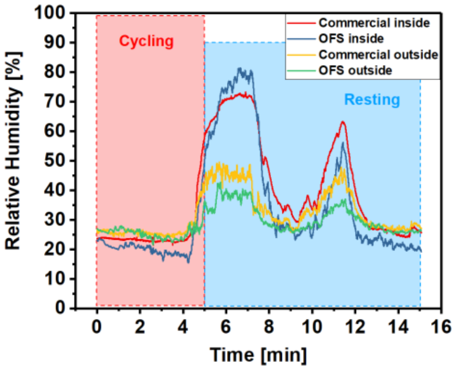

(f)

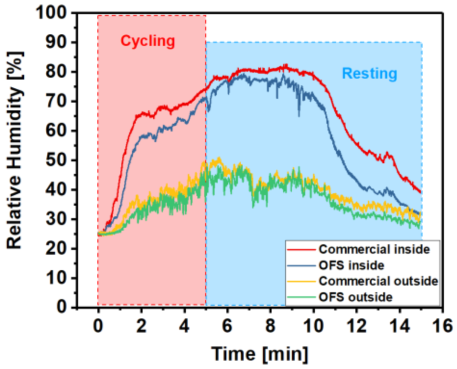
Cycling
Resting
Commercial inside
OFS inside
Commercial outside
OFS outside
Relative Humidity [%]
0 10 20 30 40 50 60 70 80 90 100
0 2 4 6 8 10 12 14 16
Time [min]

(g)

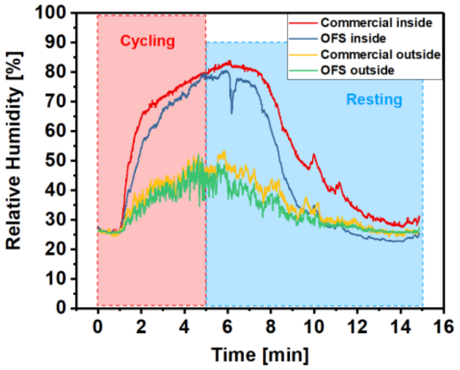
Cycling
Resting
Commercial inside
OFS inside
Commercial outside
OFS outside
Relative Humidity [%]
0 10 20 30 40 50 60 70 80 90 100
0 2 4 6 8 10 12 14 16
Time [min]

(h)

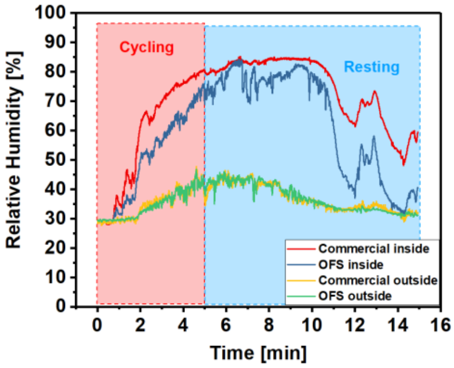
Cycling
Resting
Commercial inside
OFS inside
Commercial outside
OFS outside
Relative Humidity [%]
0 10 20 30 40 50 60 70 80 90 100
0 2 4 6 8 10 12 14 16
Time [min]

(i)

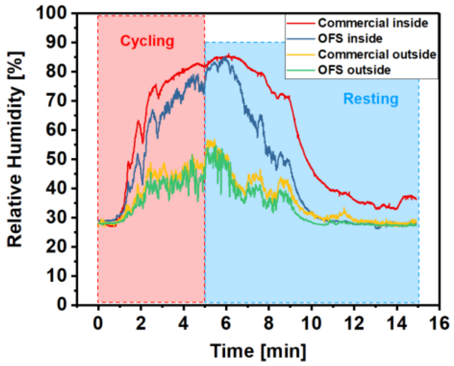
Cycling
Resting
Commercial inside
OFS inside
Commercial outside
OFS outside
Relative Humidity [%]
0 10 20 30 40 50 60 70 80 90 100
0 2 4 6 8 10 12 14 16
Time [min]

(j)

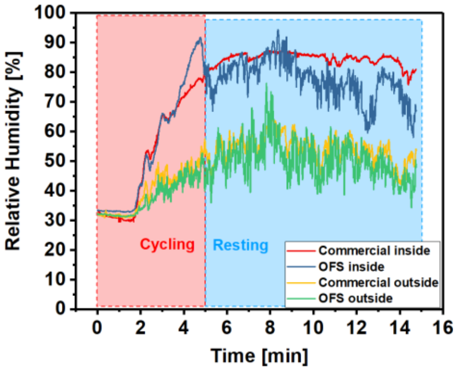
Cycling
Resting
Commercial inside
OFS inside
Commercial outside
OFS outside
Relative Humidity [%]
0 10 20 30 40 50 60 70 80 90 100
0 2 4 6 8 10 12 14 16
Time [min]

(k)

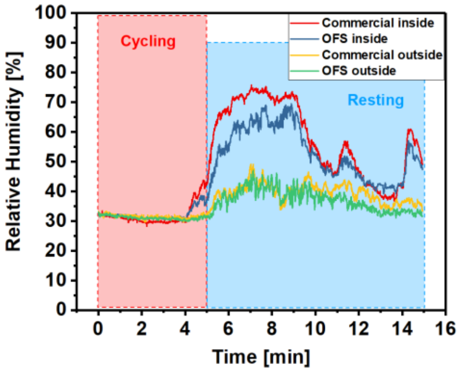
Cycling
Resting
Commercial inside
OFS inside
Commercial outside
OFS outside
Relative Humidity [%]
0 10 20 30 40 50 60 70 80 90 100
0 2 4 6 8 10 12 14 16
Time [min]

(l)

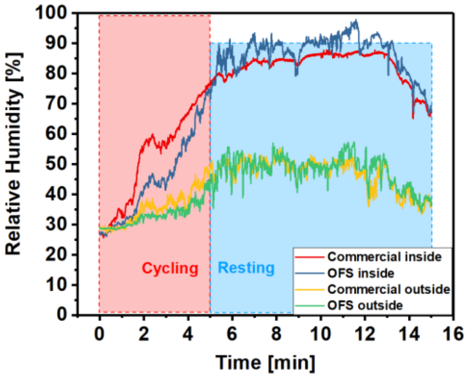
Cycling
Resting
Commercial inside
OFS inside
Commercial outside
OFS outside
Relative Humidity [%]
0 10 20 30 40 50 60 70 80 90 100
0 2 4 6 8 10 12 14 16
Time [min]

(m)

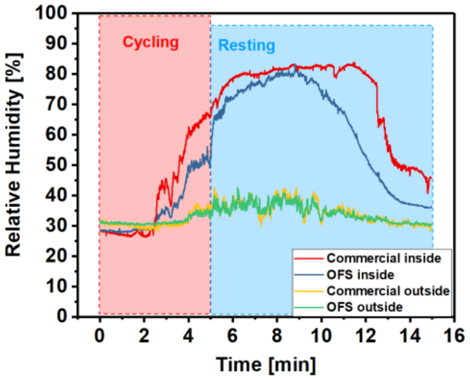
Cycling
Resting
Commercial inside
OFS inside
Commercial outside
OFS outside
Relative Humidity [%]
0 10 20 30 40 50 60 70 80 90 100
0 2 4 6 8 10 12 14 16
Time [min]

(n)

Appendix

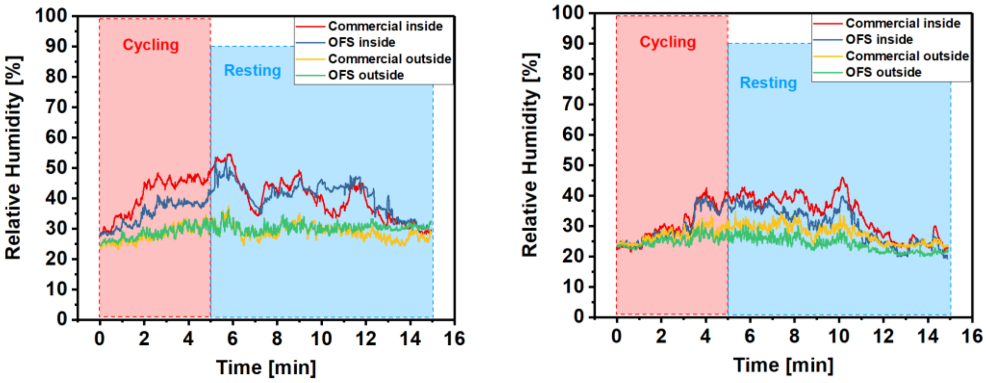

(o) (p)

Figure S 1 The RH reading from the sensing probe (inner, blue line and outer, green line) and commercial sensor (inner, red line and outer, yellow line) measured during the cycling exercise with 100% cotton T-shirt (a) and 100% polyester T-shirt (b) for V2, cotton (c) and polyester (d) for V3, cotton (e) and polyester (f) for V4, cotton (g) and polyester (h) for V5, cotton (i) and polyester (j) for V6, cotton (k) and polyester (l) for V7, cotton (m) and polyester (n) for V8, cotton (o) and polyester (p) for V9.

Appendix C: Investigation of the thermochromic material on the substrates

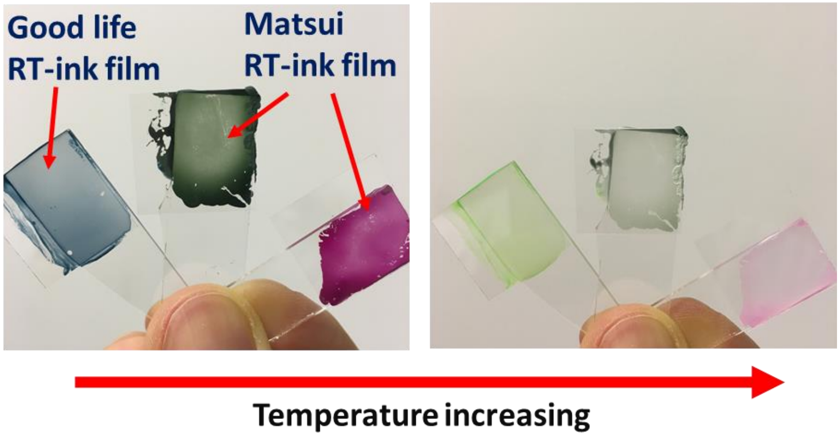

Figure S 2 Preliminary thermochromism test of RT-leuco-ink in dry film.

The RT-ink solution is dropped on the substrates using pipette and then covered by cover slides and left at room temperature over night for drying naturally. For further thermochromism investigation of the RT-leuco-ink after drying, as Figure S 2 shown, heating the dry ink film using a heat gun, the same phenomenon appears in the case of the substrate as those in solution. Therefore, the RT-leuco-ink has the potential to be a temperature sensitive film using an optical fibre sensing technique.

Appendix

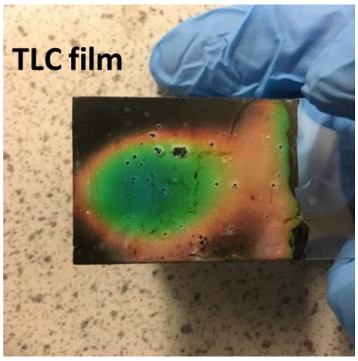

(a)

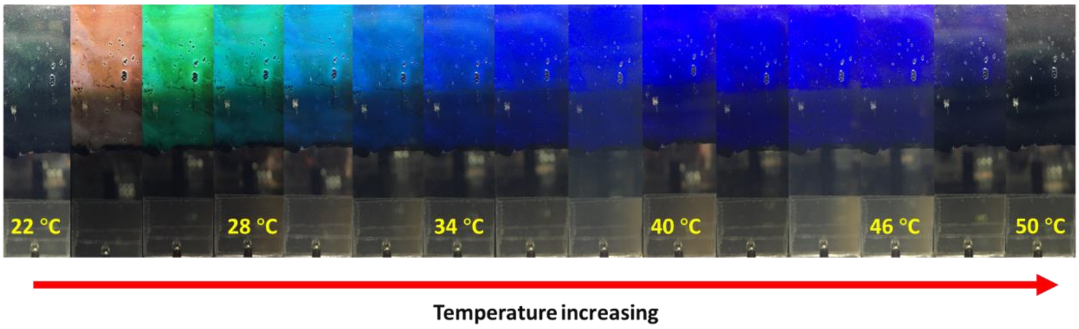

(b)

Figure S 3 (a) Fingerprint temperature mapping of TLC film. (b) Thermochromism investigation of TLC using climatic chamber.

The TLC was coated on a black background precoated glass substrate for improving visualization of the thermochromic process. A fingerprint temperature mapping can be observed in the Figure S 3(a). Since the edge of the finger is not touching the substrate, the temperature should decrease from the centre to the surrounding area gradually. The colour of the fingerprint is blue (higher temperature) to green and red (lower temperature) from the centre to edge area of the finger.

In addition, the TLC film coated substrate was tested thoroughly using the climatic chamber. Figure S 3(b) illustrates the colour change of TLC film at different temperatures. It should be noted that the colour turns from red to green and cyan, while the temperature has only increased by around 4 °C. However, the colour of the membrane remains blue between 30 to 46 °C (16 °C). This phenomenon would be also observed in spectral measurements, i.e. significant spectral signal change in the temperature range between 24 to 28 °C as compared to temperatures above 28 °C.